

AN INVESTIGATION OF INJECTORS FOR  
USE WITH HIGH VAPOR PRESSURE PROPELLANTS  
WITH APPLICATIONS TO HYBRID ROCKETS

A DISSERTATION  
SUBMITTED TO THE DEPARTMENT OF  
AERONAUTICS & ASTRONAUTICS  
AND THE COMMITTEE ON GRADUATE STUDIES  
OF STANFORD UNIVERSITY  
IN PARTIAL FULFILLMENT OF THE REQUIREMENTS  
FOR THE DEGREE OF  
DOCTOR OF PHILOSOPHY

Benjamin S. Waxman

June 2014

© 2014 by Benjamin Stephen Waxman. All Rights Reserved.  
Re-distributed by Stanford University under license with the author.



This work is licensed under a Creative Commons Attribution-  
Noncommercial 3.0 United States License.  
<http://creativecommons.org/licenses/by-nc/3.0/us/>

This dissertation is online at: <http://purl.stanford.edu/ng346xh6244>

I certify that I have read this dissertation and that, in my opinion, it is fully adequate in scope and quality as a dissertation for the degree of Doctor of Philosophy.

**Brian Cantwell, Primary Adviser**

I certify that I have read this dissertation and that, in my opinion, it is fully adequate in scope and quality as a dissertation for the degree of Doctor of Philosophy.

**Juan Alonso**

I certify that I have read this dissertation and that, in my opinion, it is fully adequate in scope and quality as a dissertation for the degree of Doctor of Philosophy.

**Gregory Zilliac**

Approved for the Stanford University Committee on Graduate Studies.

**Patricia J. Gumpert, Vice Provost for Graduate Education**

*This signature page was generated electronically upon submission of this dissertation in electronic format. An original signed hard copy of the signature page is on file in University Archives.*

# Abstract

Interest in nitrous oxide based hybrid rockets is at an all time high. Nitrous oxide ( $N_2O$ ) is a unique oxidizer because it exhibits a high vapor pressure at room temperature ( $\approx 730$  psia or 5.03 MPa). Due to this high vapor pressure, liquid nitrous oxide can be expelled from a tank without the use of complicated pumps or pressurization systems required by most traditional liquid rocket systems. This results in weight savings and design simplicity. Additional benefits of nitrous oxide include storability, ease of handling, and relative safety compared to traditional liquid oxidizers.

The design and modeling of injectors for use with high vapor pressure propellants such as nitrous oxide is made complicated due to the possibility of two-phase flow. The operating pressures within rocket propellant feed systems can often drop below the vapor pressure for these unique propellants, especially within the injector. Injectors operating under these conditions are likely to exhibit cavitation, resulting in significant vapor formation and limitation of mass flow rate. A variety of two-phase flow models which attempt to account for this phenomenon are presented and discussed, however none have proven reliable enough to replace traditional experimental injector flow studies. For this reason, a small scale experimental injector cold flow rig was designed, and a test campaign was carried out in an effort to characterize the mass flow rate performance of nitrous oxide rocket injectors over a broad range of operating conditions. Some representative results from this campaign are presented.

The Peregrine Sounding Rocket is a hybrid rocket that runs on paraffin wax and nitrous oxide. Its development is a joint effort between NASA Ames Research Center,

Stanford University, and Space Propulsion Group, Inc. For years, progress of the Peregrine program has been hampered by combustion instability problems. Based upon results from the aforementioned small scale injector experiments, a powerful, yet simple solution to the so-called feed system coupled combustion instability was discovered, the details of which are presented. This work also led to the invention of a new class of rocket propellant injectors designed specifically to decrease the likelihood of this type of combustion instability. An in-depth discussion of the proposed design and operation of this novel injection scheme is included, along with the presentation of some prototype cold flow testing results which served as a successful proof of concept.

# Acknowledgements

The completion of my Ph.D. and this dissertation was only possible thanks to the tremendous support from my colleagues, friends, and family. I would like to thank a few of the individuals who have helped make my years at Stanford the most enjoyable and productive of my life.

First I would like to thank my adviser, Professor Brian Cantwell, for launching my career in the field of rocket propulsion. Brian enthusiastically welcomed me into his research group, and matched me with the Peregrine Sounding Rocket program at NASA Ames Research Center, which served as the backbone of my graduate work. As an adviser, Brian guided me in the process of selecting the topic for my thesis work, while allowing me to determine the course of my research, of which I am extremely grateful. I would also like to thank the other members of my reading committee, Professor Juan Alonso and Greg Zilliac, for their commitment to helping make the completion of this dissertation a reality.

I would like to express my immense gratitude to Greg Zilliac for his invaluable guidance and teaching while acting as my mentor over the past five years. So much of my development as a rocket propulsion engineer is owed to him, and I could not have completed my Ph.D. without his support, encouragement, and innumerable stimulating technical discussions that I will miss dearly moving forward. I would also like to thank Arif Karabeyoglu for introducing me to the design and analysis of hybrid rockets. I have the utmost respect for his expertise in rocket propulsion, especially in the area of combustion stability, and I greatly value his willingness to always offer

assistance and enlightening discussion when it comes to solving challenging technical problems. I am also extremely grateful to Kurt Long and Rabi Mehta who were my gracious and supportive hosts while I interned and worked from the Fluid Mechanics Lab at NASA Ames. The FML team made me feel welcome from day one.

The experimental work described in this dissertation would not have been possible without the help of my lab mate, Jonah Zimmerman. Jonah and I worked together in the construction of the cold flow test rig, and Jonah volunteered much of his time, effort, and even humor to assist in my testing. I would also like to thank the rest of my lab mates, including Ashley Chandler, Tim Szwarc, and Beth Jens for making lab not just a place to come for work, but a place to spend time with friends.

I will value the friends I have made at Stanford for the rest of my life, and thanks to them, I have had more fun in graduate school than I could have ever imagined. Thanks to Orion King, Steven Petsche, Joe Orsini, and Josh Mollner for being the best roommates anybody could ask for, listening to me play videos of rocket tests or kayaking on repeat, and giving me your honest advice whenever I needed it. Also, thank you to all of the great friends (and paddlers) I have met through kayaking at Stanford, including Orion King, Allen Roberts, Ruth Emerson, and Ross Allen, among others. It is comforting to know that you've had my back both on and off the river.

Finally, I am only in the position to be writing this now thanks to the unyielding love and support I have received from my family. To my mother Stephanie, you are truly a superhero, and my biggest role model. I could never have made it through without the encouragement and support that you and Gary have always given me. Thanks to my father Jeff for sparking my interest in aerospace at a young age. You and Lisa have also helped to foster my lifelong love for music for which I am extremely grateful. And thank you to my sister Hallie, for inspiring me to be creative and for being the best sister there is.

This work would not have been possible without the financial support from the National Defense Science and Engineering Graduate Fellowship (NDSEG) and the Department of Aeronautics & Astronautics at Stanford University. Additionally, some of my work on the Peregrine Sounding Rocket was supported by the National Aeronautics and Space Administration under Prime Contract Number NAS2-03144 awarded to the University of California, Santa Cruz, University Affiliated Research Center (UARC), as well as by the NASA Ames Fluid Mechanics Lab.

# Contents

<b>Abstract</b>	<b>iv</b>
<b>Acknowledgements</b>	<b>vi</b>
<b>List of Tables</b>	<b>xiv</b>
<b>List of Figures</b>	<b>xx</b>
<b>Nomenclature</b>	<b>xxi</b>
<b>1 Introduction</b>	<b>1</b>
1.1 Chemical Rocket Classification . . . . .	1
1.2 Hybrid Rocket Background . . . . .	6
1.3 Nitrous Oxide . . . . .	11
1.4 Propellant Injectors . . . . .	12
1.5 Combustion Instability . . . . .	16
1.6 Organization of this Dissertation . . . . .	17
<b>2 Injector Flow Rate Modeling</b>	<b>18</b>
2.1 Single-Phase Flow in Propellant Injectors . . . . .	19
2.1.1 Single-Phase Liquid Flow . . . . .	19
2.1.1.1 Incompressible Liquid Flow . . . . .	20
2.1.1.2 Compressibility Effects . . . . .	27
2.1.1.3 Effect of Inlet Geometry on $C_{vc}$ . . . . .	30
2.1.1.4 Frictional Effects (Inlet Geometry and $Re_D$ ) . . . . .	32

2.1.2	Single-Phase Gas Flow: Perfect Gas Model . . . . .	36
2.2	Two-Phase Flow in Propellant Injectors . . . . .	42
2.2.1	Equilibrium Models . . . . .	49
2.2.1.1	Homogeneous Models . . . . .	50
2.2.1.1.1	Homogeneous Equilibrium Model . . . . .	50
2.2.1.1.2	Babitskiy . . . . .	55
2.2.1.2	Non-Homogeneous Models . . . . .	60
2.2.1.2.1	Moody . . . . .	64
2.2.1.2.2	Fauske . . . . .	66
2.2.2	Non-Equilibrium Models . . . . .	66
2.2.2.1	Frozen Non-Equilibrium Methods . . . . .	71
2.2.2.1.1	Burnell . . . . .	71
2.2.2.1.2	Zaloudek . . . . .	74
2.2.2.1.3	Proposed Model . . . . .	76
2.2.2.2	Generalized Non-Equilibrium Methods . . . . .	78
2.2.2.2.1	Dyer . . . . .	78
2.3	Injector Flow Rate Modeling Conclusions . . . . .	83
<b>3</b>	<b>Injector Cold Flow Experiments</b>	<b>84</b>
3.1	Experimental Cold Flow Testing Campaign . . . . .	85
3.1.1	Cold Flow Apparatus Design . . . . .	85
3.1.1.1	Test Section . . . . .	85
3.1.1.2	Auxiliary Systems . . . . .	87
3.1.1.3	Injector Inserts . . . . .	89
3.1.2	Design Analysis . . . . .	90
3.1.2.1	Structural . . . . .	90
3.1.2.2	Fluid . . . . .	91
3.1.3	Operation . . . . .	94
3.1.3.1	$CO_2$ as an Analog to $N_2O$ . . . . .	94
3.1.3.2	Operating Procedure . . . . .	95
3.1.3.2.1	Test Preparation . . . . .	97

3.1.3.2.2	Running a Test . . . . .	97
3.1.3.2.3	Data Analysis . . . . .	98
3.2	Sample Cold Flow Testing Results . . . . .	103
3.2.1	Effect of Supercharge Level . . . . .	103
3.2.2	Effect of Injector Hole Diameter and L/D Ratio . . . . .	105
3.2.3	Comparison of $N_2O$ and $CO_2$ Results . . . . .	108
3.2.4	Effect of Injector Hole Inlet Geometry . . . . .	110
3.3	Comparison with Two-Phase Flow Models . . . . .	112
3.4	Cold Flow Testing Conclusions . . . . .	115
<b>4</b>	<b>Peregrine Hybrid Sounding Rocket</b>	<b>117</b>
4.1	Program Objectives . . . . .	117
4.2	Sounding Rocket Architecture and Early Testing . . . . .	121
4.3	Heavyweight Ground Testing Combustion Facility . . . . .	125
4.4	Ground Testing Combustion Instabilities . . . . .	130
4.4.1	Peregrine Test E2 . . . . .	130
4.4.2	Peregrine Test E3-2 . . . . .	134
<b>5</b>	<b>Feed System Coupled Combustion Instability</b>	<b>138</b>
5.1	Classification of Combustion Instabilities . . . . .	138
5.2	Feed System Coupled Instability Theory and Modeling . . . . .	140
5.2.1	Transient Physical Model . . . . .	141
5.2.1.1	Injector Model . . . . .	141
5.2.1.2	Pipe Model . . . . .	143
5.2.1.3	Combustion Chamber Model . . . . .	146
5.2.2	Mathematical Solution . . . . .	147
5.2.2.1	Transfer Function Formalism . . . . .	148
5.2.2.2	Example Case with No Feed System Isolation . . . . .	150
5.2.2.3	Example Case with Feed System Isolation . . . . .	153
5.3	Suppression of Feed System Coupled Instabilities . . . . .	161
5.3.1	Feed System Isolation . . . . .	162
5.3.1.1	Cavitating Venturis . . . . .	162

5.3.1.2	Injector as an Isolating Element . . . . .	163
5.3.2	Cold Flow Testing: Simulated Chamber Pressure Oscillation .	166
5.3.2.1	Mass Flow Rate Insensitivity to Chamber Pressure .	166
5.3.2.2	Pressure Disturbance Isolation . . . . .	170
5.4	Application to Peregrine Combustion Stabilization . . . . .	173
5.4.1	Test E3-4 Results . . . . .	175
5.4.2	Test E4-1 Results . . . . .	178
5.5	Combustion Instability Conclusions . . . . .	181
<b>6</b>	<b>A Novel Hybrid Rocket Injection Scheme</b>	<b>183</b>
6.1	Undesired Consequences of Stabilization Criteria . . . . .	184
6.2	Improved Isolating Injection Scheme . . . . .	185
6.2.1	Goal . . . . .	185
6.2.2	Approach . . . . .	186
6.2.3	Sample Analysis . . . . .	188
6.3	Sample Design/Performance Cases . . . . .	195
6.3.1	Case #1 . . . . .	196
6.3.2	Case #2 . . . . .	196
6.3.3	Case #3 . . . . .	199
6.3.4	Case #4 . . . . .	199
6.4	Prototype Development and Cold Flow Testing . . . . .	199
6.4.1	Prototype Design . . . . .	202
6.4.2	Cold Flow Testing . . . . .	202
6.5	Novel Injection Scheme Conclusions . . . . .	205
<b>7</b>	<b>Summary and Conclusions</b>	<b>206</b>
7.1	Mass Flow Rate Modeling . . . . .	206
7.2	Experimental Cold Flow Testing . . . . .	208
7.3	Applications to Hybrid Rocket Combustion Instability . . . . .	209
7.4	Future Work . . . . .	210
<b>A</b>	<b>Cold Flow Reference Test Data</b>	<b>212</b>

<b>B Cold Flow Visualization Experiments</b>	<b>224</b>
B.1 Background . . . . .	224
B.2 Experimental Setup . . . . .	227
B.3 Visualization Results and Discussion . . . . .	230
<b>C Instrumentation Specifications</b>	<b>237</b>
<b>D Uncertainty Analysis</b>	<b>239</b>
<b>Bibliography</b>	<b>241</b>

# List of Tables

1.1	Sample Values of Hybrid Rocket Ballistic Coefficients $a$ and $n$ . . . . .	9
1.2	Important Thermodynamic Properties of $N_2O$ . . . . .	12
2.1	Classification of Different Two-Phase Flow Models . . . . .	48
3.1	Cold Flow Apparatus Injector Geometries . . . . .	90
3.2	Comparison of Thermodynamic Properties of $N_2O$ and $CO_2$ . . . . .	95
4.1	Peregrine Sounding Rocket Design and Performance Overview . . . . .	121
5.1	Simulated Chamber Pressure Oscillation Tests: Data Summary . . . . .	170
5.2	Operating Parameters for Tests E2, E3-2, and E3-4 . . . . .	175
A.1	Reference Injector Design Geometry . . . . .	212
A.2	Reference Cold Flow Data Outline . . . . .	213
B.1	Overview of Injector Designs for Visualization Experiments . . . . .	228
C.1	Instrumentation Specifications . . . . .	237

# List of Figures

1.1	Liquid Propellant Rocket Schematic . . . . .	3
1.2	Solid Propellant Rocket Schematic . . . . .	4
1.3	Hybrid Propellant Rocket Schematic . . . . .	6
1.4	Schematic of Diffusion Flame in Hybrid Rockets . . . . .	7
1.5	Properties of $N_2O$ vs. Temperature . . . . .	13
1.6	Two Hybrid Rocket Firings with Different Injection Schemes . . . . .	14
1.7	$C_d$ Variations Using $N_2O$ in Full-Scale Hybrid Rocket Tests . . . . .	15
2.1	Conceptual Orifice Style Injector Hole . . . . .	20
2.2	$\dot{m}_{SPI}$ vs. $\Delta P$ for Saturated $N_2O$ . . . . .	26
2.3	$\dot{m}_{SPI}$ vs. $P_2$ for Saturated $N_2O$ . . . . .	26
2.4	$\dot{m}_{SPI}$ vs. $\Delta P$ for Supercharged $N_2O$ . . . . .	28
2.5	$\dot{m}_{SPI}$ vs. $P_2$ for Supercharged $N_2O$ . . . . .	28
2.6	Compressible Liquid Correction Factor . . . . .	30
2.7	$C_{cv}$ vs $r/D$ . . . . .	33
2.8	$C_{cv}$ vs $r$ . . . . .	33
2.9	$C_d$ vs $Re_D$ for Square Edged Injectors of Varying $L/D$ (Laminar) . .	37
2.10	$C_d$ vs $Re_D$ for Square Edged Injectors of Varying $L/D$ (Turbulent) . .	37
2.11	$C_d$ vs $Re_D$ for an Injector of Varying Inlet $K$ value (Laminar) . . . .	38
2.12	$C_d$ vs $Re_D$ for an Injector of Varying Inlet $K$ value (Turbulent) . . . .	38
2.13	$\dot{m}_{PG}$ vs. $P_2/P_1$ for Gaseous $N_2O$ . . . . .	43
2.14	$\dot{m}_{crit\ PG}$ vs. $P_1$ for $N_2O$ at Varied Temperatures . . . . .	43
2.15	$\gamma_1$ vs. $P_1$ for $N_2O$ at Varied Temperatures . . . . .	44
2.16	$\rho_1$ vs. $P_1$ for $N_2O$ at Varied Temperatures . . . . .	44

2.17	Conceptual Pressure Evolution Within a Propellant Injector . . . . .	46
2.18	Mass Flow Rate of $CO_2$ Through Orifices . . . . .	47
2.19	Homogeneous Equilibrium Model . . . . .	53
2.20	$\dot{m}_{HEM}$ vs. $\Delta P$ for Supercharged $N_2O$ . . . . .	56
2.21	$C_{d_{HEM}}$ vs. $\Delta P$ for Supercharged $N_2O$ . . . . .	56
2.22	$\dot{m}_{HEM}$ vs. $P_2/P_v$ for Supercharged $N_2O$ . . . . .	57
2.23	$C_{d_{HEM}}$ vs. $P_2/P_v$ for Supercharged $N_2O$ . . . . .	57
2.24	$C_{d_{HEM}}$ vs. Cavitation Number $K$ for Supercharged $N_2O$ . . . . .	58
2.25	$\dot{m}_{crit\ HEM}$ vs. $P_{super}^1$ for Supercharged $N_2O$ . . . . .	59
2.26	$\dot{m}_{crit\ HEM}$ vs. $P_v$ for Saturated $N_2O$ . . . . .	59
2.27	$\dot{m}_{BAB}$ vs. $\Delta P$ for Supercharged $N_2O$ . . . . .	61
2.28	$C_{d_{BAB}}$ vs. $\Delta P$ for Supercharged $N_2O$ . . . . .	61
2.29	$\dot{m}_{crit\ BAB}$ vs. $P_{super}^1$ for Supercharged $N_2O$ . . . . .	62
2.30	$\dot{m}_{crit}$ vs. $P_{super}^1$ for Supercharged $N_2O$ (Babitskiy vs. HEM) . . . . .	63
2.31	$\dot{m}_{crit}$ vs. $P_v$ for Saturated $N_2O$ (Babitskiy vs. HEM) . . . . .	63
2.32	$\dot{m}_{MOODY}$ vs. $\Delta P$ for Supercharged $N_2O$ . . . . .	67
2.33	$C_{d_{MOODY}}$ vs. $\Delta P$ for Supercharged $N_2O$ . . . . .	67
2.34	$\dot{m}_{crit}$ vs. $P_{super}^1$ for Supercharged $N_2O$ (Moody vs. Babitskiy and HEM) . . . . .	68
2.35	$\dot{m}_{crit}$ vs. $P_v$ for Saturated $N_2O$ (Moody vs. Babitskiy and HEM) . . . . .	68
2.36	Metastable States Overview . . . . .	70
2.37	$C$ Coefficient vs. $P_v$ for Burnell's Critical Flow Model . . . . .	72
2.38	$\dot{m}_{BURNELL}$ vs. $P_2/P_v$ for Supercharged $N_2O$ . . . . .	73
2.39	$C_{d_{BURNELL}}$ vs. $P_2/P_v$ for Supercharged $N_2O$ . . . . .	73
2.40	$\dot{m}_{crit}$ vs. $P_{super}^1$ for Supercharged $N_2O$ (Burnell Comparison) . . . . .	75
2.41	$\dot{m}_{crit}$ vs. $P_v$ for Saturated $N_2O$ (Burnell Comparison) . . . . .	75
2.42	$\dot{m}_{crit}$ vs. $P_{super}^1$ for Supercharged $N_2O$ Using Proposed Model . . . . .	77
2.43	$\dot{m}_{crit}$ vs. $P_v$ for Saturated $N_2O$ Using Proposed Model . . . . .	77
2.44	$\dot{m}_{DYER}$ vs. $\Delta P$ for Supercharged $N_2O$ . . . . .	80
2.45	$\dot{m}_{crit}$ vs. $P_{super}^1$ for Supercharged $N_2O$ (Dyer Comparison) . . . . .	82
2.46	$\dot{m}_{crit}$ vs. $P_v$ for Saturated $N_2O$ (Dyer Comparison) . . . . .	82

3.1	Cold Flow Apparatus Test Section . . . . .	86
3.2	Test Section Diffuser and Pre-Injector Volume . . . . .	87
3.3	Cold Flow Apparatus Run Tank and Overall Assembly . . . . .	88
3.4	Cold Flow Apparatus Injector Insert . . . . .	91
3.5	Sample Test Section Structural Analysis (FEA) . . . . .	92
3.6	Sample Test Section Diffuser CFD Results . . . . .	93
3.7	Comparison of Thermodynamic Properties of $N_2O$ and $CO_2$ . . . . .	96
3.8	Example Pressure Time-Histories for Cold Flow Test . . . . .	99
3.9	Example Temperature Time-History for Cold Flow Test . . . . .	99
3.10	Example Mass Flow Rate Time-History for Cold Flow Test . . . . .	100
3.11	Mass Flow Rate vs. Injector $\Delta P$ for Typical Cold Flow Test . . . . .	102
3.12	Effective $C_d$ vs. Injector $\Delta P$ for Typical Cold Flow Test . . . . .	102
3.13	Mass Flow Rate vs. Injector $\Delta P$ with Varied Supercharge . . . . .	106
3.14	Effective $C_d$ vs. Injector $\Delta P$ with Varied Supercharge . . . . .	106
3.15	Single Phase $C_d$ for Orifices of Varied Diameter . . . . .	107
3.16	Mass Flow Rate vs. $P_2/P_v$ for Injectors of Varied L/D . . . . .	109
3.17	Critical Mass Flow Rate vs. Supercharge for Injectors of Varied L/D	109
3.18	Comparison of $N_2O$ to $CO_2$ : Mass Flow Rate . . . . .	110
3.19	Comparison of $N_2O$ to $CO_2$ : Critical Mass Flow Rate . . . . .	111
3.20	Comparison of $N_2O$ to $CO_2$ : Single-Phase $C_d$ . . . . .	111
3.21	Single Phase $C_d$ for Injectors of Varied Inlet Geometry . . . . .	113
3.22	Critical Mass Flow Rate for Injectors of Varied Inlet Geometry . . . . .	113
3.23	Comparison of Two-Phase Flow Models to Experimental Results . . . . .	116
4.1	Hybrid Rocket Liquefying Fuel Concept . . . . .	119
4.2	Multi-Port and Single-Port Fuel Grain Designs . . . . .	119
4.3	Sub-Scale Hybrid Rocket Testing at Stanford . . . . .	120
4.4	Peregrine Sounding Rocket Cross Section . . . . .	121
4.5	Model of Early Peregrine Flight Weight Oxidizer Tank . . . . .	122
4.6	Peregrine Payload and Nosecone . . . . .	123
4.7	Model of Early Peregrine Flight Weight Combustion Chamber . . . . .	124

4.8	Horizontal Ground Test Setup . . . . .	124
4.9	Peregrine Hot Fire Using Near Flight Weight Chamber . . . . .	125
4.10	Peregrine Heavyweight Combustion Facility Chamber Cross-Section .	126
4.11	Structural Analysis of Heavyweight Fore End . . . . .	127
4.12	Structural Analysis of Heavyweight Blow Out Nozzle . . . . .	128
4.13	Heavyweight Blow Out Nozzle Test . . . . .	129
4.14	Hot Fire Test in the Peregrine Heavyweight Combustion Facility . . .	129
4.15	Peregrine Test E2: Chamber Pressure Time-History . . . . .	133
4.16	Peregrine Test E2: Chamber Pressure (Zoomed In) . . . . .	133
4.17	Peregrine Test E2: FFT . . . . .	134
4.18	Peregrine Test E3-2: Chamber Pressure Time-History . . . . .	136
4.19	Peregrine Test E3-2: Chamber Pressure (Zoomed In) . . . . .	136
4.20	Peregrine Test E3-2: FFT . . . . .	137
5.1	Schematic for Injector Hole Used in Transient Analysis. . . . .	142
5.2	Schematic for the Feed System Pipe Used in Transient Analysis. . . .	144
5.3	Schematic for the Combustion Chamber Used in Transient Analysis. .	146
5.4	Example Case Transfer Function Surface Plot: No Isolation . . . . .	152
5.5	Example Case Transfer Function Contour Plot: No Isolation . . . . .	152
5.6	Feed System Response Amplification vs. $\theta_o$ and $R_p$ : No Isolation . .	154
5.7	Feed System Response Frequency vs. $\theta_o$ and $R_p$ : No Isolation . . . .	154
5.8	Feed System Response Amplification vs. $\theta_o$ and $R_v$ : No Isolation . . .	155
5.9	Feed System Response Frequency vs. $\theta_o$ and $R_v$ : No Isolation . . . .	155
5.10	Example Case Transfer Function Surface Plot: Isolation . . . . .	157
5.11	Example Case Transfer Function Contour Plot: Isolation . . . . .	157
5.12	Feed System Response Amplification vs. $\theta_o$ and $R_p$ : Isolation . . . .	158
5.13	Feed System Response Frequency vs. $\theta_o$ and $R_p$ : Isolation . . . . .	158
5.14	Feed System Response Amplification vs. $\theta_o$ and $R_v$ : Isolation . . . .	159
5.15	Feed System Response Frequency vs. $\theta_o$ and $R_v$ : Isolation . . . . .	159
5.16	Example Case Transfer Function Surface Plot: Isolation ( $R_p = 0$ ) . .	160
5.17	Cavitating Venturi Schematic . . . . .	164

5.18	Mass Flow Rate vs. $P_2/P_v$ with Varied Supercharge . . . . .	166
5.19	Oscillatory Tests ( $T = \text{const.}$ ): Pressure Time-Histories . . . . .	168
5.20	Oscillatory Tests ( $T = \text{const.}$ ): Mass Flow Rate Time-Histories . . . . .	168
5.21	Oscillatory Tests ( $T$ Varied): Pressure Time-Histories . . . . .	171
5.22	Oscillatory Tests ( $T$ Varied): Mass Flow Rate Time-Histories . . . . .	171
5.23	Saturation Pressure $P_v$ of Carbon Dioxide vs. Temperature . . . . .	172
5.24	Disturbance Isolation in Oscillatory Tests: . . . . .	173
5.25	Peregrine Test E3-4: Chamber Pressure Time-History . . . . .	177
5.26	Peregrine Test E3-4: Chamber Pressure (Zoomed In) . . . . .	177
5.27	Peregrine Test E3-4: FFT . . . . .	178
5.28	Peregrine Test E4-1: Chamber Pressure Time-History . . . . .	180
5.29	Peregrine Test E4-1: Chamber Pressure (Zoomed In) . . . . .	180
5.30	Peregrine Test E4-1: FFT . . . . .	181
6.1	Proposed Injection Scheme Design Schematic . . . . .	187
6.2	Notional Cross-Section of Proposed Novel Injection Scheme . . . . .	189
6.3	Sample Analysis Case #1: $N_2O$ at -20 °C (253 K) . . . . .	197
6.4	Sample Analysis Case #1: LOX at -200 °C (73 K) . . . . .	197
6.5	Sample Analysis Case #2: $N_2O$ at 1000 psia (6.89 MPa) . . . . .	198
6.6	Sample Analysis Case #2: Methane at 1000 psia (6.89 MPa) . . . . .	198
6.7	Sample Analysis Case #3: $N_2O$ with $A_2/A_t = 2$ . . . . .	200
6.8	Sample Analysis Case #3: $N_2O$ with $A_2/A_t = 5$ . . . . .	200
6.9	Sample Analysis Case #4: $N_2O$ at -60 °C (213 K) . . . . .	201
6.10	Sample Analysis Case #4: Ethanol at 20 °C (293 K) . . . . .	201
6.11	Cross-Section of Novel Injector Prototype Design . . . . .	203
6.12	$\dot{m}$ vs. $P_2$ for Novel Injector Prototype Cold Flow Tests . . . . .	204
6.13	$C_d$ vs. $P_2$ for Novel Injector Prototype Cold Flow Tests . . . . .	204
A.1	Injector 1: Mass Flow Rate ( $N_2O$ ) . . . . .	214
A.2	Injector 1: $C_d$ ( $N_2O$ ) . . . . .	214
A.3	Injector 1: Mass Flow Rate ( $CO_2$ ) . . . . .	215
A.4	Injector 1: $C_d$ ( $CO_2$ ) . . . . .	215

A.5	Injector 2: Mass Flow Rate ( $N_2O$ ) . . . . .	216
A.6	Injector 2: $C_d$ ( $N_2O$ ) . . . . .	216
A.7	Injector 2: Mass Flow Rate ( $CO_2$ ) . . . . .	217
A.8	Injector 2: $C_d$ ( $CO_2$ ) . . . . .	217
A.9	Injector 3: Mass Flow Rate ( $N_2O$ ) . . . . .	218
A.10	Injector 3: $C_d$ ( $N_2O$ ) . . . . .	218
A.11	Injector 3: Mass Flow Rate ( $CO_2$ ) . . . . .	219
A.12	Injector 3: $C_d$ ( $CO_2$ ) . . . . .	219
A.13	Injector 4: Mass Flow Rate ( $CO_2$ ) . . . . .	220
A.14	Injector 4: $C_d$ ( $CO_2$ ) . . . . .	220
A.15	Injector 5: Mass Flow Rate ( $N_2O$ ) . . . . .	221
A.16	Injector 5: $C_d$ ( $N_2O$ ) . . . . .	221
A.17	Injector 6: Mass Flow Rate ( $CO_2$ ) . . . . .	222
A.18	Injector 6: $C_d$ ( $CO_2$ ) . . . . .	222
A.19	Injector 7: Mass Flow Rate ( $N_2O$ ) . . . . .	223
A.20	Injector 7: $C_d$ ( $N_2O$ ) . . . . .	223
B.1	Critical Jakob and Weber Number Correlations for Flashing . . . . .	226
B.2	Cross-sections of Injector Inserts for Visualization Experiments . . . . .	229
B.3	Brass and Plastic Injectors for Visualization Experiments . . . . .	230
B.4	Visualization Injector (1) Images . . . . .	232
B.5	Visualization Injector (2) Images . . . . .	232
B.6	Visualization Injector (3) Images . . . . .	233
B.7	Visualization Injector (4) Images . . . . .	233
B.8	Visualization Injector (5) Images . . . . .	234
B.9	Visualization Images of Non-Flashing Injector Flow . . . . .	236
C.1	Process & Instrumentation Diagram . . . . .	238
D.1	Sample Uncertainty Analysis . . . . .	240

# Nomenclature

$a$	=	effective average sound speed
$a$	=	regression rate ballistic coefficient
$A$	=	cross-sectional area
$A_{nt}$	=	nozzle throat area
$c^*$	=	characteristic exhaust velocity
$C$	=	circumference
$C_{cv}$	=	contraction coefficient (vena contracta coefficient)
$C_d$	=	discharge coefficient
$C_{dn}$	=	nozzle discharge coefficient
$C_f$	=	skin friction coefficient (Fanning friction factor)
$C_p$	=	specific heat at constant pressure
$C_v$	=	specific heat at constant volume
$D$	=	injector hole diameter
$f$	=	Darcy friction factor
$f$	=	natural mode frequency

$g_o$	=	standard acceleration due to gravity at sea level ( $9.807\text{m/s}^2$ )
$G$	=	oxidizer mass flux
$h$	=	specific enthalpy
$h_f$	=	frictional head loss
$h_{fg}$	=	latent heat of vaporization
$I$	=	impulse
$I_{sp}$	=	specific impulse
$I_t$	=	total impulse
$Ja$	=	Jakob number
$k$	=	slip ratio ( $u_{2v}/u_{2l}$ )
$K$	=	cavitation number
$K$	=	compressibility parameter of the feed system
$l$	=	wavelength of the natural acoustic mode
$L$	=	injector hole length
$L^*$	=	ratio of chamber volume to nozzle throat area
$m$	=	mass
$m$	=	regression rate ballistic coefficient
$\dot{m}$	=	mass flow rate
$M$	=	molecular weight
$M$	=	Laplace transform mass variable
$n$	=	isentropic power law exponent

$n$	=	regression rate ballistic coefficient
$O/F$	=	motor operating oxidizer to fuel ratio by mass
$P$	=	pressure
$Q$	=	volumetric flow rate
$r$	=	inlet radius
$\dot{r}$	=	fuel regression rate
$R$	=	non-dimensional characteristic time
$R$	=	specific gas constant
$Re_D$	=	Reynolds number based on diameter
$s$	=	non-dimensional Laplace transform variable
$s$	=	specific entropy
$s_d$	=	dimensional Laplace transform variable
$t$	=	time
$T$	=	temperature
$T$	=	thrust force
$u$	=	fluid velocity
$V$	=	volume
$We$	=	Weber number
$x$	=	axial distance (along the fuel port)
$x$	=	vapor mass fraction
$x_i$	=	impingement distance

$\bar{y}$	=	pipe vapor mass fraction
$Y$	=	compressibility correction factor
$Z$	=	compressibility factor

*Subscripts*

1	=	location upstream of injector
2	=	location at exit or downstream of injector
$b$	=	bubble growth
$bl$	=	boundary layer
$c$	=	combustion chamber
$c$	=	thermodynamic critical conditions
$crit$	=	critical flow
$diff$	=	diffuser
$i$	=	injector
$inj$	=	injector
$l$	=	liquid
$o$	=	stagnation
$ox$	=	oxidizer tank
$ox$	=	oxidizer
$p$	=	pipe
$p$	=	propellant

$r$	=	residence within injector
$s$	=	saturation
$super$	=	supercharge
$t$	=	throat
$trip$	=	thermodynamic triple point
$v$	=	vapor
$v$	=	vaporization
$vc$	=	vena contracta

### *Symbols*

$\alpha$	=	void fraction
$\alpha_{1,2,3}$	=	coefficients of the pipe dynamic equation
$\beta_s$	=	compressibility of liquid in pipe
$\Delta$	=	difference across injector
$\eta_c$	=	combustion efficiency
$\gamma$	=	ratio of specific heats $C_p/C_v$
$\kappa$	=	Dyer's non-equilibrium parameter
$\lambda$	=	pipe dynamics constant
$\mu$	=	dynamic viscosity
$\omega$	=	acentric factor
$\omega$	=	cavitating venturi injector analysis geometry based coefficient

$\Phi$	=	density ratio correction
$\phi$	=	parameter for vapor mass fraction weighted averaging
$\Pi$	=	Laplace transform pressure variable
$\rho$	=	density
$\sigma$	=	surface tension
$\tau$	=	characteristic time
$\theta$	=	included impingement angle
$\theta_{0,1,2}$	=	non-dimensional coefficients of the combustion chamber dynamic equation

*Superscripts*

$^-$	=	mean values
$^{\wedge}$	=	non-dimensional variables
$^{\sim}$	=	first order perturbation variables

# Chapter 1

## Introduction

Hybrid rocket propulsion has seen considerable renewed interest over the past decade. Universities, private companies, and governmental organizations around the globe are currently developing a wide range of hybrid rocket technologies. Additionally, the use of nitrous oxide as an hybrid rocket oxidizer is on the rise due to its self-pressurizing characteristics and relative ease of handling. In recent years, multiple full-scale hybrid rocket development programs have utilized nitrous oxide as a liquid oxidizer [1, 2]. The following sections will provide a background into the classification of different types of rocket propulsion systems, detail the advantages and disadvantages of hybrid rockets, and describe the benefits and drawbacks of using nitrous oxide as an oxidizer, with an emphasis on considerations related to the performance of injectors, which will be the focus of this dissertation.

### 1.1 Chemical Rocket Classification

Chemical rocket propulsion systems can typically be split into the following four categories:

- Gaseous propellant rocket engines
- Liquid propellant rocket engines
- Solid propellant rocket motors

- Hybrid propellant rocket motors

Gaseous rockets generally consist of a single gas stored under high pressure (e.g. nitrogen, helium, etc.). The gaseous propellant is often expelled through a thrust chamber and nozzle to produce thrust without a chemical reaction, resulting in low temperatures throughout the flow path. For this reason they are often referred to as cold gas thrusters. Sometimes the propellant is heated by an external energy source (combustion, electrical energy, etc.) in order to improve performance. This type of system is referred to as a warm gas thruster. Due to the requirement of high pressure gas storage, the propellant storage tanks for gaseous rockets tend to be heavy in comparison to those of liquid rocket systems. This, combined with the fact that no combustion takes place to impart additional thermal energy to the flow, results in the relatively low performance of gaseous rocket systems. However, these systems are still used for some rocket attitude or reaction control applications due to their simplicity and reliability.

Liquid rockets are characterized by the use of liquid propellants which are fed to a thrust chamber under pressure, driven by either a pump or by high pressure gas. Liquid rockets utilize either a single liquid propellant (monopropellant) or the combination of a liquid fuel and liquid oxidizer (bipropellant). In bipropellant liquid rockets, the fuel and oxidizer mix and react in the thrust chamber, which is often referred to as a combustion chamber. During the combustion reaction, the propellants release energy and form hot gases, which are expanded and exhausted through a nozzle, resulting in the production of thrust. Monopropellant rockets consist of a propellant that is either a single component which can be decomposed into hot gases under a special catalyzation process (e.g. hydrazine, hydrogen peroxide, etc.), or contains both the fuel and oxidizer (e.g. nitrous oxide fuel blends [3]). The flow of liquid propellants is generally controlled by some type of valve, allowing for the control (throttling), shutdown, and restart of engine operation. A simplified schematic of a turbopump fed liquid propellant rocket system is shown in Fig. 1.1.

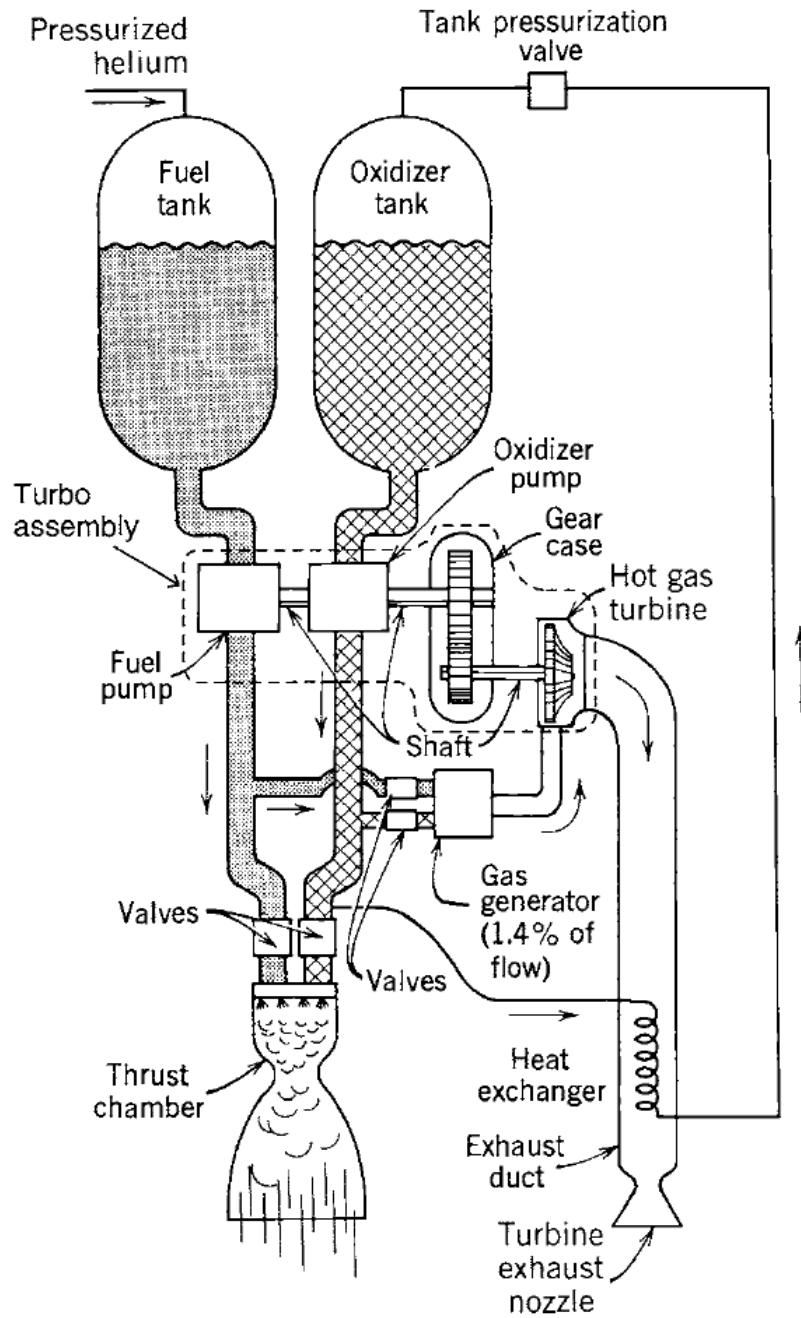


Figure 1.1: Simplified schematic of a liquid propellant rocket engine with a turbopump feed system. Pressure fed systems are also commonly used (reprinted from Ref. [4] with permission).

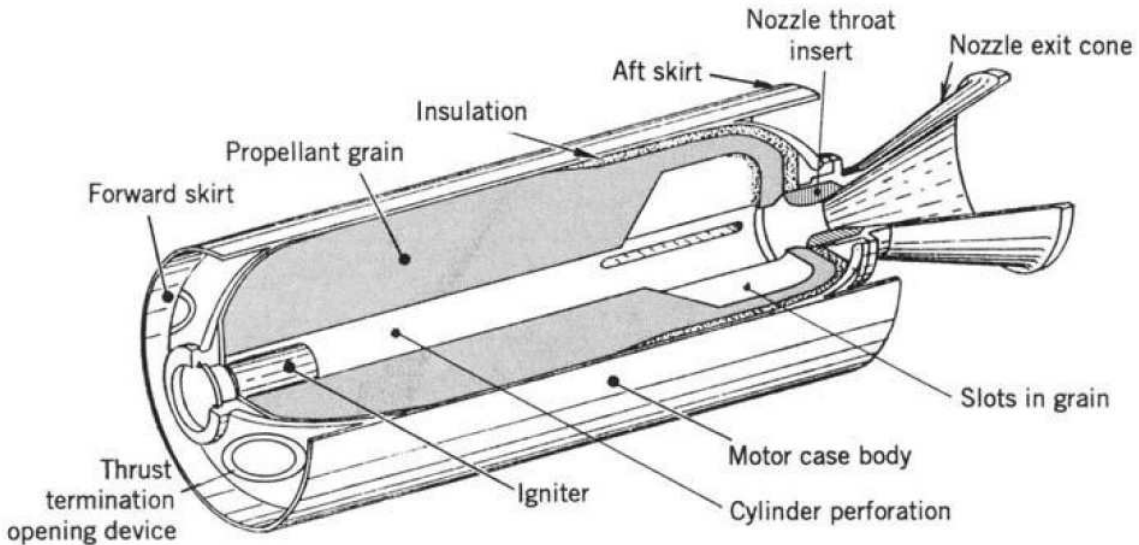


Figure 1.2: Sectioned drawing of a typical (simplified) solid propellant rocket motor (reprinted from Ref. [4] with permission).

Solid rockets consist of fuel and oxidizer which are carefully pre-mixed and stored as a solid propellant “grain” which is located within the combustion chamber (sometimes referred to as the case). This is a notably different strategy than that of liquid rockets, where the propellants are stored in tanks external to the combustion chamber. During operation, the solid propellant burns on all exposed surfaces to create hot gas for the production of thrust. This process proceeds until essentially all of the propellant is consumed, which unfortunately results in the absence of shut down capabilities. Without the ability to throttle the flow rate of propellant, the geometry of the exposed surfaces of the propellant grain must be carefully designed to achieve a desired thrust profile. The propellant grain is generally cylindrical in nature with an internal open port consisting of cylindrical and fin like geometries. A sectioned drawing of a typical (simplified) solid propellant rocket motor is shown in Fig. 1.2.

In order to compare the performance of liquid and solid rocket systems, the well known and important performance parameter specific impulse, or  $I_{sp}$ , is defined as in Eq. (1.1):

$$I_{sp} = \frac{I_t}{m_p g_o} \quad (1.1)$$

where  $I_t$  is the total impulse delivered over the course of operation,  $m_p$  is the total propellant mass burned, and  $g_o$  is the standard acceleration due to gravity at sea level ( $9.807 \text{ m/s}^2$ ). The specific impulse can be described as the impulse provided per unit weight of propellant. Under conditions of constant thrust,  $T$ , and propellant mass flow rate,  $\dot{m}_p$ , the specific impulse can be expressed as in Eq. (1.2):

$$I_{sp} = \frac{T}{\dot{m}_p g_o} \quad (1.2)$$

Due to the availability of several high performance and practical liquid oxidizers such liquid oxygen (LOX), liquid rockets generally exhibit high performance in terms of  $I_{sp}$ . For this reason, most core stages on large launch vehicles are powered by liquid propellant rocket engines. Due to the lack of high performance and storable solid oxidizers, solid rockets tend to exhibit significantly lower values of  $I_{sp}$ , indicating a lower performance by mass than liquid rocket engines. However, due to their high propellant densities, solid rockets can typically be packaged into smaller volumes than liquid rockets of comparable total impulse. For this reason, solid rockets are often used in volume constrained applications, such as tactical missiles and launch vehicle strap-on boosters.

Hybrid rockets combine the usage of both liquid and solid propellants. Virtually all hybrid rockets are made up of a liquid (or gaseous) oxidizer paired with a solid fuel. Reverse hybrids (i.e. solid oxidizer, liquid fuel) are less common, again, due to the lack of high performance and storable solid oxidizers. In a typical hybrid rocket, the solid fuel is stored in the combustion chamber and the liquid oxidizer in an external tank. Operation is started when an oxidizer control valve is opened in sequence with the initiation of an igniter, at which point the oxidizer is driven under pressure to the combustion chamber where it passes over and reacts with the solid fuel. Due to the nature of this process, hybrid rockets exhibit similar control,

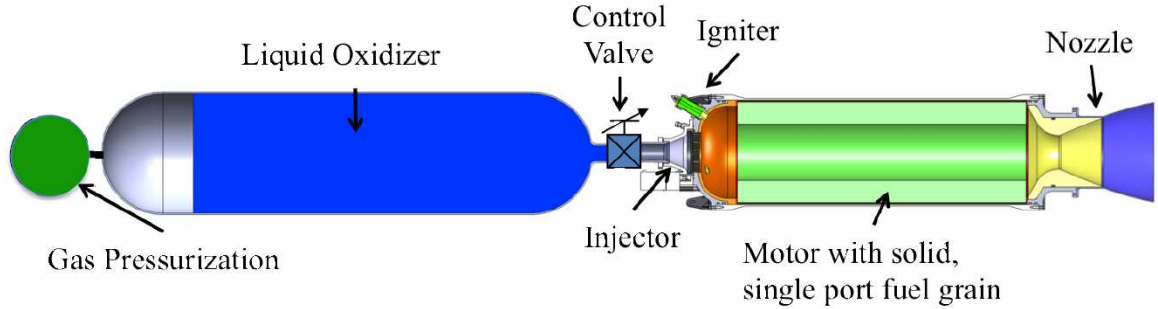


Figure 1.3: Schematic of a typical pressure-fed hybrid rocket propulsion system. Turbopump and self-pressurized systems can also be used.

throttleability, and shut down capabilities as liquid rockets. In terms of performance, hybrid rockets are considered somewhat of a compromise between that of liquid and solid rockets. Hybrid rockets exhibit a significant increase in performance over solid rockets in terms of  $I_{sp}$ . In fact, hybrids rockets have been shown to be capable of achieving demonstrated values of  $I_{sp}$  very close to those of comparable liquid systems [5]. With regard to propellant density, hybrid rockets typically occupy the region between that of liquid and solid systems, with the actual value highly dependent on propellant selection and operating conditions. A schematic of a typical hybrid rocket propulsion system is shown in Fig. 1.3. Some more details on the physics, operation, and advantages of hybrid rockets will be covered in Section 1.2 below.

## 1.2 Hybrid Rocket Background

As mentioned in Section 1.1 above, hybrid rockets operate by passing vaporized oxidizer over the surface of a solid fuel grain within the combustion chamber. In order to initiate combustion, an igniter is used to vaporize some of the fuel and to ignite the resulting combustible mixture when oxidizer is introduced. After ignition, a diffusion flame forms within the turbulent boundary layer covering the entire surface of the solid fuel grain where there exists a combustible mixture of propellants. The heat generated from this relatively thin diffusion flame vaporizes additional fuel, resulting in a self-sustaining combustion process. Operation continues until the entirety of the

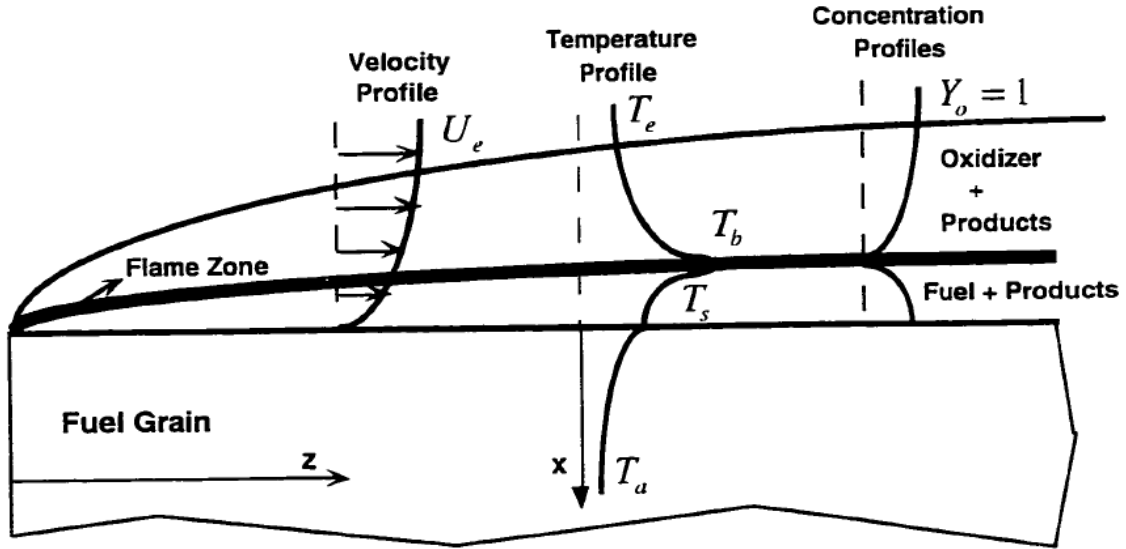


Figure 1.4: Schematic of diffusion flame that exists within the turbulent boundary layer on the surface of a solid fuel grain within a hybrid rocket (reprinted from Ref. [6] with permission).

fuel is consumed, or the flow of oxidizer into the combustion chamber is interrupted or shut off. A schematic depicting the turbulent diffusion flame structure complete with hypothetical velocity, temperature, and species concentration profiles is included in Fig. 1.4.

One of the key parameters in developing an understanding of the operation and design of hybrid rockets is the fuel regression rate,  $\dot{r}$ . Assuming a simple cylindrical fuel port shape, the regression rate is defined as the instantaneous time derivative of the solid fuel grain port radius, essentially describing the rate at which the fuel surface burns away. This regression rate directly determines the mass flow rate of fuel into the port and the diffusion flame. Work by Marxman et al. provided a successful theory for determining the regression rate law for hybrid rockets called the “Diffusion Limited Model” [7, 8, 9, 10]. The combustion in a hybrid rocket flame is diffusion limited due to the fact that the characteristic times associated with the reaction chemical kinetics are small in comparison to the characteristic times of the diffusion process within the boundary layer. A simplified form of the classical hybrid fuel

regression rate law based on that formulated by Marxman et al. is shown in Eq. (1.3):

$$\dot{r} = aG^n x^m \quad (1.3)$$

where  $G$  is the local mass flux through the port, including both the oxidizer and fuel accumulated along the length of the port,  $x$  is the longitudinal location along the port, and  $a$ ,  $n$ , and  $m$ , are all empirically determined ballistic coefficients. Eq. (1.3) is often presented in an even simpler form by employing the assumption that the regression rate is independent of the longitudinal location along the port, corresponding to a ballistic coefficient of  $m = 0$ . The resulting estimation is the commonly used form of the classical hybrid regression rate law relating instead to the oxidizer mass flux,  $G_{ox}$ , as shown in Eq. (1.4). While this is essentially a space-averaged estimation of the regression rate law, it is still quite useful for the design of hybrid rockets. However, more accurate predictions can be obtained by applying corrections based on the operating oxidizer to fuel ratio O/F as presented by Karabeyoglu in Ref. [11]. The ballistic coefficients  $a$  and  $n$  are empirically determined and are mainly functions of the specific propellant combination in use. The  $a$  and  $n$  ballistic coefficients for some sample hybrid rocket propellant combinations are included in Table 1.1.

$$\dot{r} = aG_{ox}^n \quad (1.4)$$

Examining Eq. (1.4), it can be seen that the main parameter which determines the regression rate of the fuel is the mass flux of oxidizer through the port. The result is that controlling the mass flow rate of oxidizer through the motor also controls the mass flow rate of fuel into the port. This is important, because only one throttling or control valve is necessary for hybrid rockets, resulting in simpler control than that of liquid rocket engines. However, this fact does demonstrate the importance of delivering a precise mass flow rate of oxidizer to the combustion chamber in order to achieve desired operating conditions. It is also clear from Eq. (1.4) that regression rate is independent of the chamber pressure, in stark contrast to that of solid rockets.

Table 1.1: Sample values of hybrid rocket ballistic coefficients  $a$  and  $n$  for a variety of propellant combinations. Ballistic coefficients correspond to the units of  $mm/s$  for regression rate and  $kg/m^2s$  for oxidizer mass flux. ( $LOX \Rightarrow$  liquid oxygen or  $O_2$ ,  $HTPB \Rightarrow$  hydroxyl-terminated polybutadiene,  $HDPE \Rightarrow$  high density polyethylene) [12].

Fuel	Oxidizer	$a$	$n$
HTPB	$LOX$	$3.043 \times 10^{-2}$	0.681
HDPE	$LOX$	$2.340 \times 10^{-2}$	0.62
Paraffin Wax	$LOX$	$11.70 \times 10^{-2}$	0.62
Paraffin Wax	$N_2O$	$15.50 \times 10^{-2}$	0.50

While there are some conditions under which the fuel regression rate in a hybrid rocket may become pressure dependent to a degree (extremely low or extremely high mass flux levels), in general, hybrids operating under practical conditions do not show any significant pressure dependance. An important result of this is that hybrid rockets exhibit a greater tolerance to perturbations in chamber pressure when it comes to the control of combustion instabilities.

The use of hybrid rockets offers a variety of potential advantages over the use of traditional liquid or solid propellant systems. However there are certainly a few disadvantages to the use of hybrid rockets over liquids or solids. These potential advantages and disadvantages are listed below:

#### **Advantages over liquid propellant rockets:**

- Safety: Fuel and oxidizer are stored in separate phases (bulk mixing is difficult)
- Potentially lower development and operational costs
- Decreased complexity
- Compact: Solid fuel results in higher density. Fuel is collocated with the combustion chamber.

- Solid fuel allows for addition of performance enhancing materials (aluminum for example)

**Advantages over solid propellant rockets:**

- Safety: Fuel and oxidizer are stored in separate phases (not pre-mixed), safer handling
- Thrust termination, restart, and throttling capability
- Generally higher specific impulse
- Higher tolerance to pressure perturbations
- Higher tolerance to changes in propellant temperature
- Higher tolerance to debonding and cracks
- Potentially lower development and operational costs
- Packaging flexibility
- Less environmental impact (no perchlorates or nitrates)

**Disadvantages:**

- Traditionally low fuel regression rates: difficult to achieve high thrust levels (this will be addressed in Chapter 4)
- O/F Shift: Oxidizer to fuel ratio can potentially shift over the course of the burn as the fuel port opens up for some fuel/oxidizer combinations
- Little heritage, resulting in low technology readiness level
- Combustion instabilities not well understood (due to lack of heritage)

### 1.3 Nitrous Oxide

Self-pressurizing rocket propellants have recently seen increased interest, especially in the field of hybrid rocket propulsion. Specifically, nitrous oxide ( $N_2O$ ) has recently seen a surge in popularity as a self-pressurizing liquid oxidizer for use in hybrid rockets, ranging from small scale amateur and academic projects to multiple full-scale development programs [1, 2]. Nitrous oxide has a vapor pressure,  $P_v$  (also called saturation pressure,  $P_s$ ) of approximately 730 psi (5.03 MPa) at room temperature. Some important thermodynamic properties of nitrous oxide are outlined in Table 1.2 and Fig. 1.5. This makes nitrous oxide an attractive propellant choice for hybrid rockets because it can be expelled from a storage tank without the need for complicated pressurization systems or turbopumps (hence the term self-pressurizing). Nitrous oxide is highly storable, relatively nontoxic, and easy to handle. Therefore, it is generally considered a safer alternative to the more traditional oxidizers typically used in launch systems today (such as  $LOX$ ,  $N_2O_4$ , etc.).

However, it should be noted that like all energetic materials and propellants, the use of nitrous oxide does have its associated risks which should always be considered. Specifically, nitrous oxide has a positive heat of formation, which introduces the possibility of exothermic decomposition into nitrogen and oxygen. In some circumstances, a chain decomposition reaction can result in explosions and the violent bursting of pressure vessels [13]. These types of explosions have occurred in rocket propulsion systems in the past, and have even resulted in fatalities. However, with appropriate handling precautions and engineering controls, safe use of nitrous oxide as a rocket propellant can be achieved [2].

To date, there has been little published data presented in the open literature on nitrous oxide feed systems in hybrid rockets with regard to the design and performance of elements such as propellant tanks, feed lines, valves, and injectors. When used in the self-pressurizing fashion, nitrous oxide is stored at or around its vapor pressure. The operating pressures within the oxidizer tank and feed system can therefore reach

Table 1.2: Important thermodynamic properties of  $N_2O$ . This data was calculated using REFPROP [14, 15].

Property	Units	$N_2O$
$M$	amu	44.013
$P_c$	psia (MPa)	1050.8 (7.25)
$P_{trip}$	psia (MPa)	12.7 (0.09)
$T_c$	$^{\circ}C$ (K)	36.5 (309.7)
$T_{trip}$	$^{\circ}C$ (K)	-90.2 (183.0)
$\rho_c$	$\frac{kg}{m^3}$	452.0
$Z_c$		0.273
$\omega$		0.160

values below the vapor pressure of the liquid, resulting in possible vaporization of the oxidizer and the introduction of two-phase flow. Additionally, it is sometimes desired to use nitrous oxide in hybrid rockets near its critical point. As nitrous oxide approaches its critical point, compressibility effects become non-negligible, even in the liquid phase. For these reasons, the modeling of nitrous oxide feed system flow can be difficult. This dissertation will address these difficulties through modeling and experiment, specifically with regard to the prediction of mass flow rate performance through nitrous oxide injectors.

## 1.4 Propellant Injectors

The propellant injector is an essential component in all liquid and hybrid rocket systems. In hybrid rockets, the oxidizer is almost always utilized as the liquid propellant, with the fuel as the solid propellant. Therefore, the purpose of the hybrid rocket injector is to provide the desired mass flow rate of oxidizer to the combustion chamber, while sufficiently atomizing the liquid to allow for rapid vaporization of droplets. An oxidizer injector generally consists of one or more holes, orifices, or passageways (potentially hundreds) which restrict the total cross-sectional flow area, thus restricting, or metering the mass flow rate. Appropriate oxidizer mass flow rate metering can be important for the control of a variety of important operating

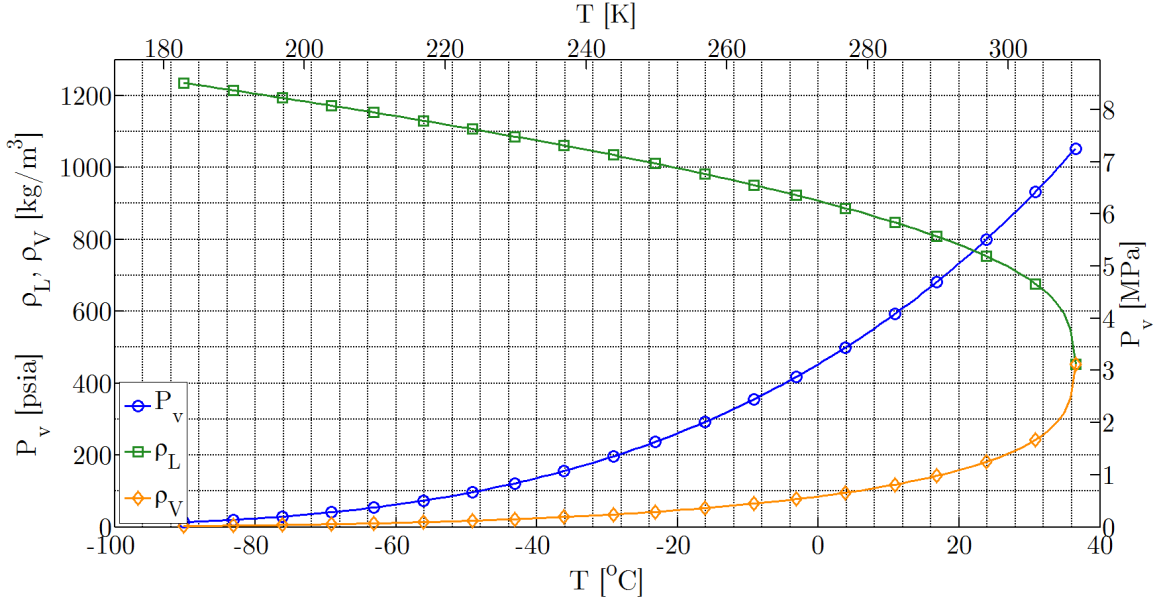


Figure 1.5: Vapor pressure, liquid density, and vapor density of saturated  $N_2O$  vs. temperature. The data used to produce this plot was calculated using REFPROP [14, 15].

parameters of the rocket, such as the pressure within the combustion chamber and the mixture ratio of the fuel and oxidizer during the combustion process. Vaporization of the oxidizer is required to allow for sufficient mixing and burning with the fuel contained in the combustion chamber.

The design of an injector can have a dramatic effect on the overall efficiency and stability of a hybrid rocket system. To demonstrate the importance of injector design, Figure 1.6 shows the pressure time histories during two hybrid rocket test firings, which are identical in every respect except for the injection schemes. It should be noted that the amplitude of the chamber pressure oscillations in the second test were large enough to shake loose the connections to the data acquisition computer which was adjacent to the test stand, resulting in the truncation of test data. The stark difference in combustion stability between the first and second configuration shows the importance of injector design to overall system performance. A detailed description of

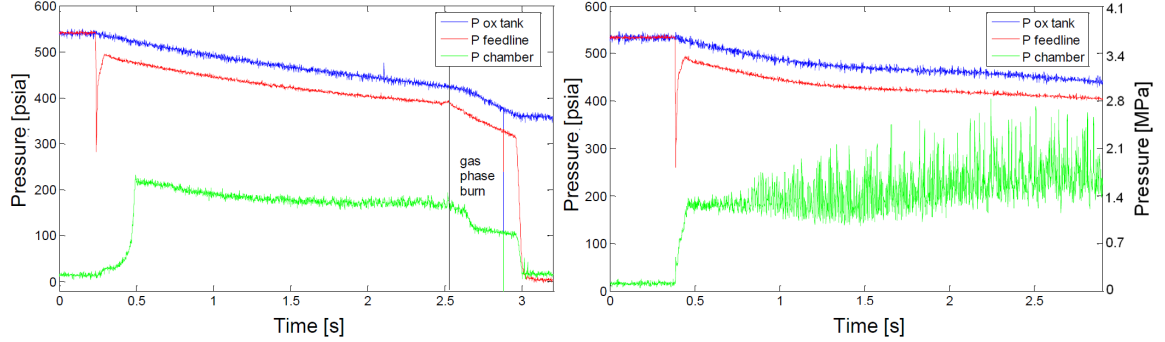


Figure 1.6: Pressure time histories from two nearly identical hybrid rocket motor firings with different injector designs. Combustion chamber geometry and feed system are fixed [16].

the rocket design and setup for these tests can be found in work by Waxman et al. [16]

In the practical design of hybrid rockets, it is important to consider both the mass flow rate metering and vaporization characteristics of the oxidizer injector. During the course of the research for this dissertation, some work has been performed addressing injector atomization and vaporization, a sample of which has been included in Appendix B. However, the focus of the present work is on the study of injector flow physics relating to mass flow rate performance through modeling and experiments.

As mentioned in Section 1.3, modeling of nitrous oxide flow in feed systems can be difficult due to compressibility and two-phase flow effects. This is certainly the case with injectors for use with nitrous oxide. To demonstrate this issue, Fig. 1.7 shows the variations that result in the measured injector discharge coefficient  $C_d$  over a series of cold flow and hot fire tests during the Peregrine Hybrid Sounding Rocket Program (which will be discussed in detail in Chapter 4). The discharge coefficient is a measure of injector performance which is described in detail in Section 2.1.1.1. Generally for low vapor pressure liquid oxidizer injectors, for a given injector geometry, the discharge coefficient should be approximately the same regardless of the pressure drop,  $\Delta P$ , across the injector. In Fig. 1.7, each cold flow data point uses the same injector geometry as a corresponding hot fire data point. It is clear from

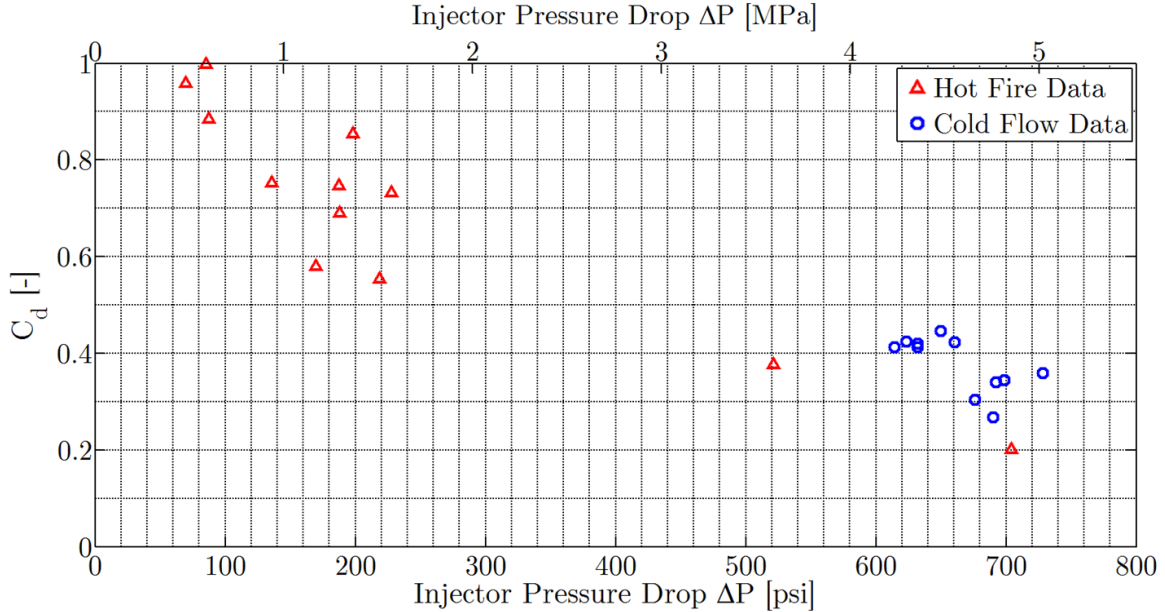


Figure 1.7:  $C_d$  vs. injector pressure drop  $\Delta P$  for injectors used in hot fire and cold flow tests with  $N_2O$  in the Peregrine Sounding Rocket Program (adapted from Ref. [17]).

Fig. 1.7 that the discharge coefficient can vary greatly, depending on the operating conditions of the injector (injector pressure drop,  $\Delta P$ ). These variations in discharge coefficient can make it extremely difficult to predict the mass flow rate through an injector *a priori*.

It has been determined that this variation in discharge coefficient is caused by the introduction of two-phase flow within the injector under certain conditions. As nitrous oxide passes through an injector orifice, the local static pressure can often drop below the vapor pressure, resulting in vaporization. This type of vaporization (by pressure drop) is termed cavitation, as opposed to the more common term, boiling, which refers to vaporization due to heat addition. More details related to the conditions which result in cavitation and the effects on mass flow rate are covered in Section 2.2. The understanding and prediction of this phenomenon will be the focus of this dissertation. Additionally, the effects of cavitation on mass flow rate

will be applied to the solution of a complex problem encountered in hybrid rocket development programs: combustion instability.

## 1.5 Combustion Instability

Combustion instabilities are widely considered one of the most challenging problems to overcome in the development of a new or modified rocket propulsion system. Combustion instability is the term used to describe the undesired and often violent pressure and thrust oscillations that can occur during operation of chemical rockets. The occurrence of combustion instabilities in rocket operation can result in extreme vibrational loading which can cause damage not only to the payload, but to the rocket structure itself. Combustion instabilities also generally result in off-nominal performance of the combustion process and can potentially lead to the destruction of the combustion chamber.

Throughout the history of rocket development, a significant body of work has been focused on the understanding and suppression of combustion instability modes in liquid and solid rocket programs. This type of work has involved both a great deal of modeling effort as well as extensive experimental test campaigns in order to eliminate combustion instabilities. Still, there have not been sufficient advances in the fundamental understanding of combustion instability to allow for accurate prediction of their onset characteristics and effects. Since there has been so little development in the field of hybrid rocket propulsion over the years as compared to liquid and solid rockets, the understanding of combustion instabilities in hybrids is even less complete. For this reason, some hybrid rocket development programs run into delays and spiraling costs during efforts to achieve sufficiently stable operation.

This dissertation will address some of the combustion instability modes that exist in, but are not unique to, hybrid rocket motors. Fig. 1.6 in Section 1.4 shows examples of both stable and unstable combustion in a single hybrid rocket motor. As described earlier, the design and operation of these hybrid rocket motor tests were

identical, except for the design of the oxidizer injector. While this suggests that the improper design of an oxidizer injection scheme can result in the occurrence of undesired combustion instabilities, it is also encouraging in that the potential exists to eliminate certain types of combustion instabilities by changing the injection scheme alone. This conjecture will be proven throughout the course of this work.

## 1.6 Organization of this Dissertation

This dissertation will essentially be split up into three main parts. First, Chapter 2 will provide a background into the methods that are commonly used to predict the mass flow rate through rocket propellant injectors. This will include models intended for the prediction of mass flow rate for both the single phase and two-phase flow regimes. Next, the design of a small scale injector cold flow test apparatus will be described in Chapter 3. Some selected cold flow experimental results from a test campaign using this apparatus will be presented. The remainder of this work (Chapters 4-6) will focus on the practical application of these small scale test results in an effort to improve the combustion stability of the Peregrine Sounding Rocket full-scale hybrid rocket development program. A brief background into the Peregrine Sounding Rocket will be given in Chapter 4. Chapter 5 will provide a theoretical background into the so-called feed system coupled instability, and describe how it was eliminated by leveraging the small scale injector cold flow test results mentioned above. Lastly, the description of a novel injection scheme aimed at the suppression of feed system coupled instabilities will be presented in Chapter 6.

A note about units: in following with typical practices in the American hybrid rocket development industry, a system of mixed units will be used throughout this dissertation. For the most part, SI units will be used (i.e.  $kg$ ,  $m$ ,  $s$ , etc.). However the two main exceptions to this are the units of pressure and temperature. Throughout this work units of  $psi$  will be used for pressure and units of  $^{\circ}C$  will be used for temperature (however conversions to MPa and K are included for pressure and temperature respectively for the readers convenience).

# Chapter 2

## Injector Flow Rate Modeling

In the design of any liquid or hybrid rocket propulsion system, it is of utmost the importance to precisely control the mass flow rate of propellants into the combustion chamber. The modeling and prediction of propellant mass flow rate is typically relatively simple for traditional rocket propellants such as liquid oxygen (LOX), liquid hydrogen (LH<sub>2</sub>), and kerosene just to name a few. These propellants are generally used at conditions where they can be accurately modeled as either purely incompressible liquid or exclusively as an ideal gas. However, the focus of this work is on hybrid rockets, and nitrous oxide ( $N_2O$ ) is a popular oxidizer choice in such systems for reasons outlined in Section 1.3. While nitrous oxide can be quite easy to handle, it is often not easy to model. Nitrous oxide is compressible even in the liquid phase. Nitrous oxide is also often used at or below its vapor pressure, resulting in two phase flow. Typical incompressible liquid or ideal gas assumptions alone are clearly ill suited for mass flow rate predictions of nitrous oxide. Fortunately, there have been significant modeling efforts in the field of two-phase, compressible fluid flow in the nuclear power industry that can be adapted for application to rocket propulsion. Some of these models may prove useful in achieving improved mass flow rate predictions of nitrous oxide flow in hybrid rocket injectors. This chapter will first give an in depth background into the traditional mass flow rate prediction techniques commonly used for hybrid rocket injector modeling, along with some discussion of their shortcomings. Subsequently, a variety of two-phase flow models from the literature will be

presented and discussed concerning their applicability to nitrous oxide injector flow rate predictions. For simplicity, only simple, straight hole orifice style injector holes will be discussed in this chapter with regard to flow modeling, however each of the models presented could be adapted to injector holes of arbitrary geometry.

## 2.1 Single-Phase Flow in Propellant Injectors

In both liquid and hybrid rockets, typical injector operation is characterized by the flow of fluid through the injector in a single-phase (either purely gaseous or purely liquid). This can also be the case with hybrid rockets using nitrous oxide; the oxidizer can be injected as either a liquid or a gas, depending on the application and design requirements of the propulsion system. This section will describe the methods for predicting the mass flow rate of propellants through single-phase injectors, both liquid and gas. These methods are examined in extensive detail, not because they are complicated (quite the opposite), but owing to their use as baseline points of reference when performing calculations of two-phase flow. Additionally, there are times when use of single-phase flow models are quite accurate, and in such cases they are extremely useful.

### 2.1.1 Single-Phase Liquid Flow

Throughout the literature there exist many simple forms of the equations for liquid flow through an orifice. However, the assumptions used in obtaining these equations are not always clear. Further, the definitions of some crucial coefficients are not always consistent from one reference to another. This section will serve as the foundation for the remainder of the chapter, so a heavy emphasis is placed upon the derivation of some commonly used equations, the necessary assumptions, and definitions of some coefficients as they will be used in this work.

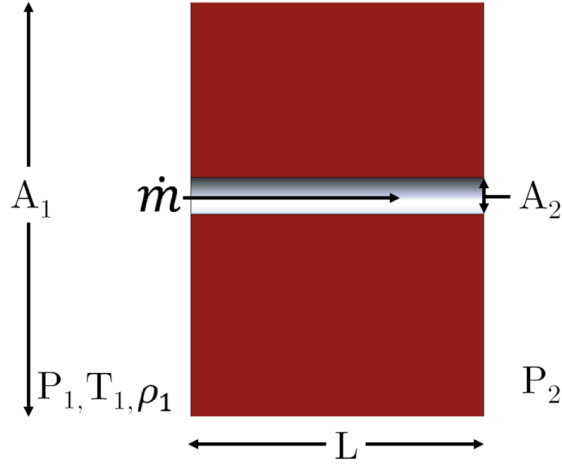


Figure 2.1: Conceptual orifice style injector hole to be used as a baseline injector geometry throughout this work. Quantities of interest for modeling are shown.

### 2.1.1.1 Incompressible Liquid Flow

Typical rocket propellants such as liquid oxygen, liquid hydrogen, and kerosene are often adequately modeled as incompressible liquids. For the analysis of single-phase incompressible (*SPI*) liquid flow through an injector orifice, we will start with the continuity equation, assuming steady state operation, as shown in Eq. (2.1) and Eq. (2.2). A conceptual orifice style injector hole is depicted in Fig. 2.1, with associated dimensions and quantities of interest shown.

$$\rho_1 Q_1 = \rho_2 Q_2 \quad (2.1)$$

$$\rho_1 u_1 A_1 = \rho_2 u_2 A_2 \quad (2.2)$$

where  $\rho$  is the liquid density,  $Q$  is the volumetric flow rate,  $u$  is the liquid velocity, and  $A$  is the cross-sectional area. The subscript 1 denotes the location upstream of the injector, and the subscript 2 denotes the location at the exit of the injector (therefore  $A_2$  is the orifice cross-sectional area for straight hole injectors). For incompressible

flow, the density is constant and the continuity equation can be simplified to the form of Eq. (2.5):

$$\rho_1 = \rho_2 = \rho \quad (2.3)$$

$$\rho u_1 A_1 = \rho u_2 A_2 \quad (2.4)$$

$$u_1 A_1 = u_2 A_2 \quad (2.5)$$

This form of the continuity equation results in two useful relations shown in Eq. (2.6) and Eq. (2.7):

$$u_1 = \frac{A_2}{A_1} u_2 \quad (2.6)$$

$$u_2 = \frac{A_1}{A_2} u_1 \quad (2.7)$$

Next we will employ the steady Bernoulli equation, which is derived from the momentum equation, resulting in a statement of Newton's second law for an inviscid, incompressible flow with no body forces as shown in Eq. (2.8) [18]:

$$P_1 + \frac{1}{2} \rho u_1^2 + \rho g_o h_1 = P_2 + \frac{1}{2} \rho u_2^2 + \rho g_o h_2 \quad (2.8)$$

where  $P_1$  is the pressure upstream of the injector,  $P_2$  is the injector exit pressure (also referred to as backpressure or chamber pressure),  $g_o$  is the standard acceleration due to gravity ( $9.807 \frac{m}{s^2}$ ) and  $h$  is the height relative to some reference height, with positive values in the direction opposite the direction of gravitational acceleration. Assuming that the difference in gravitational potential energy between locations 1 and 2 is negligible, the resulting form of the Bernoulli equation is shown in Eq. (2.9). This is the most commonly used form of the Bernoulli equation.

$$P_1 + \frac{1}{2} \rho u_1^2 = P_2 + \frac{1}{2} \rho u_2^2 \quad (2.9)$$

Combining Eq. (2.6) and Eq. (2.9), a useful expression for the velocity at the exit,  $u_2$ , can be found and is shown in Eq. (2.10):

$$u_2 = \sqrt{\frac{2(P_1 - P_2)}{\rho \left[1 - \left(\frac{A_2}{A_1}\right)^2\right]}} \quad (2.10)$$

The theoretical mass flow rate through the injector for single phase incompressible liquid flow,  $\dot{m}_{SPI}$ , can then be calculated as shown in Eq. (2.11) and Eq. (2.12):

$$\dot{m}_{SPI} = \rho Q_2 = \rho u_2 A_2 \quad (2.11)$$

$$\dot{m}_{SPI} = A_2 \sqrt{\frac{2\rho(P_1 - P_2)}{\left[1 - \left(\frac{A_2}{A_1}\right)^2\right]}} \quad (2.12)$$

Often due to separation of flow around the inlet of the injector, a vena contracta can form, resulting in an effective exit cross sectional area  $A_{vc}$  that is smaller than the actual orifice area  $A_2$ . A vena contracta coefficient (or contraction coefficient) is introduced to account for this effect and is shown in Eq. (2.13) and Eq. (2.14). This is only applicable in the case of relatively thin plate orifices, where the vena contracta extends through the exit of the orifice. However for longer injector holes, the separation region often reattaches to the wall of the orifice, and the injector flows full by the time the exit plane is reached. For purely liquid flow under these conditions, the contraction coefficient is effectively equal to 1, even though a vena contracta does exist upstream of the exit.

$$C_{vc} \equiv \frac{A_{vc}}{A_2} \quad (2.13)$$

$$\dot{m}_{SPI} = C_{vc} A_2 \sqrt{\frac{2\rho(P_1 - P_2)}{\left[1 - \left(\frac{A_2}{A_1}\right)^2\right]}} \quad (2.14)$$

It should be noted that the theory above assumed inviscid flow. In reality, frictional losses occur at both the inlet to the orifice and along the length of longer injector holes. Therefore, the discharge coefficient  $C_d$  defined in Eq. (2.15) is used to

account for both the vena contracta effects and frictional losses. This results in the well known “ $C_dA$ ” equation for the single phase incompressible liquid mass flow rate as shown in Eq. (2.16).

$$C_d \equiv \frac{\dot{m}_{viscous\ w/\ v.c.}}{\dot{m}_{inviscid\ no\ v.c.}} \quad (2.15)$$

$$\dot{m}_{SPI} = C_d A_2 \sqrt{\frac{2\rho\Delta P}{\left[1 - (\frac{A_2}{A_1})^2\right]}} \quad (2.16)$$

where  $\Delta P$  is defined as the pressure drop across the injector and is equal to  $P_1 - P_2$ . In many practical cases relating to injectors,  $A_2 \ll A_1$ , and the denominator under the square root in Eq. (2.16) approaches unity, resulting in the commonly used form of the “ $C_dA$ ” equation shown in Eq. (2.17). Even when  $A_2$  and  $A_1$  are comparable, the denominator under the square root is often wrapped into  $C_d$ .

$$\dot{m}_{SPI} = C_d A_2 \sqrt{2\rho\Delta P} \quad (2.17)$$

This is the form of the “ $C_dA$ ” equation typically used for rocket injector design as presented by Sutton and Biblarz [4], and is the form that the experimental portion of the current work will use when referring to the discharge coefficient (sometimes referred to as the SPI discharge coefficient). The value of this single-phase discharge coefficient is highly dependent on the injector design, but generally ranges from about 0.6 to 0.9 for straight hole liquid propellant injectors, depending on the inlet geometry (this variation will be addressed in Section 2.1.1.4).

Throughout the remainder of this chapter, plots of predicted injector flow rate performance will be shown in order to promote an improved understanding of the different flow models that are presented, and their respective behavior. To provide continuity between sections and to ease in the comparison between models, a common hypothetical straight hole orifice injector design will be used throughout.

The diameter of the orifice,  $D_2$ , is fixed at 1.5 mm, and the discharge coefficient  $C_d$  corresponding to single-phase operation is arbitrarily chosen at 0.75. Additionally, a value of 0.1 was used for the quantity  $\frac{A_2}{A_1}$  for this hypothetical injection scheme. This value is actually quite large compared to what is exhibited in most hybrid rocket injection schemes. However it can be shown that even for this large area ratio value, the effect on the total calculated mass flow rate is approximately only one half of one percent.

In order to perform the mass flow rate predictions presented in this chapter, it is always necessary to calculate the various fluid properties over a range of thermodynamic conditions. Fortunately, highly accurate equations of state exist for nitrous oxide which have been programmed by the National Institute of Standards and Technology in the user friendly REFPROP computer program [14, 15]. Throughout this work, any calculations of thermodynamic and transport properties will be made using this program.

Fig. 2.2 and Fig. 2.3 show the mass flow rate predictions using the single-phase incompressible liquid assumption for nitrous oxide stored as a saturated liquid. This means that the pressure upstream of the injector is equal to the vapor pressure of the fluid. The operating pressures chosen for these modeling exercises lie within the range of values often observed in nitrous oxide based hybrid rocket systems. These two figures show identical flow rate data in the y-axis, with two different independent variables used for the x-axis. When examining flow rate prediction plots, it is important not only to compare the results between models and under different operating parameters, but also to compare the merits of presenting the flow rate prediction data vs. different independent variables. For instance, Fig. 2.2 shows the mass flow rate vs.  $\Delta P$  across the injector, for saturated  $N_2O$  at a variety of temperatures (and thus for varied values of vapor pressure  $P_v$ ; see Fig. 1.5 for the relation between temperature and vapor pressure of saturated nitrous oxide). As expected, the mass flow rate increases with increasing  $\Delta P$ . However, plotted in this manner, it is easily visible that for a given value of  $\Delta P$ , higher mass flow rates are achieved with nitrous

oxide at lower temperatures (due to the higher value of liquid density). It can be ascertained through Fig. 2.2 that after  $\Delta P$ , the nitrous oxide density upstream of the injector element is the second most important parameter in determining mass flow rate through a given injector of incompressible, purely liquid flow. Additionally, at low backpressure  $P_2$ , it can be seen from Fig. 2.3 that the incompressible liquid model does not always show an increase in mass flow rate by increasing the vapor pressure and thus  $P_1$ . This is due to the fact that as the saturation pressure approaches the critical point, the liquid density decreases rapidly. While this does illustrate the potential usefulness of examining one set of data in various formats, at these low downstream pressures, two-phase flow effects will dominate the mass flow rate prediction for nitrous oxide, as will be shown through modeling in Section 2.2 and through experimental cold flow testing in Chapter 3.

It is useful at this point to introduce the concept of supercharge. While nitrous oxide is often stored in a tank as a saturated liquid, it is common to pressurize the nitrous oxide to levels above its vapor pressure. This pressurization, referred to as supercharging in this work, is typically achieved with some type of inert gas (helium, nitrogen, etc.), but reactive gases such as gaseous oxygen can also be used (note: hydrocarbon compounds should NEVER be used to supercharge a nitrous oxide tank due to the risk of explosive decomposition reactions outline in Ref. [13]). The local supercharge pressure is defined as the instantaneous difference between the static pressure and the vapor pressure of nitrous oxide at any point in the system. The expression for the supercharge pressure upstream of the injector is shown in Eq. (2.18), where the vapor pressure is evaluated at the local instantaneous temperature ( $T_1$  in this case).

$$P_{super}^1 = P_1 - P_v \Big|_{T=T_1} \quad (2.18)$$

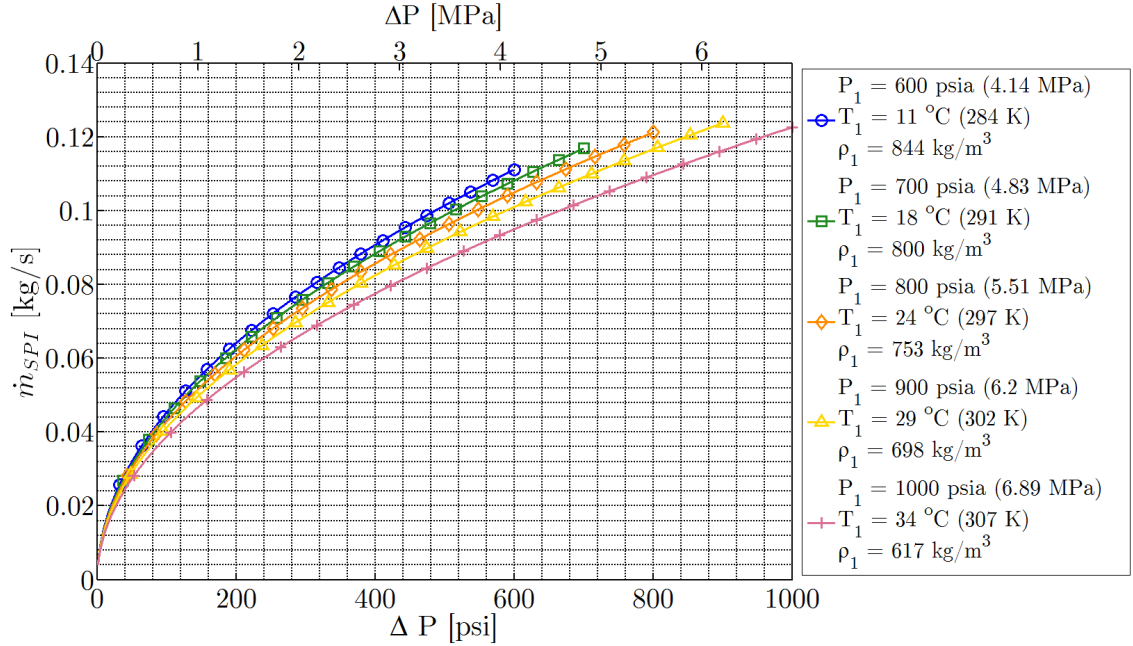


Figure 2.2:  $\dot{m}_{SPI}$  vs.  $\Delta P$  using the single-phase incompressible liquid assumption for saturated  $N_2O$  at a variety of upstream pressures ( $D_2 = 1.5$  mm,  $C_d = 0.75$ ).

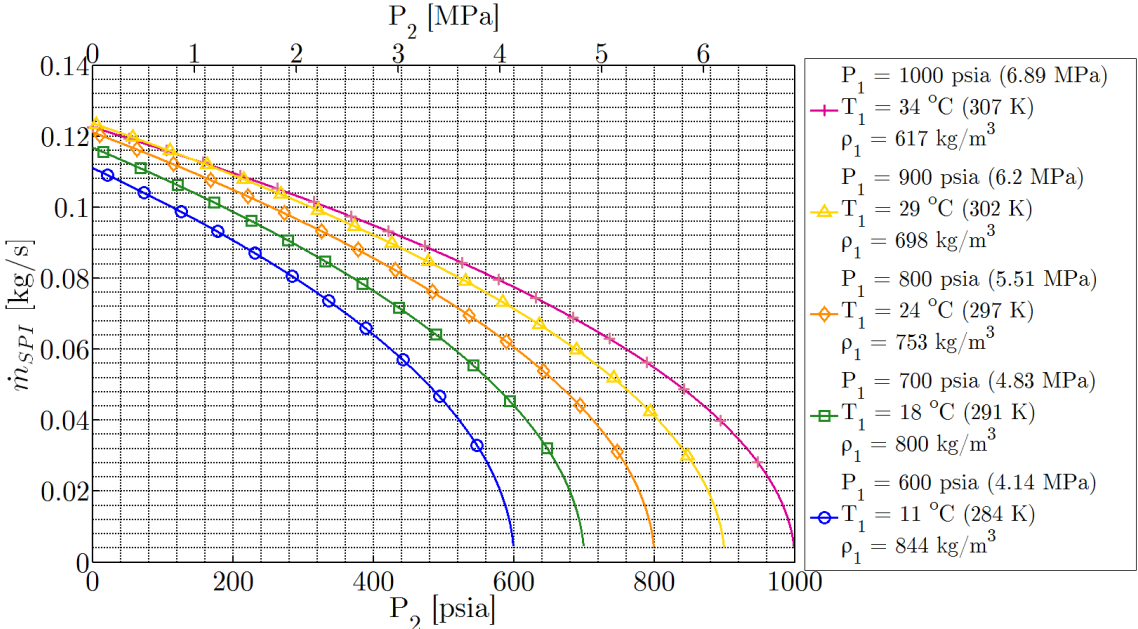


Figure 2.3:  $\dot{m}_{SPI}$  vs.  $P_2$  using the single-phase incompressible liquid assumption for saturated  $N_2O$  at a variety of upstream pressures ( $D_2 = 1.5$  mm,  $C_d = 0.75$ ).

Fig. 2.4 and Fig. 2.5 show single-phase incompressible mass flow rate predictions for nitrous oxide at  $0^{\circ}\text{C}$  (273 K) that has been pressurized to varying levels of supercharge, including the non supercharged, saturated case where  $P_1 = P_v = 453$  psia (3.12 MPa). Fig. 2.4 plots the mass flow rate against  $\Delta P$ , and it is immediately clear that the supercharge does not impact the mass flow rate performance when the temperature and thus vapor pressure are held constant. Unlike the saturated case, the increase in upstream pressure by supercharging is not accompanied by a significant decrease in density. However, Fig. 2.5 does show that for a fixed value of downstream pressure  $P_2$ , increased supercharge allows for greater  $\Delta P$  values and in turn higher mass flow rates. This is not surprising, but when practical considerations result in chamber pressure constraints, it is valuable to look at the injector mass flow rate performance data in this fashion.

### 2.1.1.2 Compressibility Effects

The “ $C_dA$ ” equation is often used in practice to predict the mass flow rate of traditional liquid propellants through an injector orifice with sufficient accuracy. Unfortunately, error is often introduced to this method for injectors of high vapor pressure propellants such as nitrous oxide due to the existence of compressibility effects, especially when used close to the critical point of the fluid (compressibility factor  $Z \sim 0.12$  for saturated liquid,  $Z \sim 0.57$  for saturated vapor at room temperature [14, 15]). To account for compressibility effects, a compressibility correction factor,  $Y$ , can be introduced as in Eqn. (2.20).

$$Y \equiv \frac{\dot{m}_{\text{compressible}}}{\dot{m}_{\text{incompressible}}} \quad (2.19)$$

$$\dot{m} = C_d Y A \sqrt{2\rho \Delta P} \quad (2.20)$$

For ideal gases, the compressibility correction factor is well known and can be found in handbooks such as that of Perry and Green[19]. However, for compressible liquids or real gases, the correction factor should be calculated in the same fashion as that of Zimmerman et al. [20] based upon the non-ideal gas flow power law theory

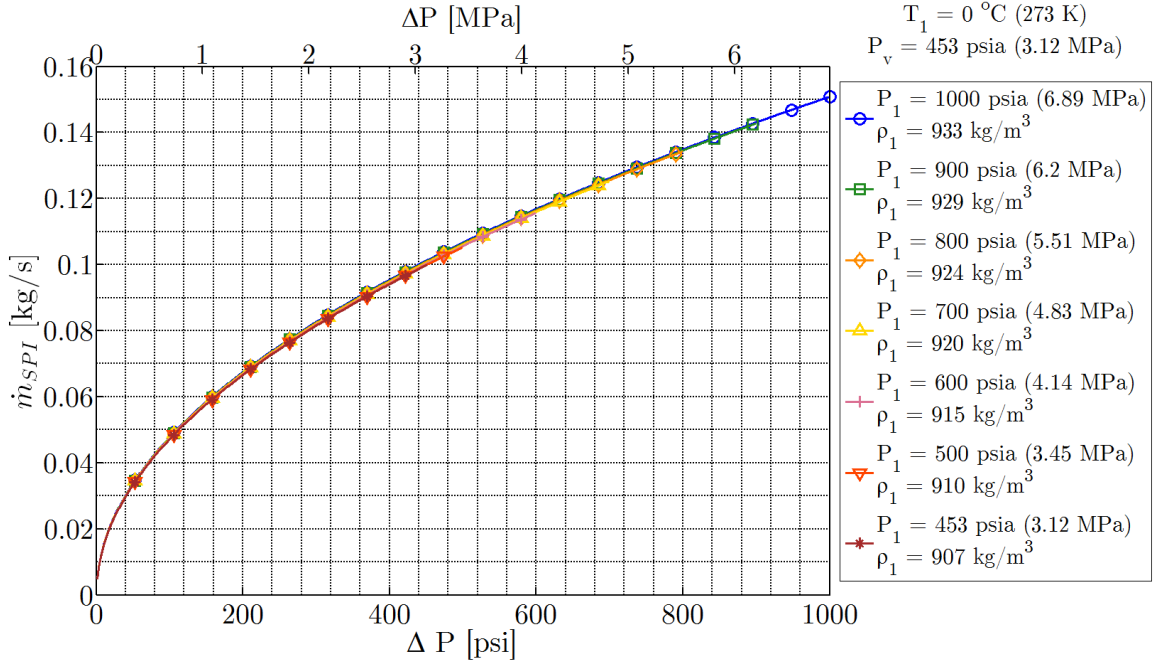


Figure 2.4:  $\dot{m}_{SPI}$  vs.  $\Delta P$  using the single-phase incompressible liquid assumption for  $N_2O$  at  $0^\circ\text{C}$  (273 K) and  $P_v = 453$  psia (3.12 MPa) for a variety of upstream pressures (supercharge values). ( $D_2 = 1.5$  mm,  $C_d = 0.75$ )

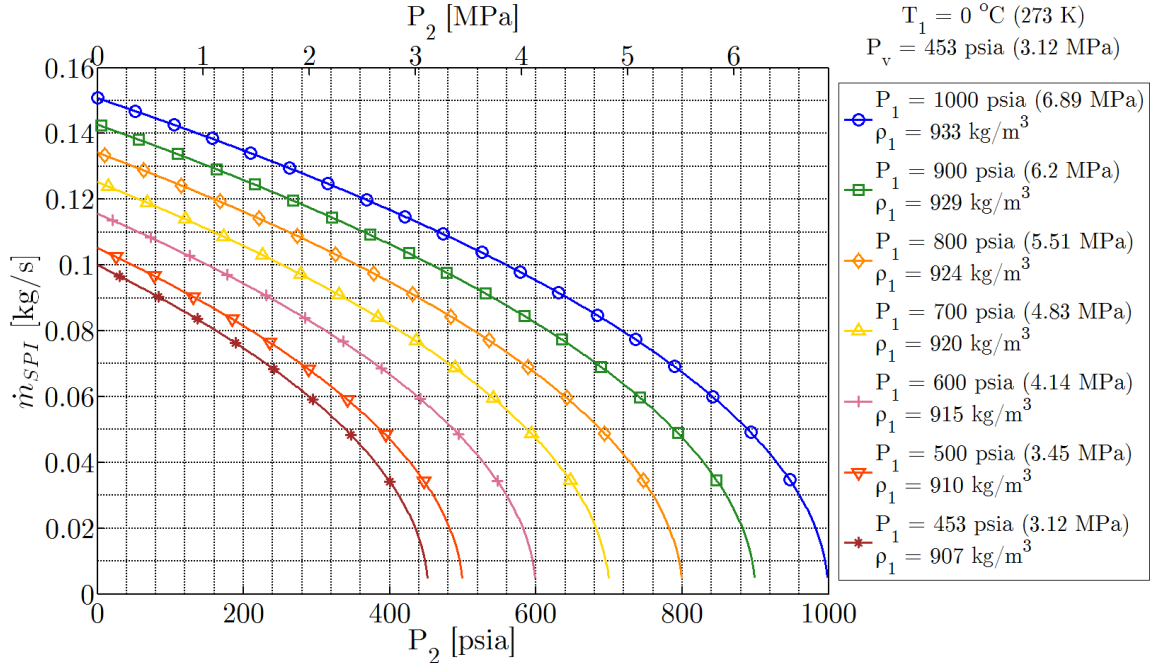


Figure 2.5:  $\dot{m}_{SPI}$  vs.  $P_2$  using the single-phase incompressible liquid assumption for  $N_2O$  at  $0^\circ\text{C}$  (273 K) and  $P_v = 453$  psia (3.12 MPa) for a variety of upstream pressures (supercharge values). ( $D_2 = 1.5$  mm,  $C_d = 0.75$ )

of Cornelius and Srinivas [21]. In that work, the correction factor was calculated for venturi flow rate measurements of nitrous oxide, which are also governed by Eqn. (2.20). This form of the compressible liquid correction factor,  $Y'$ , is outlined in Eqns. (2.21) and (2.22) and is also valid for injectors, but only under the assumption of isentropic flow through the orifice:

$$Y' = \sqrt{\frac{P_o}{2 \Delta P} \left( \frac{2n}{n-1} \right) \left( 1 - \frac{\Delta P}{P_o} \right)^{\frac{2}{n}} \left[ 1 - \left( 1 - \frac{\Delta P}{P_o} \right)^{\frac{n-1}{n}} \right]} \quad (2.21)$$

$$n = \gamma \left[ \frac{Z + T \left( \frac{\partial Z}{\partial T} \right)_\rho}{Z + T \left( \frac{\partial Z}{\partial T} \right)_P} \right] \quad (2.22)$$

where  $P_o$  is the upstream stagnation pressure, and  $n$  is the isentropic power law exponent as defined by Cornelius and Srinivas [21]. When  $A_2 \ll A_1$ , the upstream pressure  $P_1$  can generally be used for  $P_o$ . As long as an appropriate method for calculating  $Z$  exists (again, the highly accurate equations of state for nitrous oxide have been programmed by the National Institute of Standards and Technology in the user friendly REFPROP computer program [14, 15]), the above equations can be applied to nitrous oxide as it can be described by the real gas equation of state shown in Eqn. (2.23) [20]:

$$P = Z \rho R T \quad (2.23)$$

where  $R$  is the specific gas constant. Zimmerman et al. concluded that in flow venturis, where the value of  $\Delta P$  is generally small ( $< 50$  psi or  $0.34$  MPa), the effects of compressibility are negligible under most conditions. However, injectors often establish very large pressure drops ( $>> 50$  psi or  $0.34$  MPa), and therefore  $Y'$  may deviate significantly from unity. Figure 2.6 shows the compressible liquid correction factor as calculated for nitrous oxide at an upstream pressure of 1000 psia (6.89 MPa) over a range of temperatures. As the nitrous oxide approaches the critical temperature of approximately  $36^\circ C$  (309 K) and the compressibility increases, the compressible liquid correction factor becomes more important. At low values of  $\Delta P$ ,

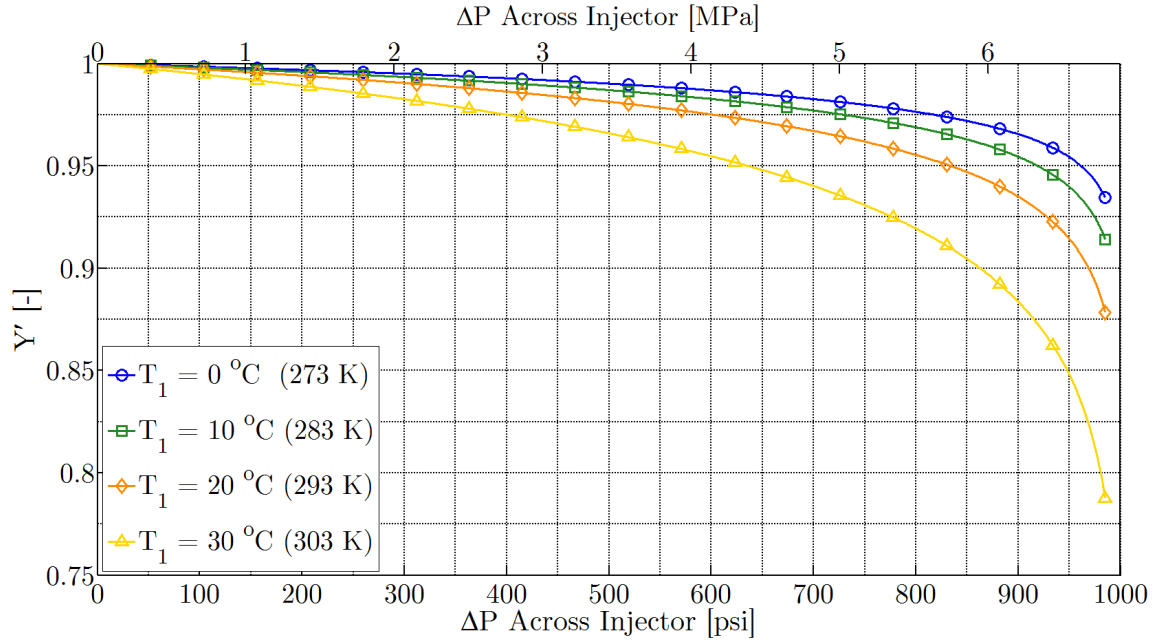


Figure 2.6: Compressible liquid correction factor vs.  $\Delta P$  across the injector for  $P_1 = 1000$  psia (6.89 MPa) over a range of  $N_2O$  temperatures. For reference the critical temperature of  $N_2O$  is  $36^\circ\text{C}$  (309 K). The data used to produce this plot was calculated using REFPROP [14, 15].

the effect is small as expected, however as  $\Delta P$  increases, so too does the importance of accounting for compressibility. However, while the use of a compressibility correction can provide improved accuracy of the “ $C_dA$ ” equation for single phase liquid nitrous oxide injectors, of greater concern is the onset of two-phase flow. As will be shown in Section 2.2, at the highest  $\Delta P$  values in Figure 2.6, the effects of two-phase flow within the injector element overshadow the compressibility effects, thus rendering the classical form of the “ $C_dA$ ” equation unsuitable for nitrous oxide under certain operating conditions.

### 2.1.1.3 Effect of Inlet Geometry on $C_{vc}$

As mentioned in Section 2.1.1.1, for short injector orifices (small values of  $L/D$ ), the vena contracta can extend all the way to the exit of the injector, decreasing the effective cross-sectional area of the orifice. Under these conditions, the value of the

contraction coefficient,  $C_{cv}$  as defined in Eq. (2.13) can become important (even for high  $L/D$  holes,  $C_{cv}$  can be quite important with regard to two-phase flow prediction as will be detailed in Section 2.2.2.1.2 and Section 2.2.2.1.3). It is well known that the existence and severity of vena contracta within an orifice is highly dependent on the geometry of the inlet. For sharp edged inlets (also referred to as square edged), the separation region just past the inlet tends to be large, resulting in lower values of  $C_{cv}$ . For well rounded inlets, separation may be nonexistent (or unnoticeable), and the contraction coefficient will be approximately equal to 1. A series of experiments were performed by Nurick flowing water and trichloroethylene through orifices of different inlet characteristics in order to establish an empirical relation between contraction coefficient and the ratio of inlet radius to orifice diameter  $r/D$  [22]. Combined with previous experimental results that show a vena contracta will not form when the entrance is rounded as little as  $r \geq 0.14D$  (Ref. [23]), Nurick's experiments resulted in a fit to his data as shown in Eq. (2.24):

$$(C_{cv})_{r/D} = \left[ \left( \frac{1}{C_{cv}} \right)^2_{\frac{r}{D}=0} - 11.4 \frac{r}{D} \right]^{-\frac{1}{2}} \quad (2.24)$$

with the limits:

$$0 \leq \frac{r}{D} \leq 0.14 \quad (2.25)$$

Eq. (2.24) only applies to conditions where  $A_2/A_1$  is large enough so that  $(C_{cv})_{r/D=0}$  is equal to 0.62. Fig. 2.7 plots Eq. (2.24) and shows the character of the effect of  $r/D$  on  $C_{cv}$ . Above  $r/D$  values of 0.14, the contraction coefficient is equal to 1. It is interesting to note the abrupt change in slope of the curve at  $r/D = 1$ . It would be interesting to determine whether there is a physical mechanism resulting in this slope discontinuity, if it is an artifact of the experimental design, or if a transitional region exists that was not included in the fitting of experimental data. Fig. 2.8 shows the variation of the value of the contraction coefficient for a range of injector orifice diameters vs. the inlet radius. This plot was included to provide a

more intuitive emphasis on the great effect that a very small inlet radius can have on the vena contracta characteristics of an injector.

#### 2.1.1.4 Frictional Effects (Inlet Geometry and $Re_D$ )

For orifices of high length to diameter ratio  $L/D$ , where the effects of vena contracta may not be realized due to reattachment of the flow well before the exit plane, the value of  $C_d$  is often affected by variations in the geometry of the orifice inlet due to frictional effects. In fact, frictional effects at both the inlet and throughout the straight length of the orifice contribute to determine the resulting physical value of  $C_d$  for high  $L/D$  injectors. This section will describe the modeling and prediction of the discharge coefficient for these types of injectors based upon classical viscous flow theory.

From classical viscous flow theory, the well known Darcy-Weisbach equation relates pressure loss due to friction along a length of pipe to the average velocity of the fluid. This equations neglects any inlet effects and is shown in Eq. (2.26):

$$h_f = f \frac{L}{D} \frac{u^2}{2g_o} \quad (2.26)$$

where  $h_f$  is the frictional head loss described by a height of a column of the fluid in use,  $L$  and  $D$  are the length and diameter of the pipe respectively,  $u$  is the mean velocity of the flow,  $g_o$  is the standard acceleration due to gravity, and the term  $f$  is the commonly used Darcy friction factor [24]. This equation can be applied to injector orifices, and is recast in terms of pressure drop instead of head loss as shown in Eq. (2.27):

$$\Delta P = f \frac{L}{D} \frac{\rho u^2}{2} \quad (2.27)$$

Rearranging Eq. (2.27) to get an expression for the mean velocity  $u$  results in Eq. (2.28). Inserting this expression into the mass flow rate equation shown in Eq. (2.11) results in the form shown in Eq. (2.29):

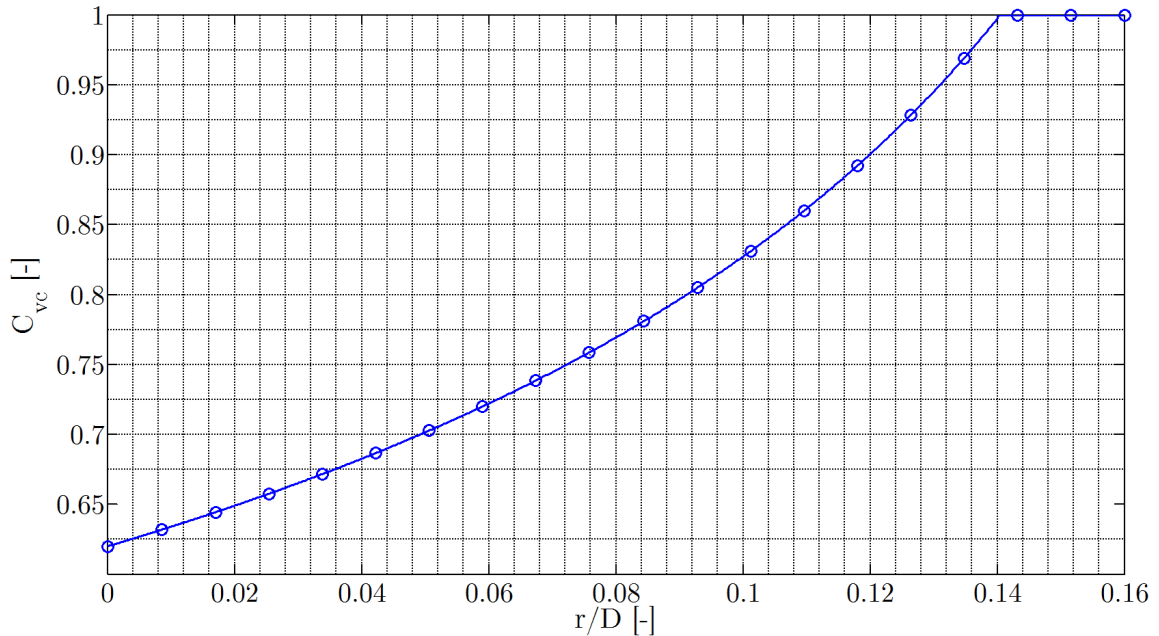


Figure 2.7:  $C_{cv}$  vs inlet radius to diameter ratio  $r/D$  based on Nurick's empirical correlation.

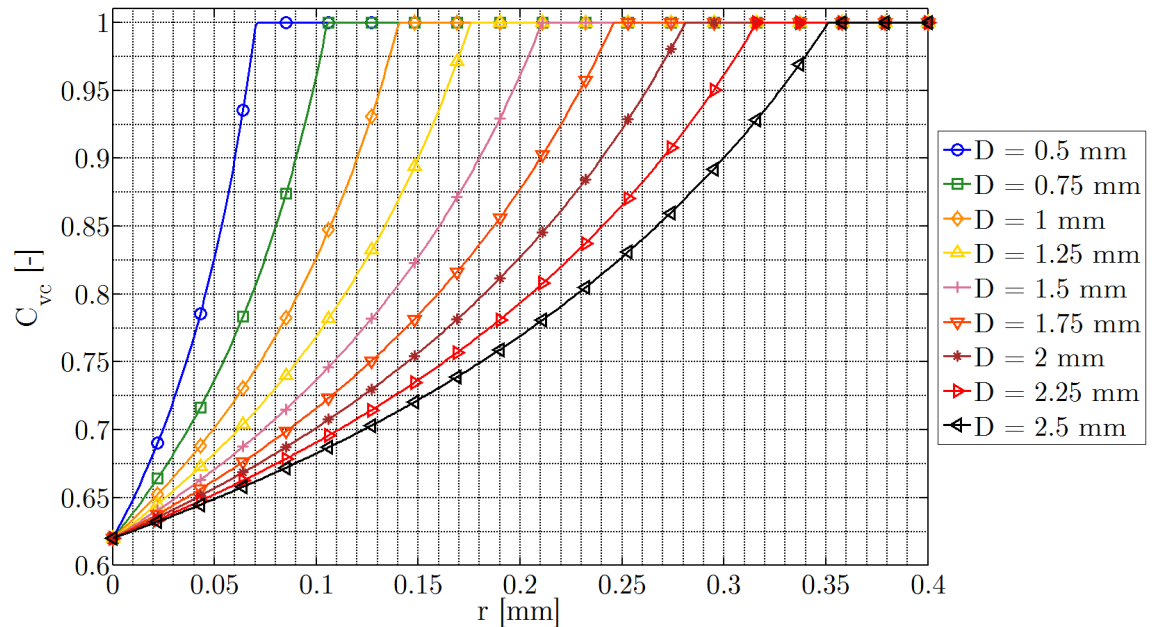


Figure 2.8:  $C_{cv}$  vs inlet radius  $r$  for injector holes of varying orifice diameter  $D$  based on Nurick's empirical correlation.

$$u = \sqrt{\frac{2\Delta P}{f_D^L \rho}} \quad (2.28)$$

$$\dot{m} = \sqrt{\frac{1}{f_D^L} A \sqrt{2\rho\Delta P}} \quad (2.29)$$

Examining Eq. (2.29), and assuming an injection scheme in which  $A_2/A_1 \ll 1$ , it is apparent that the square root term containing the Darcy friction factor is analogous to the discharge coefficient  $C_d$ . From the definition of the Fanning friction factor (also known as the skin-friction coefficient  $C_f$ ) as shown in Eq. (2.30), the discharge coefficient can be expressed in terms of frictional losses along the length of the pipe only, and is shown in Eq. (2.31):

$$C_f = \frac{1}{4} f \quad (2.30)$$

$$C_d = \sqrt{\frac{1}{4C_f \frac{L}{D}}} \quad (2.31)$$

Under the assumption of smooth-walled orifices and fully developed Poiseuille type flow, there are several well known methods for determining the value of the skin-friction coefficient, which is dependent only on the Reynolds number of the flow,  $Re_D$ , based on the orifice diameter as shown in Eq. (2.32). For laminar flow, the Poiseuille form of the skin-friction coefficient can be used, and is shown in Eq. (2.33). It should be noted that the establishment of fully developed flow is not guaranteed for general injector orifices. However, as the value of  $L/D$  increases for an injector, the likelihood of fully developed flow is increased and this analysis becomes more reliable.

$$Re_D = \frac{\rho u D}{\mu} \quad (2.32)$$

$$C_f = \frac{16}{Re_D} \quad (\text{laminar flow}) \quad (2.33)$$

For turbulent flow, the well known Blasius curve fit can be used to estimate the skin-friction coefficient for smooth-walled orifices as shown in Eq. (2.34). Prandtl actually derived a better approximation to the skin-friction coefficient for turbulent pipe flow, but for simplicity the Blasius form will be used herein [25]. For a given injector geometry, Eqns. (2.31), (2.33), and (2.34) are all that are needed to provide an estimate of the frictional losses along the length of the orifice, but neglecting losses at the entrance.

$$C_f \approx 0.0791 Re_D^{-1/4} \quad (\text{turbulent flow}) \quad (2.34)$$

In order to take into account the frictional losses at the entrance associated with accelerating the flow into the orifice and into a Poiseuille paraboloid profile, an excess pressure drop constant  $K$  is introduced as in Eq. (2.35). This value of the excess pressure drop constant is empirically determined and depends on the geometry of the inlet [26]. The value of  $K$  for high  $L/D$  injectors with sharp edged inlets has been studied experimentally by numerous groups with the exact values varying slightly depending on the experimental setup and assumptions [27, 28, 26]. The value of  $K$  for sharp-edged inlets proposed by Langhaar (2.28) falls in the middle of the majority of the values reported, and will be used as a representative value. Fig. 2.9 and Fig. 2.10 show the variation of  $C_d$  based on this analysis for orifices of sharp-edged inlet injectors in the laminar and turbulent regions respectively. Universally, as  $Re_D$  increases, so too does  $C_d$ . As the value of  $L/D$  increases, the frictional losses in the straight segment of the orifice increase, resulting in the decrease of  $C_d$  as shown in Fig. 2.9 and Fig. 2.10. As  $Re_D$  drops toward zero and creeping flow is approached, the values of  $C_d$  appears to be near zero. The dynamics and determination of the velocity profile and skin friction coefficient at very low Reynolds numbers are not expected to be described adequately by the current analysis.

$$C_d = \sqrt{\frac{1}{4C_f \frac{L}{D} + K}} \quad (2.35)$$

Fig. 2.11 and Fig. 2.12 show the variation of  $C_d$  assuming a fixed value of  $L/D$  and varying the excess pressure drop coefficient  $K$ . As the value of  $K$  decreases down

from the sharp-edged inlet value of 2.28, the discharge coefficient increases. It can be ascertained therefore, that as the inlet to an orifice becomes more and more rounded ( $r/D$  increasing), the value of  $K$  must decrease. The exact value of  $K$  for rounded inlet injectors must still be determined empirically.

### 2.1.2 Single-Phase Gas Flow: Perfect Gas Model

The problem of single-phase gaseous propellant flow is one that is well studied. In fact, it is often used as an example problem in most elementary compressible flow course. A treatment of this type of flow will be presented including derivation and discussion in order to discuss some issues that can be problematic when applied to the prediction of gaseous nitrous oxide flow.

The Perfect Gas model is used almost universally for the prediction gaseous flow through propellant injectors. This model assumes that the gas is thermally and calorically perfect, meaning that it is assumed to follow the ideal gas law as stated in Eq. (2.36). Additionally, the specific heats  $C_p$  and  $C_v$  are assumed constant which results in the simple equations for specific enthalpy,  $h$ , and specific energy,  $e$ , as shown in Eq. (2.37) and Eq. (2.38). A complete list of the assumptions used in the Perfect Gas injector flow model are included below:

- Thermally and calorically perfect (Eqns. 2.36 - 2.38)
- Isentropic flow
- Stationary flow upstream of injector
- Wall friction is negligible

$$P = \rho RT \quad (2.36)$$

$$h = C_p T \quad (2.37)$$

$$e = C_v T \quad (2.38)$$

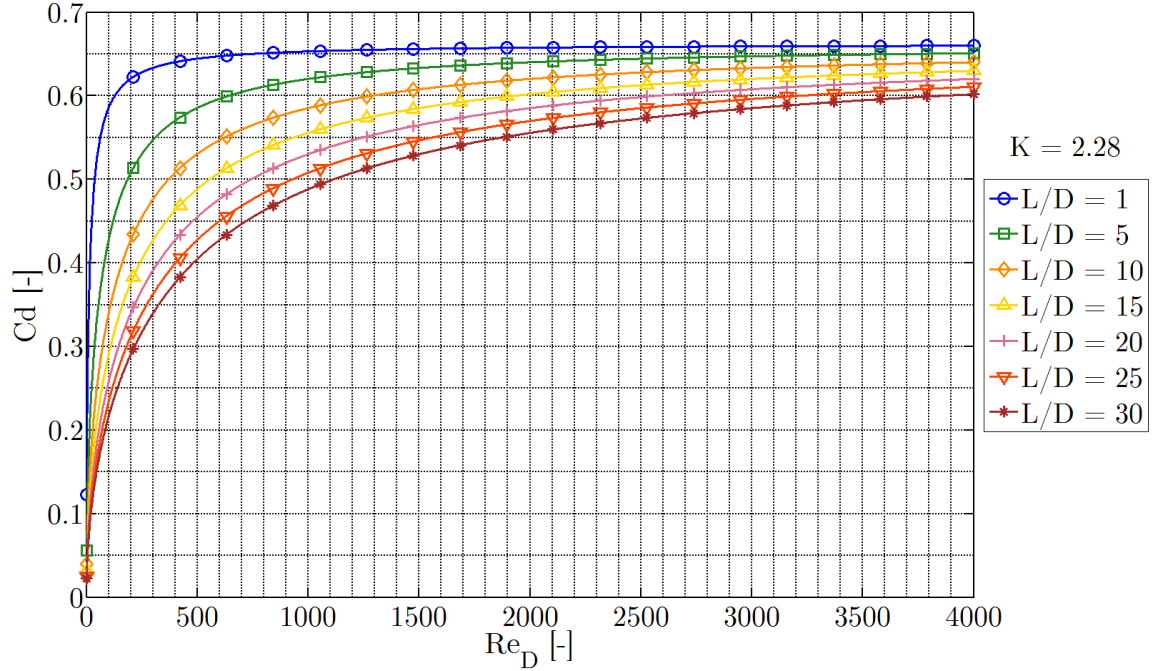


Figure 2.9:  $C_d$  vs  $Re_D$  for square edged inlet orifices ( $K = 2.28$ ) of various length to diameter ratios  $L/D$  in the laminar flow region ( $C_f = \frac{16}{Re_D}$ )

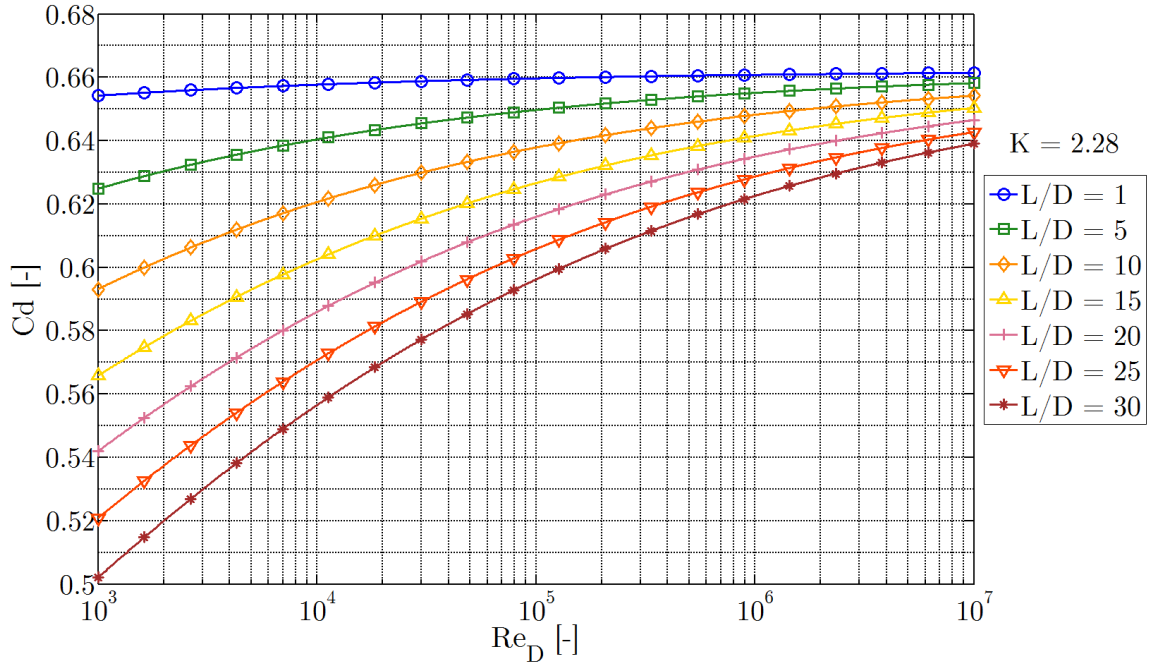


Figure 2.10:  $C_d$  vs  $Re_D$  for square edged inlet orifices ( $K = 2.28$ ) of various length to diameter ratios  $L/D$  in the turbulent flow region ( $C_f = \frac{0.0791}{Re_D^{1/4}}$ )

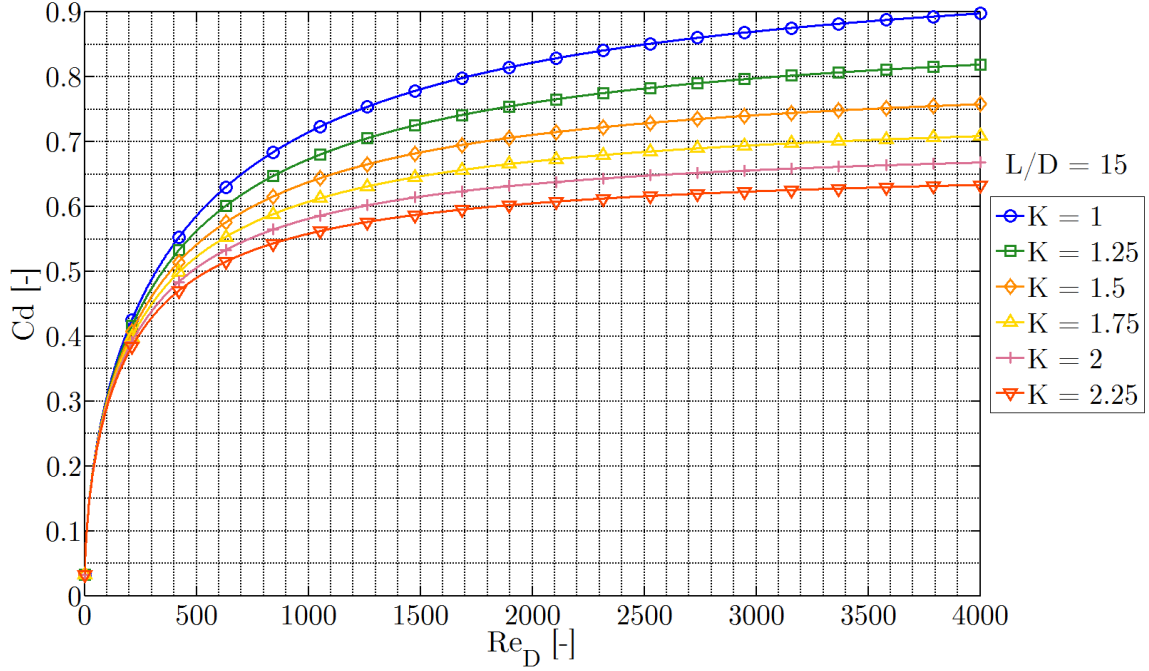


Figure 2.11:  $C_d$  vs  $Re_D$  for injector orifice with  $L/D = 15$  for various inlet geometry  $K$  values in the laminar flow region ( $C_f = \frac{16}{Re_D}$ )

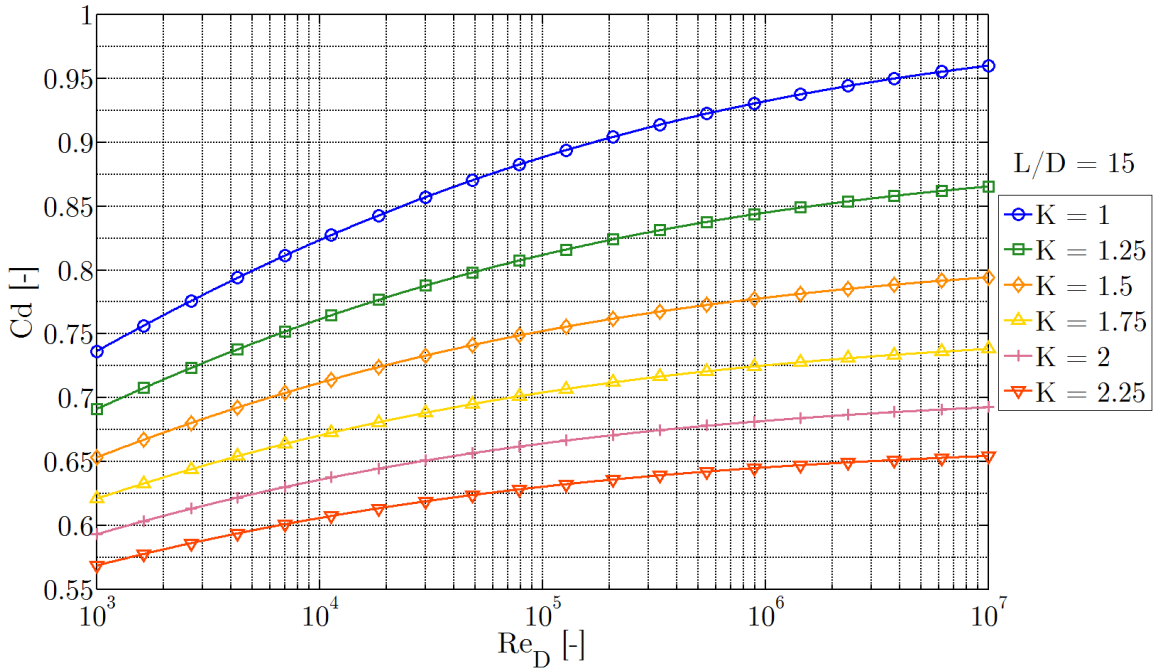


Figure 2.12:  $C_d$  vs  $Re_D$  for injector orifice with  $L/D = 15$  for various inlet geometry  $K$  values in the turbulent flow region ( $C_f = \frac{0.0791}{Re_D^{1/4}}$ )

The last assumption (neglecting boundary layer thickness) is only valid when the injector is large compared to the boundary layer thickness. For most injector or nozzle designs, this is not the case and it should be necessary to take these boundary layer effects into consideration. Nevertheless, this assumption is kept in the classical treatment of the Perfect Gas model, with the introduction of the empirically determined frictional discharge coefficient  $C_d$  as presented earlier in Section 2.1.1.1 [29].

Analysis starts with the continuity equation and the energy equation simplified for calorically perfect gases as shown in Eq. (2.39) and Eq. (2.40) respectively:

$$\dot{m} = \text{const.} = \rho_2 u_2 A_2 \quad (2.39)$$

$$C_p T_1 = C_p T_2 + \frac{1}{2} u_2^2 \quad (2.40)$$

where the subscript 1 is for values upstream of the injector and the subscript 2 is for the values at the injector exit, the same as in previous sections of this work. Eq. (2.40) can be re-written as in Eq. (2.41) to find an expression for  $u_2$ .

$$u_2 = \sqrt{2C_p T_1 \left(1 - \frac{T_2}{T_1}\right)} \quad (2.41)$$

Using the ideal gas equation in Eq. (2.36), the isentropic pressure-density relation shown in Eq. (2.42), the form of the energy equation shown in Eq. (2.41), all combined with the continuity equation results in the equation for mass flow rate under the Perfect Gas assumption as shown in Eq. (2.44):

$$\frac{P_2}{P_1} = \left(\frac{\rho_2}{\rho_1}\right)^\gamma \quad (2.42)$$

$$\gamma = \frac{C_p}{C_v} \quad (2.43)$$

$$\dot{m}_{PG} = C_d A_2 \rho_1 \sqrt{2C_p T_1 \left[ \left( \frac{P_2}{P_1} \right)^{\frac{2}{\gamma}} - \left( \frac{P_2}{P_1} \right)^{\frac{\gamma+1}{\gamma}} \right]} \quad (2.44)$$

where  $\gamma$  is the ratio of specific heats as shown in Eq. (2.43). It should be noted that the discharge coefficient  $C_d$  related to frictional losses in the orifice is included at this step. Eq. (2.44) is extremely useful in that all that is needed to determine the mass flow rate is the upstream thermodynamic conditions and the ratio of downstream to upstream pressure  $\frac{P_2}{P_1}$ . It can be seen that Eq. (2.44) exhibits a clear maximum when the pressure ratio  $\frac{P_2}{P_1}$  is equal to:

$$\frac{P_2}{P_{1 crit}} = \left( \frac{2}{\gamma + 1} \right)^{\frac{\gamma}{\gamma-1}} \quad (2.45)$$

As shown in Eq. (2.45), the critical pressure ratio, as it is termed, corresponds to the initial existence of sonic flow at the orifice exit. When the pressure ratio  $\frac{P_2}{P_1}$  drops below this value, the mass flow rate becomes solely dependent on the upstream conditions, and the orifice is said to have become “choked”. This is an important concept, especially for the remainder of this work and will be referred to interchangeably as either “choked” or “critical” flow. As will be described in Section 2.2, choked flow is not unique to gas phase flow, and can occur with the existence of two-phase flow within the injector. Once choked, changes in the downstream conditions do not affect the region upstream of the sonic point. The mass flow rate under the choked conditions is presented quite commonly in the form shown in Eq. (2.46).

$$\dot{m}_{PG crit} = C_d A_2 \sqrt{\gamma \rho_1 P_1 \left( \frac{2}{\gamma + 1} \right)^{\frac{\gamma+1}{\gamma-1}}} \quad (2.46)$$

Fig. 2.13 shows mass flow rate predictions using the Perfect Gas model for gaseous nitrous oxide at 20 °C (293 K) for a range of upstream pressures, from the saturation pressure of 733 psia (5.05 MPa) down to 300 psia (2.07 MPa). This time the data is presented vs. the pressure ratio  $P_2/P_1$ . From this point on, when presenting mass flow rate predictions that exhibit critical flow, the dotted lines represent the mass flow rate that would be calculated based strictly on the equations presented in the

models. As can be seen in Fig. 2.13, the mass flow rate value calculated using Eq. (2.44), increases up until the point of  $\frac{P_2}{P_{1 crit}}$ , and then decreases back down to zero as the downstream pressure  $P_2$  approaches zero. This is not a physical description of the flow, because in reality once the flow becomes critical, the mass flow rate remains constant as the downstream pressure is decreased. In the calculations of the mass flow rate that follow in this work, this factor is accounted for, and the predicted values will be shown in solid lines (with added point marks).

The data in Fig. 2.14 shows the critical mass flow rate for nitrous oxide over a range of storage temperatures and pressures. The upper right end of each curve is associated with the condition where saturated nitrous oxide vapor is used ( $P_1=P_v$ ). It can be seen that for a given upstream pressure, the critical mass flow rate predicted by the Perfect Gas model decreases with increasing temperature. From Fig. 2.14 it is difficult to ascertain why this is the case. However, by observing Fig. 2.15 and Fig. 2.16, the cause of this behavior is clear. With increasing temperature, both the density and  $\gamma$  value of nitrous oxide are increasing, both contributing to an increase in critical mass flow as calculated from Eq. (2.46).

As it turns out, the prediction of critical mass flow rate using the Perfect Gas model is highly sensitive to the value of  $\gamma$ . This hints at one of the significant issues with using the Perfect Gas model for the prediction of gaseous nitrous oxide mass flow rates. Specifically, there is not extensive data for the specific heats of nitrous oxide, especially as the pressures and temperatures of operation approach the thermodynamic critical point. To make matters worse, the critical point acts to a certain degree as a singularity, with many of the thermodynamic properties exhibiting large swings in value with small changes in temperature and pressure. This is the case with the ratio of specific heats,  $\gamma$ , reaching values in excess of 50 for gaseous nitrous oxide near the critical point, resulting in possible over-predictions of mass flow rate in this region. Additionally, nitrous oxide most certainly does not behave as an ideal gas, especially near the critical point, where the vapor compressibility factor  $Z$  deviates significantly from unity ( $Z=1$  for an ideal gas). For these reasons, care should be

taken to verify any gaseous nitrous oxide predictions using the Perfect Gas model, especially at operating conditions approaching the thermodynamic critical point.

The single phase liquid and gas flow models presented in this section are based off of simple physical laws enhanced with empirical correlations. Hybrid rocket injectors typically consist of simple orifice style holes, and most of the empirically based efforts for developing these single phase predictive mass flow models were performed for this same type of geometry. For this reason, many of the above described models are widely accepted and have been employed with great success and validation over a broad range of disciplines (e.g. aerospace, industrial, automotive, etc.). However, care must still be taken to recognize the practical considerations which lead to deviations from the above predictive model results (e.g. non-uniform inlet flow, dynamic operation, etc.). One particular example which is important in the prediction of nitrous oxide flow rates is the presence of two-phase flow, which will be discussed in the next section.

## 2.2 Two-Phase Flow in Propellant Injectors

Most traditional propellants are used as sub-cooled liquids due to their low vapor pressures and typically high operating pressures. Assuming the discharge coefficient is well characterized for a given injector design, the “ $C_dA$ ” equation resulting from the Single Phase Incompressible analysis as shown in Eq. (2.17) can be used with a high degree of confidence for these traditional propellants. Unfortunately, this method is often applied to injectors of high vapor pressure propellants such as nitrous oxide, with error often introduced by compressibility effects (compressibility factor  $Z \sim 0.12$  for saturated liquid,  $Z \sim 0.57$  saturated vapor at room temperature [14, 15]) and the development of two-phase flow within the orifice. A description of modeling the compressibility effects in nitrous oxide injectors is included in Section 2.1.1.2. However, the effects of compressibility are usually overshadowed by the introduction of two-phase flow. Therefore, this section and the rest of this work will

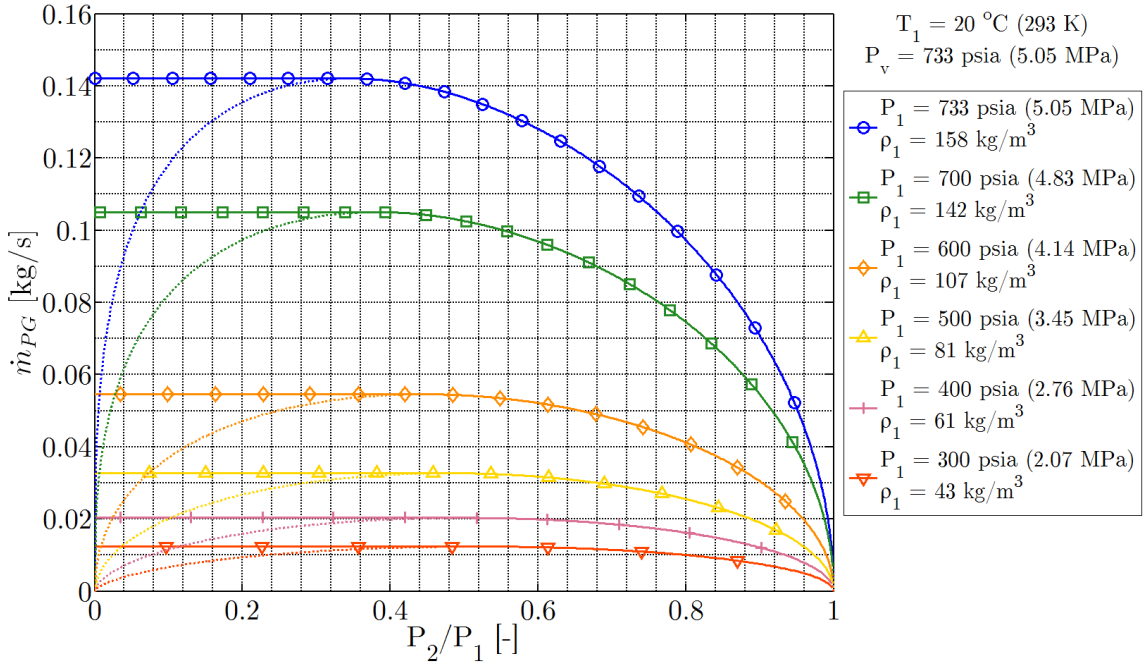


Figure 2.13:  $\dot{m}_{PG}$  vs.  $\frac{P_2}{P_1}$  using the perfect gas assumption for gaseous  $N_2O$  at  $20^\circ\text{C}$  (293 K) for a variety of upstream pressures ( $D_2 = 1.5 \text{ mm}$ ,  $C_d = 0.75$ ).

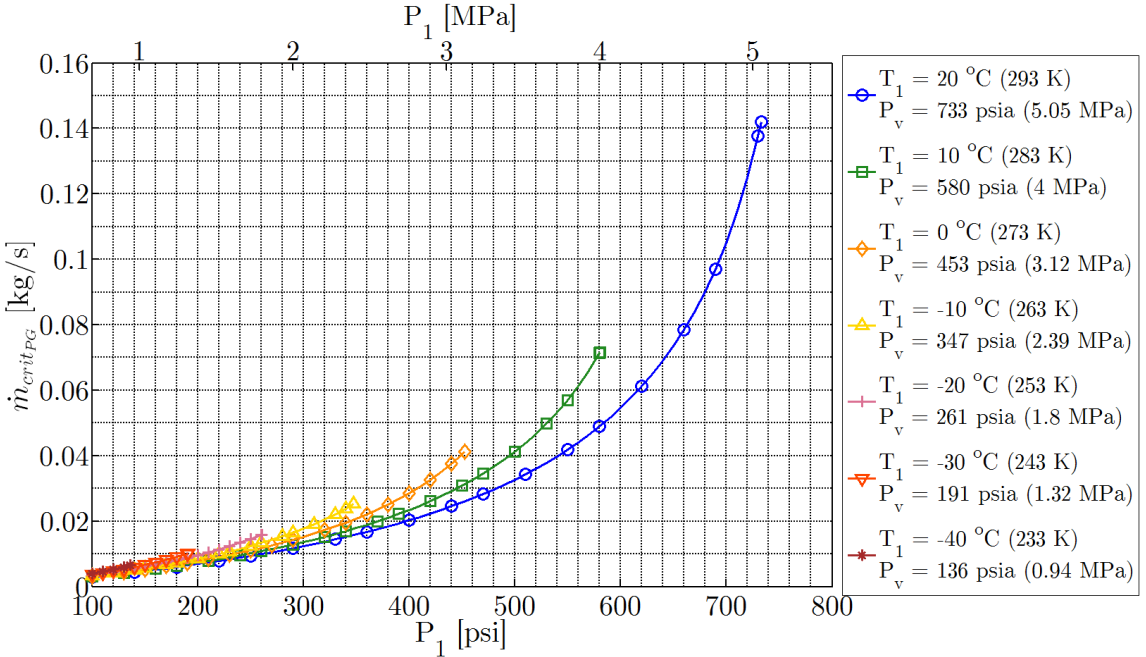
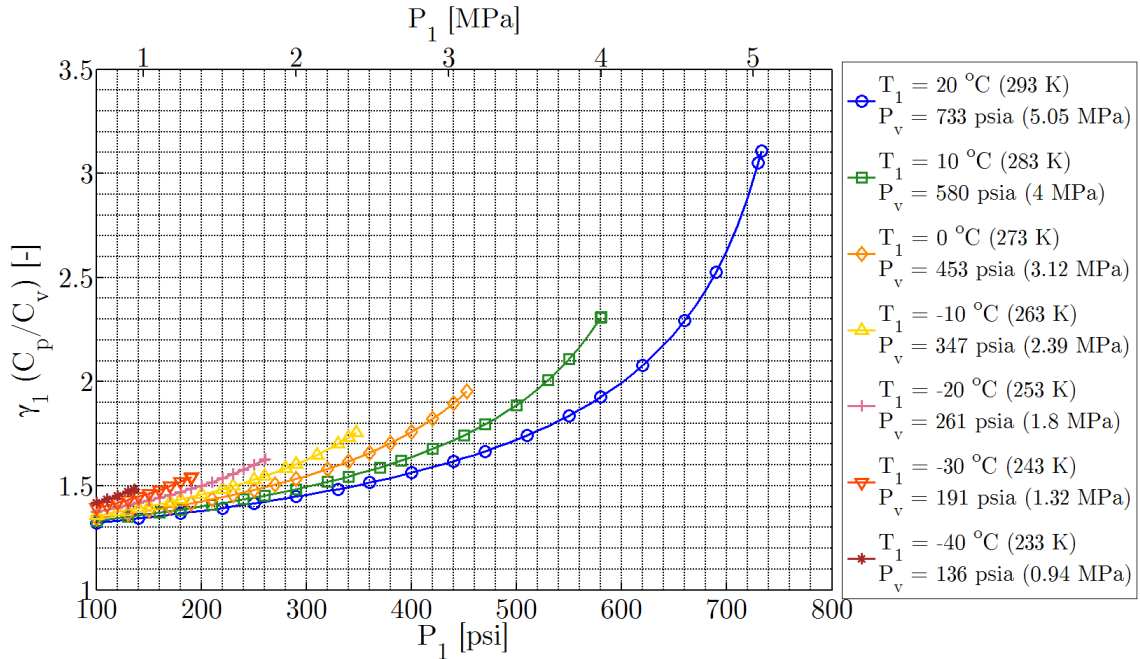
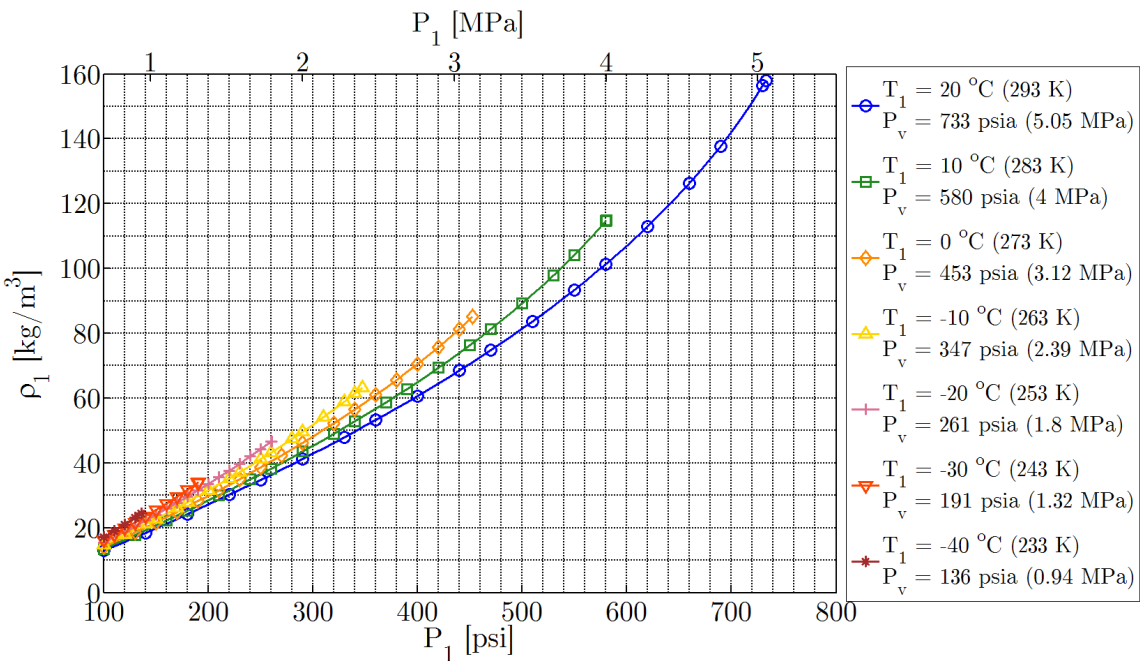


Figure 2.14:  $\dot{m}_{crit PG}$  vs.  $P_1$  using the perfect gas assumption for  $N_2O$  at varied temperatures ( $D_2 = 1.5 \text{ mm}$ ,  $C_d = 0.75$ ).

Figure 2.15:  $\gamma_1$  vs.  $P_1$  for gaseous  $N_2O$  at varied temperatures.Figure 2.16:  $\rho_1$  vs.  $P_1$  for gaseous  $N_2O$  at varied temperatures.

focus on the effects of two-phase flow on injector mass flow rate performance and modeling.

For self-pressurizing propellants such as nitrous oxide, the operating pressures in the feed system upstream of the injector are often very close to the vapor pressure. As a result, local static pressures within the injector can reach values well below the vapor pressure as the liquid accelerates and expands. Under these conditions, cavitation can occur within the injector orifice, resulting in the production of a significant amount of vapor, greatly decreasing the bulk fluid density. Fig. 2.17 (adapted from Dyer et al. [30]) schematically illustrates the evolution of static pressure throughout an injector for a low vapor pressure propellant in comparison to that of a high vapor pressure propellant.

Fig. 2.17a shows a typical static pressure profile for a low vapor pressure propellant as it passes through an injector. It should be noted that the vena contracta (v.c.) depicted in Fig. 2.17a is caused by flow separation and may or may not contain vapor pockets, depending on the pressure level in the vicinity of the sharp edge. In cases where the bulk static pressure drops below the vapor pressure within the injector as shown in Fig. 2.17b, significant vapor formation will occur, and the mass flow rate will be limited. This effect was demonstrated by the work of Hesson and Peck, in which the mass flow rate of saturated carbon dioxide ( $CO_2$ ) flow through simple short orifices was studied (orifice length to diameter ratio  $L/D \sim 1.7$ ) [31]. Similar to nitrous oxide, carbon dioxide is a high vapor pressure liquid at room temperature. In fact, often carbon dioxide is used as an analog to nitrous oxide because the thermodynamic and transport properties of the two are so similar (this will be discussed in detail in Section 3.1.3.1). Fig. 2.18 shows mass flux versus downstream pressure,  $P_2$ , for lines of constant upstream pressure  $P_1$  as presented by Hesson and Peck [31]. This figure shows that for a given upstream pressure, a maximum mass flow rate is achieved as the downstream pressure drops below some critical value, essentially choking the orifice with regard to mass flow (analogous to the behavior predicted by the Perfect Gas model in Section 2.1.2). This regime is

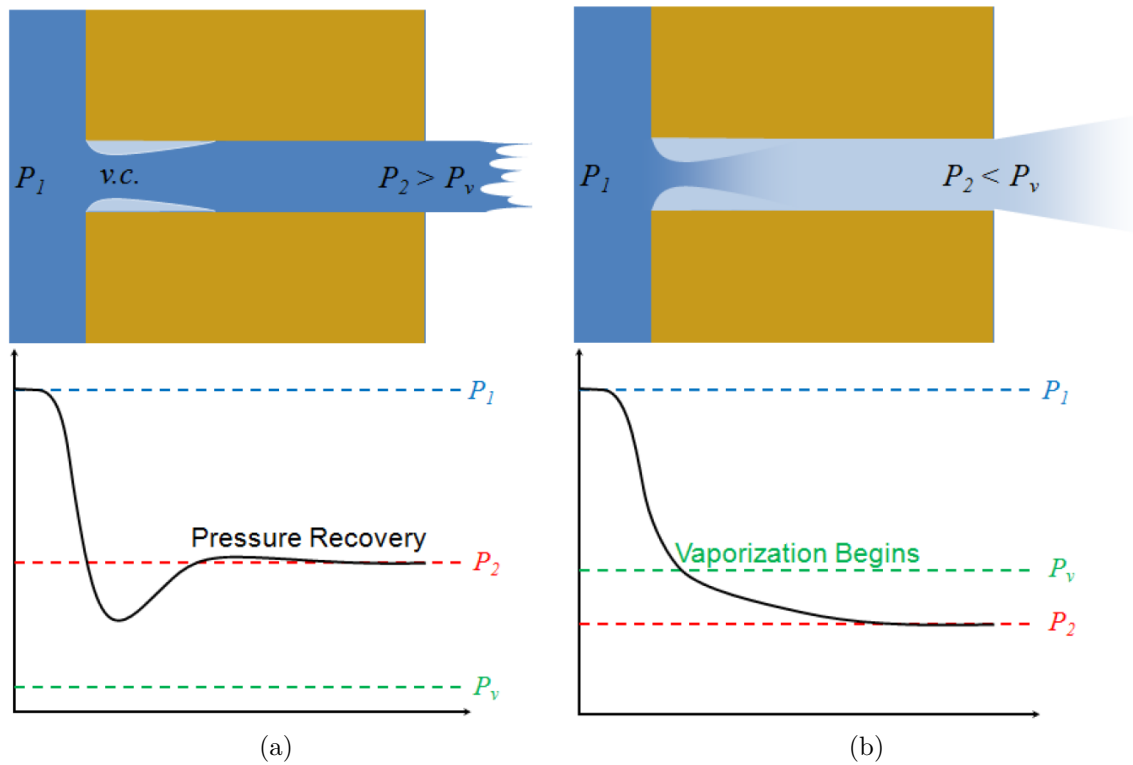


Figure 2.17: Conceptual injector pressure history as adapted from work by Dyer et al. showing (a) low vapor pressure propellant and (b) high vapor pressure propellant with flow from left to right [30]. The minimum area of contraction due to flow separation is denoted by v.c. (vena contracta).

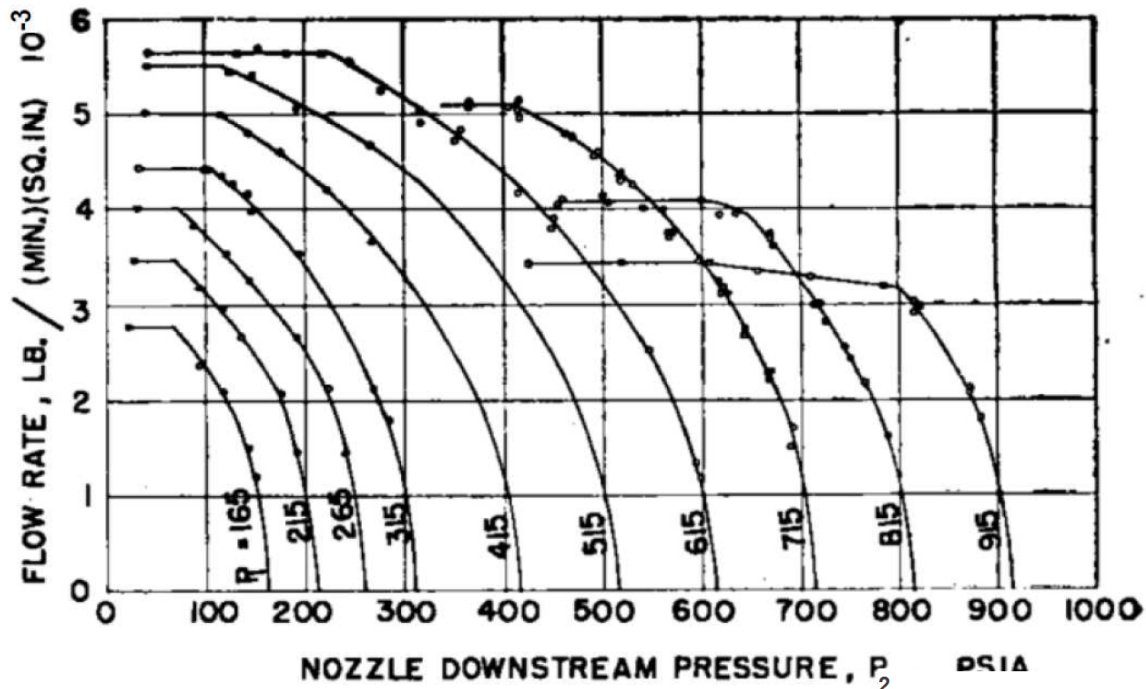


Figure 2.18: Sample of saturated carbon dioxide flow rate mapping data collected by Hesson and Peck using orifices with length to diameter ratio  $L/D \sim 1.7$  (reproduced from Ref. [31] with permission).

referred to as critical flow, and in this regime the mass flow rate is independent of the downstream pressure. A two-phase injector flow model must accurately predict this critical flow phenomenon in order to be useful.

Fortunately, a significant body of work has been performed by members of the nuclear power engineering community relating to the prediction of two-phase mass flow rates through flow openings or restrictions. In particular, nuclear engineers are concerned about accidents during which a rupture occurs in the water cooling lines, resulting in the discharge of high pressure hot water and steam to the environment. These types of studies are interested in determining with some degree of accuracy the maximum expected flow rates of coolant from the system in order to determine the blowdown characteristics and timescales of the coolant system. This happens to be a

Table 2.1: Classification of Different Two-Phase Flow Models

Model Classification		Models Presented
Thermodynamic Equilibrium	Homogeneous ( $k = 1$ )	Homogeneous Equilibrium Babitskiy
	Non-Homogeneous ( $k \neq 1$ )	Moody Fauske
Thermodynamic Non-Equilibrium	Frozen ( $k \neq 1$ but fixed)	Burnell Zaloudek
		Proposed Model
	Generalized ( $k \neq 1$ )	Dyer

two-phase critical flow problem, and fortunately, most of the development work has involved modeling of the rupture environment as a simple pipe or orifice type opening. The remainder of this section will present and discuss some representative models which originated from these types of coolant release studies and can be classified into two main categories:

- Models assuming thermodynamic equilibrium between the liquid and gaseous phases throughout expansion
- Non-equilibrium theories

The models can further be broken down into those assuming equal velocities of the liquid and vapor phases (homogeneous) and those allowing for “slip” between the two phases (non-homogeneous). A slip ratio  $k$  is defined later in Section 2.2.1.2 to account for the non-homogeneous effects. Table 2.1 outlines the two-phase flow models that will be discussed in the following sections. These models in general allow for the fluid upstream of the injector to either exist in the saturated liquid state, exhibit some degree of supercharge (sub-cooled liquid), or exist as a two-phase mixture. Both the first and second conditions mentioned will be examined extensively during this work. Operating conditions with two-phase mixtures of nitrous oxide upstream of the injector will not be considered for a variety of reasons. First, the determination of the vapor fraction of nitrous oxide incoming to the injector can be extremely difficult and

is not expected in the development of practical hybrid rocket systems. Additionally, as discussed in Section 1.3 and later in Section 5.3, nitrous oxide has a positive heat of formation and can undergo explosive decomposition reactions, especially in the vapor phase. The existence of nitrous oxide vapor in a feed system not specifically designed for vapor can be extremely dangerous and should be avoided whenever possible. Therefore, all analysis that follows will assume that the fluid at location 1 (upstream of the injector) is liquid at either saturation or with some degree of supercharging.

### 2.2.1 Equilibrium Models

The main assumption employed in the two-phase flow models presented in this section is the existence of thermodynamic equilibrium between the liquid and vapor phases throughout the entirety of the discharge geometry. In the case of the present work this includes the flow from upstream of the injector all the way through to the injector exit. Thermodynamic equilibrium implies the following conditions:

- Temperature of the liquid and vapor phases are equal
- Pressure and temperature can be related by the thermodynamic saturation curve

In these models, the mixture quality or vapor mass fraction is allowed to change axially along the length of the injector. Physically, in order for vapor formation to occur, a finite difference in temperature or pressure of the two phases is required. This is at odds with the assumptions outlined above. Therefore, in order to reconcile this discrepancy, the quality change within the fluid occurs infinitely fast, resulting in instantaneous vaporization. Equilibrium models can further be split up into two distinct categories [32]:

- Homogeneous models: equal velocities in the liquid and vapor phase
- Non-homogeneous models: different velocities between the liquid and vapor phase

### 2.2.1.1 Homogeneous Models

Homogeneous equilibrium models are the simplest form of two-phase mass flow rate prediction models (except for purely empirical models). As outlined above, the phases are assumed to be in thermodynamic equilibrium, and the velocities of the liquid and vapor phases are treated as equal. This section will describe two such methods and compare the resulting mass flow rate predictions.

#### 2.2.1.1.1 Homogeneous Equilibrium Model

The most simple homogeneous equilibrium model that is commonly used to predict the two-phase critical flow rate through an injector orifice is simply called the Homogeneous Equilibrium Model (HEM). In this model, it is assumed that the fluid in a pressure vessel outflows through a pipe that is much smaller than the vessel diameter. This description is consistent with that of many hybrid rocket injector designs. Additionally it assumed that the flow is isentropic throughout. Analysis again starts from the continuity equation and the energy equation as shown in Eq. (2.47) and Eq. (2.48). Note that now the fluid at location 2 is allowed to contain a mixture of liquid and vapor, and can potentially exhibit a non-zero vapor mass fraction as defined in Eq. (2.49).

$$\dot{m} = \text{const.} = \rho_2 u_2 A_2 \quad (2.47)$$

$$h_1 = h_2 + \frac{1}{2} u_2^2 \quad (2.48)$$

$$x_2 \equiv \frac{\dot{m}_v}{\dot{m}_v + \dot{m}_l} \quad (2.49)$$

where the subscripts  $v$  and  $l$  indicate the vapor and liquid states respectively. Combining Eq. (2.47) and Eq. (2.48) and including the discharge coefficient described in Section 2.1.1.1 results in an expression for the predicted mass flow rate using the Homogeneous Equilibrium Model as shown in Eq. (2.50).

$$\dot{m}_{HEM} = C_d A \rho_2 \sqrt{2(h_1 - h_2)} \quad (2.50)$$

For traditional presentations of this method, it is assumed that the thermodynamic properties of arbitrary vapor/liquid mixtures at the exit plane are not readily available (such as  $\rho_2$  and  $h_2$ ). For this reason, the properties at the injector exit are traditionally calculated as a vapor mass fraction weighted average of the saturated vapor and liquid properties respectively. Formally this means that any property  $\phi$  at the exit can be estimated as in Eq. (2.51):

$$\phi_{2,HEM} = x_2 \phi_2^v + (1 - x_2) \phi_2^l \quad (2.51)$$

However, with the existence of highly accurate equations of state for nitrous oxide in the REFPROP package, the calculation of the mixture properties at the exit becomes trivial, and the estimation shown in Eq. (2.51) becomes unnecessary [14, 15]. Specifically, due to the isentropic assumption, as long as the upstream temperature and pressure ( $T_1$  and  $P_1$ ) are known, as well as the backpressure  $P_2$ , the downstream mixture properties can be found by following a line of constant entropy as shown in Eq. (2.52).

$$s_1 = s_2 \quad (2.52)$$

At critical flow, the predicted mass flow exhibits a maximum with respect to the downstream pressure as described by Ref. [33] and [34] and shown in Eq. (2.53)[30]:

$$\dot{m}_{crit\ HEM} = \dot{m}_{HEM} \Big|_{\left(\frac{\partial \dot{m}_{HEM}}{\partial P_2} = 0\right)} \quad (2.53)$$

While this is a good physical description of the onset of critical flow, it will be seen later in this section that the mass flow rate predictions using the Homogeneous Equilibrium Method often exhibit discontinuities in slope at the critical point. Therefore, a more robust description of the onset of critical flow is simply:

$$\dot{m}_{crit\ HEM} = \max (\dot{m}_{HEM})_{w.r.t. P_2} \quad (2.54)$$

or equivalently:

$$(\dot{m}_{HEM})_{P_2 < P_{2,crit}} = \max (\dot{m}_{HEM})_{w.r.t. P_2} \quad (2.55)$$

A graphical representation of this type of critical flow calculation is included in Fig. 2.19, which models an injector for initially saturated liquid nitrous oxide at room temperature of approximately 20 °C (293 K). It is clear from the plot that for downstream pressures below the critical value, the equilibrium model does not level off and remain constant in the same way seen in the experimental data from the work of Hesson and Peck [31]. As described similarly in Section 2.1.2, this is not a physical description of the flow, because beyond the critical point, the mass flow rate remains constant as the downstream pressure is decreased. The handling of this behavior will be done in the same fashion as in Section 2.1.2 (dotted lines show the calculated value, solid lines show the physical value).

It is expected that if the assumption of equilibrium is valid, the HEM should do a good job of predicting the critical mass flow rate. However, thermodynamic equilibrium is only a limiting case, and gives a lower-bound estimate for the critical mass flow rate [35]. Furthermore, experimental data suggest that the critical mass flow rate for many short tube injectors is significantly underpredicted using the Homogeneous Equilibrium Model, likely due to non-equilibrium effects. In fact, as an orifice approaches the thin plate limit, it is likely that no critical flow regime will be observed.

For this first two-phase flow model, a variety of different presentations of some sample mass flow rate predictions will be included, in order to facilitate complete understanding of the behavior of the types of models presented in this section. Subsequent models will not receive this treatment. First, Fig. 2.20 and Fig. 2.21 show the mass flow rate and effective  $C_d$  predictions for 0 °C (273 K) nitrous oxide over a range of supercharge values for the baseline injector design presented in Section

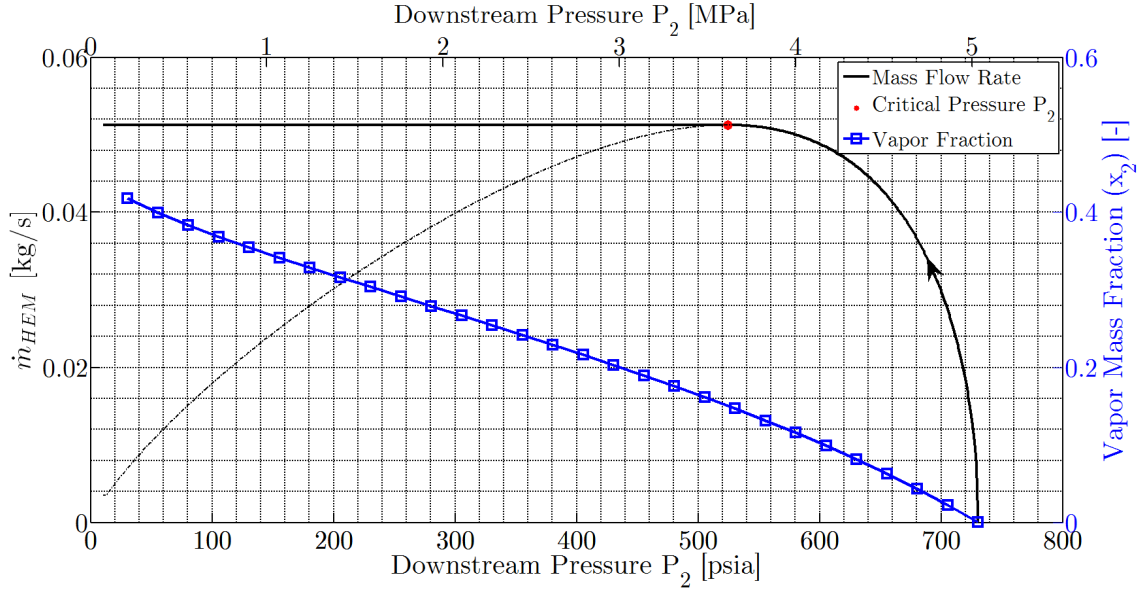


Figure 2.19: Critical mass flow rate prediction using the Homogeneous Equilibrium Model for initially saturated liquid nitrous oxide at 730 psia (5.03 MPa) corresponding to room temperature of approximately 20 °C (293 K). The data used to produce this plot was calculated using REFPROP [14, 15].

2.1.1.1. The effective  $C_d$  value, or  $C_{d,HEM}$  in this case is the based on the ratio of predicted mass flow rate vs. that predicted by the Single Phase Incompressible model. When the Homogeneous Equilibrium Model predicts purely liquid flow, the value of  $C_{d,HEM}$  will be identical to that of the Single Phase Incompressible model. Once two-phase flow is predicted within the injector,  $C_{d,HEM}$  begins to drop below the SPI value. As can be seen in Fig. 2.20 and Fig. 2.21, at the lowest vales of  $\Delta P$ , the predicted value matches exactly that of the Single Phase Incompressible model. While following this curve up to larger values of  $\Delta P$ , the predictions reach critical flow at various points, in order of supercharge value (lower supercharge values reach critical flow earlier).

While the presentation of the data in Fig. 2.20 and Fig. 2.21 allows for an intuitive comparison between the Homogeneous Equilibrium Model predictions and those of the Single Phase Incompressible model, Fig. 2.22 and Fig. 2.23 show more

clearly the important factors for the inception of critical flow. These figures plot the data with respect to the ratio of downstream pressure to the vapor pressure of the incoming liquid ( $P_2/P_v$ ). It is clearly visible that deviations from the Single Phase Incompressible model occur once the downstream pressure drops below the vapor pressure. This indicates that the inception of two-phase flow is predicted at approximately the same point for each supercharge level as easily seen in Fig. 2.23. However, the actual critical flow regime is achieved at different values of  $P_2/P_v$  depending on the supercharge level. Specifically, the predictions for saturated nitrous oxide show that the critical flow is achieved at downstream pressures well below the vapor pressure, even though vapor formation begins right as the downstream pressure drops below the vapor pressure. This is not the case with the predictions for highly supercharged nitrous oxide.

Sometimes it can be useful to plot the effective  $C_d$  value versus a parameter termed the cavitation number. The cavitation number can be defined equivalently a number of ways, but the most simple form is shown in Eq. (2.56). While the cavitation number can be useful for examining the behavior of supercharged nitrous oxide model predictions and experimental results, it is essentially useless for application to saturated nitrous oxide data because it is always equal to zero ( $P_1 = P_v$ ). Fig. 2.24 plots  $C_{d,HEM}$  vs. the cavitation number. It is obvious right away that this presentation can be useful due to the relatively linear nature of the drop off in  $C_d$  vs.  $K$ , as  $K$  decreases in the two-phase region, at least for the predictions using the Homogeneous Equilibrium Method.

$$K = \frac{P_1 - P_v}{P_1 - P_2} \quad (2.56)$$

Fig. 2.25 compares the critical mass flow rate predictions for  $N_2O$  at various temperatures over a range of supercharge values. At high levels of supercharge, the predicted critical flow rate is slightly dependent on temperature, with lower critical flow rates predicted for higher temperature nitrous oxide. This is due to the variation of the density of nitrous oxide with temperature similar to that described in Section

2.1.1. However, it can be observed for the lower values of supercharge that the critical flow rate becomes much more sensitive to the temperature of the oxidizer, especially under the saturated conditions ( $P_{sup}^1 = 0$  psi). This is explored in more detail in Fig. 2.26 which plots the predicted critical mass flow rate for saturated  $N_2O$  over broad range of temperatures (and thus  $P_v$ ). Fig. 2.25 and Fig. 2.26 will be used as baseline results for the comparison of each of the subsequent two-phase flow models throughout the rest of this work.

### 2.2.1.1.2 Babitskiy

An interesting approach to the Homogeneous Equilibrium Method is that of Babitskiy [36, 32]. In this approach, both Eq. (2.47) and Eq. (2.48) are used, but instead of using the isentropic assumption, the momentum equation (Bernoulli's equation) is used in the form shown in Eq. (2.57). This results in two versions of the mass flow rate equation, shown in Eq. (2.58) and Eq. (2.59):

$$P_1 = P_2 + \frac{1}{2}\rho_2 u_2^2 \quad (2.57)$$

$$\dot{m} = C_d A_2 \rho_2 \sqrt{2(h_1 - h_2)} \quad (2.58)$$

$$\dot{m} = C_d A_2 \sqrt{2\rho_2 (P_1 - P_2)} \quad (2.59)$$

In order to reconcile the energy and momentum based mass flow rate equations, the specific entropy is treated as a free variable. In practice, the entropy is allowed to increase in increments, and the mass flow rate from Eq. (2.58) and Eq. (2.59) are compared. When the appropriate entropy increase is achieved for this iterative method, the two forms of the mass flow rate will be equal, resulting in the mass flow rate and corresponding change in entropy predicted using Babitskiy's approach. The iterative nature of this process can result in increased computational expense over the Homogeneous Equilibrium Method, even though the method is still quite simple.

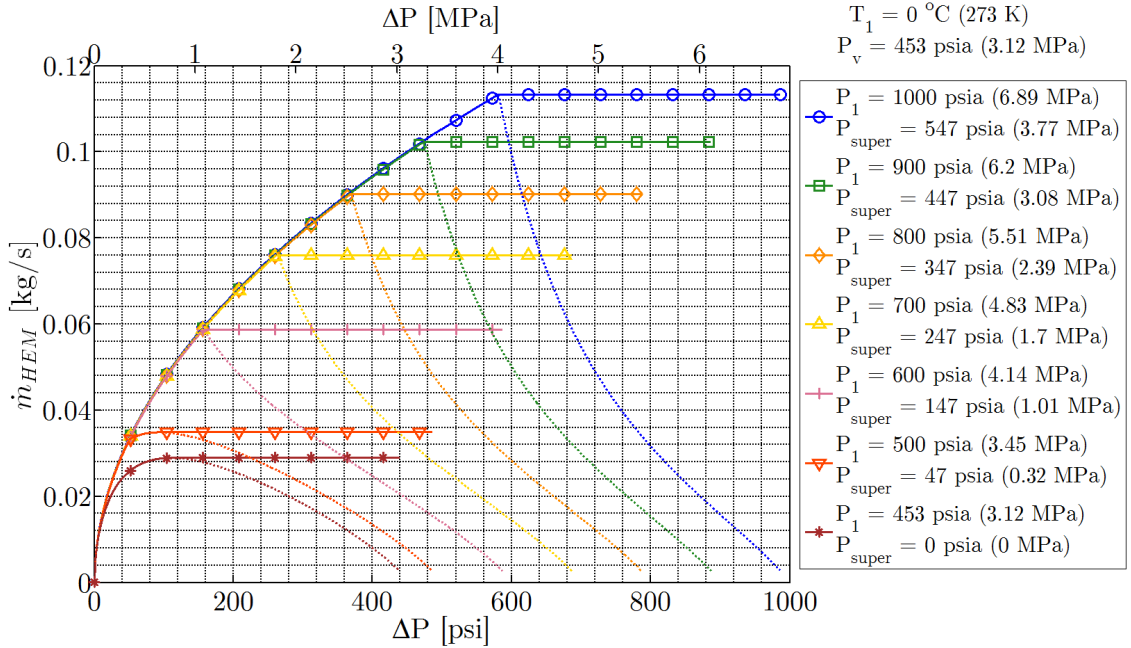


Figure 2.20:  $\dot{m}_{HEM}$  vs.  $\Delta P$  using the Homogeneous Equilibrium Model for  $N_2O$  at  $0^\circ C$  (273 K) for a variety of upstream pressures (supercharge values). ( $D_2 = 1.5$  mm,  $C_d = 0.75$ )

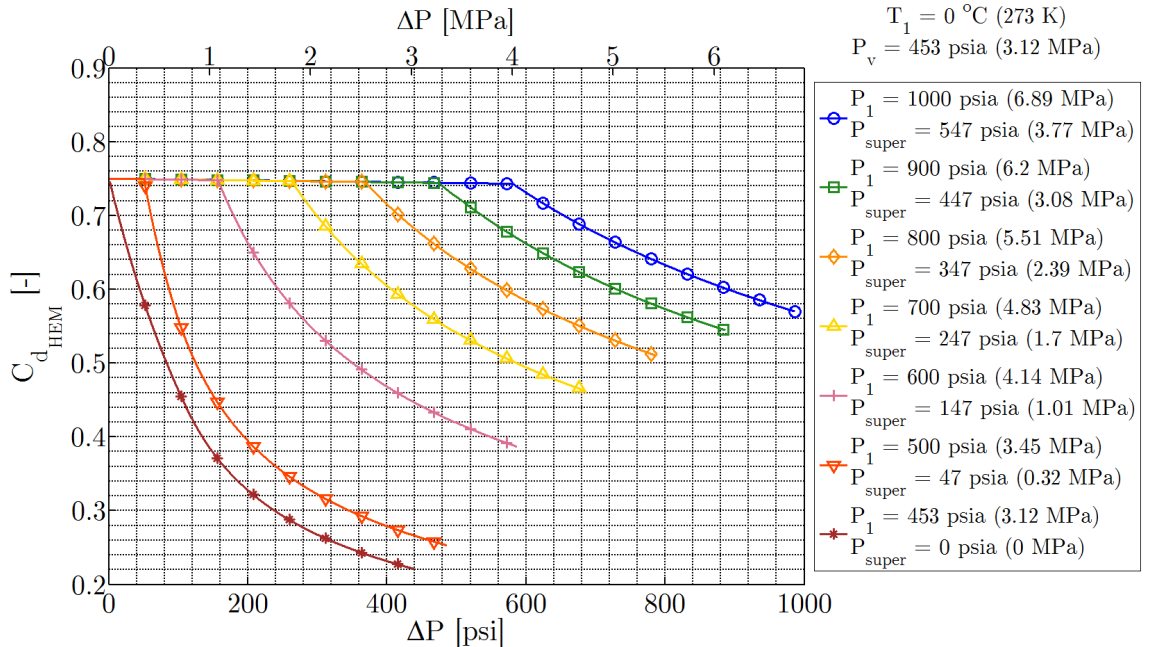


Figure 2.21:  $C_{d_{HEM}}$  vs.  $\Delta P$  using the Homogeneous Equilibrium Model for  $N_2O$  at  $0^\circ C$  (273 K) for a variety of upstream pressures (supercharge values). ( $D_2 = 1.5$  mm,  $C_d = 0.75$ )

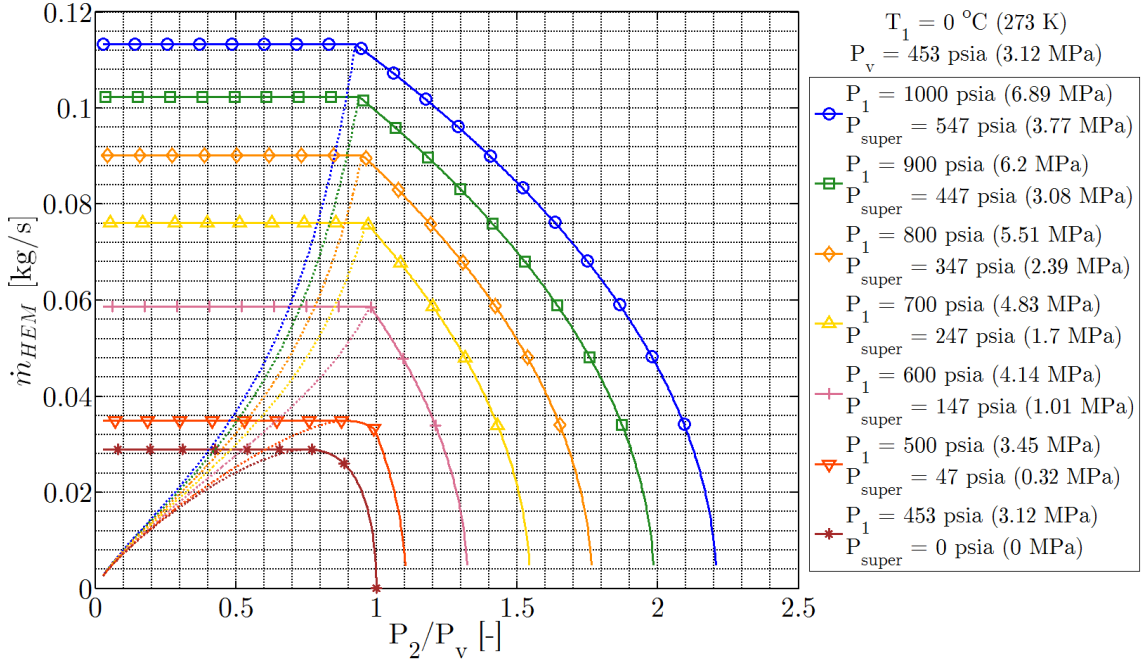


Figure 2.22:  $\dot{m}_{HEM}$  vs.  $\frac{P_2}{P_v}$  using the Homogeneous Equilibrium Model for  $N_2O$  at  $0^\circ C$  (273 K) for a variety of upstream pressures (supercharge values). ( $D_2 = 1.5$  mm,  $C_d = 0.75$ )

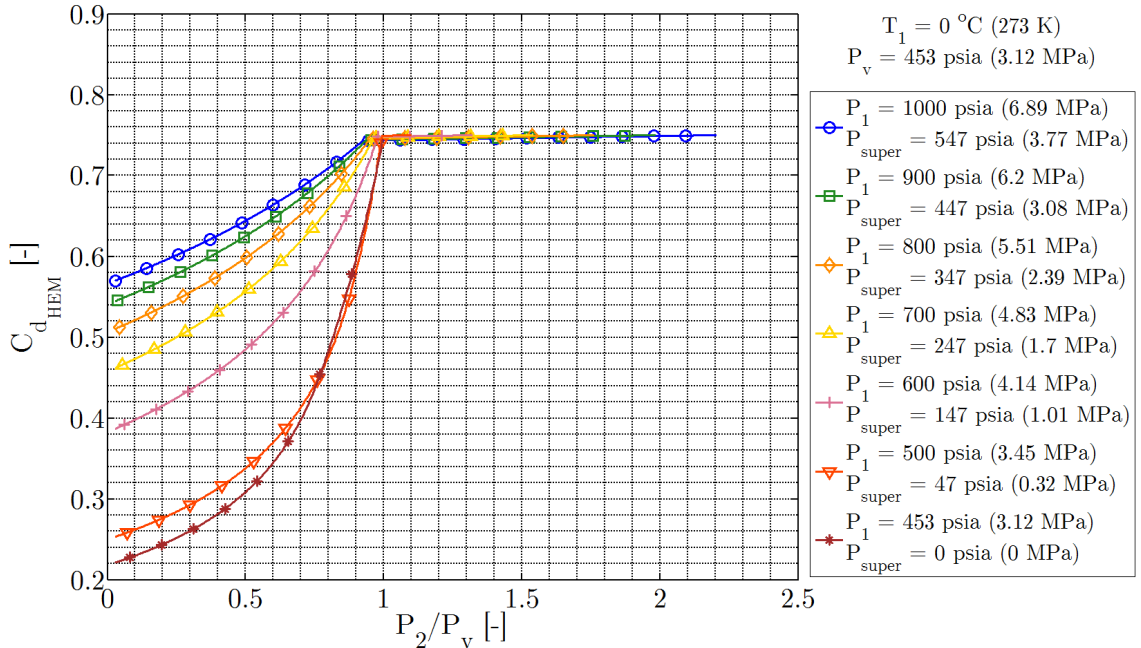


Figure 2.23:  $C_{d_{HEM}}$  vs.  $\frac{P_2}{P_v}$  using the Homogeneous Equilibrium Model for  $N_2O$  at  $0^\circ C$  (273 K) for a variety of upstream pressures (supercharge values). ( $D_2 = 1.5$  mm,  $C_d = 0.75$ )

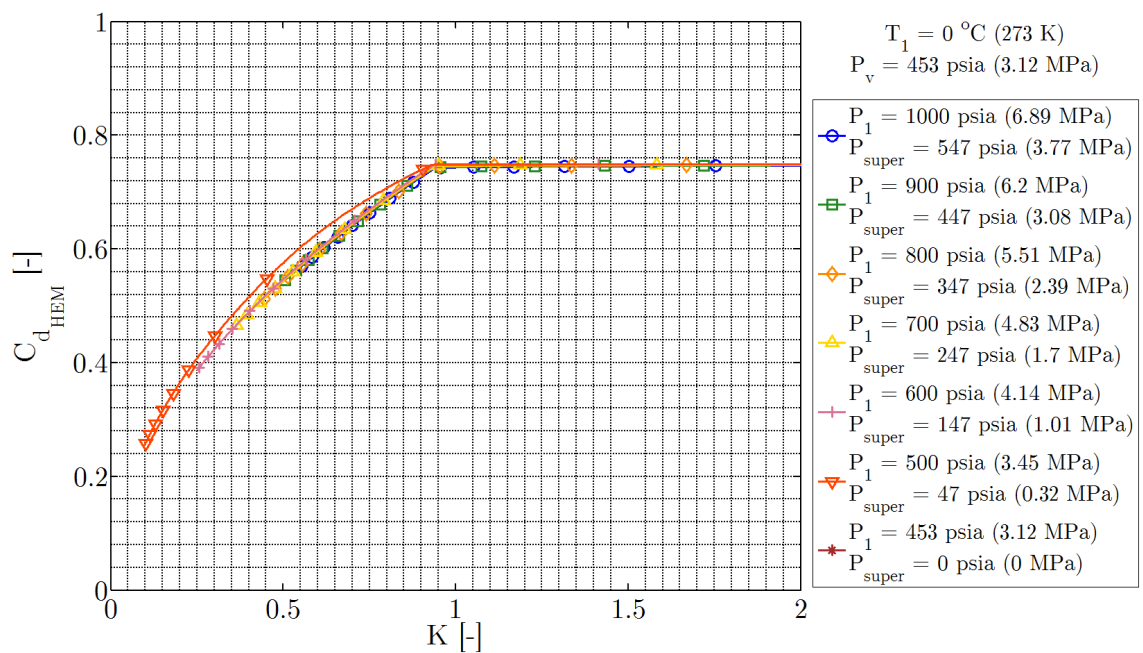


Figure 2.24:  $C_{d,HEM}$  vs. cavitation number  $K$  using the Homogeneous Equilibrium Model for  $N_2O$  at  $0^\circ\text{C}$  (273 K) for a variety of upstream pressures (supercharge values). ( $D_2 = 1.5$  mm,  $C_d = 0.75$ ). Note saturated case not included because  $K = 0$ .

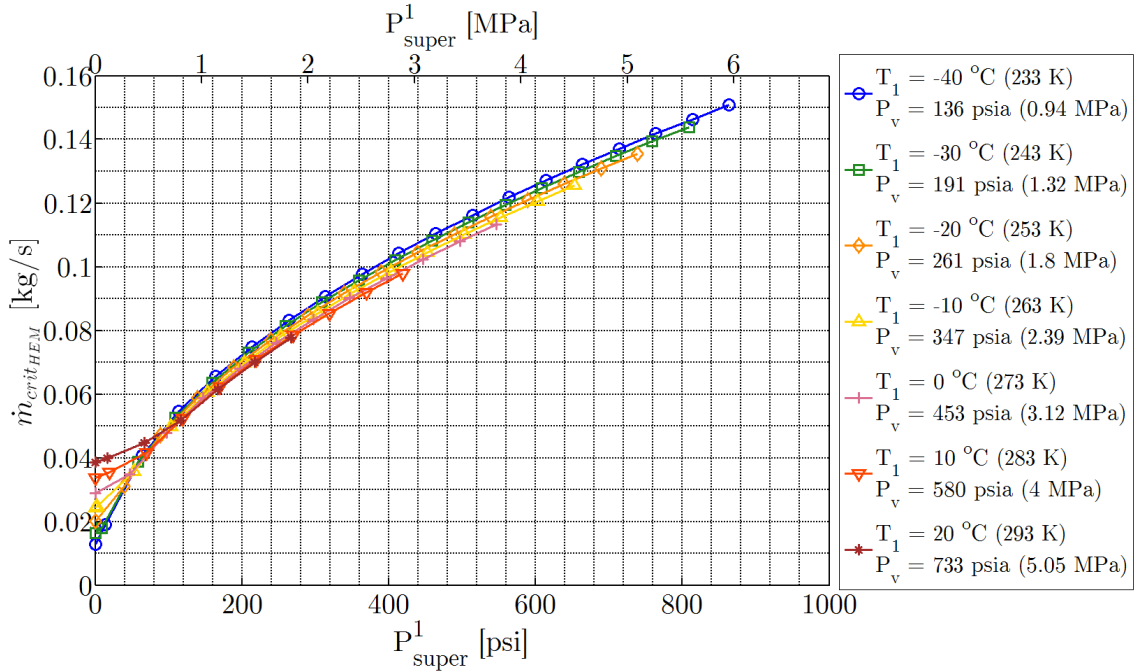


Figure 2.25:  $\dot{m}_{crit\ HEM}$  vs.  $P_{super}^1$  using the Homogeneous Equilibrium Model for  $N_2O$  over a range of temperatures. ( $D_2 = 1.5\text{ mm}$ ,  $C_d = 0.75$ )

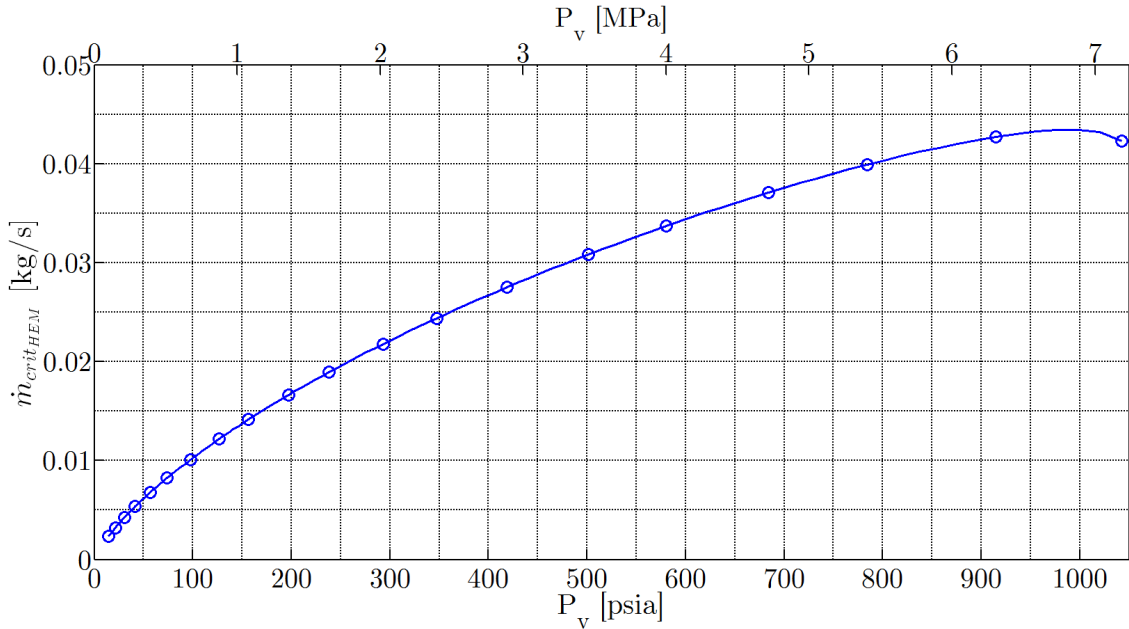


Figure 2.26:  $\dot{m}_{crit\ HEM}$  vs.  $P_v$  using the Homogeneous Equilibrium Model for saturated  $N_2O$  ( $D_2 = 1.5\text{ mm}$ ,  $C_d = 0.75$ ).

$$s_1 \neq s_2 \quad (2.60)$$

$$\dot{m}_{BAB} = C_d A_2 \rho_2 \sqrt{2(h_1 - h_2)} = C_d A_2 \sqrt{2\rho_2 (P_1 - P_2)} \quad (2.61)$$

The mass flow rate and  $C_d$  values predicted by the Babitskiy model are shown in Fig. 2.27, Fig. 2.28, and Fig. 2.29. For most of the range of  $\Delta P$  and supercharge values plotted, the mass flow rate data looks identical to that of the standard Homogeneous Equilibrium Model. However, upon close examination of the predictions at low supercharge near saturation, it can be seen that the predicted critical mass flow rates are slightly higher for the Babitskiy model. In order to more directly compare the differences in predictions between the two homogeneous methods, Fig. 2.30 and Fig. 2.31 show predictions of the critical mass flow rate from both models on the same plot. Fig. 2.30 shows the corresponding critical flow rate predictions for 0 °C (273 K) nitrous oxide at various supercharge values. The predictions are indeed identical for all but low values of supercharge, where the entropy increase determined using Babitskiy's approach is evidently non-zero. Fig. 2.31 shows critical flow rate predictions using both methods for saturated nitrous oxide over a broad range of temperatures and thus vapor pressures. Babitskiy's method predicts higher flow rates over the entire range of temperatures for saturated nitrous oxide.

### 2.2.1.2 Non-Homogeneous Models

In contrast to the homogeneous models presented above, non-homogeneous models allow for the liquid and vapor phases to exist as separate phases as opposed to a homogeneous mixture. This means that the velocities of the two phases are not assumed to be equal, and so-called slip can occur between them. In order to account for this difference, a dimensionless quantity called the “slip” ratio is defined as in Eq. (2.62) [37]:

$$k \equiv \frac{u_{2,v}}{u_{2,l}} \quad (2.62)$$

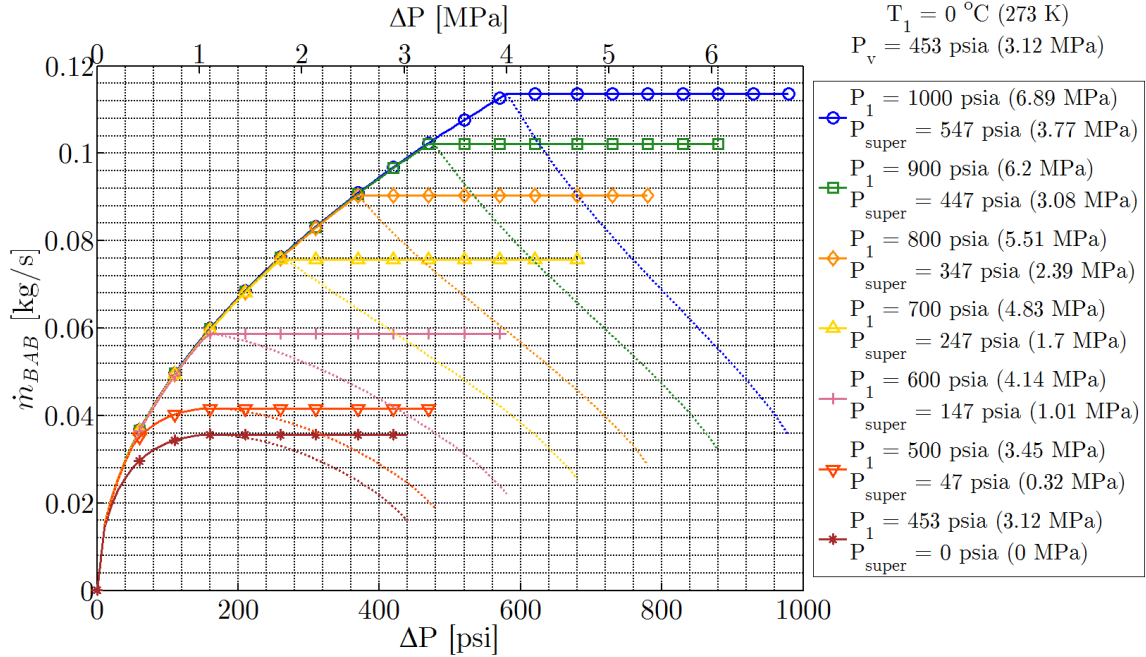


Figure 2.27:  $\dot{m}_{BAB}$  vs.  $\Delta P$  using Babitskiy's homogeneous equilibrium approach for  $N_2O$  at  $0^\circ C$  (273 K) for a variety of upstream pressures (supercharge values). ( $D_2 = 1.5$  mm,  $C_d = 0.75$ )

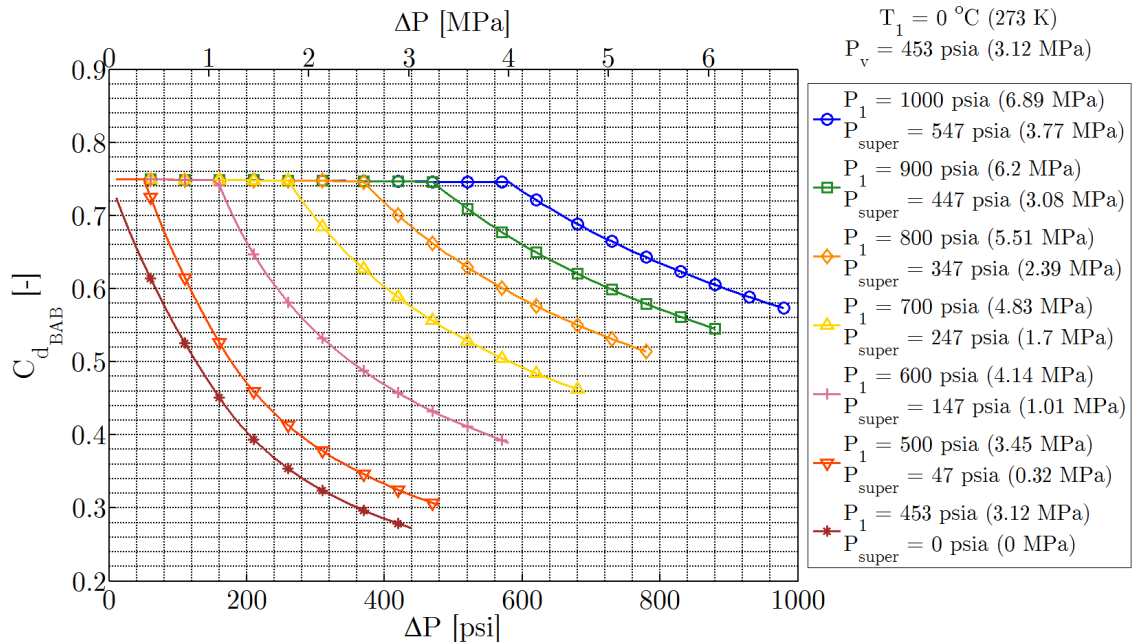


Figure 2.28:  $C_{d,BAB}$  vs.  $\Delta P$  using Babitskiy's homogeneous equilibrium approach for  $N_2O$  at  $0^\circ C$  (273 K) for a variety of upstream pressures (supercharge values). ( $D_2 = 1.5$  mm,  $C_d = 0.75$ )

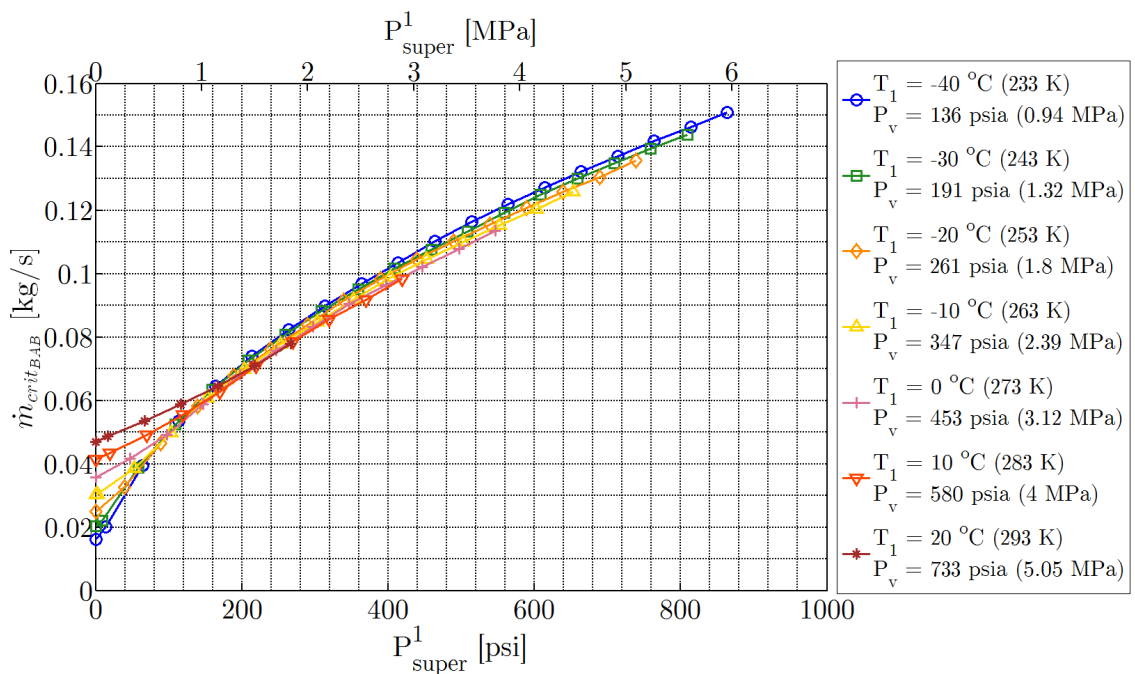


Figure 2.29:  $\dot{m}_{crit\,BAB}$  vs.  $P_{super}^1$  using Babitskiy's homogeneous equilibrium approach for  $N_2O$  over a range of temperatures. ( $D_2 = 1.5$  mm,  $C_d = 0.75$ )

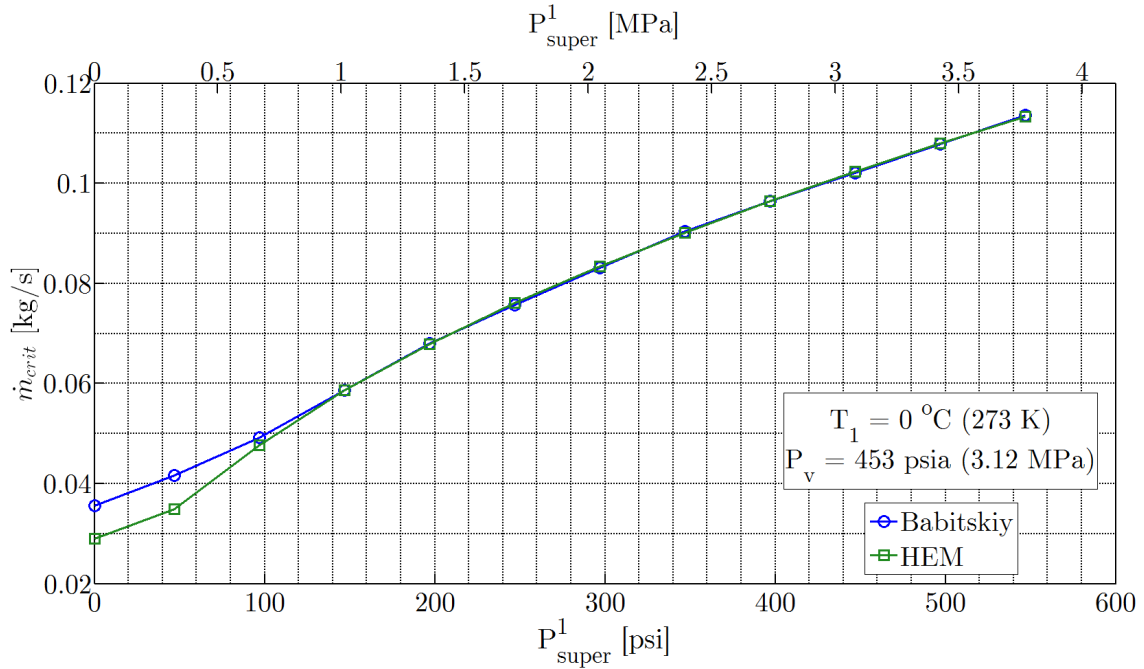


Figure 2.30: Comparison of  $\dot{m}_{crit}$  vs.  $P_{super}^1$  predictions using Babitskiy's homogeneous equilibrium approach and the standard Homogeneous Equilibrium Model for  $N_2O$  at  $0^\circ C$  (273 K). ( $D_2 = 1.5$  mm,  $C_d = 0.75$ )

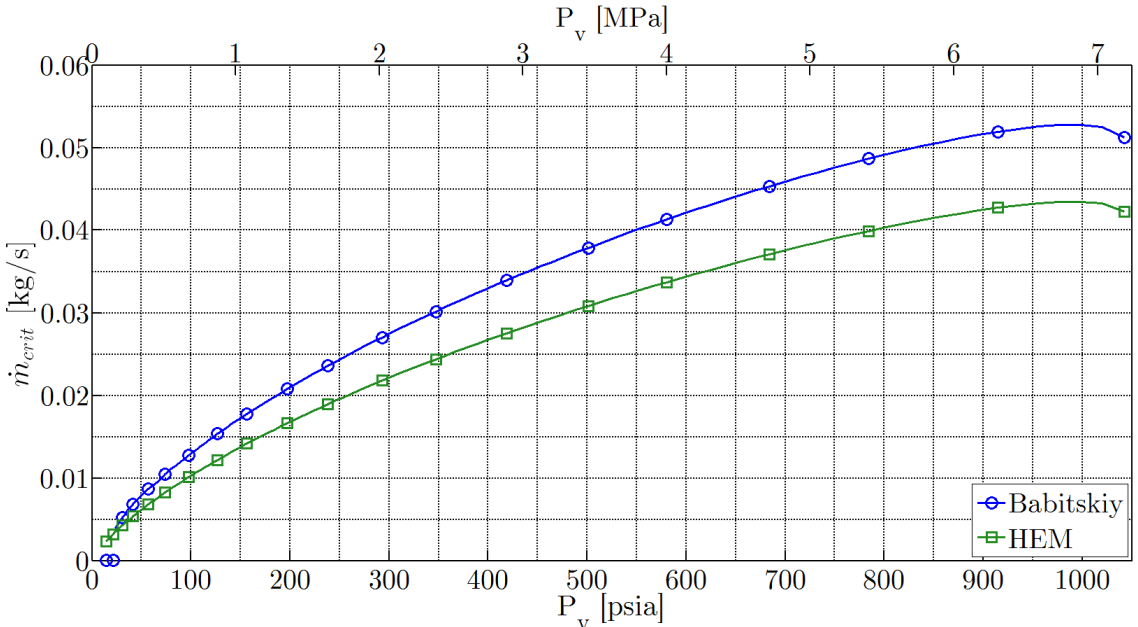


Figure 2.31: Comparison of  $\dot{m}_{crit}$  vs.  $P_v$  predictions using Babitskiy's homogeneous equilibrium approach and the standard Homogeneous Equilibrium Model for saturated  $N_2O$  over a range of vapor pressures. ( $D_2 = 1.5$  mm,  $C_d = 0.75$ )

where  $u_{2,v}$  and  $u_{2,l}$  are the vapor and liquid velocities at the injector exit respectively. The method of determining the actual value of the slip ratio  $k$  is an important characteristic of each non-homogeneous model. Following the definition of the slip ratio, the void fraction can now also be defined as in Eq. (2.63):

$$\alpha_2 \equiv \frac{1}{1 + k \left( \frac{1-x_2}{x_2} \right) \frac{\rho_v}{\rho_l}} \quad (2.63)$$

### 2.2.1.2.1 Moody

The most commonly used non-homogeneous equilibrium two-phase flow model is that presented by Moody, which assumes an isentropic frictionless process in addition to thermodynamic equilibrium assumption. Additionally, the flow-pattern is assumed to be annular with the liquid phase along the wall of the injector orifice with a vapor core. The velocities of each phase are uniform at the exit, with the slip ratio an independent variable. This model was actually developed with gradual converging nozzle flows in mind, but in this case the derivation applies equally well to injector orifices which exhibit instead an abrupt change in area at the start of the flow element. For the non-homogeneous flow field, the continuity and energy equations can be fashioned as in Eq. (2.64) and Eq. (2.65) [37].

$$\dot{m} = \text{const.} = \frac{\alpha_2}{x_2} \rho_{2,v} u_{2,v} \quad (2.64)$$

$$h_1 = x_2 \left( h_{2,v} + \frac{u_{2,v}^2}{2} \right) + (1 - x_2) \left( h_{2,l} + \frac{u_{2,l}^2}{2} \right) \quad (2.65)$$

Using the definition of slip ratio in Eq. (2.62), the energy equation can be manipulated to achieve an expression for  $u_{2,v}$  as shown in Eq. (2.66). Combining Eq. (2.66) and the continuity equation (again, along with the addition of the discharge coefficient) results in Eq. (2.67), the mass flow rate predicted by the Moody model [37]:

$$u_{2,v} = \sqrt{\frac{2k^2(h_1 - h_2)}{x_2(k^2 - 1) + 1}} \quad (2.66)$$

$$\dot{m}_{MOODY} = C_d A_2 \frac{k}{x_2 + k(1 - x_2)^{\frac{\rho_{2,v}}{\rho_{2,l}}}} \rho_{2,v} \sqrt{\frac{2(h_1 - h_2)}{x_2(k_2^2 - 1) + 1}} \quad (2.67)$$

It can be observed that if either the slip ratio  $k = 1$  or the injector exit vapor fraction  $x_2 = 0$ , the model presented by Moody is identical to that of the Homogeneous Equilibrium Model, which is to be expected (homogeneous or single phase liquid flow respectively). However, the slip ratio is still a free variable, so the mass flow rate predicted by Moody's model varies depending on the actual slip ratio between the phases. However, in order to determine the critical flow rate predicted by Moody's model, the mass flow rate must be maximized not only with respect to downstream pressure  $P_2$ , but also with respect to the slip ratio,  $k$ . Moody showed that maximum flow rate occurs for slip ratios equal to the value shown in Eq. (2.68). While this is technically only the value for critical flow, it will be used at all times for the example predictions shown in this section.

$$k_{crit, MOODY} = \left(\frac{\rho_l}{\rho_v}\right)^{1/3} \quad (2.68)$$

Fig. 2.32 and Fig. 2.33 show the predicted mass flow rate and  $C_d$  values for saturated and supercharged nitrous oxide at 0 °C (273 K), in order to verify expected behavior. For the sake of continuity, Fig. 2.34 compares critical flow values predicted by Moody's model to the two homogeneous models presented previously for 0 °C (273 K) nitrous oxide at various supercharge values. It is surprising to see that Moody's method and Babitskiy's predict nearly identical mass flow rates over the entire range of conditions, even in the region approaching saturation. However, this is proven to be coincidental by Fig. 2.35 which compares the predicted critical flow rates for saturated conditions over a range of  $N_2O$  temperatures and thus vapor pressures. It can be seen that at low temperatures and values of vapor pressure, Moody's model predicts higher values of critical mass flow rate, and as the temperature and vapor pressure increase, predictions from Moody's model approach that of the Homogeneous

Equilibrium Model. However, over most of the range of interest for the saturated case, Moody's model does demonstrate the increased mass flow rates predicted with the absence of the homogeneous assumption and thus the introduction of slip between the phases.

### 2.2.1.2.2 Fauske

Another popular non-homogeneous model was proposed by Fauske that is very similar to that of Moody [38]. Instead of using the energy equation to derive the expected mass flow rate, Fauske based his model on the momentum equation. Fauske's derivation assumes a gradual converging nozzle flow, similar to that of Moody's, however he also assumed that the largest pressure gradients in the direction of flow are at the exit of the flow element. This is inconsistent with (in fact opposite) the pressure evolution expected in orifice type flows, so the resulting mass flow rate predictions of this model will not be presented. However it is interesting to note that for the derivation based on the momentum equation, Fauske shows that the slip ratio resulting in critical flow can be determined by a similar expression as that of Moody, but with a different exponential term, as shown in Eq. (2.69).

$$k_{crit,FAUSKE} = \left( \frac{\rho_l}{\rho_v} \right)^{1/2} \quad (2.69)$$

## 2.2.2 Non-Equilibrium Models

The equilibrium models described above begin to break down when the finite rate of heat and mass transfer between the liquid and vapor phases prohibits the injector flow from reaching thermodynamic equilibrium before reaching the injector exit. As described earlier, in hybrid rocket feed systems, nitrous oxide is either used as a saturated liquid, or a secondary pressurization system is used to supercharge (or sub-cool) the liquid. In both cases, the static pressure drops as it accelerates and expands through the injector. As the pressure falls below the saturation pressure, vapor formation may initiate almost immediately, especially locally at nucleation

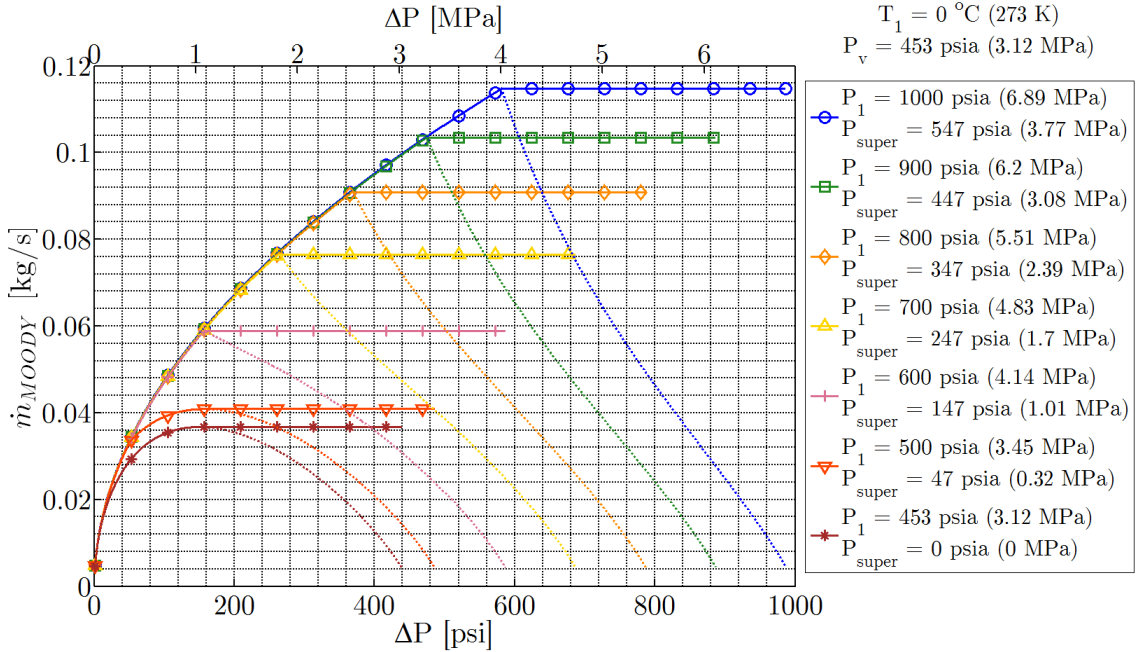


Figure 2.32:  $\dot{m}_{MOODY}$  vs.  $\Delta P$  using Moody's non-homogeneous equilibrium approach for  $N_2O$  at  $0^\circ C$  (273 K) for a variety of upstream pressures (supercharge values). ( $D_2 = 1.5$  mm,  $C_d = 0.75$ )

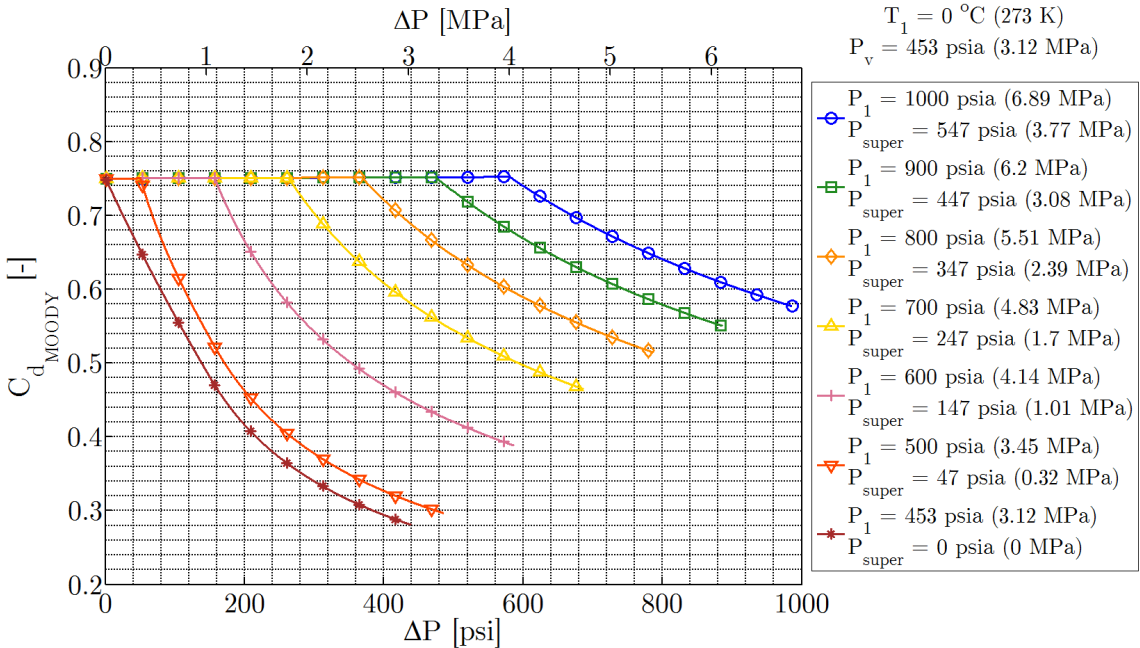


Figure 2.33:  $C_{d_{MOODY}}$  vs.  $\Delta P$  using Moody's non-homogeneous equilibrium approach for  $N_2O$  at  $0^\circ C$  (273 K) for a variety of upstream pressures (supercharge values). ( $D_2 = 1.5$  mm,  $C_d = 0.75$ )

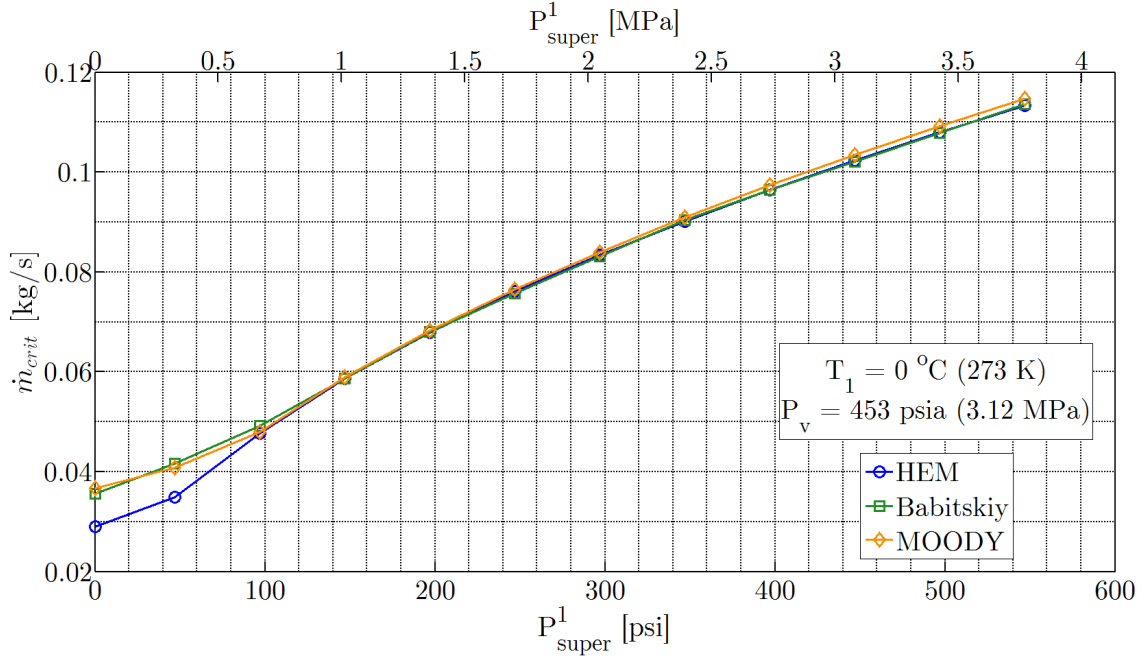


Figure 2.34: Comparison of  $\dot{m}_{crit}$  vs.  $P_{super}^1$  predictions using Moody's non-homogeneous approach, Babitskiy's homogeneous approach and the standard Homogeneous Equilibrium Model for  $N_2O$  at  $0^\circ\text{C}$  (273 K). ( $D_2 = 1.5 \text{ mm}$ ,  $C_d = 0.75$ )

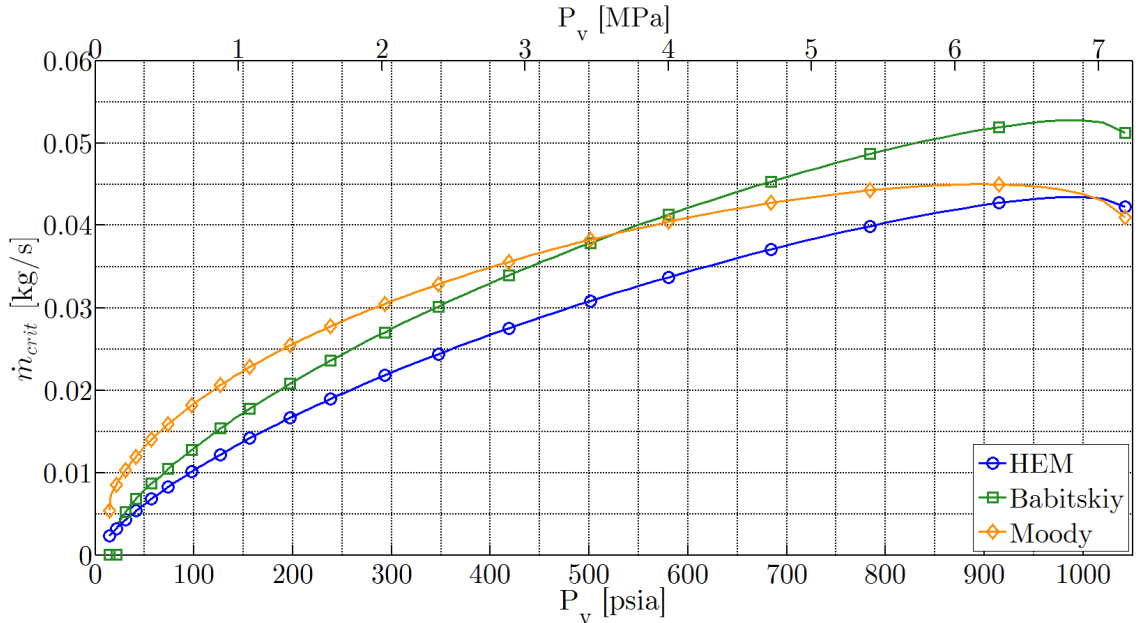


Figure 2.35: Comparison of  $\dot{m}_{crit}$  vs.  $P_v$  predictions using Moody's non-homogeneous approach, Babitskiy's homogeneous approach and the standard Homogeneous Equilibrium Model for saturated  $N_2O$  over a range of vapor pressures. ( $D_2 = 1.5 \text{ mm}$ ,  $C_d = 0.75$ )

sites when they are readily available. However, often this is not the case, and instead the liquid enters a metastable state in which vaporization does not occur. In this scenario, the nitrous oxide becomes a superheated liquid, at which point very small disturbances or the introduction of nucleation sites can result in rapid and widespread cavitation of the liquid to vapor [30].

The extent to which the liquid can theoretically be superheated in the metastable state is bounded by the liquid spinodal line. The spinodal lines mark the limits of the region where only unstable fluid can exist, therefore homogeneous nucleation must occur at some point before reaching the spinodal line [39]. Thus, the metastable region is located between the saturation line and the spinodal line, which is depicted graphically by the purple region in Fig. 2.36. The spinodal lines can be calculated by following the traverse of the outermost isothermal local extrema (i.e. the extrema closest to the saturation curves). Specifically, the liquid and vapor spinodal lines are collocated with the outermost isothermal local minima and maxima respectively, and they meet at the thermodynamic critical point. The ability of the metastable liquid to approach the spinodal limit is dependent upon the extent to which the liquid is mechanically stressed. This depends on a variety of parameters, such as the rate of depressurization, the availability of nucleation sites, and the level of disturbances that would tend to cause heterogeneous nucleation and cavitation [39, 40]. In reality, no experimental data exists to determine the actual physical metastability limit, so the spinodal is a purely numerical and theoretical boundary. Depending on the rate of depressurization, the liquid follows a process bounded by the isentropic and isothermal curves as shown in Fig. 2.36. The isentropic path corresponds to an infinitely fast depressurization and the isothermal line corresponds to an extremely slow process, whereas an actual fluid trajectory will lie somewhere between the two [40]. Due to the complexities in determining how far into the metastable region the fluid travels and the actual thermodynamic path that it takes, some models do not attempt to resolve this trajectory, but find other ways to account for the non-equilibrium effects [30].

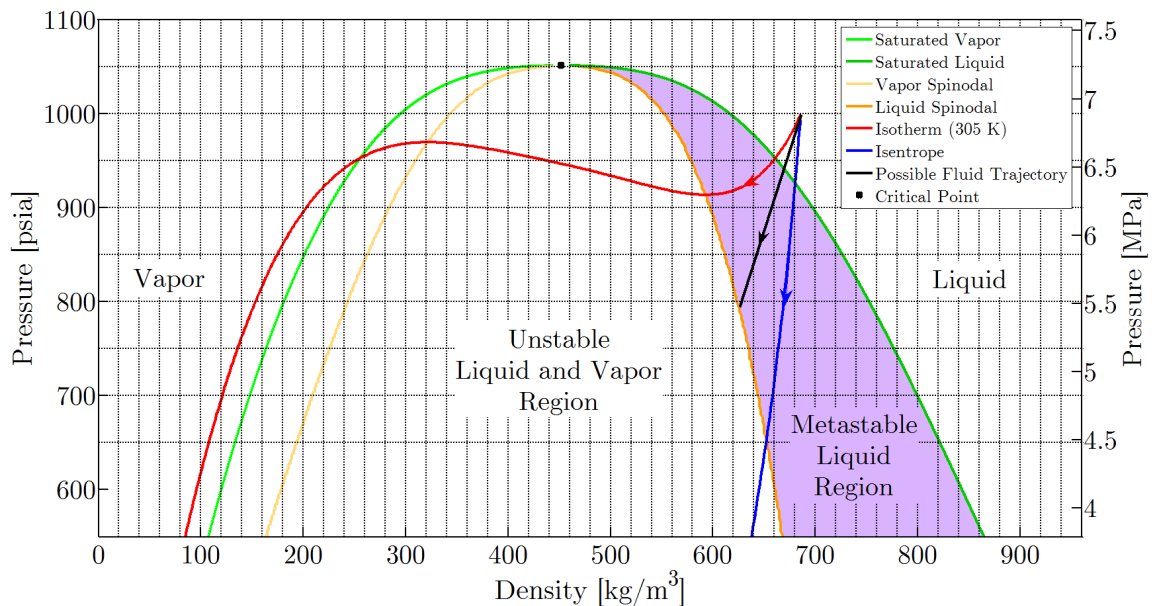


Figure 2.36:  $P - \rho$  diagram for nitrous oxide. Lines of a constant temperature of 32  $^{\circ}\text{C}$  (305 K) and constant entropy are included for a sub-cooled liquid which starts at 1000 psia (6.89 MPa) and transitions into the metastable region. The data used to produce this plot was calculated using REFPROP [14, 15].

### 2.2.2.1 Frozen Non-Equilibrium Methods

The first, and simplest type of non-equilibrium models presented in the literature admit no variation in the mixture composition throughout the flow. These are termed frozen non-equilibrium models. A result of this assumption is that the slip ratio between the two phases can be non-zero, but is fixed. However, for the types of flow of interest in the present work (saturated or sub-cooled liquid flow), the frozen assumption means that no physical treatment of two-phase flow is included. This leaves only a few simple models, which are semi-empirically based.

#### 2.2.2.1.1 Burnell

A semi-empirical model proposed early on by Burnell relates the non-equilibrium in two-phase flow to the surface tension of the liquid/vapor interface of the bubble surfaces in cavitating flow. In this model, the critical flow rate is described by equation Eq. (2.70) [41].

$$\dot{m}_{BURNELL\ crit} = C_d A_2 \sqrt{2\rho_1 [P_1 - (1 - C) P_v]} \quad (2.70)$$

In Burnell's equation for the critical mass flow rate, the empirical coefficient  $C$  is a function of saturation pressure and it essentially simulates a decrease of the value of vapor pressure. This simulated behavior corresponds to two potential physical process: (a) the superheating of the propellant as it enters the metastable region and/or (b) a decrease in temperature during the expansion process and thus a decrease in the vapor pressure. Burnell's correlation for the coefficient  $C$  versus the saturation pressure is shown in Fig. 2.37. It should be noted that this correlation was developed from fits of data produced during studies of critical water flow, and its applicability to high vapor pressure propellants is likely marginal. Similar empirical correlations could be developed for flow of high vapor pressure propellants such as nitrous oxide. However, for simplicity the fit for the coefficient  $C$  presented in Fig.

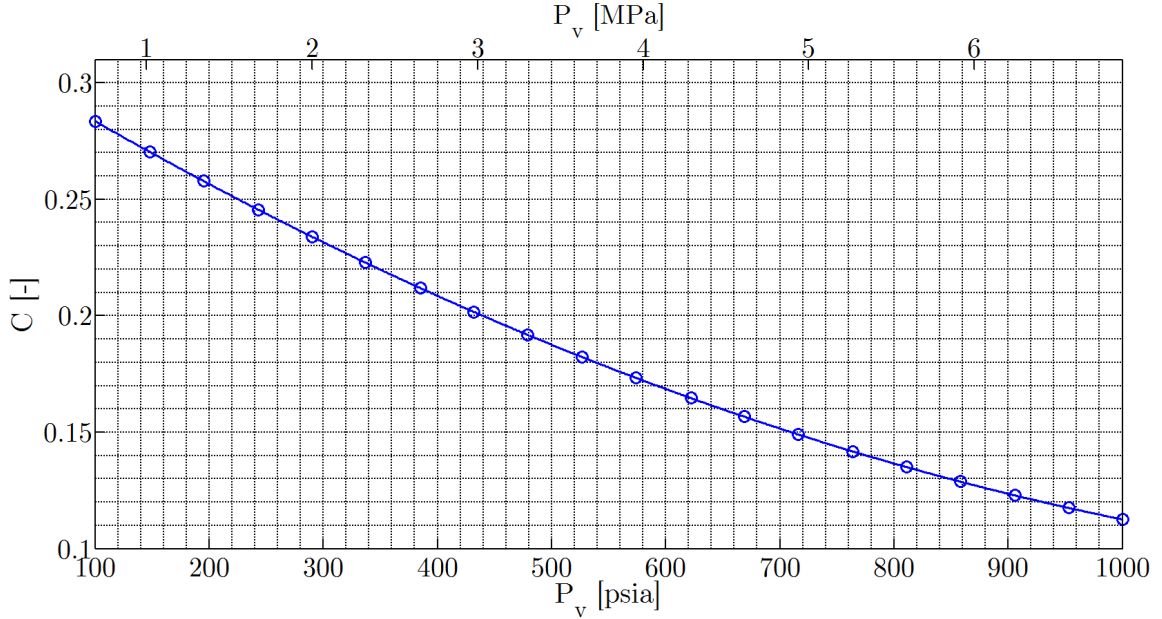


Figure 2.37:  $C$  coefficient vs.  $P_v$  for Burnell's critical flow model based on critical water flow experiments.

2.37 will be used in the predictions presented in this section.

Fig. 2.38 and Fig. 2.39 shows the mass flow rate and  $C_d$  values predicted by Burnell's model over a range of operating conditions. These plots result from calculating the Single Phase Incompressible values until the critical value determined from Eq. (2.70) is reached. It can be seen from Fig. 2.38 and Fig. 2.39 that for nitrous oxide at a given temperature and vapor pressure, the transition to critical flow predicted by Burnell's models occurs at the same value of  $P_2/P_v$  regardless of the supercharge level (which is expected from examining Eq. (2.70) and Fig. 2.37. However the inception of critical flow is expected to change as the temperature and thus vapor pressure of the nitrous oxide changes.

In order to compare the predictions from this model to those of the equilibrium models described in Section 2.2.1, Fig. 2.40 and Fig. 2.41 plot the critical mass flow rate predicted by Burnell, Moody and the Homogeneous Equilibrium Model

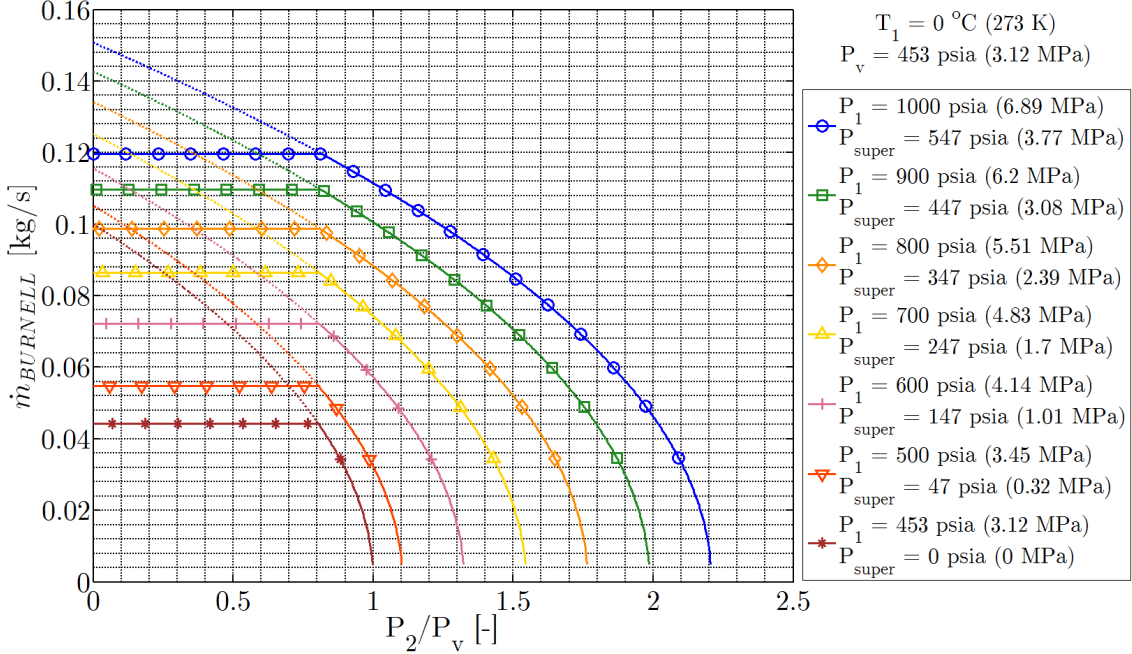


Figure 2.38:  $\dot{m}_{BURNELL}$  vs.  $\frac{P_2}{P_v}$  using the Burnell model for  $N_2O$  at  $0^\circ\text{C}$  (273 K) for a variety of upstream pressures (supercharge values). ( $D_2 = 1.5 \text{ mm}$ ,  $C_d = 0.75$ )

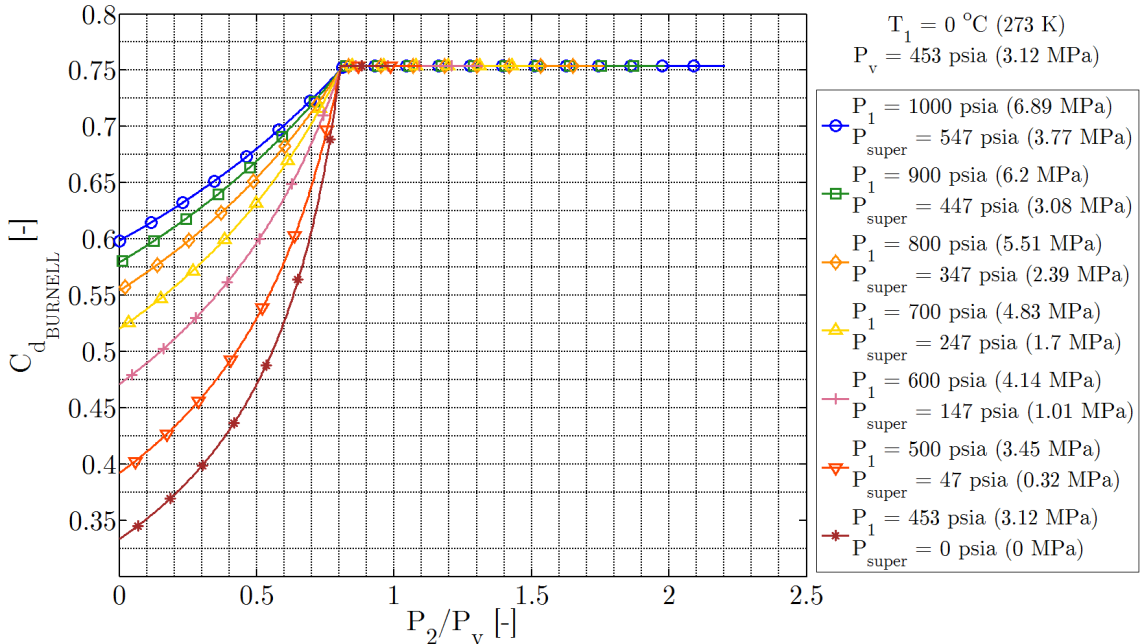


Figure 2.39:  $C_{d_{BURNELL}}$  vs.  $\frac{P_2}{P_v}$  using the Burnell model for  $N_2O$  at  $0^\circ\text{C}$  (273 K) for a variety of upstream pressures (supercharge values). ( $D_2 = 1.5 \text{ mm}$ ,  $C_d = 0.75$ )

for supercharged and saturated nitrous oxide respectively. As can be seen in Fig. 2.40, Burnell's model predicts critical mass flow rates that are significantly greater than those predicted by both equilibrium methods for the entire range of supercharge values. This is expected because the non-equilibrium effects delay the inception of cavitation and the critical flow regime. However, for saturated nitrous oxide as shown in Fig. 2.41, while Burnell's model does predict values of critical mass flow rate greater than that of the equilibrium models for most of the range of vapor pressures, as the critical point is approached the values predicted by Burnell's model drop below those of the equilibrium models. This may be a result of the fact that the correlation for the coefficient  $C$  was not developed using experimental data from nitrous oxide cold flow studies as mentioned earlier.

### 2.2.2.1.2 Zaloudek

Instead of accounting for a simulated vapor pressure depression, an approach presented by Zaloudek accounts for choking at the upstream vena contracta location [42]. The equation presented by Zaloudek for the critical mass flow rate prediction can be found in Eq. (2.71).

$$\dot{m}_{ZALOUDK\ crit} = C_{cv} C_d A_2 \sqrt{2\rho_1 (P_1 - P_v)} \quad (2.71)$$

As described in Eq. (2.13),  $C_{cv}$  is the contraction coefficient. This approach essentially accounts for the fact that the vena contracta location exhibits the maximum flow velocity and thus minimum pressure. Therefore critical flow is predicted when the pressure at the vena contracta location is equal to the vapor pressure. However, some method for predicting the value of  $C_{cv}$  is required in order to use this model (such as that of Nurick in Section 2.1.1.3). While this method is generally considered a non-equilibrium method throughout the literature, the author of this work believes that this model does not account for any non-equilibrium effects, but does account for an important fluid dynamic effect ignored by most of the other two-phase flow models presented. No predictions of mass flow rate or  $C_d$  are presented in this section because of the simplicity of this technique and the fact that it will be combined with

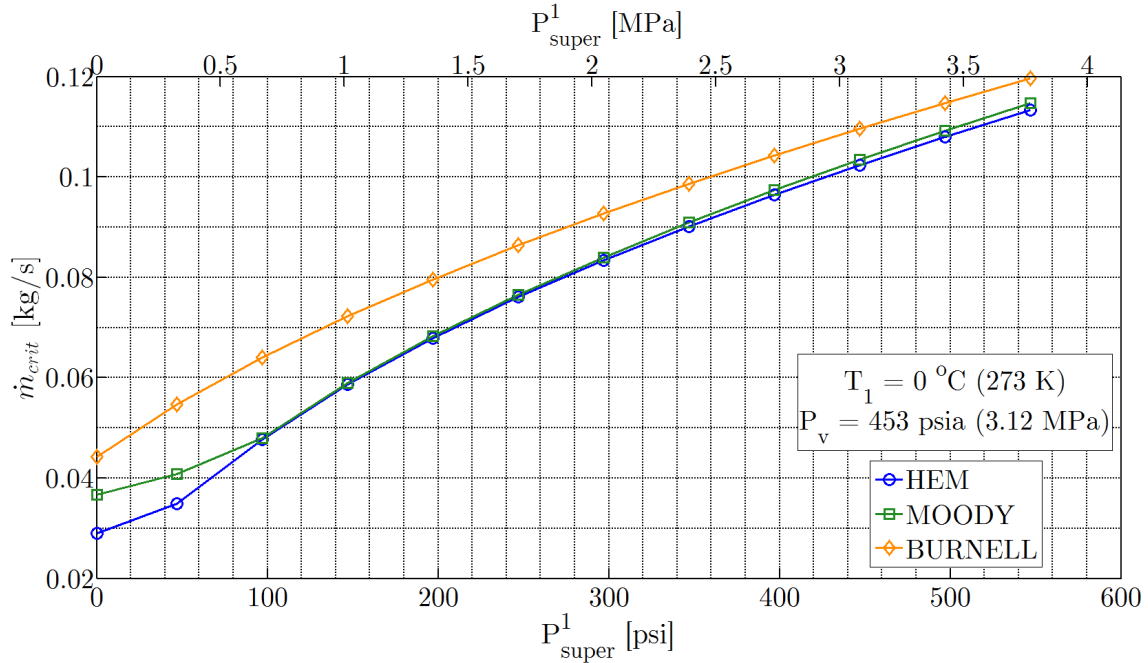


Figure 2.40: Comparison of  $\dot{m}_{\text{crit}}$  vs.  $P_{\text{super}}^1$  predictions using Burnell's frozen non-equilibrium approach, compared with the equilibrium models presented for  $N_2O$  at  $0^\circ\text{C}$  (273 K). ( $D_2 = 1.5 \text{ mm}$ ,  $C_d = 0.75$ )

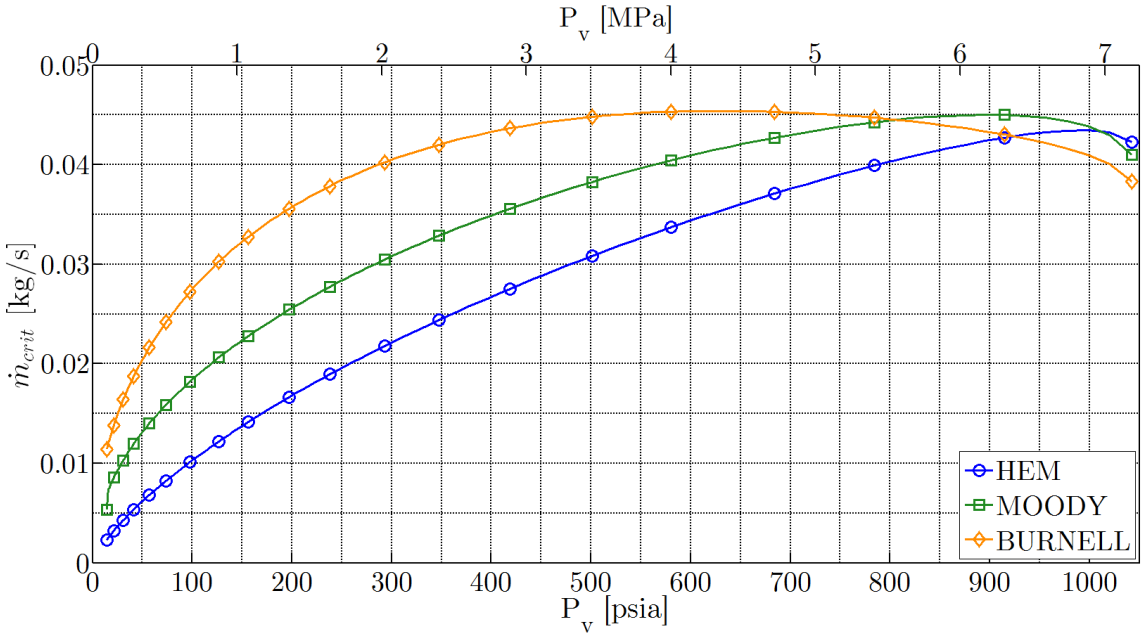


Figure 2.41: Comparison of  $\dot{m}_{\text{crit}}$  vs.  $P_v$  predictions using Burnell's frozen non-equilibrium approach, compared with the equilibrium models presented for saturated  $N_2O$  over a range of vapor pressures. ( $D_2 = 1.5 \text{ mm}$ ,  $C_d = 0.75$ )

that of Burnell in the next section, in which plots of model output will be included.

### 2.2.2.1.3 Proposed Model

The author proposes a simple model combining the ideas presented by both Burnell and Zaloudek. In this model, both the simulated vapor pressure depression as well as the vena contracta effect are included. The resulting form of the proposed critical flow rate equation is included in Eq. (2.72).

$$\dot{m}_{PROPOSED\ crit} = C_{cv} C_d A_2 \sqrt{2\rho_1 [P_1 - (1 - C) P_v]} \quad (2.72)$$

Essentially, this model describes the inception of critical flow as the point at which the minimum pressure at the vena contracta position drops below the vapor pressure to a degree determined by the  $C$  coefficient presented by Burnell. The value of  $C_{cv}$  in this proposed model is determined using Nurick's experimental correlation in which  $C_{cv}$  is dependent on the ratio of inlet radius to injector hole diameter as shown in Eq. (2.24). Fig. 2.42 and Fig. 2.43 show the critical mass flow rate predicted by the proposed model for supercharged and saturated nitrous oxide respectively. It is clear that injectors with sufficient inlet rounding to eliminate the vena contracta are predicted by the proposed model to provide identical critical mass flow rates as that predicted by the Burnell model. However, as the inlet rounding radius is decreased and the vena contracta grows, the critical mass flow rate predicted by the proposed model drops below that of the Burnell model, but maintains a similar character. This is to be expected based on the Zaloudek influence on this model, because the cavitation starts sooner with the lower minimum pressure, resulting in lower critical mass flow rates predictions. In the same way as Nurick's fit for the contraction coefficient, this model depends upon precise measurements of the inlet rounding radius, which can be difficult to obtain in practice. Therefore, it is expected that the practical application of the proposed model may be quite limited.

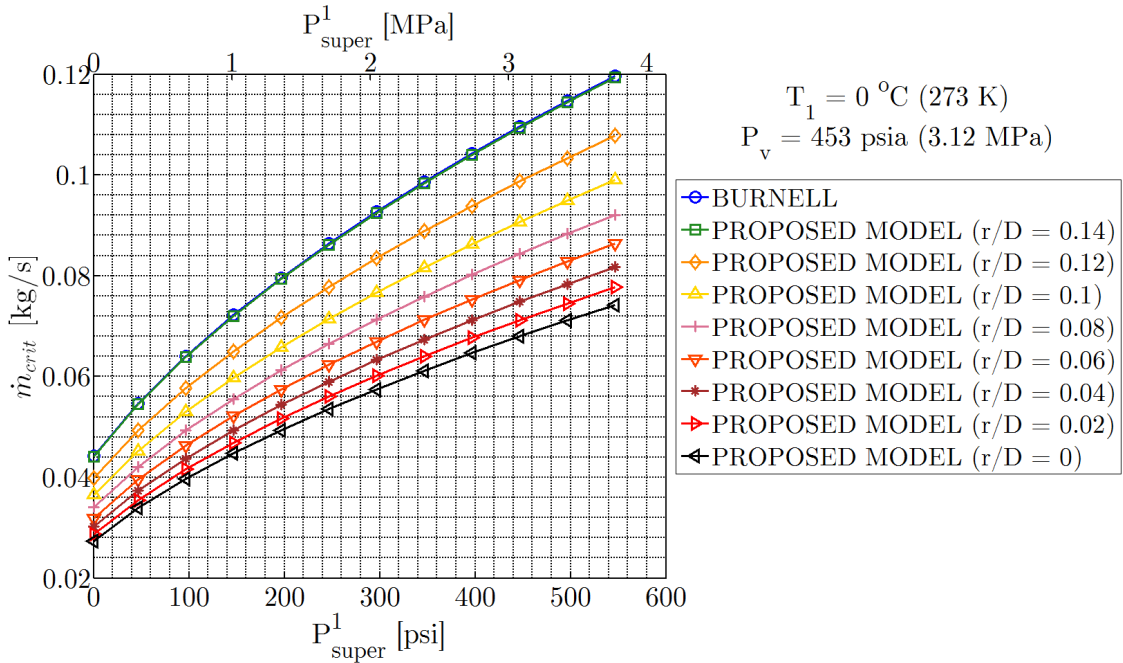


Figure 2.42:  $\dot{m}_{crit}$  vs.  $P_{super}^1$  predictions using the model proposed by the author for  $N_2O$  at  $0^\circ C$  (273 K) for a variety values of inlet radius to diameter ratio  $r/D$ . ( $D_2 = 1.5$  mm,  $C_d = 0.75$ )

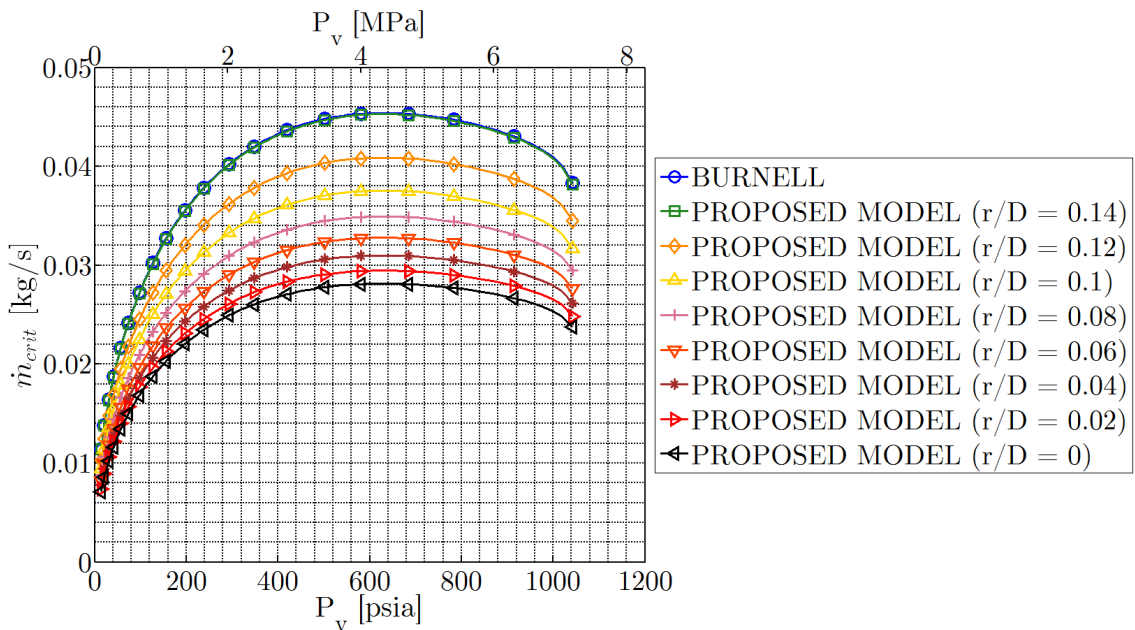


Figure 2.43:  $\dot{m}_{crit}$  vs.  $P_v$  predictions using the model proposed by the author for saturated  $N_2O$  for a variety values of inlet radius to diameter ratio  $r/D$ . ( $D_2 = 1.5$  mm,  $C_d = 0.75$ ).

### 2.2.2.2 Generalized Non-Equilibrium Methods

In contrast to the frozen theories presented above, non-equilibrium two-phase flow theories are not required to assume that the mixture composition remains constant throughout the injector. In fact, the generalized category of non-homogeneous, non-equilibrium models are often formulated based upon characteristics of the shifting mixture composition. One examples of these generalized non-equilibrium models will be described in this section.

#### 2.2.2.2.1 Dyer

Dyer et al. proposed that non-equilibrium effects were predominantly caused by two processes: superheating of the liquid during expansion and finite vapor bubble growth rates [30]. In order to account for the finite rate of vapor bubble growth, Dyer et al. defined a characteristic bubble growth time as shown in Eq. (2.73).

$$\tau_b \equiv \sqrt{\frac{3}{2} \frac{\rho_l}{P_v - P_2}} \quad (2.73)$$

The amount of vaporization that can occur within an injector element is dependent upon the ratio of the bubble growth time to the fluid residence time, which is inversely proportional to the velocity of the flow as shown in Eq. (2.74).

$$\tau_r \equiv \frac{L}{u} = \frac{L}{\sqrt{\frac{2\Delta P}{\rho_l}}} = L \sqrt{\frac{\rho_l}{2\Delta P}} \quad (2.74)$$

By comparing the bubble growth time with the liquid residence time, Dyer et al. introduced a non-equilibrium parameter,  $\kappa$ , which is shown in Eq. (2.75).

$$\kappa = \sqrt{\frac{P_1 - P_2}{P_v - P_2}} \propto \frac{\tau_b}{\tau_r} \quad (2.75)$$

The model first proposed by Dyer et al. and later clarified by Solomon accounts for non-equilibrium effects by allowing the flow rate to vary smoothly between that predicted by the Homogeneous Equilibrium Model and that using the Single Phase Incompressible model [30, 43]. This form of the Dyer model is shown in Eq. (2.76) and is referred to by Solomon as the Non-Homogeneous Non-Equilibrium (NHNE) model.

$$\dot{m}_{DYER} = A \left( \frac{\kappa}{1 + \kappa} \dot{m}_{SPI} + \frac{1}{1 + \kappa} \dot{m}_{HEM} \right) \quad (2.76)$$

This model attempts to account for the fact that when the residence time of bubbles  $\tau_r$  is much less than the characteristic time for bubble growth  $\tau_b$ , very little vapor will be formed by the exit, and the single-phase assumption is likely valid. However, when  $\tau_b \ll \tau_r$ , it is proposed that the flow rate should approach the critical value predicted by the Homogeneous Equilibrium Model. It has been observed that this is indeed the case for injectors with large length to diameter ratio  $L/D$ , which is attributed to the fact that there is enough time for the fluid to reach thermodynamic equilibrium [33].

Fig. 2.44 shows the mass flow rate predictions vs.  $\Delta P$  using the Dyer model for supercharged nitrous oxide at 0 °C (273 K) for a variety of supercharge levels. One interesting result seen in this plot is that the increasing segment of the mass flow rate curves for the lowest supercharge (and also the saturated conditions) do persist further into the two-phase region before achieving critical flow than all of the other models presented thus far.

Fig. 2.45 and Fig. 2.46 show the critical mass flow rate predictions of Dyer's model compared to that of the Burnell, Moody, and Homogeneous Equilibrium Methods. For high values of supercharge, the Dyer model performs essentially identically to the

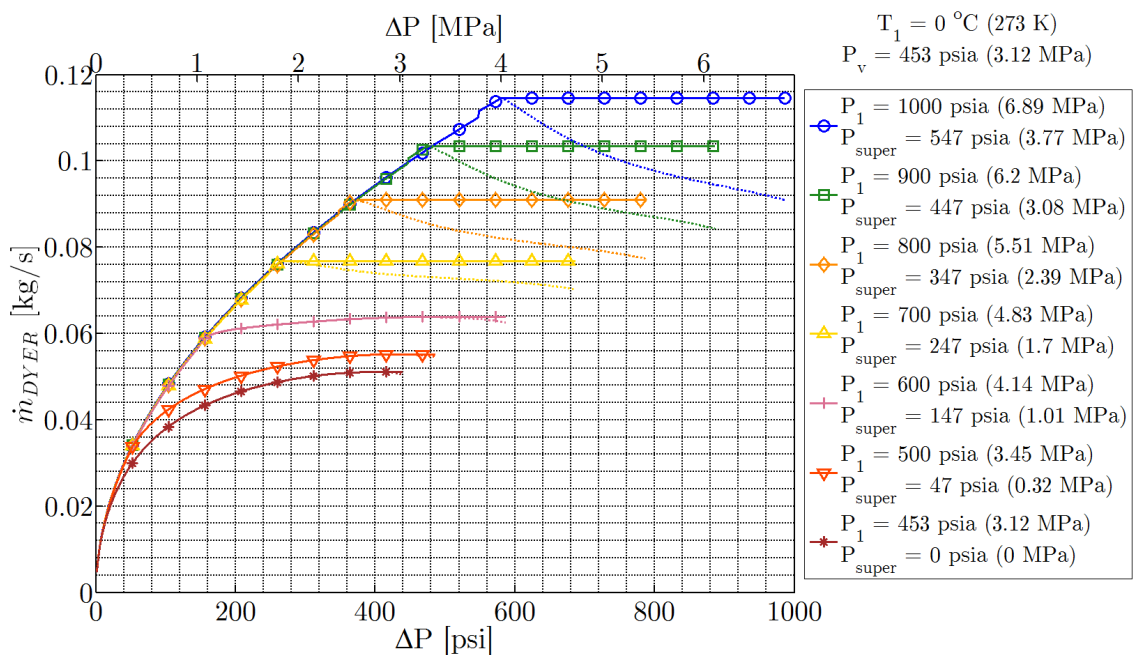


Figure 2.44:  $\dot{m}_{DYER}$  vs.  $\Delta P$  using Dyer's non-homogeneous, non-equilibrium approach for  $N_2O$  at  $0^\circ\text{C}$  (273 K) for a variety of upstream pressures (supercharge values). ( $D_2 = 1.5$  mm,  $C_d = 0.75$ )

homogeneous equilibrium methods, as should be expected based upon the formulation of this model. However, for saturated tests shown in the left portion of Fig. 2.45 and all of Fig. 2.46, the Dyer model predicts almost universally the highest critical mass flow rates of all the models, and often by quite large margins. This is a good demonstration of the effect of relaxing the homogeneous and equilibrium assumptions when modeling two-phase flow through injectors.

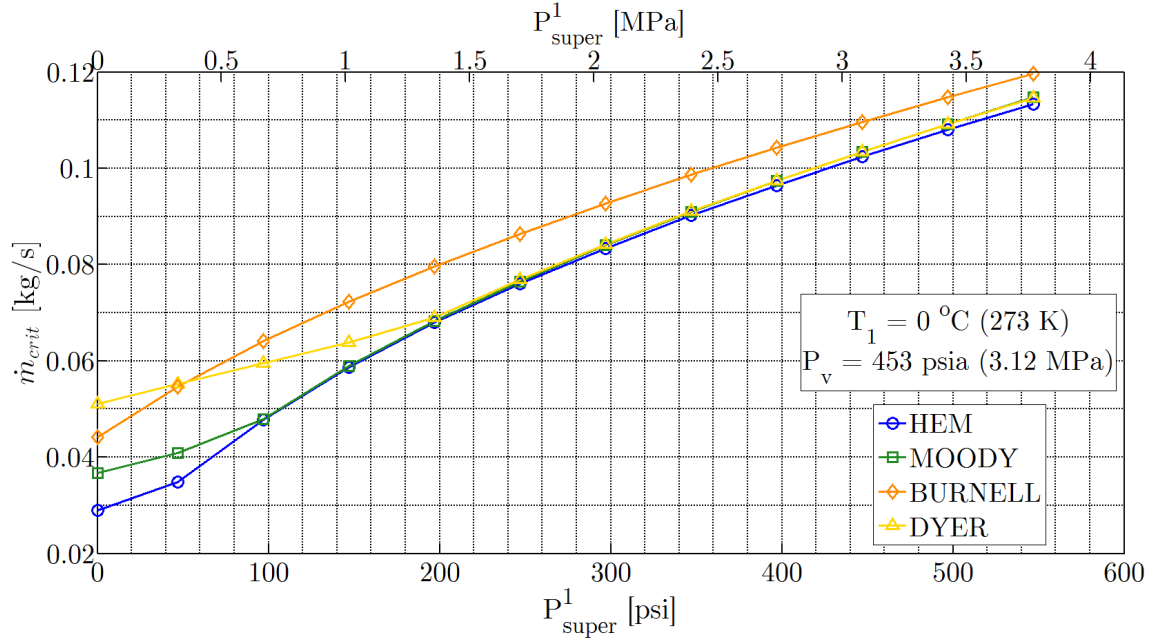


Figure 2.45: Comparison of  $\dot{m}_{\text{crit}}$  vs.  $P_{\text{super}}^1$  predictions using Dyer's non-homogeneous, non-equilibrium approach, compared with the earlier models presented for  $N_2O$  at  $0^\circ C$  (273 K). ( $D_2 = 1.5$  mm,  $C_d = 0.75$ )

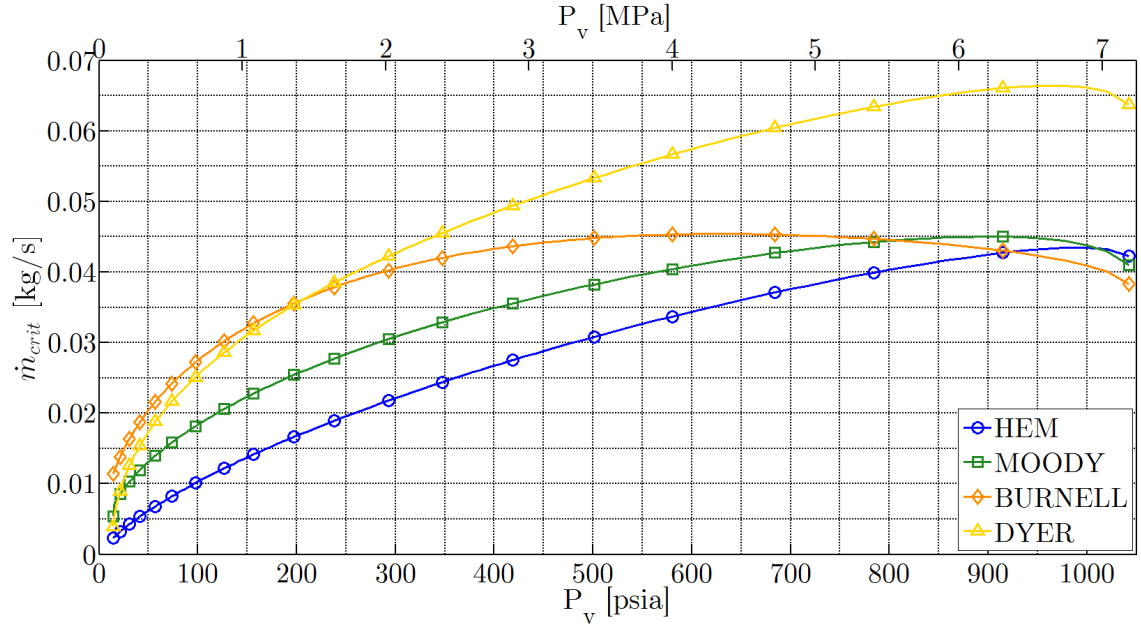


Figure 2.46: Comparison of  $\dot{m}_{\text{crit}}$  vs.  $P_v$  predictions using Dyer's non-homogeneous, non-equilibrium approach, compared with the earlier models presented for saturated  $N_2O$  over a range of vapor pressures. ( $D_2 = 1.5$  mm,  $C_d = 0.75$ )

## 2.3 Injector Flow Rate Modeling Conclusions

The simple “ $C_dA$ ” equation as shown in Eq. (2.17) is often the first method used to predict the mass flow rate of liquid propellants in rocket systems (followed by CFD). However, even for purely liquid injector operation, there are a variety of important factors which the engineer must consider in order to achieve accurate mass flow rate predictions. Additionally, this chapter has made it clear that with the introduction of two-phase flow, the simple “ $C_dA$ ” equation is not applicable with regard to mass flow rate predictions (though it can still be used as a baseline for determining “effective” discharge coefficients). A variety of two-phase flow models attempt to account for the effects of two-phase flow, and do seem to capture the general mass flow rate behavior that should be expected. However, none of these models are in close agreement when it comes to the prediction of actual critical mass flow rate values over a wide range of operating conditions, and it is not obvious which models are the most accurate for application to rocket propellant injectors. This will be discussed further in Chapter 3, where in fact it will be shown that none of the models predict the critical mass flow rate of high vapor pressure propellants to sufficient levels of accuracy. Therefore, cold flow testing of nitrous oxide injectors is still necessary for the reliable prediction of injector mass flow rates during hot fire testing, and can be useful for assessing the accuracy of the different two-phase flow models. This type of cold flow testing has been performed and will be described in Chapter 3.

# Chapter 3

## Injector Cold Flow Experiments

The models outlined in Chapter 2 are useful in developing an understanding of the effects of two-phase flow on injector mass flow rate performance. However, without well characterized injector discharge coefficient data for a particular injector design, it is often not possible to achieve reliable mass flow rate predictions using these models. While the discharge coefficient for most traditional rocket propellant injectors is relatively well characterized, there is a great deal of uncertainty when it comes to the design and performance of nitrous oxide injectors. Additionally, in the open literature there has been little in the way of experimental injector testing and model validation for injectors operating at realistic operating conditions with high vapor pressure propellants. This chapter will describe the development of an experimental facility for the cold flow testing of nitrous oxide injectors at realistic operating pressures. The goal of this testing is to record and compile injector performance data over a broad range of operating conditions, which can be leveraged in hybrid rocket development programs and can also be used to compare the accuracy of the different mass flow rate prediction techniques described in Chapter 2 and elsewhere in the literature. The experimental results from this apparatus will be used to directly support the design efforts of the Peregrine Sounding Rocket hybrid rocket development programs at NASA Ames Research Center as described in Chapter 4 and Chapter 5. A selection of the cold flow testing results will be presented, discussed, and compared to predictions from a variety of two-phase flow models.

## 3.1 Experimental Cold Flow Testing Campaign

While it is standard practice in the development of hybrid rockets to perform cold flow testing (oxidizer flow only, no ignition) in order to characterize a given injector design in terms of mass flow rate and atomization, many cold flow tests are not performed at the actual operating backpressure observed during combustion testing. Often cold flow tests are performed with the combustion chamber removed and the injector flowing to ambient pressure, resulting in a much larger  $\Delta P$  than would be expected during tests involving combustion for the same hardware. As should be clear from the theoretical treatment in Chapter 2, the downstream pressure,  $P_2$ , and the pressure drop,  $\Delta P$  are important parameters affecting the actual performance and modeling of injector mass flow.

### 3.1.1 Cold Flow Apparatus Design

#### 3.1.1.1 Test Section

In order to effectively characterize the mass flow rate performance for a variety of injector designs, a facility has been developed to allow for the establishment of realistic operating pressures upstream and downstream of an interchangeable injector plate. Transparent polycarbonate tubes are closed on each end by aluminum end caps to create a pressure vessel with optical access (ID = 25.4 mm). This transparent setup was chosen to facilitate an ongoing study of nitrous oxide atomization using high-speed photography and laser illumination as described in previous work by the author, with some of the results included in Appendix B. The optical access allows for observations of the flow conditions upstream and downstream of the injector. A cross-section model of the test section is shown in Fig. 3.1 along with a photo of the assembled hardware. Pressure and temperature are measured in both the upstream and downstream polycarbonate chambers at sampling rates from 500 Hz up to 5 kHz, allowing for the instantaneous measurement of  $\Delta P$  and determination of the upstream thermodynamic state. Details about the instrumentation system regarding the types of sensors used and the corresponding accuracy of the measurements can

be found in Table C.1 in Appendix C. The upstream aluminum end cap was designed with a diffuser in order to allow for the testing of more complicated impinging type injector designs. A 3-D model cutaway view that shows the diffuser and pre-injector volume is shown in Fig. 3.2. This figure also more clearly shows the instrumentation access points which are used for pressure and temperature measurements. Similar access taps are included in the downstream aluminum end cap.

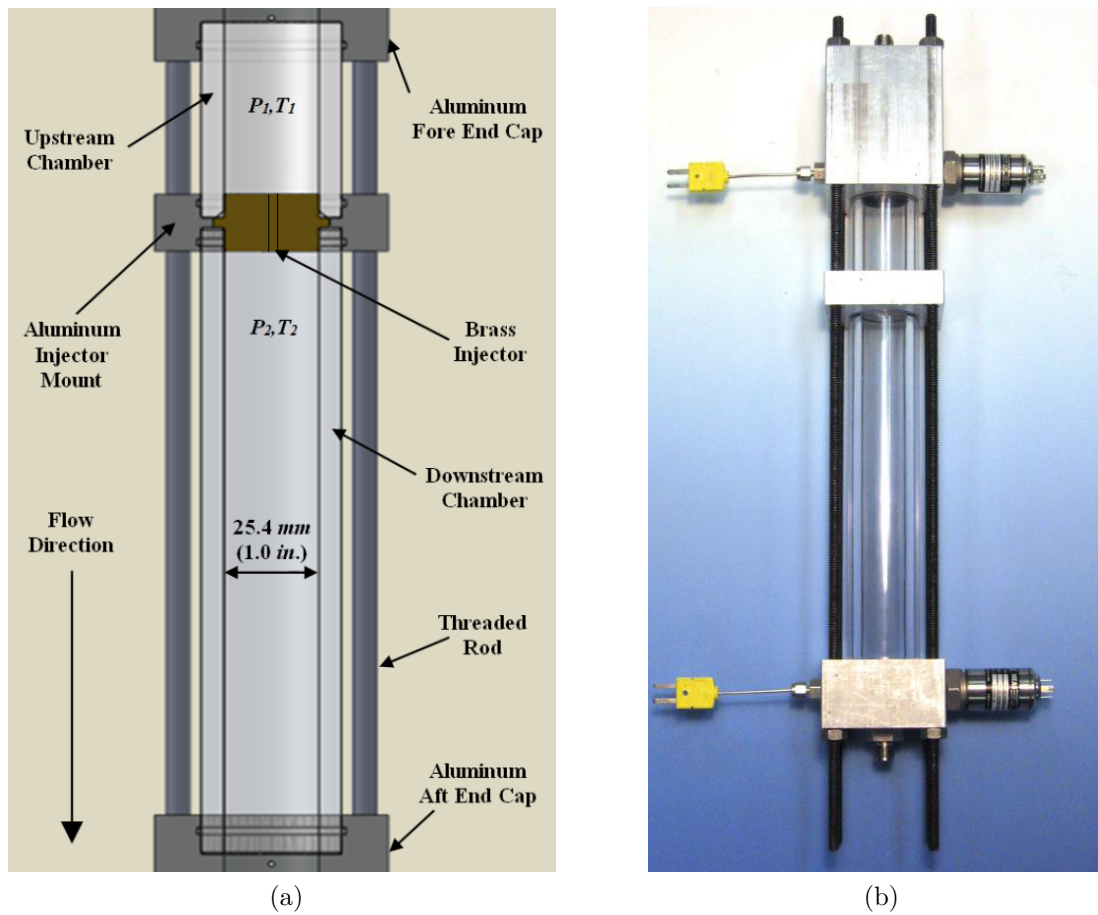


Figure 3.1: (a) Cross-section model of the test section with main components labeled  
(b) Photo of the assembled test section hardware and instrumentation.

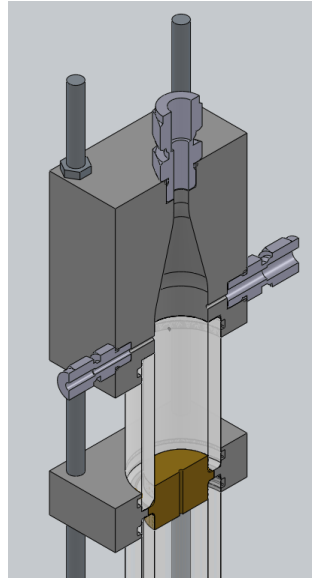


Figure 3.2: Test section 3-D model cutaway showing details of the diffuser, pre-injector volume, and instrumentation access.

### 3.1.1.2 Auxiliary Systems

Liquid is supplied to the test section by a separate transparent pressure vessel which is also used for experiments investigating expulsion dynamics for self-pressurized propellant tanks. The tank is shown in Fig. 3.3a and serves as an intermediate run tank between the test section and the compressed gas cylinders (K size) that the nitrous oxide is delivered and stored in. More information on the tank dynamics experiments can be found in the work of Zimmerman et al. [20, 44]. Liquid flows from the intermediate run tank to the test section through 6.35 mm diameter tubing, a pneumatically actuated ball valve, and a venturi flow meter. A standard pressure transducer and a differential pressure transducer are used in conjunction with the flow venturi to calculate mass flow rate. A photo of the full system setup is shown in Fig. 3.3b.

The run tank is filled using a pneumatically driven pump, but under certain conditions the self-pressurization within the storage tank is sufficient to drive the nitrous

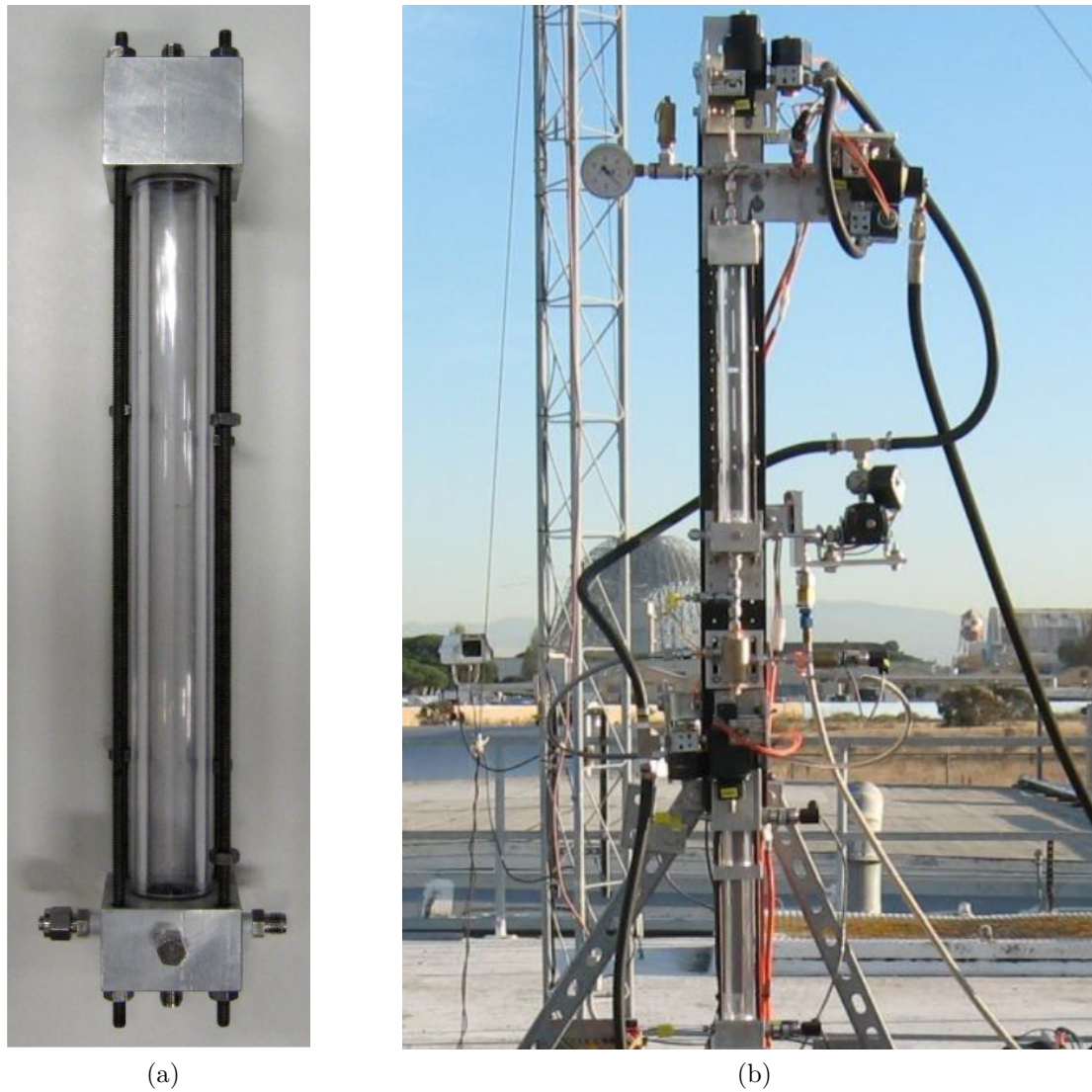


Figure 3.3: Photos of (a) the intermediate run tank and (b) the overall system setup.

oxide from the store tank into the run tank. Many practical systems employ supercharging in order to avoid cavitation in the feed system caused by localized pressure drops. In order to sub-cool the liquid in this fashion, the run tank can be pressurized with helium up to approximately 1000 psig (7.00 MPa). The pressurization system allows for flexibility when it comes to setting the thermodynamic state of nitrous oxide in the tank and upstream of the injector. Helium is widely chosen as the supercharging gas in practical pressurization systems due to its low molecular weight. However, if helium becomes dissolved in a self-pressurizing propellant there can be significant effects on cavitation due to helium desorption throughout feed system [45]. In current tests, it is believed that helium is not appreciably dissolved in the nitrous oxide because of the short time between supercharging and completion of the test. Nevertheless, future work should address the potentially undesirable effects of helium absorption and desorption with regard to cavitation and mass flow rate. A process and instrumentation diagram (P&ID) with more details on the fluid handling and instrumentation of the system can be found in Appendix C.

### 3.1.1.3 Injector Inserts

In order to allow for the testing of a wide range of injector designs, an injector insert was designed to be easily interchangeable. The brass insert is mounted within an aluminum block that serves as the junction between the upstream and downstream polycarbonate pressure vessels as shown above in Fig. 3.1a. Silicone O-rings are used to provide seals at each junction. A large assortment of injector inserts have been manufactured for testing in this facility. The main injectors tested for the current work were designed to investigate mass flow rate characteristics with the variation of injector orifice diameter  $D$  and hole inlet geometry (square edged, rounded, chamfered). For most of this work, the length  $L$  of each injector hole was fixed at a value of 18.4 mm. However, some work was performed to study the effect of varying overall injector length and the length to diameter ratio  $L/D$ , so one injector was designed with an overall length of 3.2 mm. All of the injectors used in the tests presented in this chapter were simple straight hole orifices. Table 3.1 details the geometry of each injector tested in this work. Rounding on the injector inlets was at a radius of

Table 3.1: Description of injector design geometry.

Injector Number	Style	$D$ [mm]	$L$ [mm]	$L/D$	Entrance Geometry
(1)	Straight	0.79	18.4	23.4	Square Edge
(2)	Straight	1.50	18.4	12.3	Square Edge
(3)	Straight	1.50	18.4	12.3	Rounded
(4)	Straight	1.50	18.4	12.3	Chamfered
(5)	Straight	1.93	18.4	9.5	Square Edge
(6)	Straight	1.50	3.2	2.1	Square Edge

0.51 mm and chamfers were machined at  $45^\circ$  to a depth of 0.76 mm. A photo of one injector insert is shown in Fig. 3.4

### 3.1.2 Design Analysis

Prior to constructing the test section, a variety of engineering analyses were performed in order to ensure safe and effective operation. These analyses included both structural and fluid studies, resulting in multiple iterations of the test section design before settling on the final design.

#### 3.1.2.1 Structural

For any pressurized system it is necessary to perform structural calculations to ensure safety of both personnel and hardware. The maximum pressure required in the test section is approximately 1000 psig (7.00 MPa). Of particular concern in the design of the test section is the polycarbonate tubing that acts as the pressure vessel. Structural simulations were performed employing finite element analysis (FEA) using the commercial Solidworks Simulation package. Details of the solution method can be found in Ref. [46]. Fig. 3.5 shows some sample FEA results for the test section under simulated pressurization. A factor of safety of approximately 2.5 with respect to yield was calculated through this analysis. Prior to pressurization with gas, the test section was hydrostatically tested to prove the structural integrity.



Figure 3.4: Photo of injector insert 3 with corner O-ring installed.

### 3.1.2.2 Fluid

As mentioned in Section 3.1.1.1, a diffuser was designed into the test section in order to allow for the testing of more complicated impinging type injector designs. However, there was some concern that the possibility of diffuser stall (flow separation) could result in unsteady flow during testing. A series of computational fluid dynamics calculations (CFD) were performed in order to address this issue using the commercial Solidworks Flow Simulation package. This software calculates solutions to the Favre-averaged Navier-Stokes equations using the finite volume method on a spatially rectangular Cartesian grid, using second-order upwind differencing and the  $k - \varepsilon$  turbulence model. In depth details of the solution method can be found in Ref. [47]. These CFD studies modeled compressible nitrous oxide flow through the diffuser for two separate geometries. The first geometry tested included the diffuser only. A sample of the CFD results from calculations using this geometry is shown in Fig. 3.6a. These results do predict diffuser stall which could be a significant problem during the test campaign. However, the second geometry that was tested included both

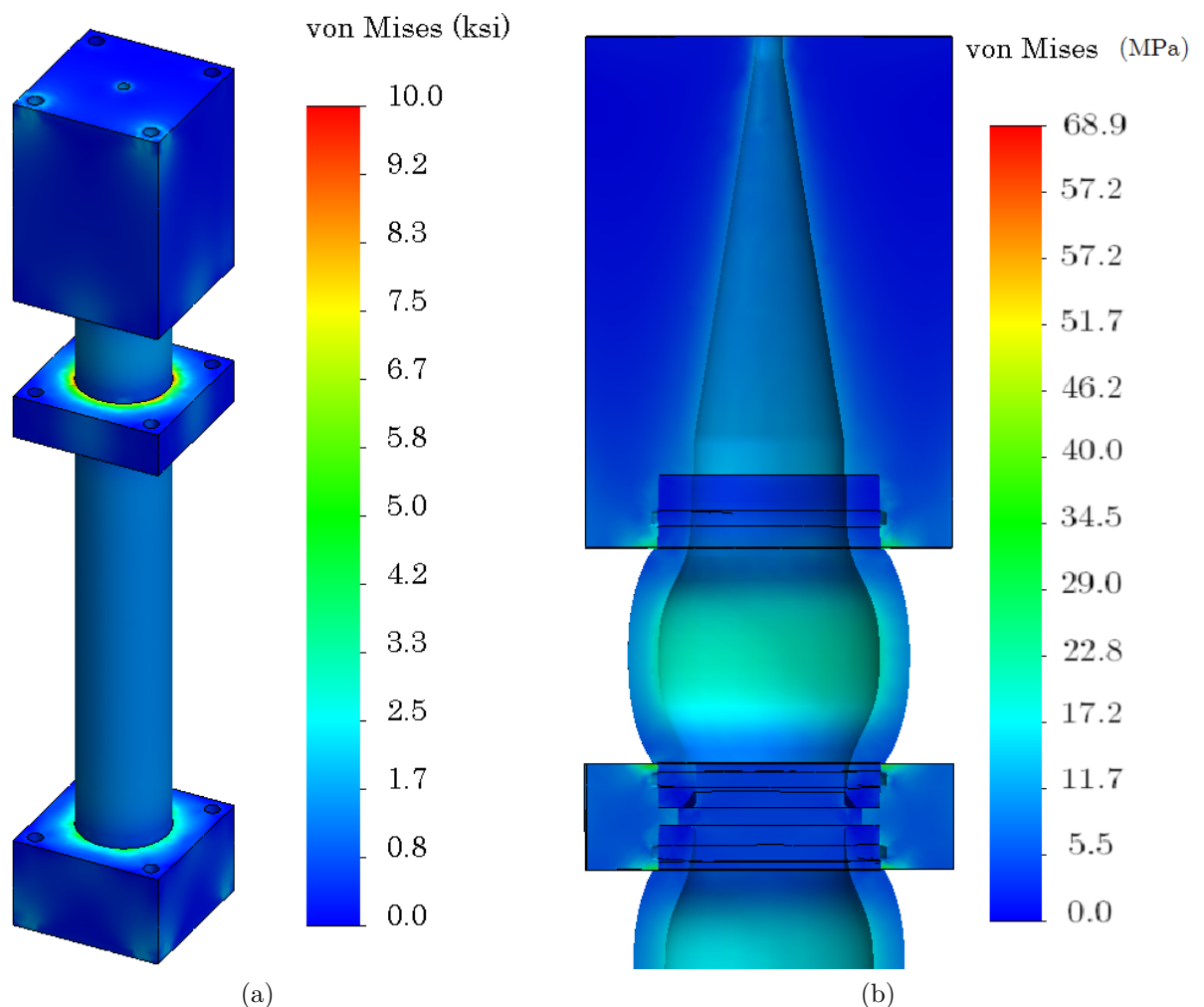


Figure 3.5: Sample FEA results for the structural simulation of the test section (deformation scale exaggerated).

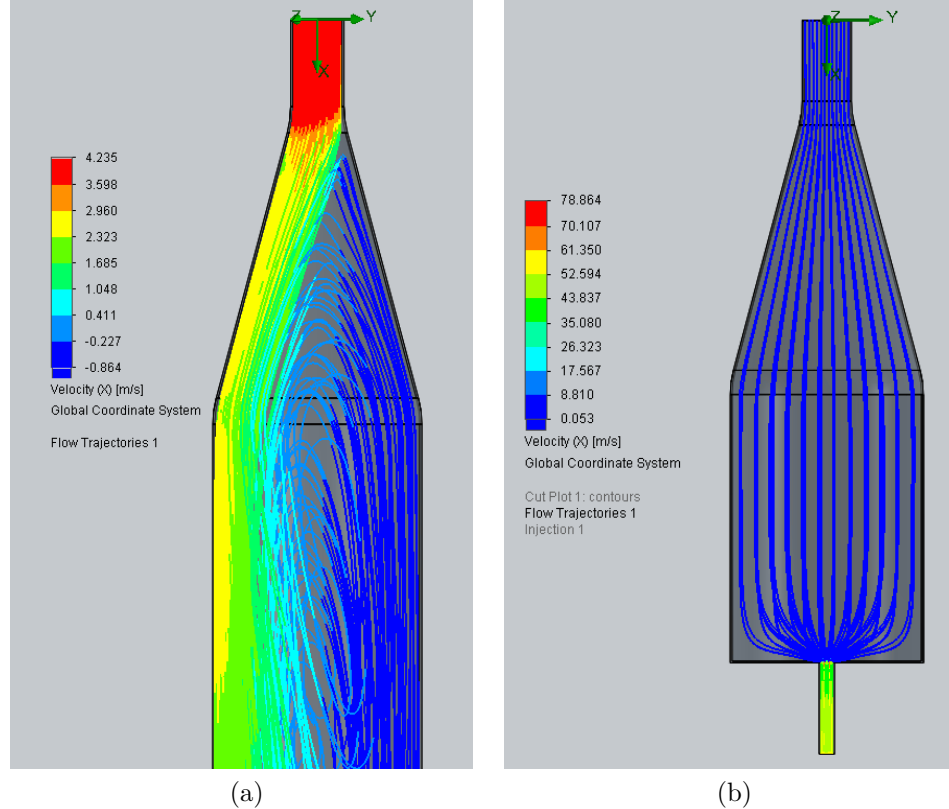


Figure 3.6: Sample CFD results for the diffuser flow fields showing a) diffuser stall with no injector element and b) attached flow with a downstream element injector element.

the diffuser and a downstream injector element. With the presence of the injector element, all CFD results showed that the flow through the diffuser remains attached. While these results were encouraging, it was determined that standard operating procedure would include monitoring of the flow field in the diffuser and pre-injector volume. However, at no point during the testing described in the remainder of this chapter did any flow separation or diffuser stall issues cause difficulties during the measurement campaign.

### 3.1.3 Operation

#### 3.1.3.1 $CO_2$ as an Analog to $N_2O$

Although nitrous oxide has properties that make it an attractive oxidizer choice for hybrid rockets, it is still a reasonably strong oxidizer and its use does pose some significant safety risks. Specifically, nitrous oxide has a positive heat of formation, and the potential exists for rapid exothermic decomposition. As described in Section 1.3, this type of runaway decomposition reaction can lead to violent and dangerous pressure vessel explosions. Multiple groups have studied these explosive events and have concluded that despite the potential hazards, nitrous oxide can be used safely with proper handling considerations [2, 13]. Stringent cleaning procedures such as those used for oxygen systems must be followed in order to minimize the possibility of explosions. However, these types of explosions do happen in the hybrid rocket industry, and have caused major hardware damage and even fatalities. Therefore, the use of nitrous oxide is not always ideal in an academic setting, and is sometimes restricted to certain areas as a means for ensuring student safety.

Fortunately, multiple groups have recognized that carbon dioxide can be used as a safe analog to nitrous oxide when it comes to fluid flow studies [20, 43]. Nitrous oxide and carbon dioxide are quite similar thermodynamically in that they have almost the same molecular weight and exhibit less than 5% variation in most of the important thermodynamic properties listed in Table 3.2. However, some thermodynamic parameters do differ greatly, such as the triple point and the acentric factor. The acentric factor is a measure of the aspherical nature of a molecule, and its tendency to behave differently than simple monatomic fluids. The difference in acentric factor between nitrous oxide and carbon dioxide can contribute to the difference in properties such as saturation pressure and vapor density [48]. As seen in Fig. 3.7, these two values can differ upwards of 20% when nearing the critical point (though saturated liquid density matches quite closely). An in depth comparison of nitrous oxide and carbon dioxide thermodynamic and transport properties away from the saturation

line is performed by Zimmerman et al. and has been applied to look at the effect of using carbon dioxide as an analog during propellant tank blow-down experiments [44].

Table 3.2: Comparison of important thermodynamic properties of  $N_2O$  and  $CO_2$  [14, 15, 49, 50].

Property	Units	$N_2O$	$CO_2$	Difference (%) $\left(\frac{CO_2 - N_2O}{N_2O}\right)$
$M$	amu	44.013	44.010	-0.007
$P_c$	psia (MPa)	1050.8 (7.25)	1070.0 (7.38)	+1.80
$P_{trip}$	psia (MPa)	12.7 (0.09)	75.1 (0.52)	+491
$T_c$	$^{\circ}C$ (K)	36.5 (309.7)	31.1 (304.3)	-1.74
$T_{trip}$	$^{\circ}C$ (K)	-90.2 (183.0)	-56.6 (216.6)	+18.8
$\rho_c$	$\frac{kg}{m^3}$	452.0	467.6	+3.45
$Z_c$		0.273	0.274	+0.366
$\omega$		0.160	0.225	+40.6

While the thermodynamic similarities are encouraging, experimental comparisons must be performed to quantify the effects of using carbon dioxide as an analog to nitrous oxide before work can be moved solely to carbon dioxide. This work will provide some initial comparisons of injector performance with the use of carbon dioxide versus nitrous oxide. To accommodate testing with nitrous oxide while ensuring the safety of all involved, this work was performed at the Outdoor Aerodynamic Research Facility (OARF) at NASA Ames Research Center in Moffett Field, CA. Experiments are controlled remotely with all personnel in a bunker 150 ft away from the test stand.

### 3.1.3.2 Operating Procedure

The procedure for operating tests involving nitrous oxide is described below. However, the same process is used for carbon dioxide and the name of the fluid can be substituted at will. The only significant difference in operating with nitrous oxide is

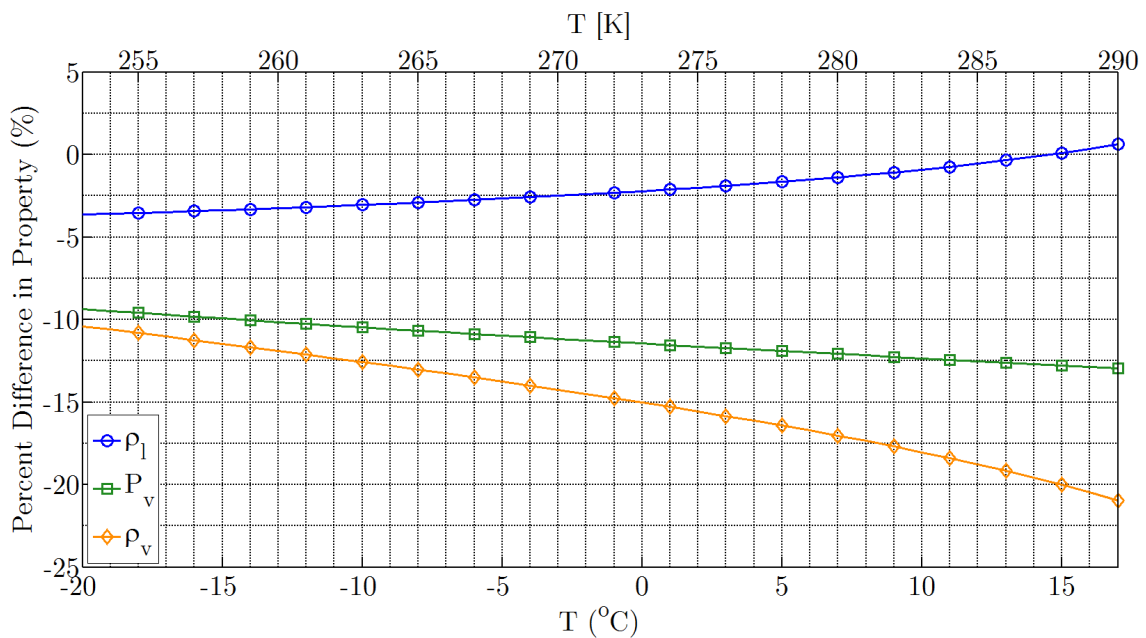


Figure 3.7: Percent difference in saturated vapor density, liquid density, and saturation pressure ( $P_v$ ) for  $CO_2$  as an analog to  $N_2O$ . (Oxidizer temperatures ranging from -20 to 15 °C (253 to 288 K) are of particular interest for large scale hybrid rocket systems using  $N_2O$ ) [14, 15, 49, 50] .

the strict cleaning and anti-contamination procedures that are used when handling hardware (not described here).

### 3.1.3.2.1 Test Preparation

A typical test is prepared by filling the run tank with nitrous oxide to a desired level using the pneumatically driven pump. If it is necessary to establish a desired liquid temperature, the nitrous oxide storage cylinder can be either heated or cooled using an insulated water or coolant (propylene glycol) bath prior to and throughout the test. Next, the helium pressurization system is used to provide the target supercharge level. As described in Chapter 2, the local supercharge is defined as the instantaneous difference between the static pressure and the vapor pressure of pure nitrous oxide at a given point in the system. To reiterate, the expression for the supercharge pressure at in the pre-injector volume located just upstream of the injector is shown in Eq. (3.1), where the vapor pressure is evaluated at the local instantaneous temperature ( $T_1$  in this case).

$$P_{super}^1 = P_1 - P_v \Big|_{T=T_1} \quad (3.1)$$

Aside from an exhaust valve that opens to ambient, the downstream chamber labeled in Fig. 3.1a is a closed vessel. The exhaust valve is generally kept closed throughout the duration of a test and if desired, the downstream chamber and pre-injector volume can be pre-pressurized with nitrogen to establish elevated backpressures at the beginning of a test.

### 3.1.3.2.2 Running a Test

Once the desired tank and chamber conditions are established, the pneumatically actuated ball valve that connects the run tank to the test section is opened to

initiate a test. Nitrous oxide immediately begins to fill the pre-injector volume, and  $P_1$  rises rapidly to a level approximately equal to that of the run tank. At the same time, nitrous oxide is flowing through the injector and the downstream pressure  $P_2$  starts to rise. Because  $P_1$  increases much faster than  $P_2$ , a large pressure drop  $\Delta P$  is established across the injector, nearing 1000 psi (6.89 MPa) in some instances. However, because the exhaust valve is closed and the downstream chamber is filling up with liquid nitrous oxide, the downstream pressure will continue to rise until  $P_1 = P_2$ , at which point the pressure drop across the injector is zero and flow stops, completing the test. By operating in this dynamic fashion, a single test can provide a broad sweep of downstream operating pressures for relatively constant upstream conditions. The inherent assumption in these tests is that the characteristic time for flow through the injector is much shorter than the characteristic time of the downstream chamber pressure sweep. A typical pressure time history is shown in Fig. 3.8 (valve opens at approximately 0.5 s).

Once the ball valve is opened, there is a rush of nitrous oxide flow into the pre-injector volume. As the liquid front of nitrous oxide expands rapidly into the pre-injector volume, much of it flashes to vapor, resulting in rapid cooling and low temperatures for a short duration in the beginning of a test as shown in Fig. 3.9. However, once the ensuing liquid fills in the volume upstream of the injector, the temperature returns to the bulk liquid temperature and stabilizes. Because the pressure transducers used in this region are susceptible to rapid changes in temperature, it is important to provide thermal insulation to ensure accurate pressure measurements. Synthetic lubricant (Krytox) is applied to the pressure transducer cavities in order to provide thermal insulation without impacting the accuracy of the pressure measurements.

### 3.1.3.2.3 Data Analysis

While the pre-injector volume is filling with liquid nitrous oxide, the flow is

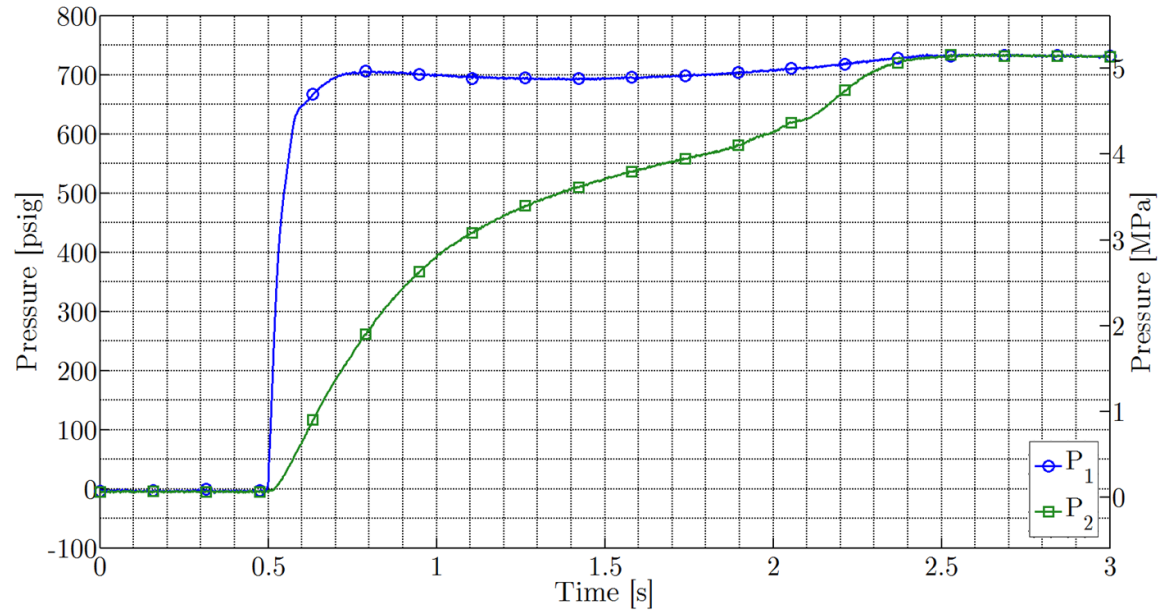


Figure 3.8: Pressure time histories for locations upstream and downstream of the injector during a typical test ( $P_1$  and  $P_2$  respectively).

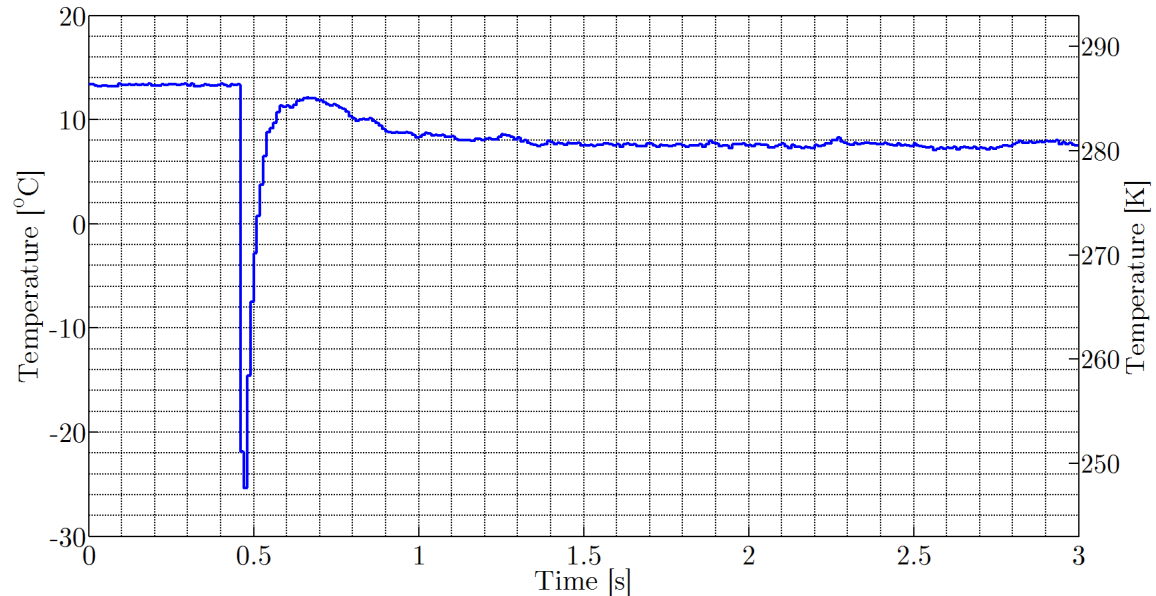


Figure 3.9: Typical time history of  $T_1$  (minimum temperature of  $-26\text{ }^{\circ}\text{C}$  (247 K)).

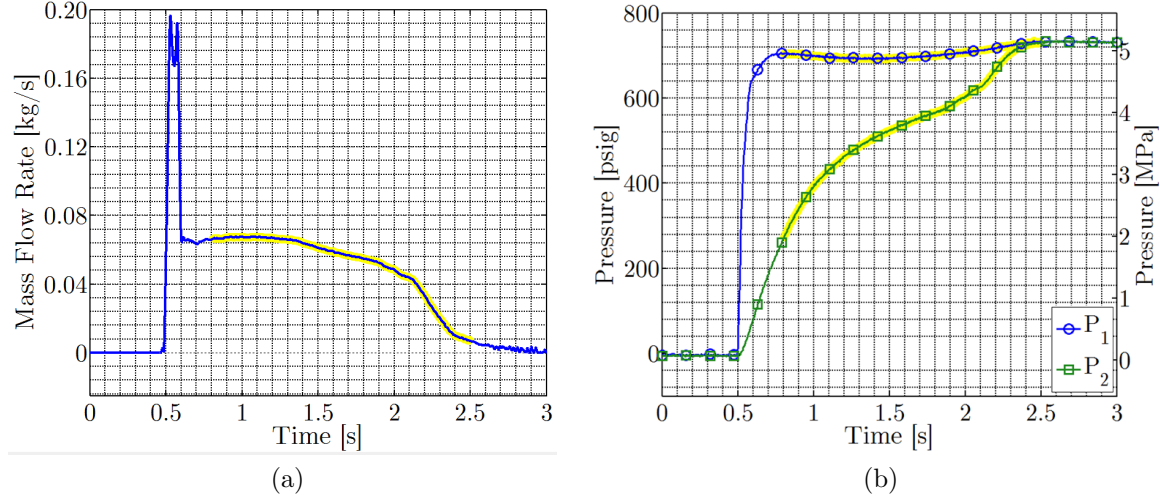


Figure 3.10: (a) Mass flow rate time history and (b) pressure time histories for a typical test of nitrous oxide flow through injector number 3.

only limited by the feed line diameter and a high mass flow rate is fed through the system. These high mass flow rates during the beginning of a test are reflected in the venturi flow rate measurements as seen in Fig. 3.10a from approximately 0.5 s until 0.6 s. Not until this volume is completely filled with liquid does the injector become the mass flow limiting device, and thus the venturi mass flow rate measurements can only be used from this point onwards during a test. For this reason, the test data used for analysis must be selected appropriately. A typical cropping of the data is shown by the highlighted segments in Fig. 3.10a and Fig. 3.10b which correspond to the same test as Fig. 3.8. The test depicted in these figures is for nitrous oxide flow through injector number 3, the geometry of which is described in Table 3.1.

Looking carefully at the plots in Fig. 3.10, it can be seen that in the early portions of the cropped section,  $\Delta P$  is dropping rapidly while the mass flow remains relatively constant. When the mass flow data is plotted versus the pressure time history, it is much easier to examine the behavior of the injector. This type of analysis results in a plot of the form shown in Fig. 3.11, created from the cropped sections above. This data corresponds to average upstream values of  $P_1 = 704$  psia (4.85 MPa),  $T_1$

$= 7^{\circ}\text{C}$  (280 K), and  $P_{super}^1 = 169$  psi (1.17 MPa). While the instantaneous values for the upstream parameters do shift a small amount during a test, for simplicity the injector performance will be studied based on the average upstream values and the instantaneous downstream values. In a similar fashion, it is possible to plot the effective discharge coefficient versus  $\Delta P$  as shown in Fig. 3.12. This effective discharge coefficient is defined by dividing the instantaneous mass flow rate during the test by the value calculated assuming single-phase incompressible flow as in Eq. (2.17) using a discharge coefficient of 1. A brief discussion regarding the uncertainty related with this calculation based on the measurement accuracy is presented in Appendix D. As  $\Delta P$  and mass flow rate approach zero, the mass flow rate measurements are on the same order as the signal noise and uncertainty, and the effective discharge coefficient shows a significant level of scatter. This region is ignored for the purposes of our analysis.

Fig. 3.11 and Fig. 3.12 are useful in identifying the different flow regimes. For low values of  $\Delta P$ ,  $30 \text{ psi} < \Delta P < 200 \text{ psi}$  in this case ( $0.21 \text{ MPa} < \Delta P < 1.38 \text{ MPa}$ ), the flow is well described by the SPI model. The experimental data in this region can be fit to Eq. (2.17) by determining the SPI discharge coefficient for this combination of injector geometry and upstream thermodynamic conditions ( $C_d \approx 0.77$  in this case). A line corresponding to the mass flow rate predicted by the Single Phase Incompressible model using this discharge coefficient is included in Fig. 3.11. While the SPI model is not physically valid in the two-phase flow region past the critical  $\Delta P$ , the results from Fig. 3.12 allow one to calculate an effective discharge coefficient for use in the two-phase region. For example, the effective discharge coefficient for injector number 3 at the upstream conditions presented above drops to a value of approximately 0.6 at a pressure drop of 330 psi (2.28 MPa). For large values of  $\Delta P$ , it is clear that we do in fact see the same critical flow effect shown by Hesson and Peck and predicted by the two-phase flow models discussed in Chapter 2, (such as the Homogeneous Equilibrium Model). As seen in Fig. 3.11 and 3.12, a region is identified indicating the transition from single-phase liquid operation into the two-phase regime.

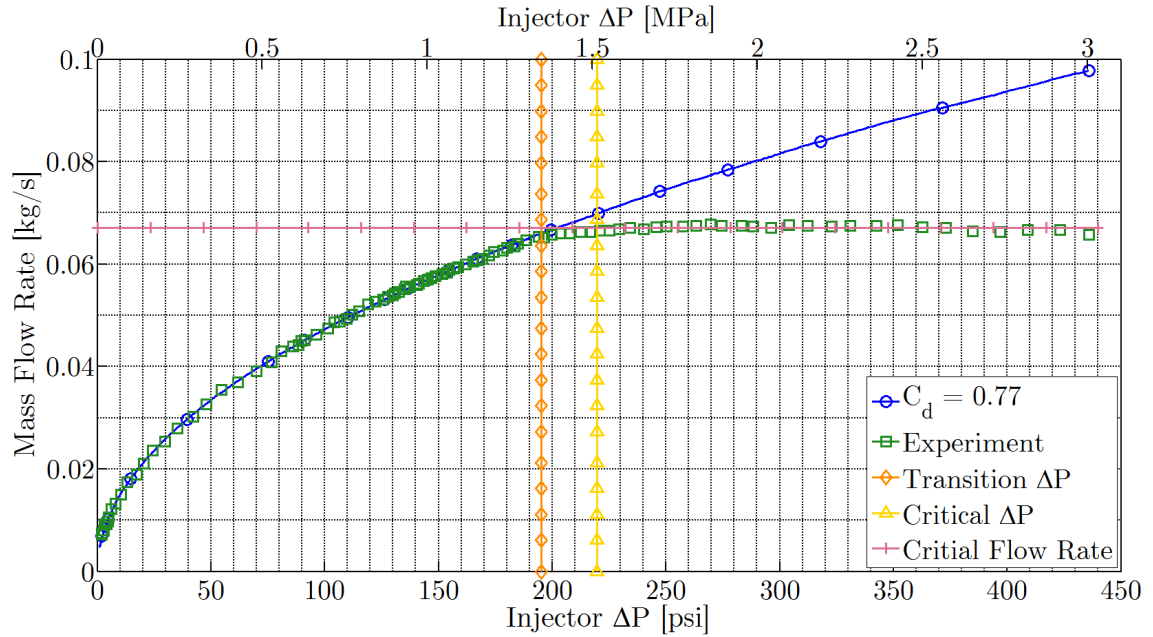


Figure 3.11: Nitrous oxide mass flow rate vs. injector  $\Delta P$  data for a test of injector number 3 at average upstream values of  $P_1 = 704$  psia (4.85 MPa),  $T_1 = 7$  °C (280 K) and  $P_{super}^1 = 169$  psi (1.17 MPa).

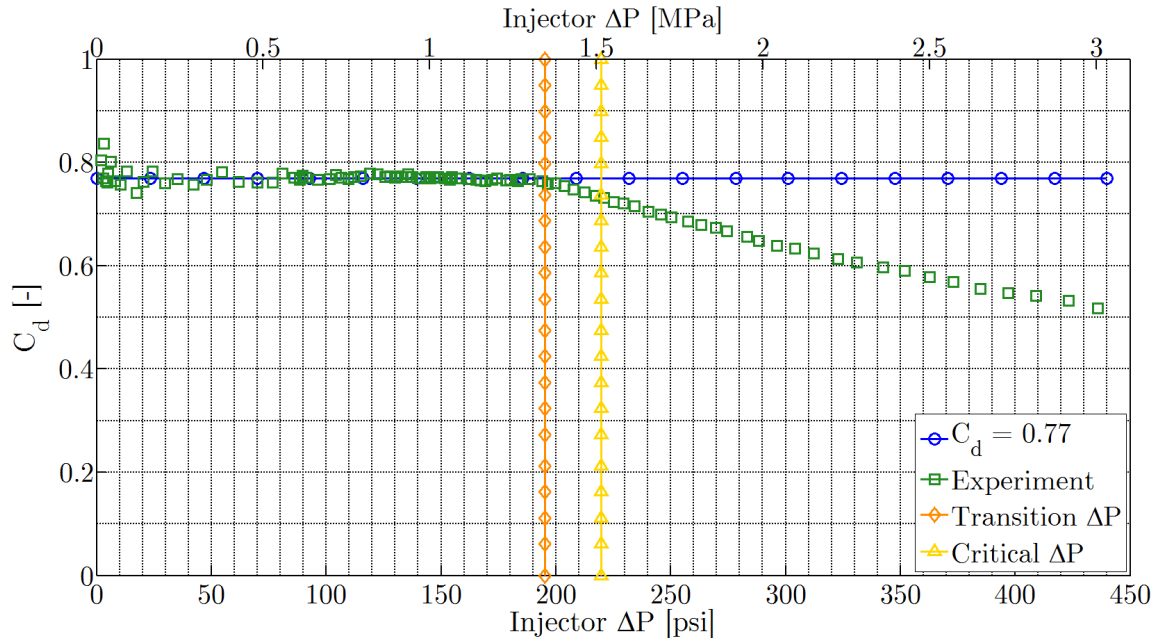


Figure 3.12: Effective discharge coefficient vs. injector  $\Delta P$  data for a test of injector number 3 at average upstream values of  $P_1 = 704$  psia (4.85 MPa),  $T_1 = 7$  °C (280 K) and  $P_{super}^1 = 169$  psi (1.17 MPa).

The limits of this region are based on the deviation of discharge coefficient away from the calculated SPI value and are defined below:

Transition  $\Delta P$ : Value of  $\Delta P$  for which the effective discharge coefficient first drops below 99% of the SPI value.

Critical  $\Delta P$ : Value of  $\Delta P$  for which the effective discharge coefficient first drops below 95% of the SPI value.

These plots can be used directly to assist in the design of injectors, however only for the specific upstream pressure and supercharge used in this test and with a rounded inlet injector. This type of test and data processing can be repeated for a multitude of upstream conditions and injector configurations in order to create a catalog of performance data for use in the design of injectors, or for validation of predictive models. The following section presents some representative sample results that are to be included in an injector performance database, along with some basic comparisons.

## 3.2 Sample Cold Flow Testing Results

To date over 1000 tests have been performed in this new facility, using both nitrous oxide and carbon dioxide as test fluids. Experiments have been performed over a wide range of operating conditions:

$P_1$ : 280 psig  $\rightarrow$  1000 psig (2.03 MPa  $\rightarrow$  7.00 MPa)

$P_2$ : 0 psig  $\rightarrow$  1000 psig (0.10 MPa  $\rightarrow$  7.00 MPa)

$T_1$ : -40 °C  $\rightarrow$  25 °C (233 K  $\rightarrow$  298 K)

$P_{super}^1$ : 0 psi  $\rightarrow$  860 psi (0 MPa  $\rightarrow$  5.93 MPa)

### 3.2.1 Effect of Supercharge Level

As described in the previous section, a single test provides a sweep of downstream conditions and a vast amount of injector performance data. In order to cover as much

of the design space as possible, a range of tests at different supercharge pressures were performed for a given injector design. Fig. 3.13 provides the resulting experimental nitrous oxide mass flow rate data for injector number 3 at a variety of supercharges, plotted against  $\Delta P$ . This figure is created by combining a number of plots similar to that shown in Fig. 3.11, and the same data processing is performed for each curve (the labeling of flow transition and critical mass flow rate however are not included in this plot). Starting at  $\Delta P = 0$  and moving up and to the right, it is evident that at low values of  $\Delta P$ , each test follows the single-phase liquid behavior, and the mass flow rate is relatively independent of supercharge. However, continuing up the curve, we encounter the critical  $\Delta P$  corresponding to the lowest supercharge test, in this case  $P_{super}^1 = 41$  psi (0.28 MPa), after which point the mass flow rate deviates from the single-phase curve, and critical flow is encountered. This process continues while moving up the curve, and the results from each test deviate from the single-phase behavior in order from lowest to highest supercharge. It becomes clear that as  $P_{super}^1$  increases, so too does the critical mass flow rate and critical  $\Delta P$ . From the same test data the effective discharge coefficient is calculated and is plotted versus supercharge and  $\Delta P$  as shown in Fig. 3.14. The behavior of the  $C_d$  curves can be examined in the same fashion, following the single-phase behavior until it deviates at the critical  $\Delta P$  value.

At this point it should be noted that all tests reported in this work are for non-zero values of supercharge. There are two main reasons for this. First, for tests with saturated liquid only, the tank operates in the blowdown mode. Therefore as the pressure in the tank drops below the vapor pressure, large amounts of vapor are formed, leading to unreliable venturi mass flow rate measurement. Additionally, with only pressure and temperature measurements upstream of the injector, it is not possible to determine the vapor fraction needed to completely describe the thermodynamic state of the fluid. The minimum supercharge used for this work is approximately 28 psi (0.19 MPa). The same plots presented above can be created for each combination of injector and fluid. For reference information, all of the data produced during experiments presented in this work are included in Appendix A. The following sections

will highlight some of the important results from these experiments by (a) first examining tests using nitrous oxide and carbon dioxide to investigate the effect of injector hole diameter  $D$  and L/D, (b) assessing the validity of using carbon dioxide as an analog to nitrous oxide in order to (c) use the results from tests with carbon dioxide to examine the effect of injector inlet geometry. Finally, the experimental data will be compared to predictions from some of the two-phase flow models presented earlier in Chapter 2.

### 3.2.2 Effect of Injector Hole Diameter and L/D Ratio

Fig. 3.15 shows the Single Phase Incompressible discharge coefficient over a range of supercharge values for three different injectors, all square edged inlet orifices with varying diameters. While there is virtually no dependence on supercharge, it can be seen that  $C_d$  decreases with increasing hole diameter. While it may seem like this result could be an artifact of including the denominator from Eq. (2.16) in the discharge coefficient, even with largest diameter orifices tested, this effect should only account for an error of approximately 0.002% in the combined discharge coefficient. However, it is likely that this inverse relationship is due to either frictional Reynolds number effects as described in Section 2.1.1.4 or the effect of inlet sharpness related to the vena contracta and contraction coefficient as studied by Nurick and presented in Section 2.1.1.3. All of these tests were performed using nitrous oxide.

It cannot be determined from the above tests alone whether these effects are due to the difference in hole diameter or the difference in hole length to diameter ratio,  $L/D$ . For this reason, a series of tests were performed with two square edged inlet injectors of the same diameter ( $D = 1.50$  mm) but of different lengths (resulting in injector L/D values of 12.3 and 2.1 for injectors 2 and 6 respectively). Fig. 3.16 shows the mass flow rate data for a variety of tests using injectors 2 and 6. Data from tests using injector 2 and 6 are plotted in blue and black respectively. It is immediately clear that tests using the higher L/D injector (injector 2) reach the critical flow regime when the downstream pressure  $P_2$  falls below approximately 80% of the vapor pressure  $P_v$ .

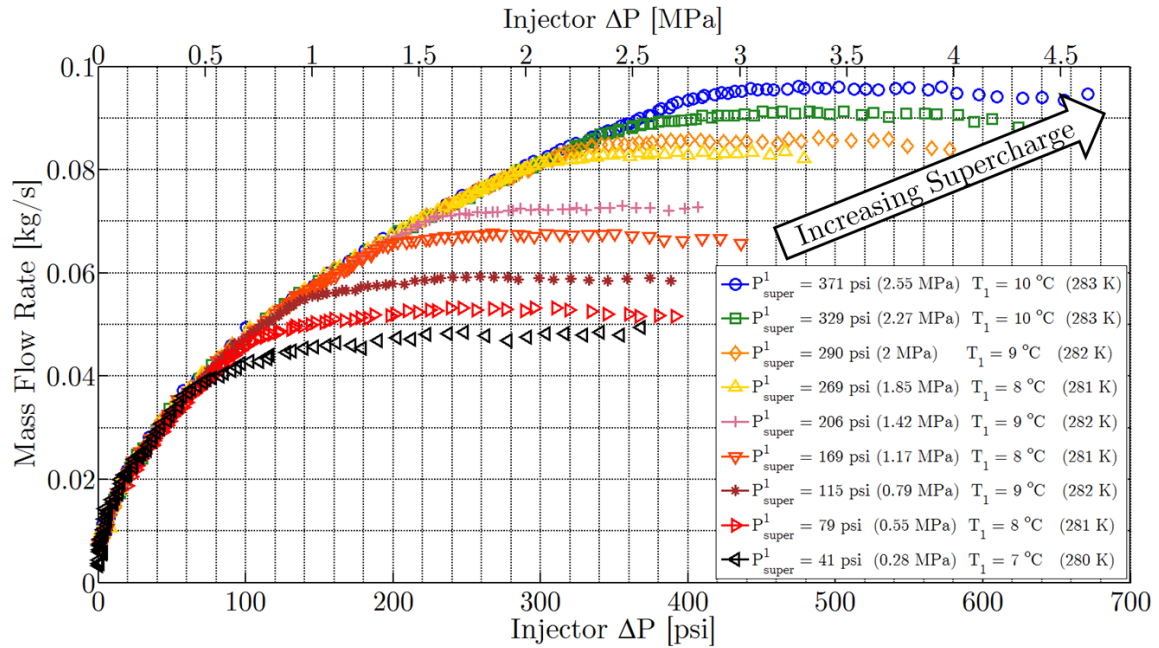


Figure 3.13: Mass flow rate vs.  $\Delta P$  at various supercharge levels for injector number 3 with nitrous oxide.

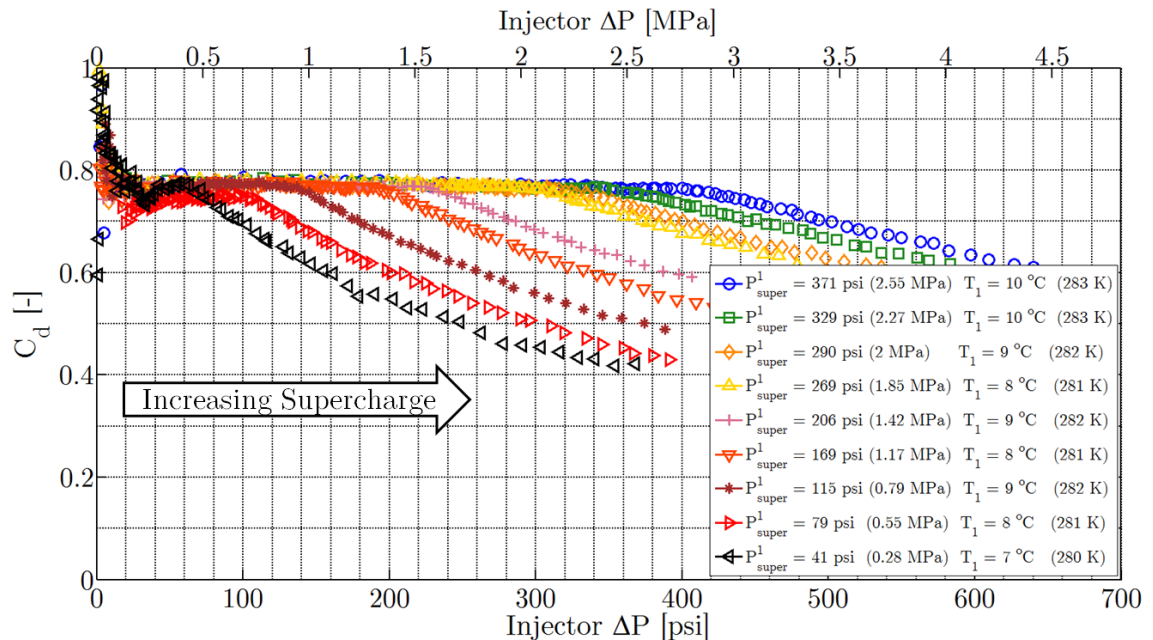


Figure 3.14:  $C_d$  vs.  $\Delta P$  at various supercharge levels for injector number 3 with nitrous oxide.

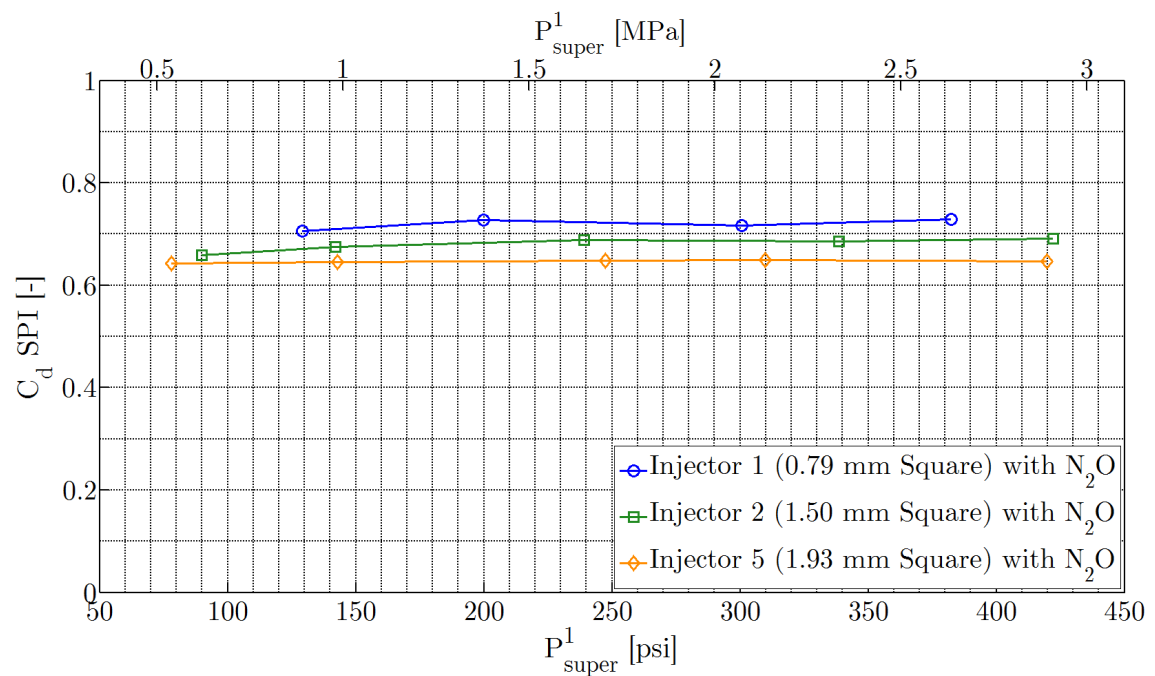


Figure 3.15:  $C_d$  in the single-phase region vs. supercharge for injectors number 1, 2 and 5 with nitrous oxide.

(this type of analysis will be revisited in Chapter 5 and will become quite important). However, for the low L/D injector (injector 6), the critical flow regime does not begin until  $P_2$  drops to around 40% of the vapor pressure. These results do indicate that for low L/D injectors, non-equilibrium effects as described in Section 2.2.2 are indeed important. Due to these non-equilibrium effects, the low L/D injector exhibits higher values of critical mass flow rate for a given supercharge than the high L/D injector, as shown in Fig. 3.17.

### 3.2.3 Comparison of $N_2O$ and $CO_2$ Results

Next we will take a look at some results that will help to determine whether or not carbon dioxide can be used as an effective analog to nitrous oxide. In contrast to the results presented above, these tests will be for a single injector geometry, and the fluid will be varied. Injector number 3 was used for this testing. Fig. 3.18 shows a compilation of the mass flow rate data used to compare the performance of nitrous oxide and carbon dioxide. Tests using carbon dioxide are plotted in blue while tests using nitrous oxide are plotted in red. This color scheme will be used for the remainder of this section. From examining this plot, it is clear that the overall character of the carbon dioxide performance mirrors that of the nitrous oxide quite well. Looking closely, it does seem that the critical  $\Delta P$  and critical mass flow rates do match relatively closely between the two fluids at similar values of supercharge. However because each test was performed at slightly different supercharge levels and temperatures, it is difficult to make any conclusions about the similarities using this figure alone.

For this reason, Fig. 3.19 plots the critical mass flow rate versus supercharge for both carbon dioxide and nitrous oxide. For a given supercharge value, the critical mass flow rate of carbon dioxide tends to be slightly higher than for nitrous oxide. However, this comparison ignores the fact that there is a slight variation in density between the two fluids. Even so, the difference in critical mass flow rate between carbon dioxide and nitrous oxide is less than 10% for the whole range of supercharge

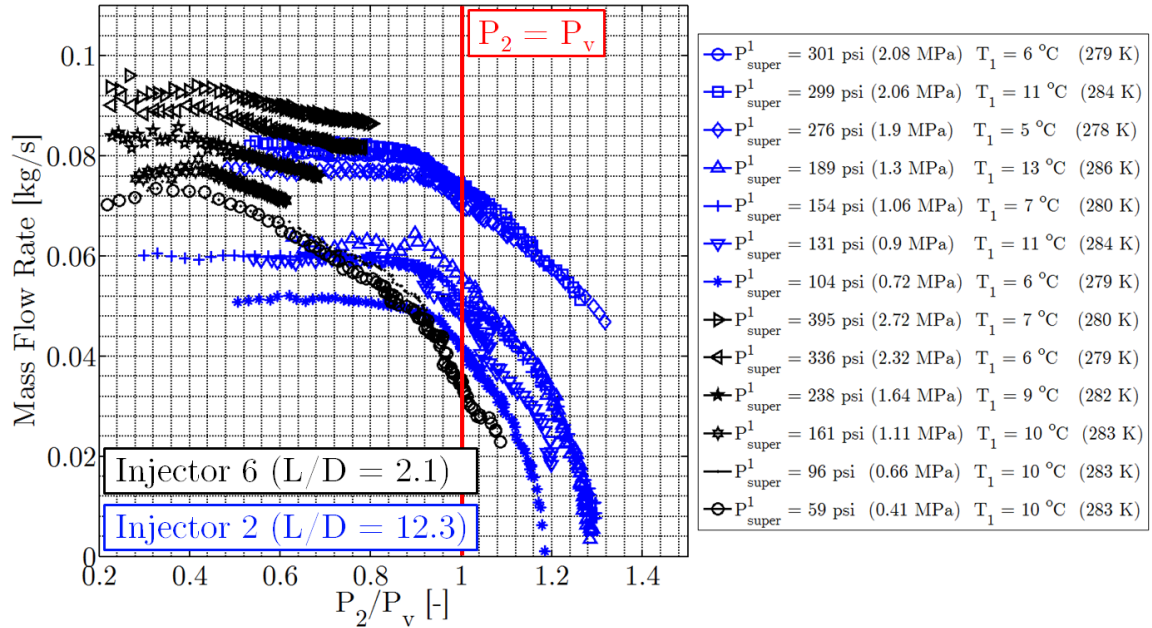


Figure 3.16: Mass flow rate vs.  $P_2/P_v$  and supercharge for injector numbers 2 and 6 both using carbon dioxide.

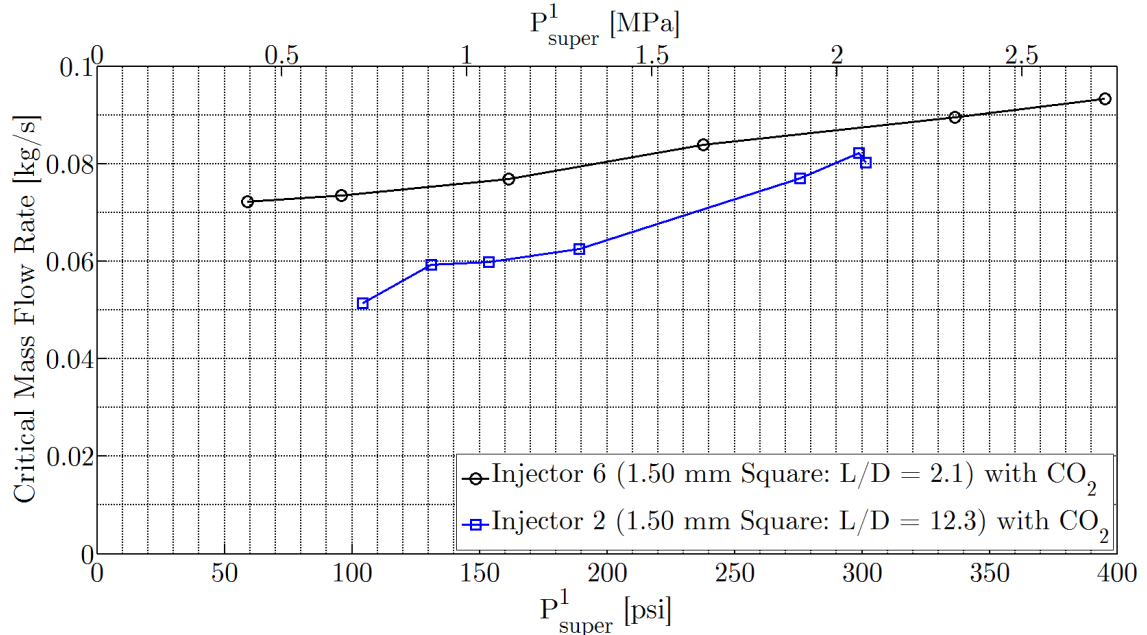


Figure 3.17: Critical mass flow rate vs. supercharge for injector numbers 2 and 6 both using carbon dioxide.

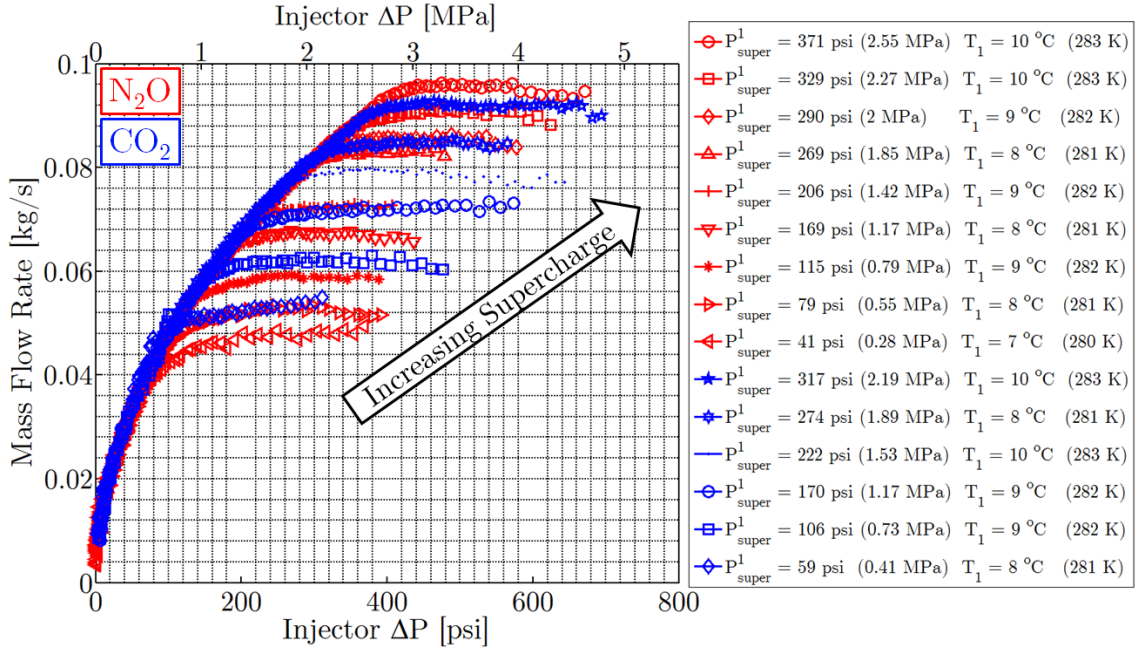


Figure 3.18: Mass flow rate vs.  $\Delta P$  and supercharge for injector number 3 using both nitrous oxide (red) and carbon dioxide (blue).

values tested. Additionally, Fig. 3.20 compares the discharge coefficient for the single-phase region of these tests and for most supercharge levels the value is identical. At points where the discharge coefficient does vary between carbon dioxide and nitrous oxide, the values generally differ by less than 5%. It can be concluded from the results presented in Fig. 3.19 and Fig. 3.20 that carbon dioxide is indeed a relatively accurate analog for injector cold flow testing, though small differences in performance do exist. Future testing could be performed to provide correlations between nitrous oxide and carbon dioxide performance.

### 3.2.4 Effect of Injector Hole Inlet Geometry

The last mass flow rate characterization tests examine the effect of varying the orifice inlet geometry on the mass flow rate performance. These tests use carbon dioxide because it has been established that it is a good analog to nitrous oxide. The injectors used for this testing all have a minimum cross-sectional diameter of 1.5 mm, but one

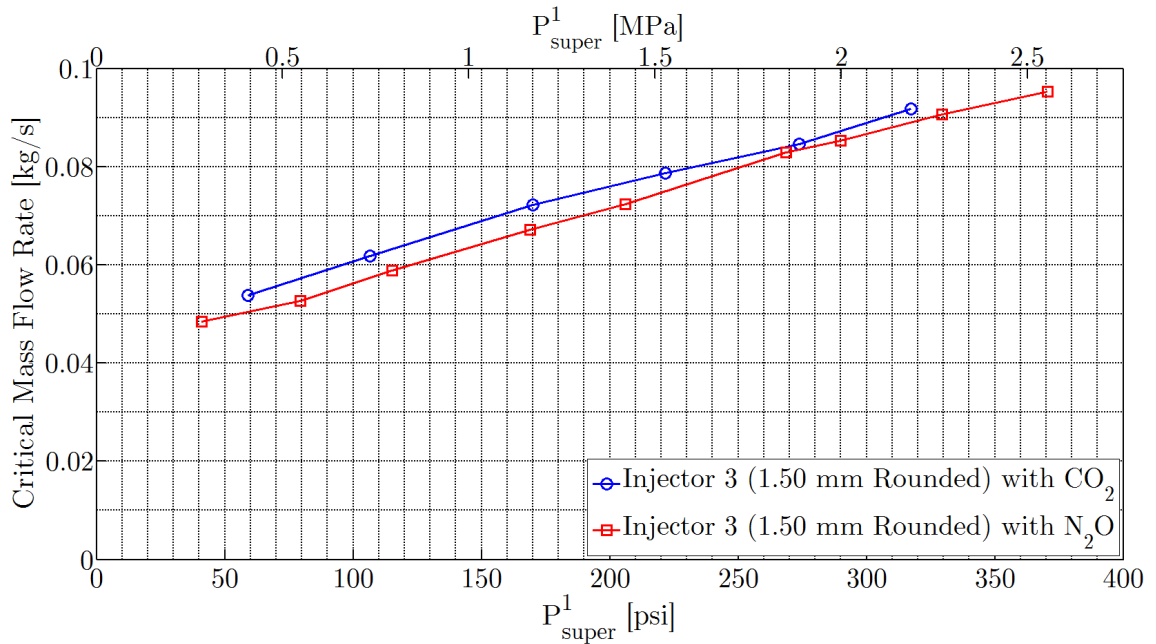


Figure 3.19: Critical mass flow rate vs. supercharge for injector number 3 using nitrous oxide and carbon dioxide.

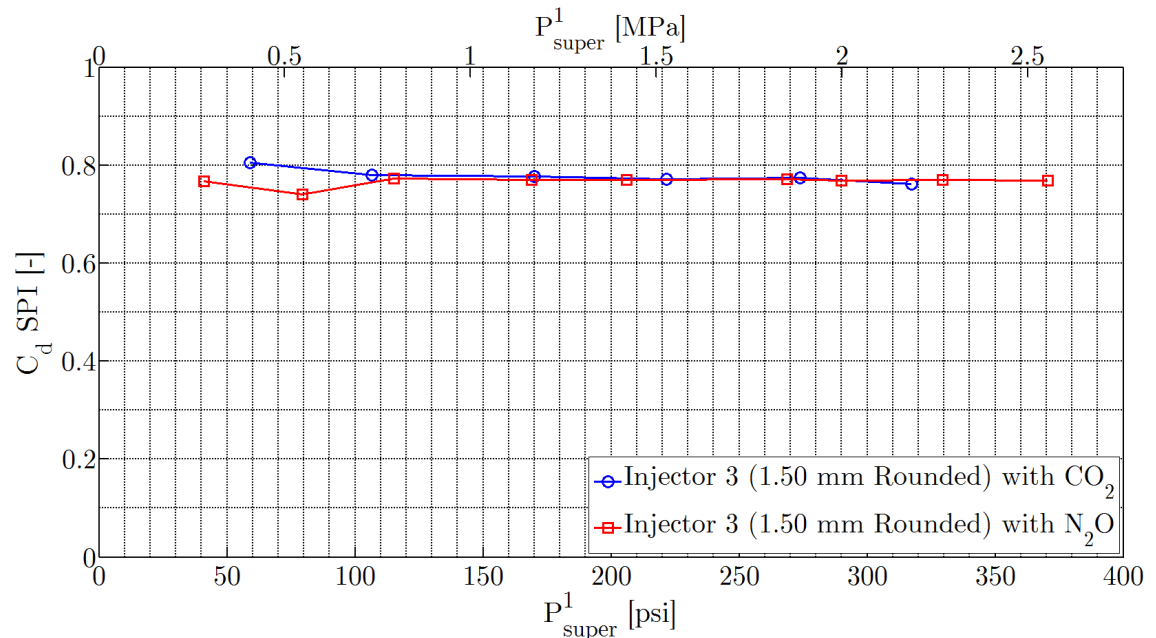


Figure 3.20:  $C_d$  in the single-phase region vs. supercharge for injector number 3 using nitrous oxide and carbon dioxide.

has a square edged inlet, one is rounded, and the last has a  $45^\circ$  chamfer (injectors number 2, 3, and 4 respectively). As with the previous analyses, we will compare the injector performance in the single-phase region and the two-phase region separately. Fig. 3.21 shows the SPI discharge coefficient versus supercharge for the three different inlet geometries. It is clear from this plot that the square edged orifice exhibits a  $C_d$  that is significantly lower than that of the rounded and chamfered injectors, which is expected. Additionally, the  $C_d$  value for the rounded injector appears to be slightly higher than that of the chamfered injector; however the difference is less than the uncertainty in the measurement.

Fig. 3.22 compares the critical mass flow rate of the same three injectors, and results in similar findings. The critical mass flow rate in the square edged injector is approximately 20% lower than that of the rounded and chamfered injector, which display nearly identical performance. In addition to serving as a useful design tool, Fig. 3.21 and Fig. 3.22 demonstrate a significant result: while the mass flow rate of an injector hole can be increased dramatically by installing a simple chamfer, there is almost no additional improvement by going through the extra effort to round the edges instead.

### 3.3 Comparison with Two-Phase Flow Models

Throughout the experimental testing campaign, mass flow rate data in the single phase region is used to determine the single phase discharge coefficient for the various injector geometries. The data is fit to the Single Phase Incompressible curve when it is clear that the injector is operating in the single-phase liquid regime. Once the experimental determination of  $C_d$  is completed, it follows that all of the models, including the two-phase flow models predict the mass flow rate in the single phase region adequately. The major difference between each of the various two-phase flow models relates to the determination of the inception of two-phase flow, and thus the value of the critical mass flow rate. Therefore, the accuracy of the critical mass flow

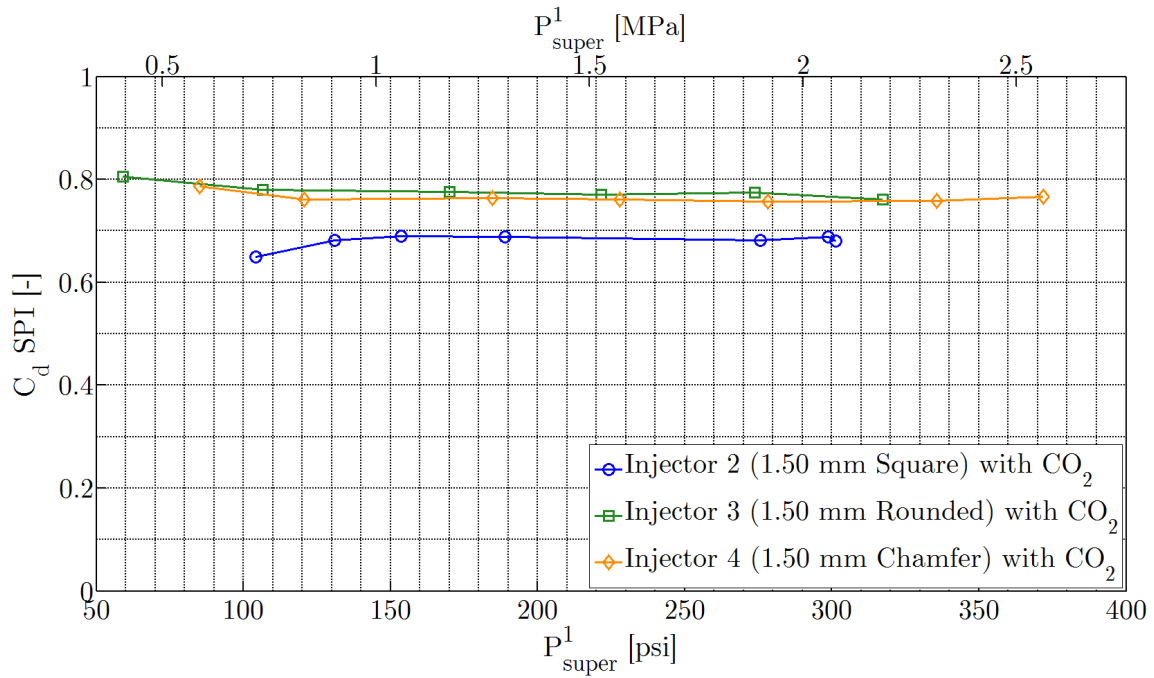


Figure 3.21:  $C_d$  in the single-phase region vs. supercharge for injectors number 2, 3, and 4 using carbon dioxide.

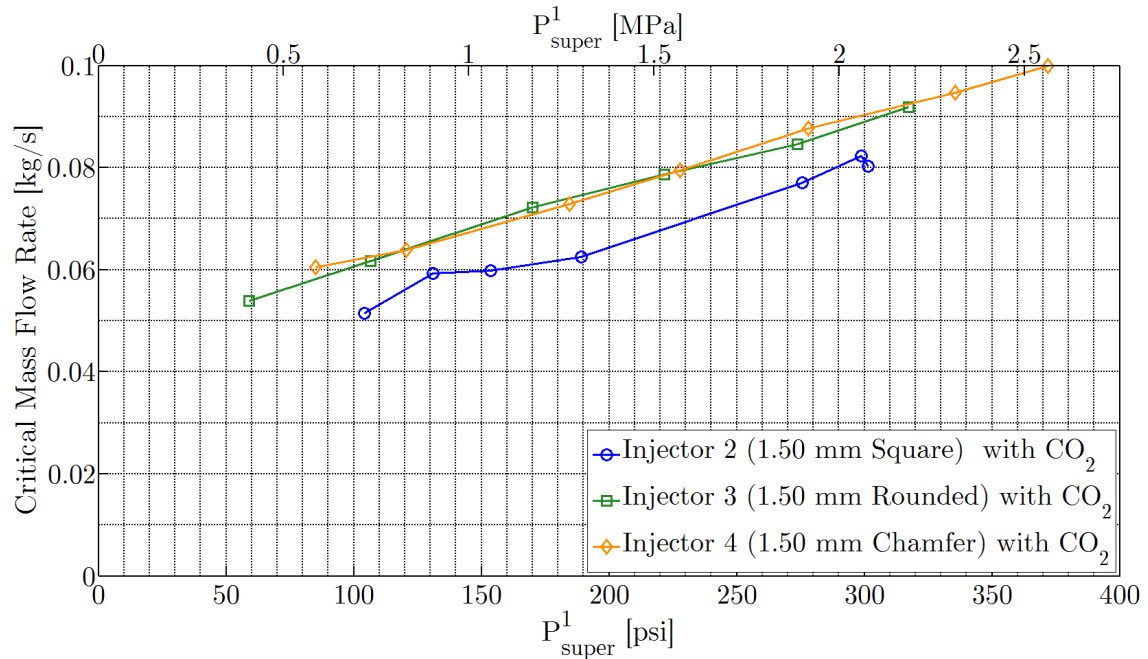


Figure 3.22: Critical mass flow rate vs. supercharge for injectors number 2, 3, and 4 using carbon dioxide.

rate predictions will be used as a metric to compare the two-phase flow models with the experimental data.

Fig. 3.23 shows four similar plots, each corresponding to one of the two-phase flow models described in Chapter 2 (HEM, Moody, Burnell and Dyer models respectively.) These figures compare the predicted mass flow rate from a given flow model vs. the experimental mass flow rate. Individual points are plotted corresponding to actual experimental test data. For a given set of experimental conditions, the critical mass flow rate is measured, and a prediction of the critical mass flow rate is calculated with the corresponding flow model. This is repeated for a multitude of tests. In order to assess the accuracy of a given model, a series of colored lines are included in the plot, corresponding to different levels of error in the critical flow rate predictions (red lines correspond to  $\pm 15\%$  error, orange lines to  $\pm 10\%$  error, and yellow lines  $\pm 5\%$  error).

From examining Fig. 3.23a, it can be seen that the Homogeneous Equilibrium Model tends to underpredict the mass flow rate over almost the entire set of data. This is expected because the Homogeneous Equilibrium Model theoretically represents a lower bound on the two-phase mass flow rate. The results from the Moody model shown in Fig. 3.23b exhibit basically the same trend as the Homogeneous Equilibrium Model, but tends to be universally shifted up closer to the area of the plot which indicates a good match between the model predictions and experimental data. It is difficult to compare the performance of the predictions using the two non-equilibrium methods. While the Burnell model shown in 3.23c seems to have less predictions that fall outside of the 15% accuracy range than the Dyer model, the Dyer model shown in Fig. 3.23d has more prediction points that lie right around the green line, showing very good predictions.

While it is clear that the Moody, Burnell and Dyer models all do a better job predicting the critical mass flow rates than the Homogeneous Equilibrium Model, using these plots alone it is not possible to definitively say which of these models is

the most accurate for predicting mass flow rates of nitrous oxide in rocket propellant injectors. More experimental data would certainly be required to make such a definitive conclusion, however this may not be possible because there are likely regions in which one model always provides the best predictions, but other regions where said model predicts the critical mass flow rate poorly. That being said, the demonstrated error levels shown for the Moody, Burnell and Dyer models in Fig. 3.23 are encouraging in that these models do predict critical mass flow rates to within 10% of the experimental values over a majority of the tests reported in this work.

### 3.4 Cold Flow Testing Conclusions

The small scale cold flow test rig developed for this work has proven to be extremely useful in the characterization of nitrous oxide injector mass flow rate performance. Not only was this test apparatus useful for learning more about the behavior of nitrous oxide injectors operating in the two-phase flow regime, but it also allowed for the favorable assessment of carbon dioxide as an analog for nitrous oxide in these types of injector experiments. Results from testing in this rig constitute the beginnings of a new database for the recording of nitrous oxide injector mass flow rate performance data. Using this data, the accuracy of a few of the two-phase flow models described in Chapter 2 has been evaluated, however more experimental cold flow data would be required to make a definitive ranking of the model performance. However, at this point it is still useful to increase confidence in the mass flow rate performance predictions of a given injector geometry and operating conditions using a cold flow test setup like the one presented in this chapter. None of the two-phase flow models can provide the confidence that comes with experimental cold flow measurements. This cold flow test apparatus will be revisited in Chapter 5, for tests supporting the Peregrine Sounding Rocket full scale hybrid rocket development program which will be described next.

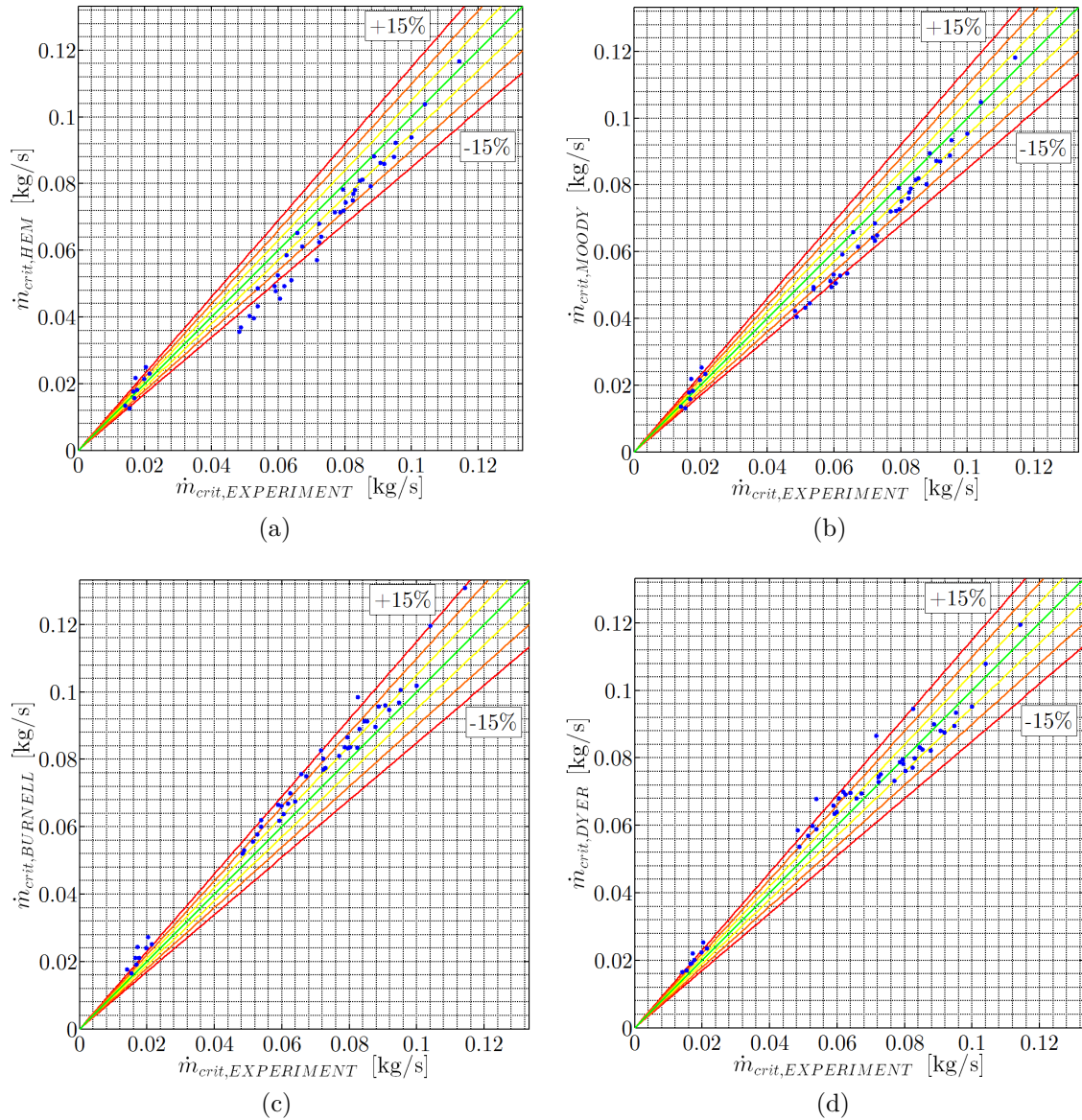


Figure 3.23: Comparison of experimental critical mass flow rate data to that predicted by the a) Homogeneous Equilibrium Model, b) Moody model, c) Burnell model, and d) Dyer model. (Red lines correspond to  $\pm 15\%$  error, orange lines to  $\pm 10\%$  error, and yellow lines  $\pm 5\%$  error).

# **Chapter 4**

## **Peregrine Hybrid Sounding Rocket**

The Peregrine Sounding Rocket program is a joint effort between Stanford University, NASA Ames Research Center in Mountain View, CA and Space Propulsion Group, Inc., a private rocket development company based in Sunnyvale, CA. The goal of this program is to develop and demonstrate the advantages of the so-called liquefying fueled hybrid rocket technology, which will be described in this chapter. To this end, a single stage sounding rocket is currently under development, capable of lifting a 5 kg payload to the edge of space (100 km). This rocket uses paraffin wax as the fuel and nitrous oxide as the oxidizer. This chapter will give a brief background into the motivation, design, and history of the program. Additionally some data from actual hot fire testing will be presented and discussed, which will serve as motivation for the remainder of this dissertation.

### **4.1 Program Objectives**

The hybrid rocket concept is not a new one. For years, hybrid rocket technology has shown the potential to allow for relatively safe and inexpensive development and operation compared to that of liquid and solid rocket systems. However, until recently, the performance of hybrid rocket systems has been held back by the relatively low regression rate (or burn rate) of the solid fuels that are traditionally used (such as hydroxyl-terminated polybutadiene, or HTPB). With low regression rates, it can be

difficult to achieve the high thrust levels required for full scale launch systems. In order to achieve sufficient fuel production rates with these slow burning fuels, it is necessary to use either extremely long fuel grains or complicated multi-port fuel grain designs to provide enough fuel surface area for burning. For this reason, past hybrid rocket development programs have typically had trouble “getting off the ground”.

However, the discovery of a class of high regression rate liquefying hybrid fuels by Arif Karabeyoglu at Stanford University essentially solved this problem, resulting in the almost immediate practical realization of high performance hybrid rocket systems. An in depth background of the theory leading to this discovery is included in Ref. [51]. In short, the formation of an unstable liquid melt layer on the fuel surface results in the entrainment of fuel droplets in the core oxidizer flow. With the introduction of these droplets, the effective burning surface of the fuel is increased, resulting in an overall higher performance design. A conceptual depiction of this liquid layer theory is shown in Fig. 4.1. The prototypical example of a high regression rate liquefying hybrid rocket fuel is paraffin wax, which is quickly becoming one of the most popular fuel choices in hybrid rocket development programs around the world. As mentioned earlier, for traditional hybrid rocket fuels, a common method for increasing the fuel burning area is to design the fuel grain with complicated multi-port designs. These designs exhibit a variety of complications and issues, including the possibility of thin webs of fuel being ejected from the combustion chamber unburned. As shown in Fig. 4.2, liquefying paraffin based fuels allow for the use of simple, single circular port fuel grains, resulting in simpler, higher performance systems.

Over the years, work at Stanford University and NASA Ames Research Center has focused on the performance characterization of paraffin wax fueled hybrid rockets. In efforts such as the sub-scale hybrid rocket test depicted in Fig. 4.3, the regression rate of paraffin fuel was characterized when burned in combination with a variety of oxidizers and fuel additives. Some results of such studies can be found in Ref. [54] and [11]. However, in order to establish increased technological maturity for liquefying paraffin fueled hybrid rocket technology, it was desired to

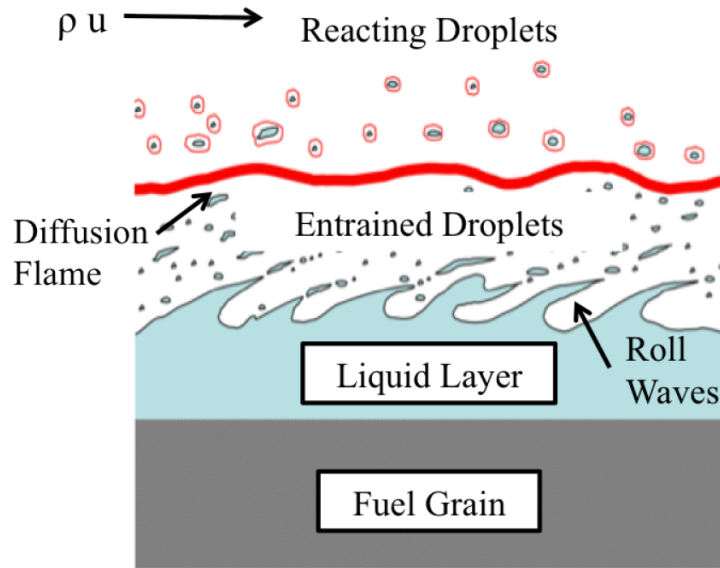


Figure 4.1: Conceptual depiction of the mechanism of liquifying hybrid rocket fuels. Oxidizer flow from left to right (reprinted from Ref. [52] with permission, originally adapted from Ref. [53]).

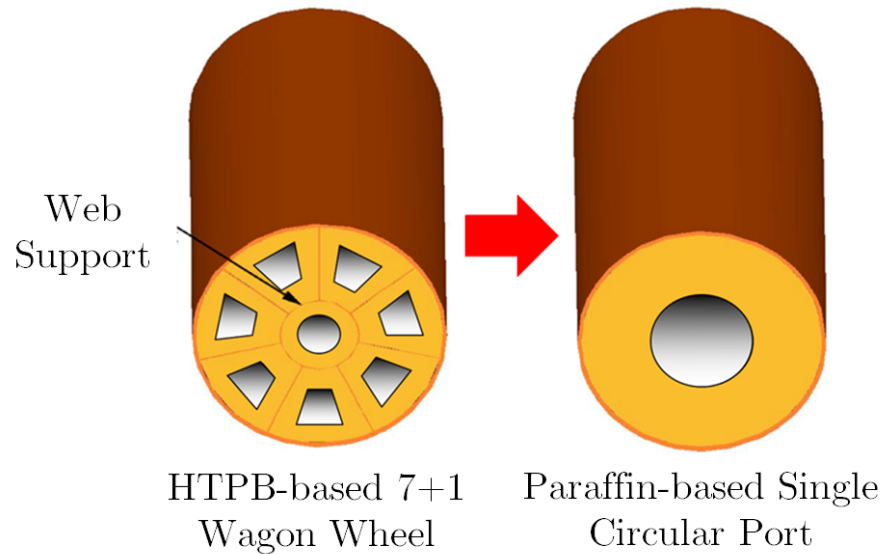


Figure 4.2: Simplification of fuel grain design due to increased regression rates provided by liquefying fuels such as paraffin wax (adapted from Ref. [53]).



Figure 4.3: Sub-scale testing of a paraffin fueled hybrid rocket motor at Stanford University. (Reprinted from Ref. [1] with permission of the American Institute of Aeronautics and Astronautics, Inc.).

demonstrate operational performance on a larger scale. As mentioned previously, the Peregrine Sounding Rocket program was initiated to accomplish this, with the goal of developing a paraffin fueled hybrid rocket launch vehicle capable of delivering a 5 kg payload to suborbital space (altitude of 100 km) in a single stage. The goals with regard to the actual hybrid rocket propulsion system to be developed for this vehicle were to achieve both stable and efficient combustion throughout the duration of the burn (combustion chamber pressure fluctuations less than  $\pm 5\%$  of the mean and average  $c^*$  efficiency greater than 95%). The Peregrine program is run out of NASA Ames Research Center, and is a partnership between NASA, Stanford University, and Space Propulsion Group, Inc. Approximately 20 past and current Stanford graduate students have participated in the development of the Peregrine Sound Rocket. While an in depth description of the flight vehicle design is not necessary based on the scope of this dissertation, a brief overview is included to provide context for Peregrine hybrid rocket propulsion system development discussed throughout the remainder of this work.

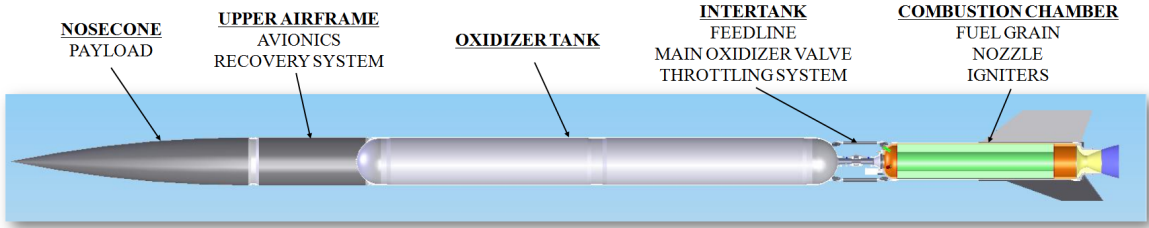


Figure 4.4: Cross-section of the proposed Peregrine Sounding Rocket architecture

Table 4.1: Peregrine Sounding Rocket proposed design and performance overview [17]

Parameter	Value
# of Stages	1
Reusability	Yes
Recovery	3-stage parachute system
Overall Dimensions	D = 0.5 m, L = 10.5 m
Gross Liftoff Mass	782 kg
Fuel	107 kg SP1A (paraffin wax based)
Oxidizer	435 kg N <sub>2</sub> O
Delivered Specific Impulse	232 s
Total Impulse	980 kN-s
Initial Acceleration	8.6 g
Apogee Altitude	100 km

## 4.2 Sounding Rocket Architecture and Early Testing

The Peregrine Sounding Rocket can be described as a single stage reusable rocket demonstrator. A cross-section showing an overview of the proposed rocket architecture is included in Fig. 4.4. The fuel is paraffin wax and the oxidizer is nitrous oxide. A collection of some initial design and predicted performance parameters is included in Table 4.1.

In order to provide adequate initial thrust, the oxidizer tank will operate in a helium-augmented blowdown mode, meaning that before the burn, the nitrous oxide will be supercharged with helium, however no on-board pressurization system will be

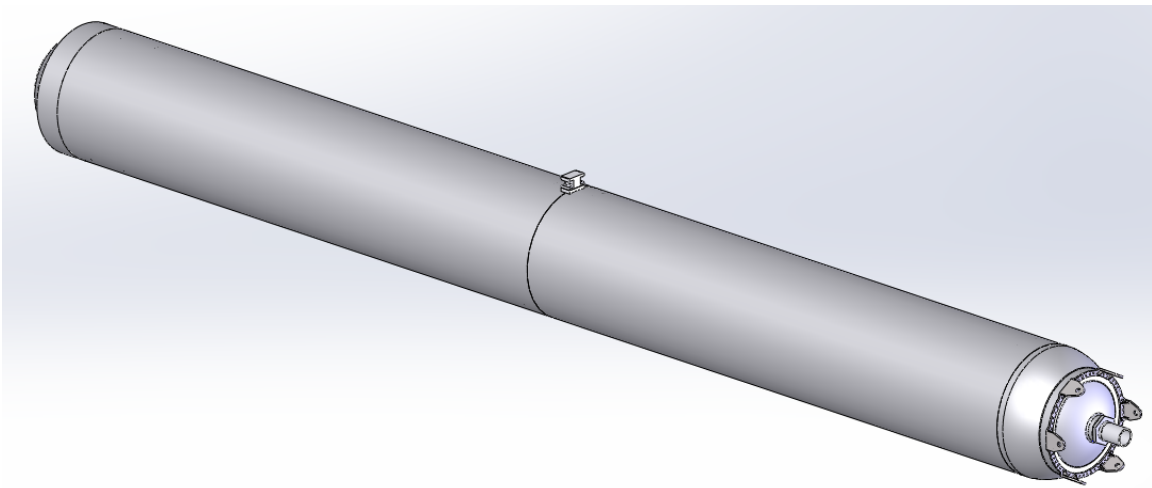


Figure 4.5: Model of an early Peregrine oxidizer tank design.

included (therefore tank pressure will not be held constant). The maximum expected operating pressure in the tank is 1000 psia (6.89 MPa). A model of an early flight weight oxidizer tank design is shown in Fig. 4.5 which was to be constructed of 2219 aluminum. The development of a new oxidizer tank design is currently underway but will not be presented here. The oxidizer leaves the tank and passes through a 5.08 cm diameter feed line, which houses a pneumatically actuated full port isolation ball valve. This feed line provides oxidizer to the fore end of the combustion chamber, ending at the injector plate. The oxidizer tank will be structurally connected to the combustion chamber by a truss structure that connects to mounting points integrated into the aft tank end cap itself. The payload and nosecone section are attached to a similarly integrated mounting point on the fore end cap of the oxidizer tank, as shown in Fig. 4.6 [17, 55].

A model of an early flight weight combustion chamber design is shown in Fig. 4.7 [1]. A near flight weight version of this combustion chamber with increased wall thickness was actually built and tested during a series of ground tests during a campaign which included both cold flow and hot fire tests. The motor was ignited by solid propellant igniters that protruded into the fore end of the combustion chamber.

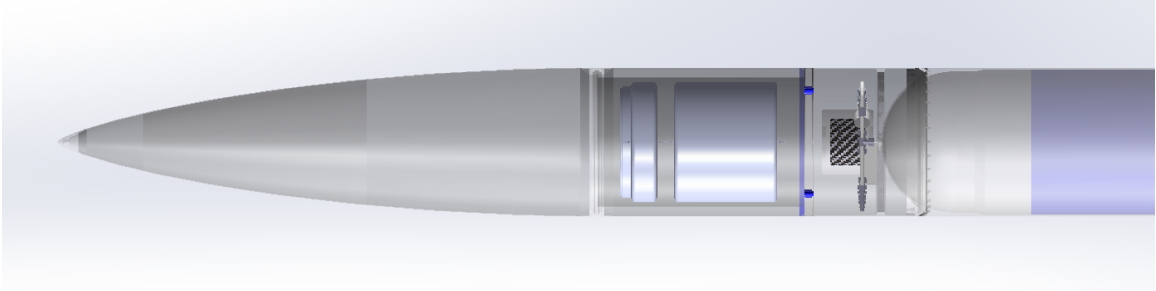


Figure 4.6: Proposed Peregrine payload and nosecone configuration in relation to the fore end of the oxidizer tank.

Ground tests were performed with both the combustion chamber and oxidizer tank (heavyweight, not flight) held horizontally. A model of the horizontal ground test setup is shown in Fig. 4.8. In order to ensure liquid delivery of nitrous oxide with the tank in a horizontal position, a custom eductor, or siphon tube was included at the exit of the oxidizer tank, which acts to position the start of the feed line near the lowest point of the tank.

A still image from one hot fire test using this early combustion chamber design is shown in Fig. 4.9. It should be noted that every test at nominal operating conditions using this motor design exhibited unstable combustion. The last test of this combustion chamber resulted in an overpressure and failure of pressure vessel due to an explosive nitrous oxide decomposition reaction within the fore end of the chamber (the same type as described in Section 3.1.3.1). Details of this test campaign, including pressure time histories of the tests, a discussion of the instabilities encountered, and a description of the cause of the chamber failure can be found in Ref. [17].

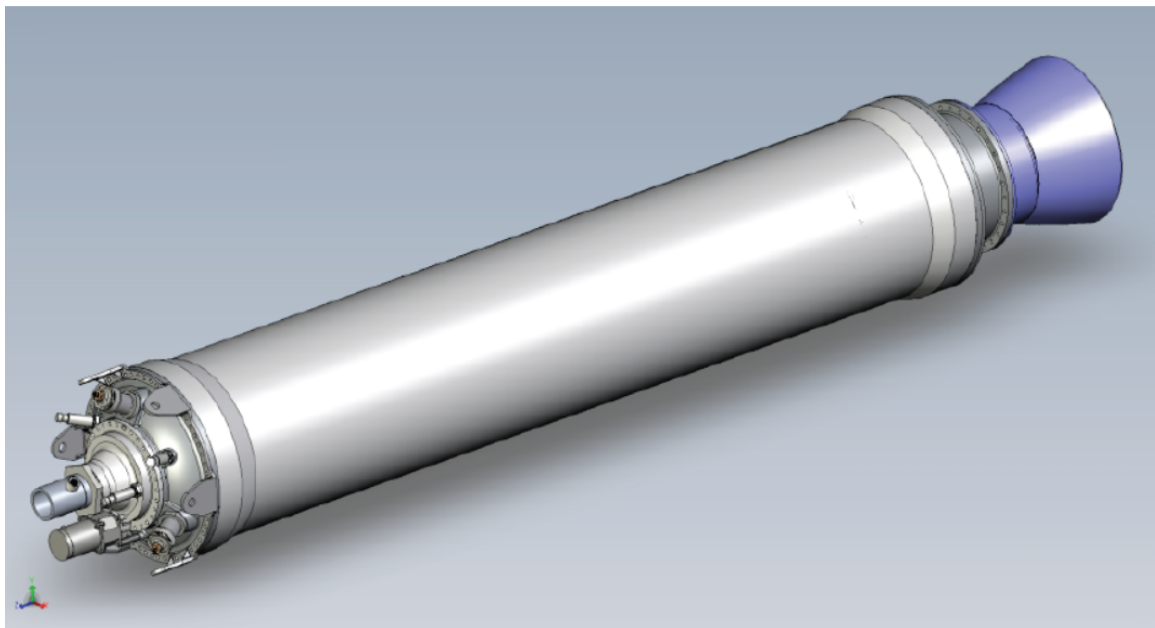


Figure 4.7: Early Peregrine flight weight combustion chamber model. (Reprinted from Ref. [1] with permission of the American Institute of Aeronautics and Astronautics, Inc.).

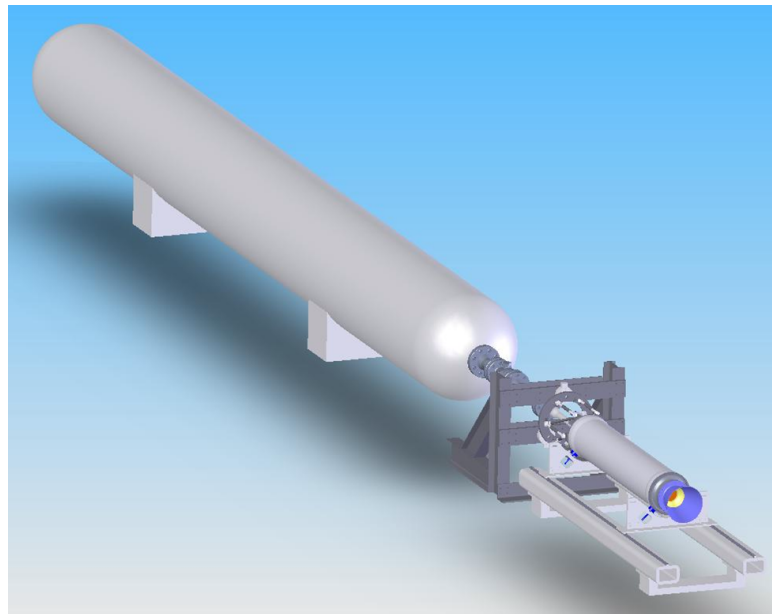


Figure 4.8: Model showing the horizontal setup for Peregrine ground testing.



Figure 4.9: Hot fire test using the near flight weight Peregrine combustion chamber [17].

### 4.3 Heavyweight Ground Testing Combustion Facility

Due to the failure of the near flight weight combustion chamber, and the persistence of combustion instabilities that were not well understood, the combustion chamber was redesigned and manufactured in a heavyweight form to facilitate further developmental ground testing, with less risk of hardware loss. The goal of development in this facility was to achieve stable and efficient combustion before returning to flight weight hardware. The heavyweight combustion chamber internal geometry was intentionally designed to be similar in the overall design of the flight weight motor. However, it was thought that the high peak initial mass flux of oxidizer through the fuel port ( $1200 \text{ kg/m}^2\text{s}$ ) contributed to the development of combustion instabilities in the initial motor design. Therefore in the design of the heavyweight chamber, the overall diameter was increased to allow for a larger initial fuel port area, thus reducing this peak oxidizer mass flux down to approximately  $650 \text{ kg/m}^2\text{s}$  [17]. The new heavyweight combustion facility was built with a thick walled steel pipe and flange design. A cross-section of the heavyweight combustion facility is shown in Fig.

4.10 with some details of the pipe and flange construction.

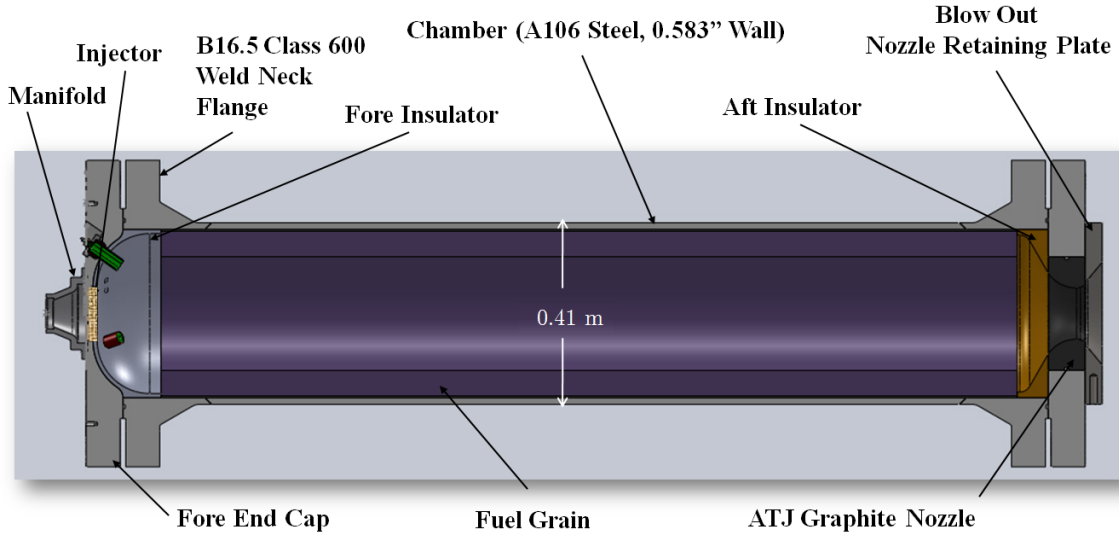


Figure 4.10: Cross-section model of the Peregrine heavyweight combustion facility chamber

The fore end cap dome design was intended to replicate the internal geometry for a flight weight design, and was machined from a blank flange. In order to achieve this domed geometry, a significant amount of material was machined away from the stock flange. For this reason, a detailed structural analysis was performed for the entirety of the heavyweight facility fore end design. Solidworks Simulation was used for this structural analysis, and some sample results are shown in Fig. 4.11a. Details on the solution technique used in this analysis are included in Ref. [46]. Approximately 20 different design iterations were analyzed throughout the design effort. While they are not shown in the visualized analysis results, all of the bolts and fasteners were modeled in the analysis of this complicated assembly. A photo of the partially assembled fore end of the heavyweight combustion facility is shown in Fig. 4.11b.

In one aspect, the thicker walled pressure vessel used as the chamber in the heavyweight design is more robust than the flight weight design in that the anticipated failure pressure is higher. However, this actually can cause added risk: if the

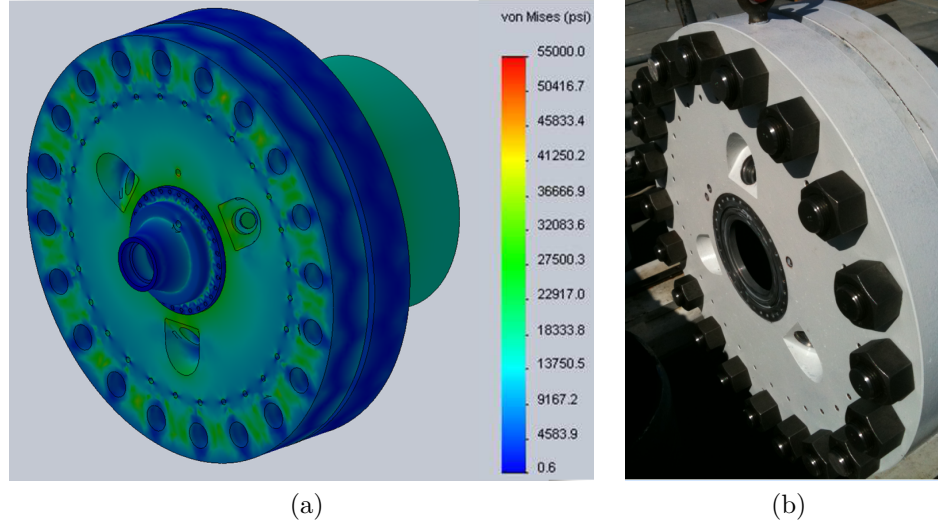


Figure 4.11: Sample FEA calculations showing von Mises stress distributions for the fore end of the heavyweight combustion facility with photo of as built hardware

heavyweight chamber were to fail, it would likely be failing at a higher pressure, resulting in greater levels of energy release. This energy usually is converted into kinetic energy of flying debris from the failed vessel. For this reason, the heavyweight combustion facility was designed with a blowout nozzle, designed to release if the combustion chamber pressure ever exceeds 1500 psig (10.44 MPa). This design was achieved by the use of a graphite nozzle insert held in place by a stainless steel retaining plate. The retaining plate was fastened to the aft end flange by a circle of precisely notched bolts, designed to fail when the chamber reaches 1500 psig (10.44 MPa). This was a critical part of the design, and while it was important that the nozzle did release at 1500 psig (10.44 MPa), it was also important to ensure that the nozzle did not release prematurely. For this reason, a detailed structural analysis was also performed for the aft end of the heavyweight combustion facility (not by the author), with results shown in Fig. 4.12. Again, the details of all fasteners (the retaining bolts in this case) were modeled in the analysis of the full assembly.

All pressurized components in the ground test facility were hydrostatically tested in order to comply with NASA safety procedures. However, in order to experimentally

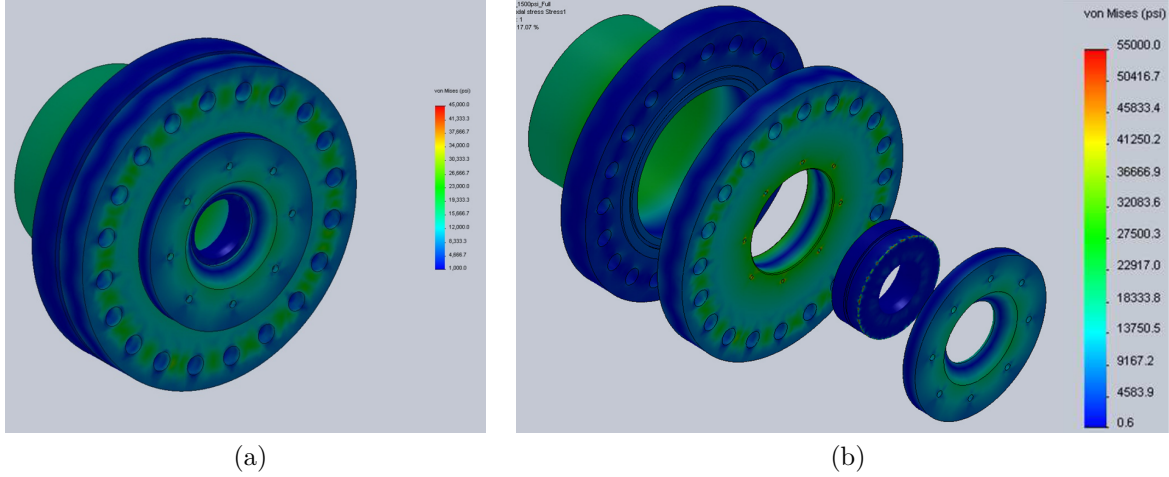


Figure 4.12: Sample FEA calculations showing von Mises stress distributions for the aft end of the heavyweight combustion facility, specifically performed to analyze the blowout nozzle.

verify the design of the blow out nozzle, a special hydrostatic test was performed to intentionally blow out the nozzle. The as built aft end of the heavyweight combustion facility is shown in Fig. 4.13 as well as a still image during the intentional nozzle blow out experiment. In order to perform this test, a nozzle blank with no opening replaced the actual nozzle insert. Because the projected area of the nozzle blank was greater than that of the actual nozzle as designed, the hydrostatic blow out was expected to occur at a predicted pressure lower than 1500 psig (10.44 MPa). The nozzle did indeed blow out at the appropriate pressure. However, no nozzle blowout events have occurred in any subsequent hot fire testing that has been performed.

After complete system assembly and sufficient check out tests (such as hydrostatic testing), a test campaign was initiated including both cold flow tests and hot fire tests. To date, approximately 15 tests have been performed in the heavyweight combustion facility (5 cold flows, 10 hot fires). Fig. 4.14 shows a still image captured during testing in the heavyweight combustion facility for a recent hot fire test.

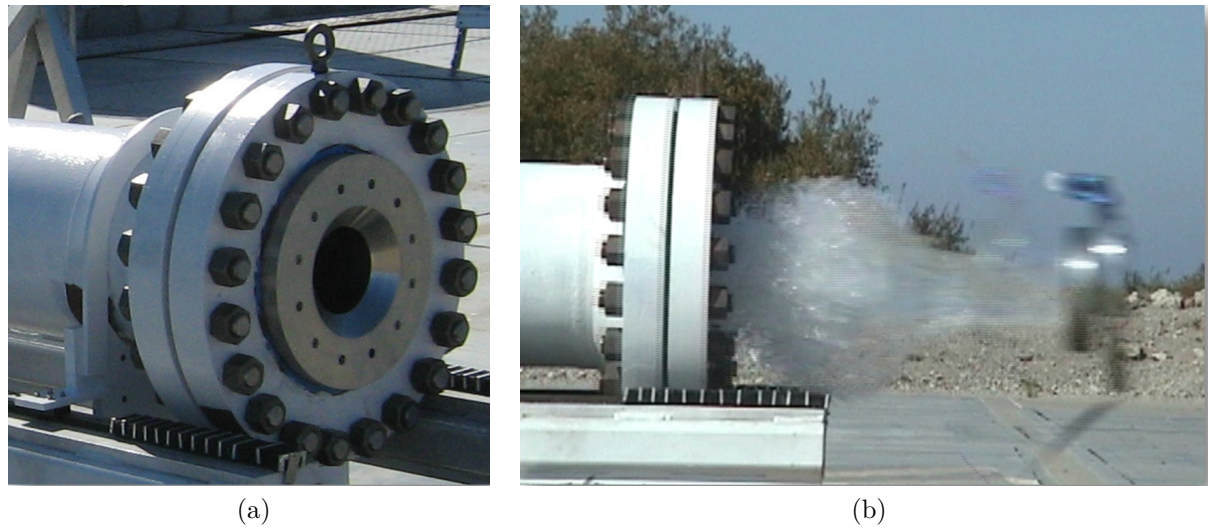


Figure 4.13: Still photos of the heavyweight combustion facility aft end and the nozzle blow out testing (water is seen flowing from the chamber).



Figure 4.14: Still photo from hot fire testing in the Peregrine heavyweight combustion facility

## 4.4 Ground Testing Combustion Instabilities

During the first tests in the Peregrine heavyweight combustion facility, it became immediately clear that decreasing the peak oxidizer mass flux in the combustion chamber port did not solve the instability problems. This section will present chamber pressure data for two of the early tests in this facility. A discussion of the corresponding combustion instabilities that are observed is included, and will serve as the motivation for the work presented in Chapter 5.

Throughout the rest of this work, when presenting test data from the Peregrine heavyweight combustion facility, the actual test numbering used by the Peregrine program will be quoted. The purpose of this is to minimize confusion should the totality of the Peregrine test data be published in the future. The results from each test will be described by presenting the following data:

- Chamber pressure time-histories
- Chamber pressure frequency content (FFT)
- Oxidizer temperature (for reasons to be discussed in Chapter 5).

### 4.4.1 Peregrine Test E2

Test E2 was the first operationally successful hot fire test achieved in the heavyweight combustion facility. The full duration of a Peregrine flight burn is approximately 18 seconds. However, because Test E2 was a development burn, the duration was limited to 5 seconds. The temperature of the nitrous oxide used in this test was approximately  $13.5^{\circ}\text{C}$  (286.7 K) throughout the duration of the burn. Fig. 4.15 shows the combustion chamber pressure time-history for this test. It is obvious that this test exhibited extremely unstable combustion, with the peak-to-peak amplitude of the chamber pressure oscillations approaching 100% of the mean value over large portions of the test. This is obviously unacceptable for a launch vehicle, even of the sounding rocket variety, and the focus of the Peregrine program was placed squarely

on eliminating these instabilities. In order to get a better sense of the character of these chamber pressure oscillations, Fig. 4.16 is included which zooms in on the data in the time domain (x-axis). The scale for the chamber pressure signal (y-axis) is kept constant, not only for these two plots, but for all of the Peregrine chamber pressure plots presented for the remainder of this work. This is done in order to make comparisons of motor performance from one test to another more straightforward. The point in time for the zoomed in plot was chosen in order to demonstrate that the character of the oscillations changes throughout the test. It can be seen from the zoomed in plot that oscillations are occurring at multiple frequencies. In the first half of the data shown in Fig. 4.16, it can be seen that there is fairly regular low frequency oscillation, with higher frequency oscillations superposed over that signal (with the peak to peak amplitude of the oscillations almost equal). The second half of the zoomed in data shows a shift in the character, with the higher frequency oscillation amplitude increasing significantly, to the point where the low frequency oscillations are not clearly visible.

While it is useful to examine this type of data in this zoomed in time window, it is often beneficial to look at the data in the frequency domain instead. This is achieved by applying a type of Fast Fourier Transform (FFT) to the time domain data, the details of which can be found in Ref. [56]. In essence, this process involves breaking down the time domain data into a summation of simple sinusoidal signals at different frequencies and determining the amplitude of each frequency. This process can be performed on data during different segments of a hot fire test in the time domain, resulting in the display of the frequency content of the chamber pressure signal over time. This type of data presentation is sometimes referred to as a spectrogram. This process does require “windowing” the data to determine, at each point in time during the burn, how many samples from the data should be used to calculate the frequency information. For all of the spectrograms included in this work, the window length is chosen as 1 second. All of the data is collected at 5000 Hz (per channel), therefore the window length is 5000 samples. These windows are usually overlapped to provide a sufficient number of time points in which to plot the frequency content. However,

the actual resolution with respect to time is dependent on the length of the windows chosen (the longer the window, the more data is being used from surrounding points in time). The choice of 1 second FFT windows was made in order to sufficiently resolve the relatively low frequency oscillations which will be seen in some of the test results.

Fig. 4.17 shows the spectrogram content of the chamber pressure signal from Test E2 plotted over the duration of the burn. It can be seen that there is strong activity around 200-210 HZ, which becomes especially coherent during the second half of the test. This frequency corresponds to the 1st longitudinal acoustic mode of the combustion chamber (acoustic resonance combustion instabilities will be discussed briefly in Chapter 5). It can also be seen that there is a significant level of frequency content down in the 10-25 Hz range. This activity is less coherent, and seems to fade after the first half of the burn. Up to this point in testing, this data was not enough to determine the cause of the low frequency response. In all of the spectrograms that are presented, there is always a strong response near 0 Hz. This is reflective of the fact that the mean value of the signal is shifting over time. This part of the data can be ignored.

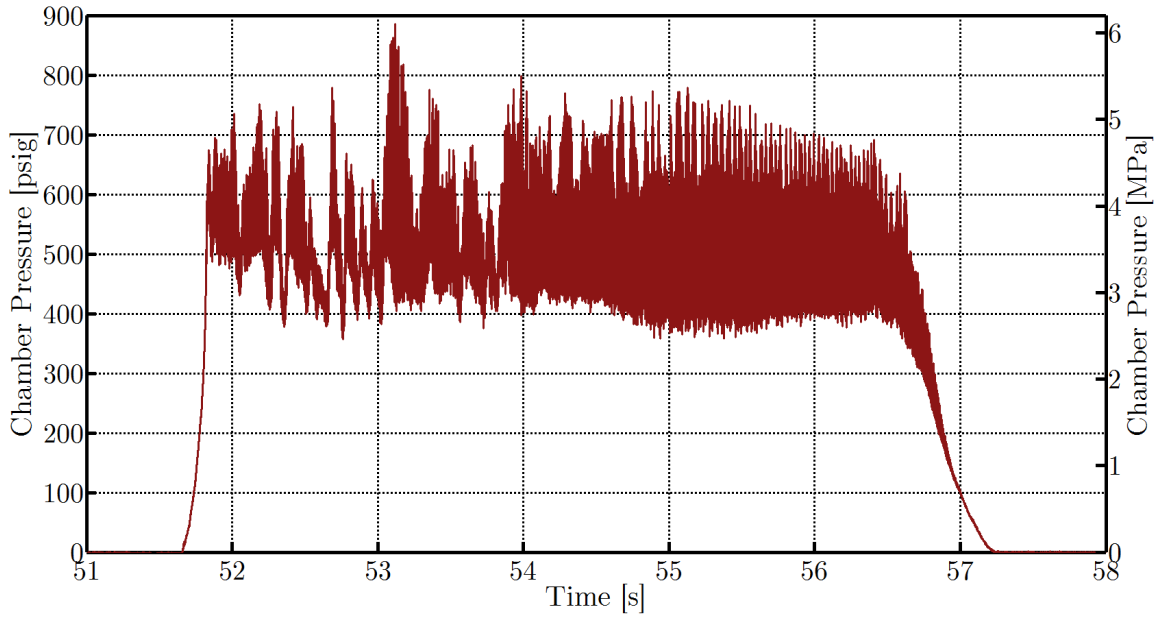


Figure 4.15: Chamber pressure time-history for Test E2 in the Peregrine heavyweight combustion tests facility with  $T_{ox} \approx 13.5^{\circ}\text{C}$  (286.7 K).

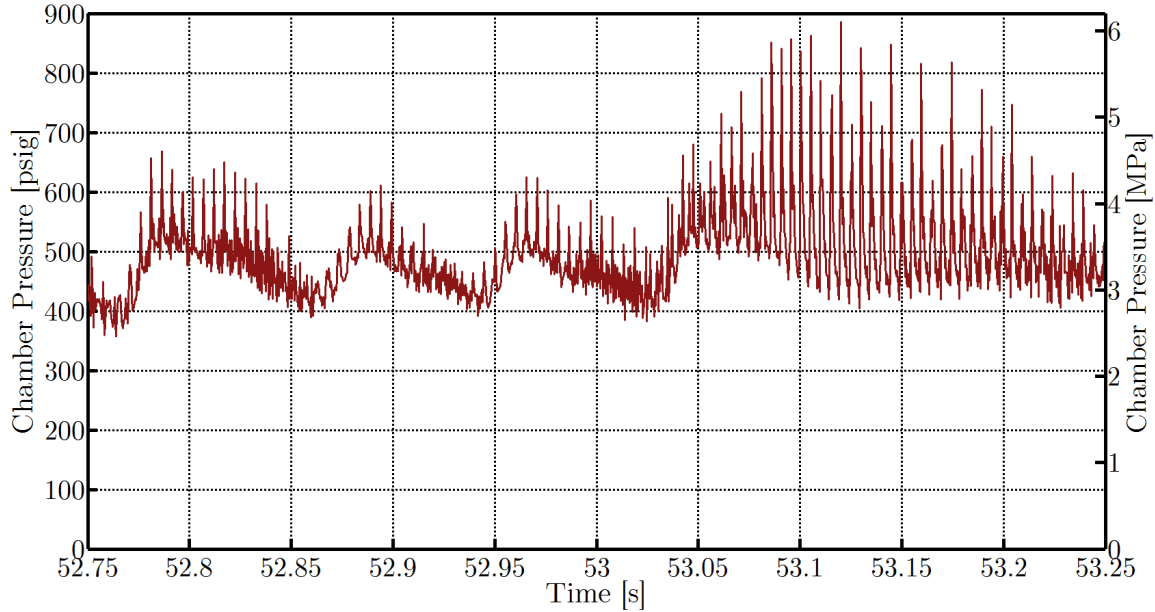


Figure 4.16: Zoomed in chamber pressure time-history for Test E2 in the Peregrine heavyweight combustion tests facility with  $T_{ox} \approx 13.5^{\circ}\text{C}$  (286.7 K).

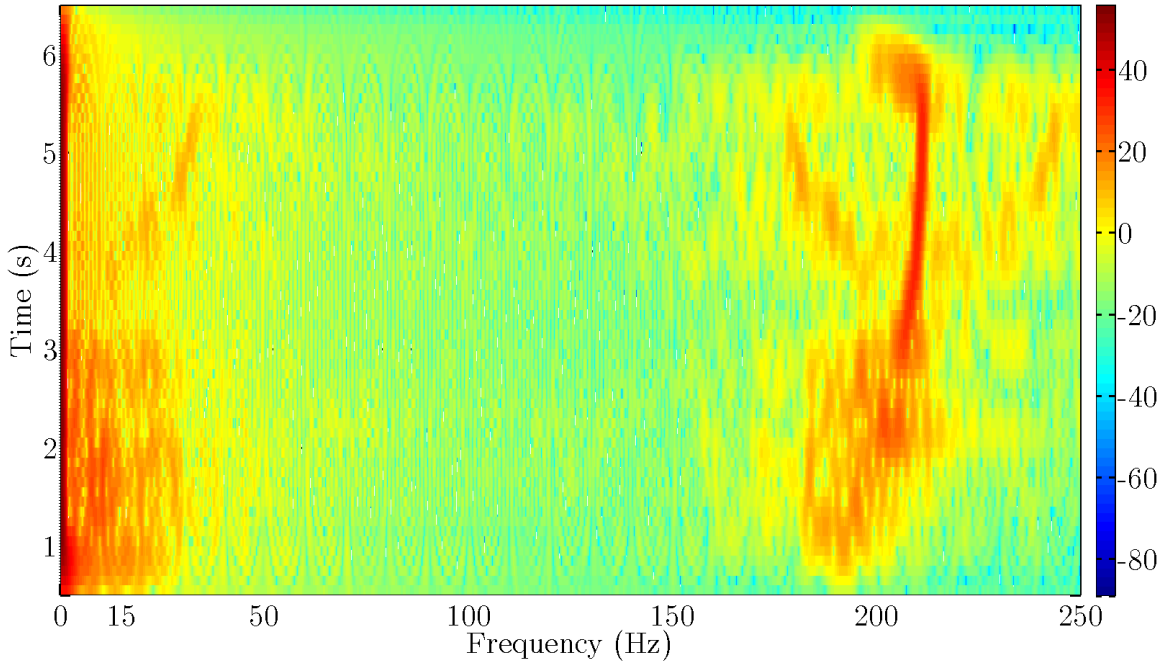


Figure 4.17: Chamber pressure signal frequency content (FFT) for Test E2 plotted over the duration of the burn with  $T_{ox} \approx 13.5^{\circ}\text{C}$  (286.7 K). Color is proportional to the power spectral density of the chamber pressure signal.

#### 4.4.2 Peregrine Test E3-2

Over the course of the Peregrine tests following Test E2, a variety of changes were made to the design, including changes to the internal combustion chamber geometry. The details of these changes will not be discussed here, but Test E3-2 is a good representation of the motor operation after these changes. Based on how this test fits in with the topic and trajectory of this dissertation, the conditions and geometry during this test can be treated as a baseline. To state this explicitly, Test E3-2 consisted of the baseline chamber geometry, and used the baseline oxidizer temperature which will be defined as  $14.5^{\circ}\text{C}$  (287.7 K). This test was also a 5 second developmental burn. Fig. 4.18 shows the pressure time history for Test E3-2, with the zoomed in data shown in Fig. 4.19.

It can be seen from Fig. 4.18 that there were significant improvements in the combustion stability from Test E2 to Test E3-2. However, while the overall character of the two tests looks very different when examined in Fig. 4.18, the zoomed in data actually shows a surprisingly similar character. Again there are low frequency oscillations with high frequency acoustic content superposed. However, the major difference between the tests is the significant reduction in the amplitude of the acoustic instability pressure oscillations, specifically during the first half of the test. The result is a very coherent low frequency, highly sinusoidal response during the first 2 seconds of the test. This can be seen clearly in the spectrogram shown in Fig. 4.20. The 15 Hz signal starts off very strong at approximately 110-120 psi (0.76-0.83 MPa) peak-to-peak amplitude and remains throughout the burn, but becomes less coherent and drifts in frequency during the second half of the test, as the acoustic instability grows on top of it. The acoustic instability can also still be seen clearly in the spectrogram, though the relative amplitude has decreased significantly (actually to levels below that of the low frequency mode in the beginning of the test), and is also less coherent than in Test E2. It was with this data that the Peregrine team was able to diagnose the cause of low frequency instability. Due to its highly regular, sinusoidal nature, comparisons with data in the literature pointed to a phenomenon termed the feed system coupled instability. This mode of combustion instability will be described and discussed in detail in Chapter 5, and its suppression will be the focus of the rest of this dissertation.

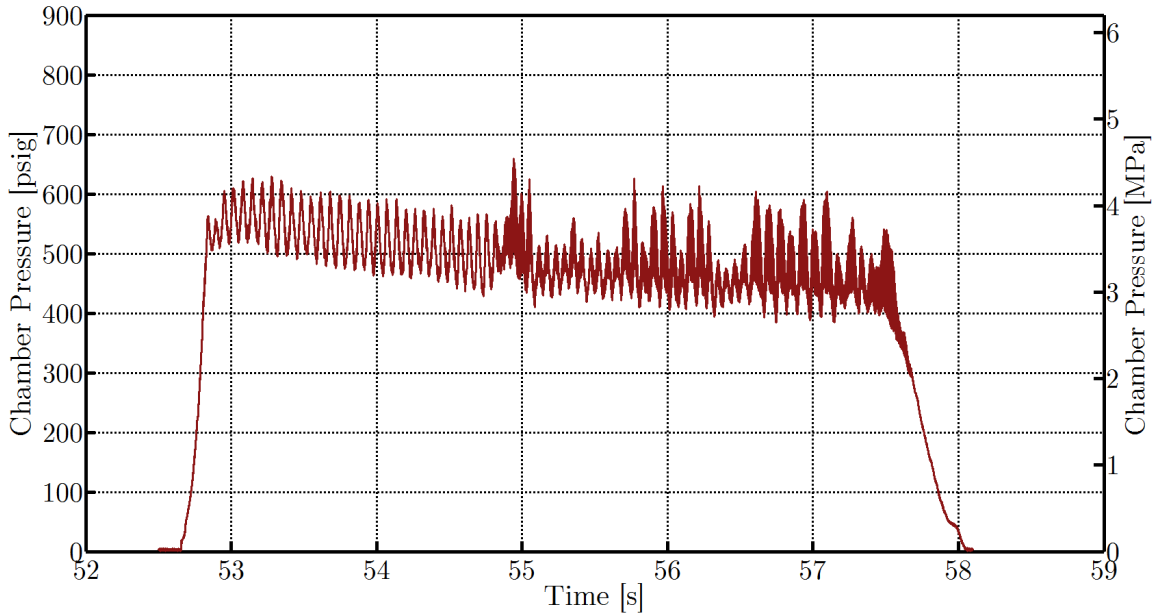


Figure 4.18: Chamber pressure time-history for Test E3-2 in the Peregrine heavyweight combustion tests facility with  $T_{ox} \approx 14.5^\circ C$  (287.7 K).

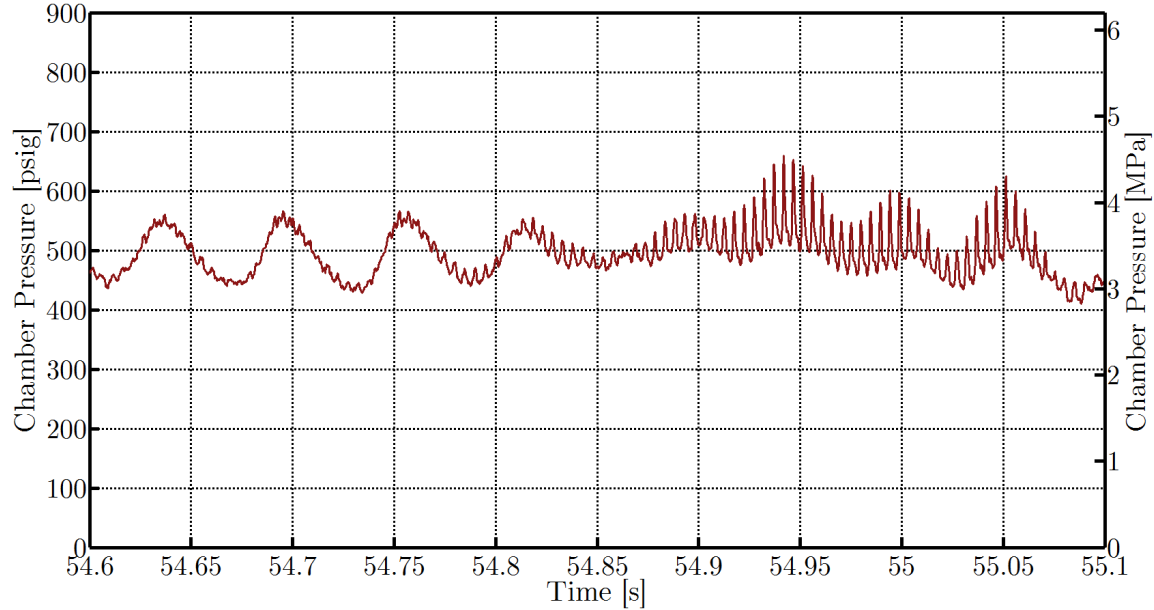


Figure 4.19: Zoomed in chamber pressure time-history for Test E3-2 in the Peregrine heavyweight combustion tests facility with  $T_{ox} \approx 14.5^\circ C$  (287.7 K).

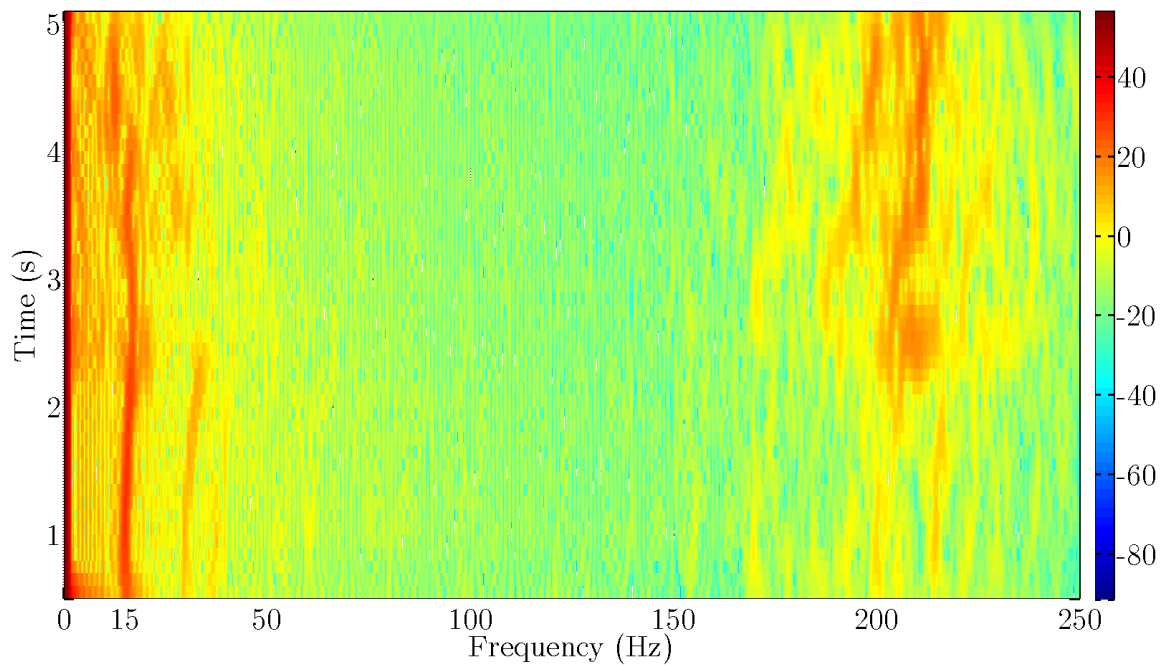


Figure 4.20: Chamber pressure signal frequency content (FFT) for Test E3-2 plotted over the duration of the burn with  $T_{ox} \approx 14.5^{\circ}\text{C}$  (287.7 K). Color is proportional to the power spectral density of the chamber pressure signal.

# Chapter 5

## Feed System Coupled Combustion Instability

Combustion instability is one of the most commonly encountered problems in the development and testing of rocket propulsion systems, including hybrids. Large amplitude chamber pressure and thrust oscillations often accompany combustion instabilities, resulting in increased vibrational loading, possible structural damage, and on rare occasions catastrophic system failure. As alluded to in Chapter 4, progress of the Peregrine Sounding Rocket program has been hampered by combustion instability problems for years. This section will give a brief background into some of the combustion instability modes that are observed in hybrid rockets, with a focus on those instabilities related to the oxidizer feed system. A simple, yet powerful solution to the so called feed system coupled instability is described, and results from a series of Peregrine hot fire tests are presented which verify the effectiveness of this solution.

### 5.1 Classification of Combustion Instabilities

Hybrid rocket instabilities can generally be split into two groups:

- High frequency (acoustic instabilities)
- Low frequency (nonacoustic)

High frequency acoustic instabilities are common in all types of rockets. These instabilities form when there is resonance between energy release from the combustion process and the natural acoustic modes of the combustion chamber internal geometry, or cavity. Combustion chambers can exhibit many natural acoustic modes, often lumped into one of three types: radial, tangential and longitudinal. These designations describe the directional orientation of the pressure waves that form within the chamber, a description of which can be found in Ref. [4]. The 1st longitudinal mode (accompanied by its harmonics the 2nd, 3rd longitudinal modes, etc.) is often observed in hybrid rocket motors, and corresponds to pressure waves set up in the axial direction, between the fore end of the combustion chamber and the nozzle contraction at the aft end. The frequencies of the natural modes can be estimated by Eq. (5.1):

$$f = \frac{a}{l} \quad (5.1)$$

where  $f$  is the frequency of the natural mode,  $a$  is the effective average sound speed of the gas within the chamber, and  $l$  is the wavelength of the natural mode, which depends on the chamber geometry. Longitudinal modes generally set up as a half-wave, meaning the wavelength is generally twice the axial length of the internal combustion chamber cavity [57]. Informally, the delineation between the high frequency and low frequency combustion instabilities is located at approximately the frequency of the first longitudinal acoustic mode. A variety of methods for the damping of acoustic instabilities have been extensively studied in both the liquid and solid rocket industries, such as Helmholtz resonating cavities in liquid rockets, and the addition of solid particulate to the flow field in solid rockets [58]. Therefore, acoustic instabilities are not a focus of this work, but will be addressed again briefly in Section 5.4.

Two different nonacoustic low frequency instabilities are often observed in hybrid rockets and receive the most attention. The first of these oscillatory behaviors is intrinsic to the interactions between turbulent boundary layer combustion and chamber fluid dynamic behavior. A detailed description of the intrinsic low frequency hybrid

rocket instability is provided by Karabeyoglu et al. and is accompanied by the development of a model capable of predicting its frequency [59]. The second common low frequency response is known as feed system coupled instability and will be the focus of the rest of this chapter due to its inherent relevance to the topic of injectors.

## 5.2 Feed System Coupled Instability Theory and Modeling

Feed system coupled instabilities have been studied extensively in the liquid rocket industry, and have been successfully modeled for a range of engine designs and operating conditions [60]. These instabilities are typically characterized by highly regular, sinusoidal pressure oscillations which are caused by hydrodynamic communication between the combustion chamber and feed system, predominantly observed in systems utilizing liquid oxidizer. Work by Karabeyoglu et al. provides an overview of the feed coupled instability as it pertains to hybrid rockets, and describes a model for predicting its transient behavior [61]. As described in the aforementioned work, the mechanisms that contribute to feed system coupling are:

- Combustion and/or vaporization delay
- Oxidizer flow rate that is dependent on chamber pressure
- Compressibility of fluid in the feed system

The following section will give an abbreviated presentation of Karabeyoglu's model, and while this model will not be used explicitly to find a solution to the feed system coupled instability, it is included to provide the reader with a working knowledge of the physics governing this type of transient behavior. A few results from Karabeyoglu's work will be replicated, along with the presentation of some additional model output and discussion of the resulting phenomena.

### 5.2.1 Transient Physical Model

In developing the following transient model, Karabeyoglu et al. sought to account for the influence of different components of the feed system. In order to achieve this, physics based models for the individual system components were developed and then integrated in order to determine the overall system dynamic response. Specifically, the hybrid rocket components that were modeled are the injector, the feed system pipe which delivers the oxidizer to the injector, and the combustion chamber itself. In the following section, some of the important dynamic equations for these models will be presented. More details on the development of these models can be found in Ref. [61].

#### 5.2.1.1 Injector Model

For steady flow, the commonly used expression to calculate mass flow rate through an injector element can be found in Eq. (2.17). However, in the process of developing transient models, the steady flow assumptions are invalid. Instead, a quasi 1-D dynamic equation for the injector can be presented as shown in Eq. (5.2):

$$L_i \frac{d\dot{m}_i}{dt} = (P_1 - P_2)A_2 - \frac{1}{2A_2\rho_l C_d^2} \dot{m}_i^2 \quad (5.2)$$

where  $L_i$  is the length of the injector,  $\dot{m}_i$  is the mass flow rate through the injector, and  $C_d$  is the same version of the discharge coefficient as shown in Eq. (2.17). In fact it can easily be shown that this dynamic equation reduces to Eq. (2.17), when the assumption of steady flow is reintroduced. It should be mentioned that this equation is not only for single injector orifices, but can also be used for a plurality of holes by using the total area and flow rate of the group. Fig. 5.1 shows the conceptual injector hole and the important flow parameters for this model.

Eq. (5.2) is linearized and normalized, resulting in the simplified dynamic equation shown in Eq. (5.3):

$$R_i \frac{d\hat{\dot{m}}_i}{d\hat{t}} = \hat{P}_1 - \hat{P}_2 - 2\hat{\dot{m}}_i \quad (5.3)$$

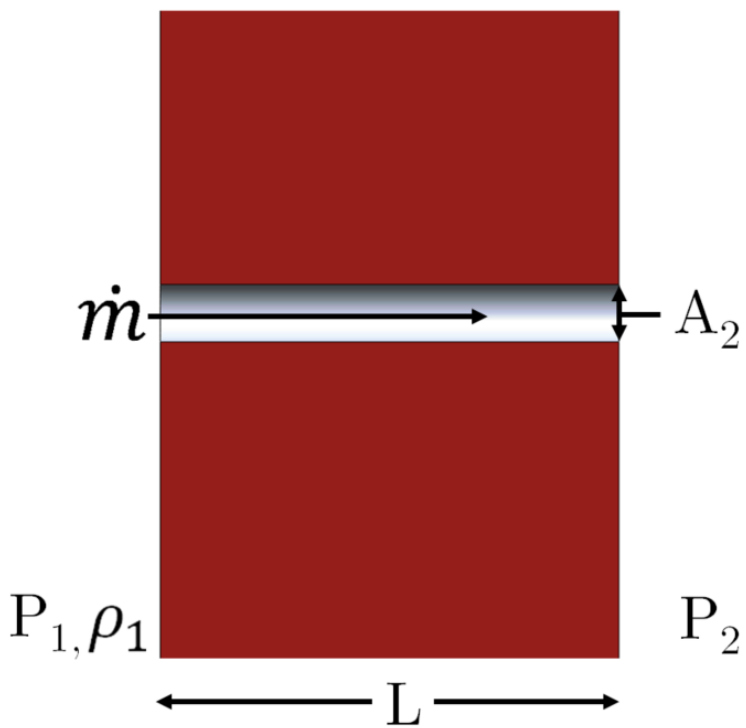


Figure 5.1: Schematic for injector hole used in transient analysis.

where the following non-dimensional variables have been introduced:

$$R_i \equiv \frac{\tau_i}{\tau_c} \quad (5.4)$$

$$\hat{t} \equiv \frac{t}{\tau_c} \quad (5.5)$$

$$\hat{\dot{m}}_i \equiv \frac{\tilde{\dot{m}}_i}{\bar{\dot{m}}_c} \quad (5.6)$$

$$\hat{P}_1 \equiv \frac{\tilde{P}_1}{\bar{P}_1 - \bar{P}_2} \quad (5.7)$$

$$\hat{P}_2 \equiv \frac{\tilde{P}_2}{\bar{P}_1 - \bar{P}_2} \quad (5.8)$$

Additionally the characteristic time of the injector as can be defined as:

$$\tau_i \equiv \frac{C_d L_i}{\sqrt{2(\bar{P}_1 - \bar{P}_2)/\rho_l}} \quad (5.9)$$

where  $\tau$  is a characteristic time, the  $\hat{\cdot}$  superscript signifies normalized variables, the over bar signifies mean value, and the  $\tilde{\cdot}$  denotes perturbation variables from the linearization process. Physically, the characteristic time of the injector  $\tau_i$  relates to the time a fluid element takes to travel the length of the injector hole (the denominator essentially describing the fluid velocity within the injector). It should be noted that the time and characteristic time variables have been normalized by the combustion chamber characteristic time  $\tau_c$ , which will be defined in Section 5.2.1.3 [61].

### 5.2.1.2 Pipe Model

The next component that was modeled by Karabeyoglu et al. is the feed system piping which delivers the oxidizer from the storage tank to the injector. For this analysis, the pipe is modeled by a simple volume of length  $L_p$  and area  $A_p$  through which the oxidizer flows, connecting the oxidizer tank at pressure  $P_{ox}$  to the injector. A simple sketch of the pipe with labeled parameters is included in Fig. 5.2. The

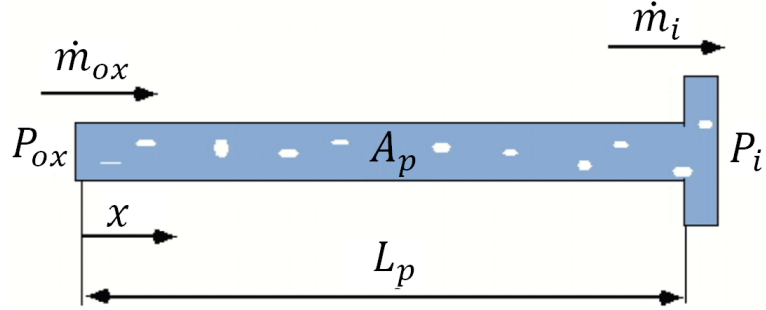


Figure 5.2: Schematic for the feed system pipe used in transient analysis (adapted from Ref. [61] with permission)

pipe is modeled in a quasi 1-D fashion, similar to that of the injector, and two-phase, compressible flow is allowed for [61].

Following a similar approach as for the injector, the linearized and normalized dynamic equations that result for the pipe are shown below:

$$R_p \left( \frac{d\hat{P}_{ox}}{dt} + \frac{d\hat{P}_1}{dt} \right) = \hat{m}_{ox} - \hat{m}_i \quad (5.10)$$

$$\frac{d\hat{m}_{ox}}{dt} + \frac{d\hat{m}_i}{dt} - \alpha_1 \left( \frac{d\hat{P}_{ox}}{dt} + \frac{d\hat{P}_1}{dt} \right) = \alpha_2 (\hat{P}_1 - \hat{P}_{ox}) + \alpha_3 (\hat{m}_{ox} - \hat{m}_i) \quad (5.11)$$

where the following non-dimensional values are defined as:

$$R_p \equiv \frac{\tau_p}{\tau_c} \quad (5.12)$$

$$\hat{P}_{ox} \equiv \frac{\tilde{P}_{ox}}{\bar{P}_1 - \bar{P}_2} \quad (5.13)$$

$$\alpha_1 \equiv 4C_d^2 \frac{A_2}{A_p} \frac{L_i}{L_p} \frac{R_p}{R_i} \quad (5.14)$$

$$\alpha_2 \equiv 2 \frac{A_p}{A_2} \frac{L_i}{L_p} \frac{1}{R_i} \left[ 1 + \frac{\bar{\rho}}{\rho} \bar{y} + 8\lambda C_d^3 \left( \frac{A_2}{A_p} \right)^3 \frac{L_i}{L_p} \frac{R_p}{R_i} \right] \quad (5.15)$$

$$\alpha_3 \equiv 4\lambda C_d^2 \frac{A_2}{A_p} \frac{L_i}{L_p} \frac{1}{R_i} \quad (5.16)$$

where:

$$\lambda \equiv 1 + \frac{C_p L_p}{2 A_p} C_{fp} \quad (5.17)$$

The characteristic time for the pipe can be defined as:

$$\tau_p \equiv K \frac{V_p \rho_g}{\dot{m}_i} \frac{(\bar{P}_1 - \bar{P}_2)}{2 \bar{P}_1} \quad (5.18)$$

where:

$$K \equiv \frac{\left[ \bar{y}/\gamma_{ox} + \beta_s \bar{P}(\rho_g/\rho_l) - \bar{P}(\partial \bar{y}/\partial \bar{P})_s \right]}{\left[ \bar{y} + \rho_g/\rho_l \right]^2} \quad (5.19)$$

In the above definitions,  $C_p$  is the circumference of the pipe,  $C_{fp}$  is the skin friction coefficient for the pipe,  $V_p$  is the volume of the pipe,  $\bar{y}$  is the vapor mass fraction in the pipe,  $\gamma_{ox}$  is the ratio of specific heat for the oxidizer vapor,  $\beta_s$  is the compressibility of the liquid, and  $\bar{P}$  is the average pressure in the pipe. The factor  $K$  is termed the compressibility parameter of the feed system, and it is the sum of three terms which account for the compressibility of the gas, the compressibility of the liquid, and the rate of shift of mass between the vapor and liquid phases with respect to changing pressure. The  $(\partial \bar{y}/\partial \bar{P})_s$  term indicates that this shift between phases is evaluated along a line of constant entropy. It should be noted that in hybrid rockets, gas formation in the feed system pipe can certainly occur, through either cavitation (likely with high vapor pressure oxidizers), local boiling (of cryogens), and desorption of pressurant gas [61].

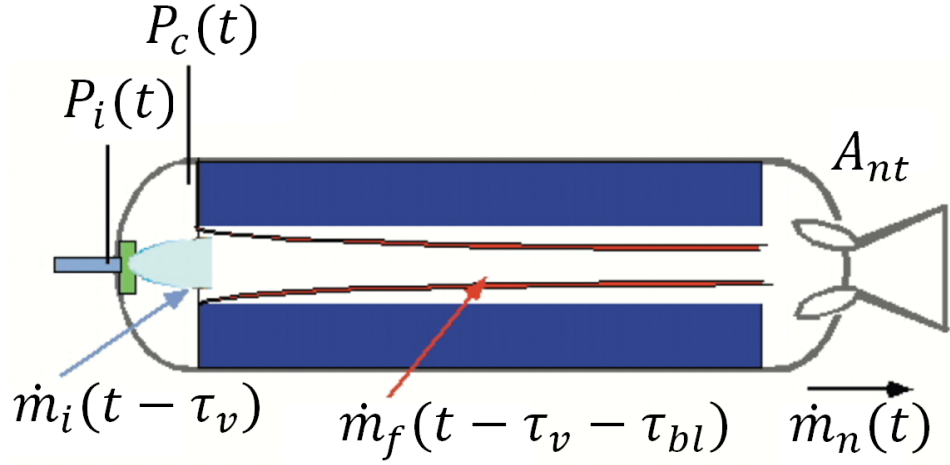


Figure 5.3: Schematic for the hybrid rocket combustion chamber used in transient analysis (adapted from Ref. [61] with permission).

### 5.2.1.3 Combustion Chamber Model

A simplified version of a full “Thermal Combustion Gas Dynamic” coupled theory from another of Karabeyoglu’s works (Ref. [59]) is used for the model of the combustion chamber. The resulting linearized and normalized dynamic equation is shown in Eq. (5.20), with a schematic of the combustion chamber included in Fig. 5.3.

$$\frac{d\hat{P}_2}{d\hat{t}} = \theta_1 [\hat{P}_1 (\hat{t} - R_v) - \hat{P}_2 (\hat{t} - R_v)] - \theta_2 [\hat{P}_1 (\hat{t} - R_v - R_{bl}) - \hat{P}_2 (\hat{t} - R_v - R_{bl})] - \hat{P}_2(\hat{t}) \quad (5.20)$$

More non-dimensional variables are defined as:

$$R_v \equiv \frac{\tau_v}{\tau_c} \quad (5.21)$$

$$R_{bl} \equiv \frac{\tau_{bl}}{\tau_c} \quad (5.22)$$

$$\theta_0 \equiv \frac{1}{2} \frac{\bar{P}_2}{\bar{P}_1 - \bar{P}_2} \quad (5.23)$$

$$\theta_1 \equiv \frac{O/F}{O/F + 1} \theta_0 \quad (5.24)$$

$$\theta_2 \equiv n \frac{O/F}{O/F + 1} \theta_0 \quad (5.25)$$

The characteristic filling/emptying time of the combustion chamber, as mentioned in the preceding sections is defined as:

$$\tau_c \equiv \frac{f_c(\gamma)}{C_{dn}} \frac{RT_c}{RT_{ave}} \frac{L^*}{c^*} \quad (5.26)$$

where:

$$L^* \equiv \frac{V_c}{A_{nt}} \quad (5.27)$$

$$f_c(\gamma) \equiv \frac{\eta_c}{\gamma} \left( \frac{\gamma + 1}{2} \right)^{(\gamma+1)/(\gamma-1)} \quad (5.28)$$

In the above dynamic equation and defined variables,  $\tau_v$  is the characteristic vaporization delay time,  $\tau_{bl}$  is the characteristic boundary layer delay time,  $O/F$  signifies the motor operating oxidizer to fuel ratio by mass,  $C_{dn}$  is the discharge coefficient of the chamber nozzle,  $c^*$  is the characteristic exhaust velocity of the motor,  $V_c$  is the volume of the combustion chamber,  $A_{nt}$  is the nozzle throat area, and  $\eta_c$  is the combustion efficiency of the motor [61].

### 5.2.2 Mathematical Solution

Now that physical models of each of the components in the dynamic system have been presented, the result is a system of linear ordinary differential equations (ODE's) which consist of Eqns. (5.3), (5.10), (5.11), and (5.20). The goal of this analysis is to end up with a transfer function which relates the chamber pressure to some control parameter such as the oxidizer tank pressure or the oxidizer mass flow rate. The development of this transfer function would allow for the prediction of the system stability with relation to the feed system coupled mode.

### 5.2.2.1 Transfer Function Formalism

In order to obtain the system response transfer function, the Laplace transform is utilized in order to cast the system of ODE's into the frequency or  $s$ -domain. In order to perform this transformation, the following Laplace transformation variables are introduced in Eq. (5.29) through Eq. (5.33):

$$\Pi_{ox} \equiv L [\hat{P}_{ox}] \quad (5.29)$$

$$\Pi_1 \equiv L [\hat{P}_1] \quad (5.30)$$

$$\Pi_2 \equiv L [\hat{P}_2] \quad (5.31)$$

$$M_{ox} \equiv L [\hat{m}_{ox}] \quad (5.32)$$

$$M_i \equiv L [\hat{m}_i] \quad (5.33)$$

Karabeyoglu notes that for most practical cases  $\alpha_1 \ll 1$  and  $\alpha_3 \ll 1$ , and can be neglected in this analysis [61]. The resulting set of algebraic equations after the Laplace transform are shown in Eq. (5.34) through Eq. (5.37):

*Injector:*

$$R_i s = \Pi_1 - \Pi_2 - 2M_i \quad (5.34)$$

*Pipe:*

$$R_p s (\Pi_{ox} - \Pi_1) = M_{ox} - M_i \quad (5.35)$$

$$s (M_{ox} - M_i) = \alpha_2 (\Pi_{ox} - \Pi_1) \quad (5.36)$$

*Combustion Chamber:*

$$(s + 1)\Pi_2 = (\Pi_1 - \Pi_2) F_d(s) \quad (5.37)$$

where:

$$F_d(s) = \theta_1 e^{-R_v s} + \theta_2 e^{-(R_v + R_{bl})s} \quad (5.38)$$

What is left is a set of 4 equations and 5 unknowns, thus one variable must be chosen to be a freely selected input. One final simplification can be made due to the fact that for most systems, the injector time scale is small compared to the time scales of the other components. Therefore, for the rest of this analysis  $R_i$  will be assumed to equal to 0. As suggested by Karabeyoglu et al., two sample feed system setups can be specified in order to arrive at the final transfer function which are described below [61].

#### *No Flow Isolation Elements in the Feed System*

The first case will consider feed systems which include no mechanism to fix the mass flow rate through the system. Therefore, the oxidizer tank pressure is the only control variable, and it is desired to develop a transfer function that relates the combustion chamber pressure to the oxidizer tank pressure. As shown by Karabeyoglu et al., Eq. (5.34) through Eq. (5.37) are used to arrive at the desired transfer function which is shown in Eq. (5.39) [61]:

$$\frac{\Pi_2}{\Pi_{ox}} = \frac{F_d(\alpha_2 - R_p s^2)}{(R_p s^2 + s + \alpha_2)(s + 1) + F_d(R_p s^2 + \alpha_2)} \quad (5.39)$$

#### *Flow Isolation Element Installed*

The second case utilizes a flow control element in order to fix or control the oxidizer flow rate that flows through the feed system. The most commonly used flow control element is the cavitating venturi, the details of which are described later in Section 5.3.1.1. Instead of the oxidizer tank pressure, the mass flow rate is now the control

variable, and a transfer function relating the chamber pressure to the mass flow rate is of interest. Again Eq. (5.34) through Eq. (5.37) can be solved accordingly, with the resulting transfer function shown in Eq. (5.40) [61].

$$\frac{\Pi_2}{M_{ox}} = \frac{F_d(\alpha_2 - R_p s^2)}{(R_p s^2 + 4\alpha_2 R_p s + \alpha_2)(s + 1) + 4\alpha_2 R_p s F_d} \quad (5.40)$$

These are the transfer functions developed by Karabeyoglu et al., and they can be used to model feed coupled instabilities for any hybrid rocket utilizing liquid oxidizer (or liquid fuel in the case of the reverse hybrid). The next sections will replicate some of the resulting model output as presented by Karabeyoglu et al. for the same sample hybrid rocket system analyzed in their work. A few additions to these results will be included beyond what was presented in their analysis.

### 5.2.2.2 Example Case with No Feed System Isolation

A small paraffin fueled hybrid rocket which was experimentally tested will be studied for this example. The system used nitrous oxide as the oxidizer and experimental data from testing of this rocket is included in Ref. [61]. No isolation elements were utilized in this setup. The reason this rocket test is used as an example is that it exhibited severe feed coupled instability, and the design and operation parameters of the system were well understood. Karabeyoglu et al. do not include the parameters explicitly, but the important modeling parameters in the transfer functions above are estimated:

$$\tau_c = 0.0033 \text{ sec} \quad R_i = 0.00 \quad R_p = 0.88$$

$$\theta_1 = 3.33 \quad \theta_2 = 0.33 \quad \alpha_2 = 0.17$$

The frequency of the feed coupled mode during these experiments was approximately 60 Hz. As it can be determined from the above equations and known parameters, the only free parameter that is left is the non-dimensional characteristic time of vaporization delay,  $R_v$ . Recalling from Section 5.2.2.1, there were 4 equations

and 5 unknowns in the linear system, so one variable is to be used as an input. However, instead the vaporization delay ratio was chosen so that the output instability frequency from the model matched that of the experiment. It is for this reason that Karabeyoglu et al. chose a value of  $R_v = 2.5$  [61].

In order to examine the overall system response, the transfer function can be plotted in the s-domain. Karabeyoglu et al. actually suggest plotting in the  $s_d$  domain, which is based on normalization by the combustion chamber emptying/filling characteristic time delay as defined in Eq. (5.41).

$$s_d = \frac{s}{\tau_c} = \sigma + 2\pi f i \quad (5.41)$$

Accordingly, the magnitude of the transfer function can be plotted as a surface or contour plot versus the dimensional frequency and amplification. This was done for the example case and the resulting surface plot of the transfer function is shown in Fig. 5.4. Each of the peaks in the surface plot show the numerical instability modes associated with the feed coupled instability. The two peaks with the greatest amplification shown in Fig. 5.4 (which happen to also be the tallest peaks) correspond to the feed coupled instability fundamental mode demonstrated in the actual hot fire testing from Ref. [61]. It is useful to observe this model output in the frequency and amplification plane as well, which can be achieved in the form of a contour plot, which is included in Fig. 5.5. From this orientation, it is easy to see that the only peaks in the positive half of the amplification axis (corresponding to unstable operation) exists at 60 Hz. Again,  $R_v$  was essentially used as a fitting parameter in order to assure this outcome.

In order to evaluate the influence of different system parameters on the feed coupled instability, the parameter values can be adjusted, and the translation of the aforementioned transfer function peak corresponding to the fundamental mode can be tracked. This type of analysis was performed in order to study the effect of changes in the value of  $\theta_0$  and  $R_p$  while keeping the rest of the parameters at their nominal values as stated above. The model output for this analysis is shown

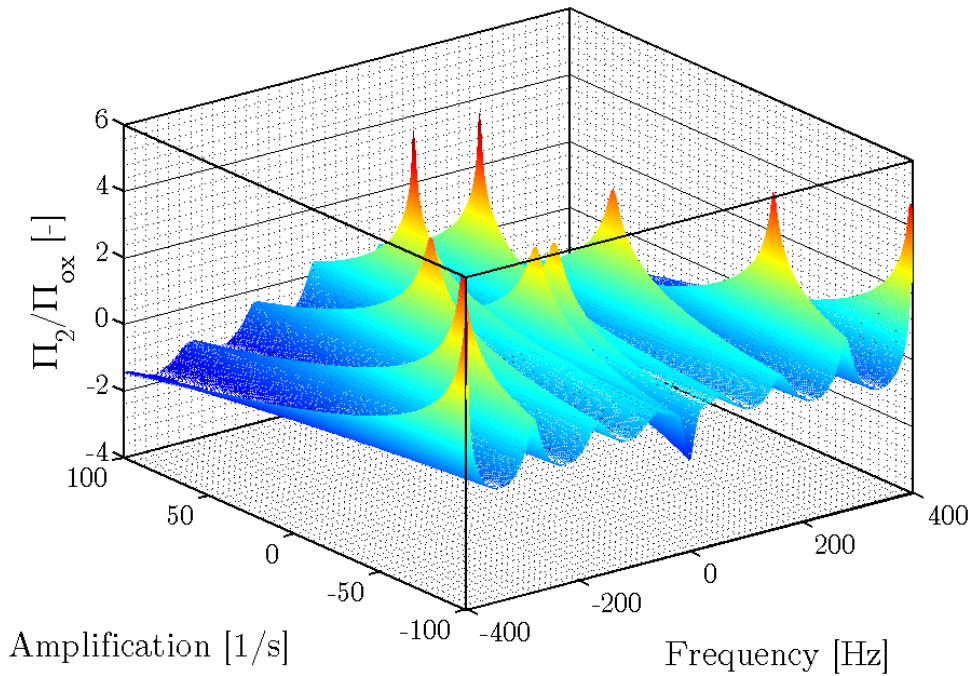


Figure 5.4: Surface plot of the transfer function for the nitrous oxide/paraffin example case with no isolation element.

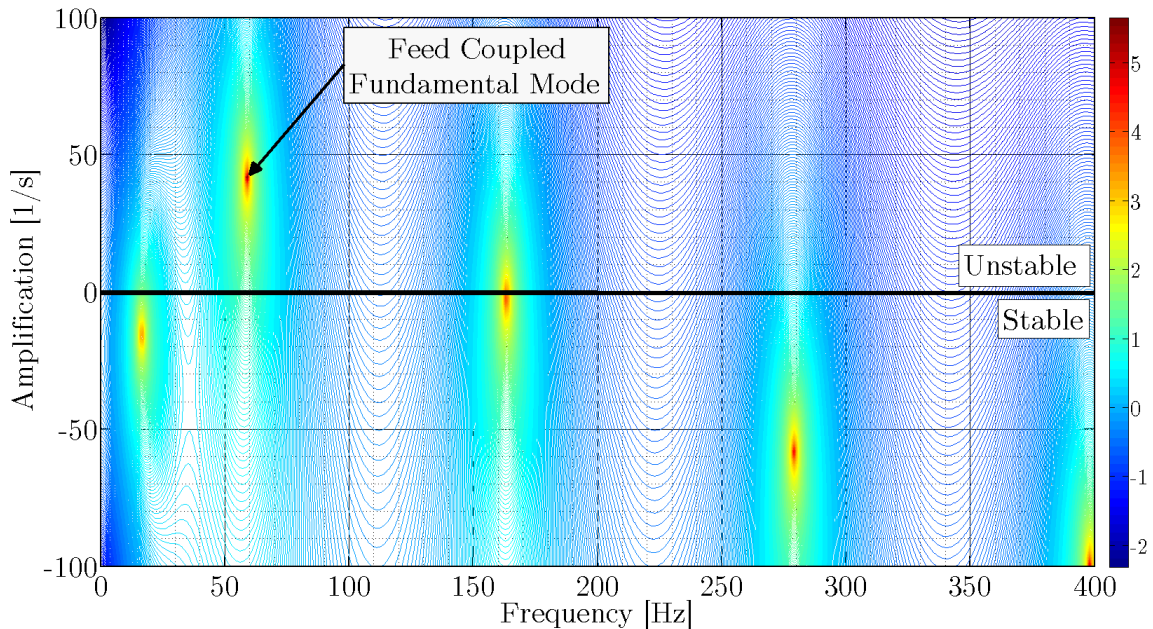


Figure 5.5: Contour plot of the transfer function for the nitrous oxide/paraffin example case with no isolation element.

in Fig. 5.6 and Fig. 5.7, which plot the amplification and frequency vs.  $\theta_0$  and  $R_p$  respectively. It can easily be seen from Fig. 5.6 that decreasing the value of  $\theta_0$  universally acts to decrease the amplification, pushing the motor towards stable operation.  $\theta_0$  is essentially a measure of the pressure drop across the injector, suggesting that increased injector pressure drop has a stabilizing effect. It can also be seen from Fig. 5.6, that decreasing  $R_p$  also decreases the amplification and drives the system towards stable operation.  $R_p$  is a measure of the time delay associated with the pipe dynamics, therefore a pipe that responds faster to changes in pressure (e.g. one with incompressible flow throughout) would promote stable operation. Fig. 5.7 shows the effect that changing the same two parameters has on the frequency of the oscillations. It is clear that changes in the value of  $\theta_0$  have little effect on the feed coupled instability frequency, but changes in  $R_p$  can affect the frequency to a significant degree.

This same type of analysis can be performed by varying  $R_v$  instead of  $R_p$ , with some interesting, and not necessarily intuitive results. As expected, decreasing the value of  $\theta_0$  has a stabilizing effect for all values of  $R_v$ . The interesting results relate to the behavior as  $R_v$  is changed. Specifically, at low values of  $R_v$ , meaning fast vaporization of the oxidizer, a decrease in vaporization rates (thus an increase in the value of  $R_v$ ) results in a destabilizing effect, which is to be expected and has been observed experimentally. However, past a certain point, the model shows that as  $R_v$  increases and vaporization times get longer, the response starts to have a slight stabilizing effect. Karabeyoglu et al. point out that this has not been validated experimentally [61]. As is expected, the frequency of the system response is rather sensitive to the vaporization delay, as shown in Fig. 5.9. It is clear to see that as vaporization times get longer, the frequency of the feed system coupled instability normal mode decreases.

### 5.2.2.3 Example Case with Feed System Isolation

The same analysis as presented above can be repeated for a system in which an isolating element is installed. For this analysis, none of the design parameters of the

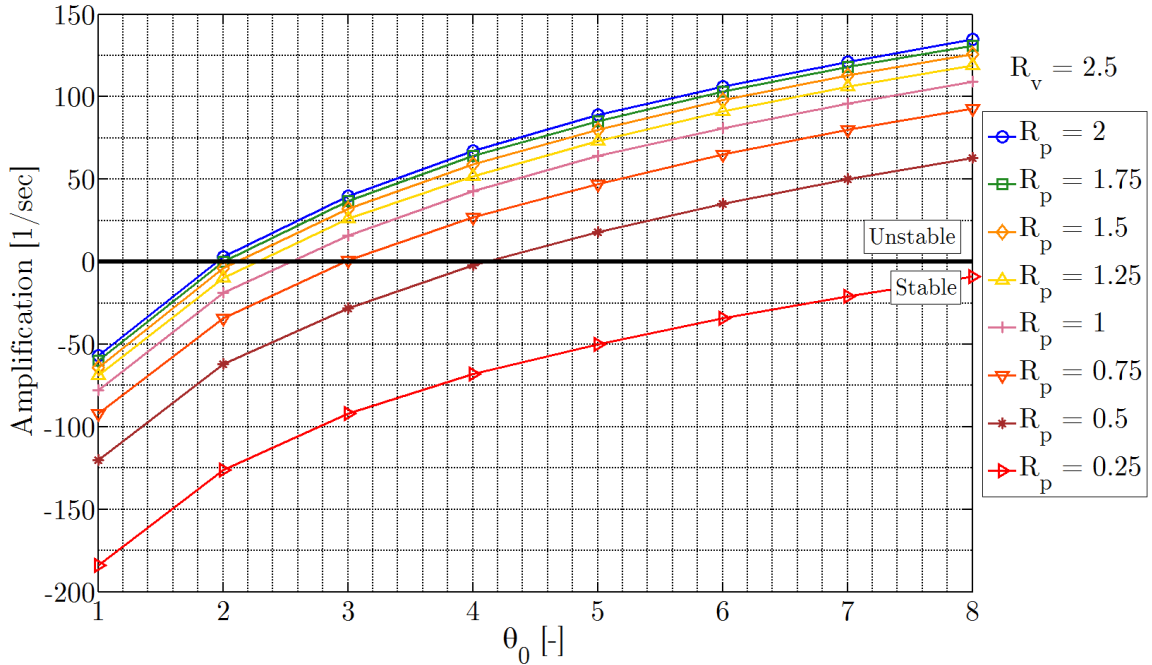


Figure 5.6: Feed coupled response amplification vs.  $\theta_o$  over a range of  $R_p$  values for the example case with no feed system isolation element.

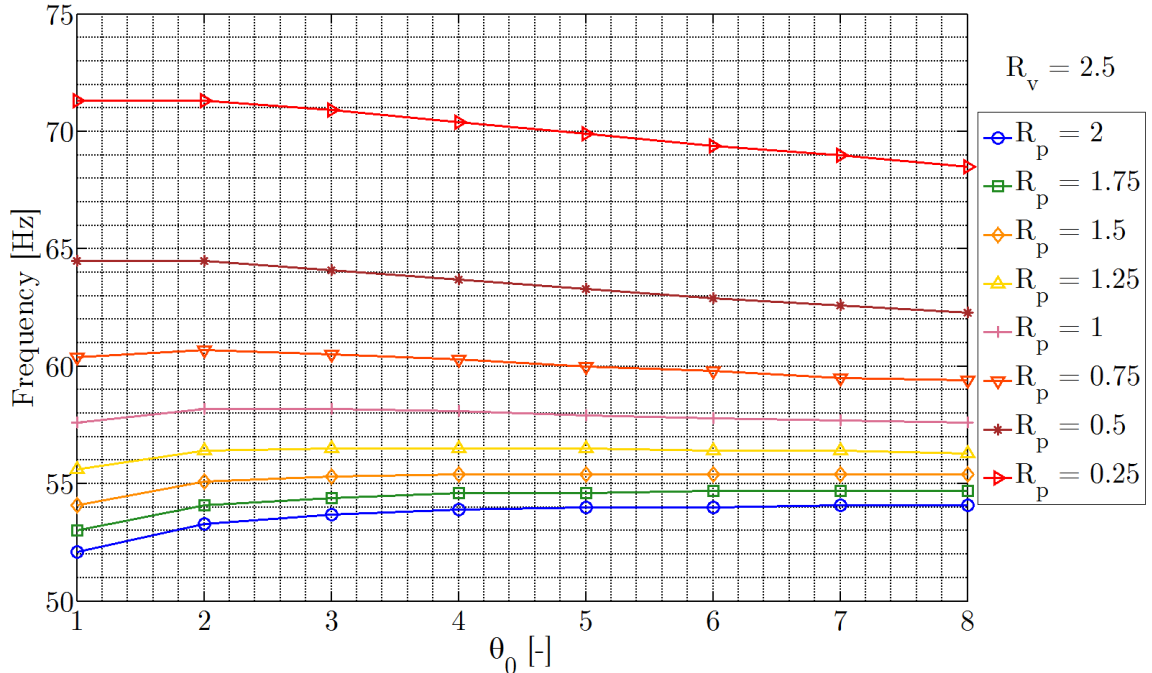


Figure 5.7: Feed coupled response frequency vs.  $\theta_o$  over a range of  $R_p$  values for the example case with no feed system isolation element.

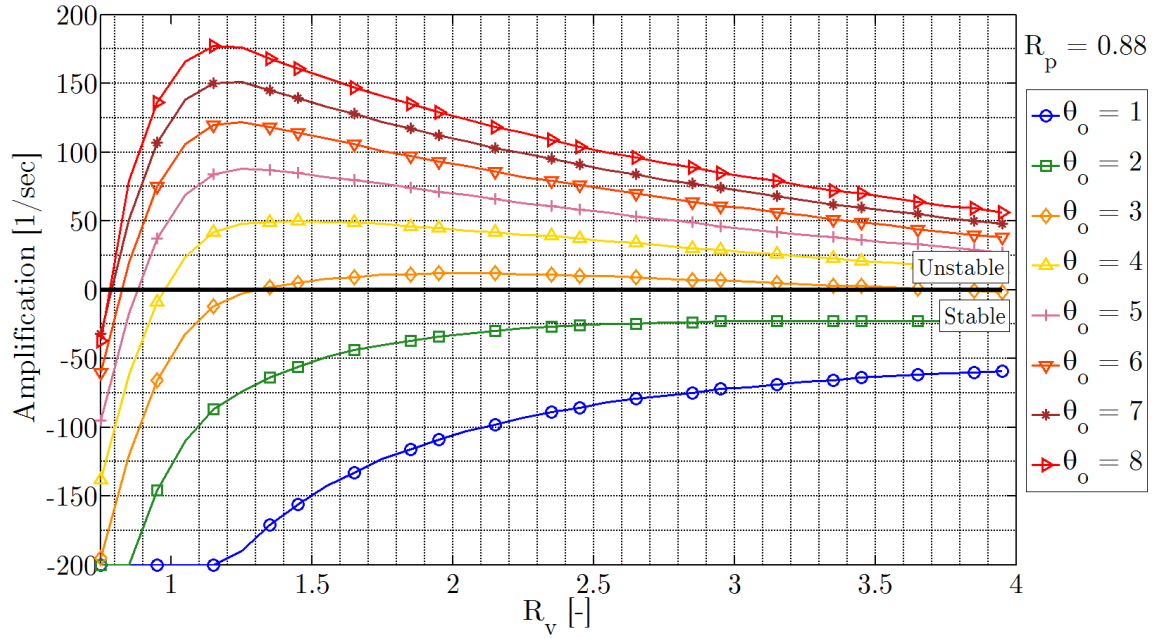


Figure 5.8: Feed coupled response amplification vs.  $R_v$  over a range of  $\theta_o$  values for the example case with no feed system isolation element.

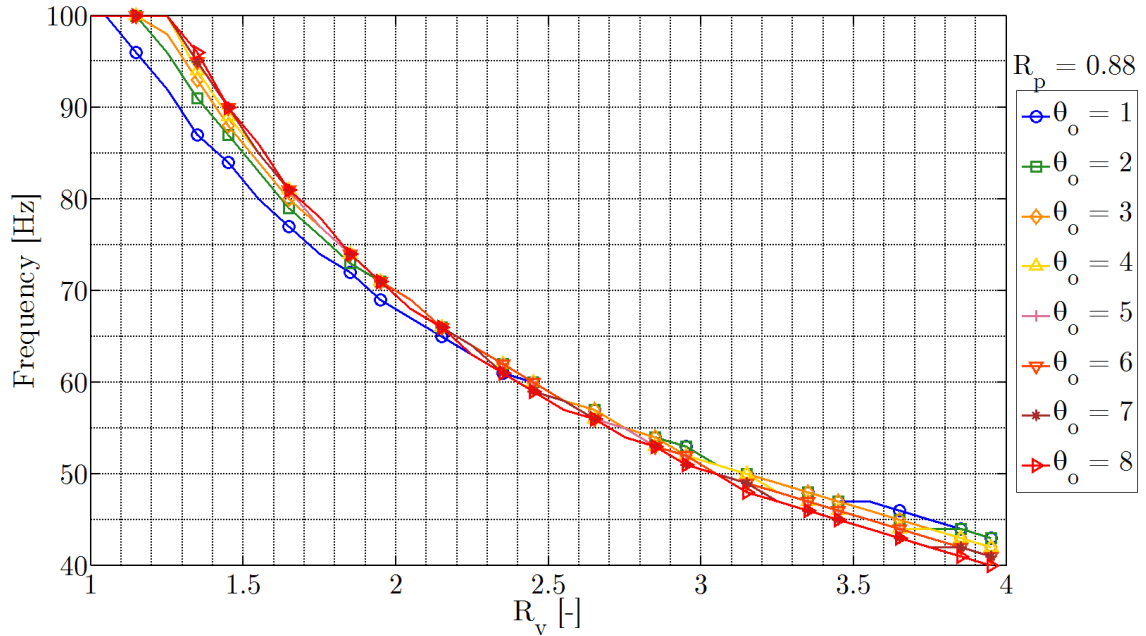


Figure 5.9: Feed coupled response frequency vs.  $R_v$  over a range of  $\theta_o$  values for the example case with no feed system isolation element.

example hybrid will be changed, but the transfer function developed for the isolated case will be used. In reality, the addition of the feed system isolating element may have an effect on the rocket parameters (such as  $R_p$  or  $\alpha_2$ ), however these effects are not obvious based on this analysis and will not be included.

First, the surface and contour plots of the transfer function were calculated and are included in Fig. 5.10 and Fig. 5.11. While it can be seen that most of the peaks have shifted off of the visible axis toward the stable region, the fundamental mode itself is still in the region of positive amplification (and thus unstable operation). This result indicates that even with the inclusion of an isolating element in the feed system, stable operation is not guaranteed.

Additional results supporting this fact are shown in Fig. 5.12 and Fig. 5.13. In fact, these results seem to suggest that the inclusion of a feed system isolating element can be detrimental to the stability of this system. Fig. 5.12 shows that now, even if  $R_p$  is decreased, no stabilizing effect is achieved. While decreasing the value of  $\theta_0$  is still beneficial, only at the lowest of  $\theta_0$  values is the system predicted to run in a stable fashion. Fig. 5.14 shows similar detrimental effects of the isolating element.

However, Karabeyoglu et al. suggest that with the inclusion of the isolating element, the effectiveness of changing some of the other design parameters can be increased. For example, Karabeyoglu et al. claim that when an isolating element is installed in the feed system, if only one of the pipe dynamics parameters is sufficiently improved (either  $R_p$  or  $\alpha_2$ ), then stable operation can be assured [61]. This idea was studied using the feed coupled instability model by setting the pipe dynamics delay time parameter  $R_p = 0$  for the isolated case, which corresponds to an infinitely fast responding pipe. The resulting surface plot of the applicable transfer function is shown in Fig. 5.16. It can be seen for this case that only one pole exists (on the 0 Hz axis in the frequency domain) and that its amplification is much less than 0. For this transfer function, stable operation should indeed be assured.

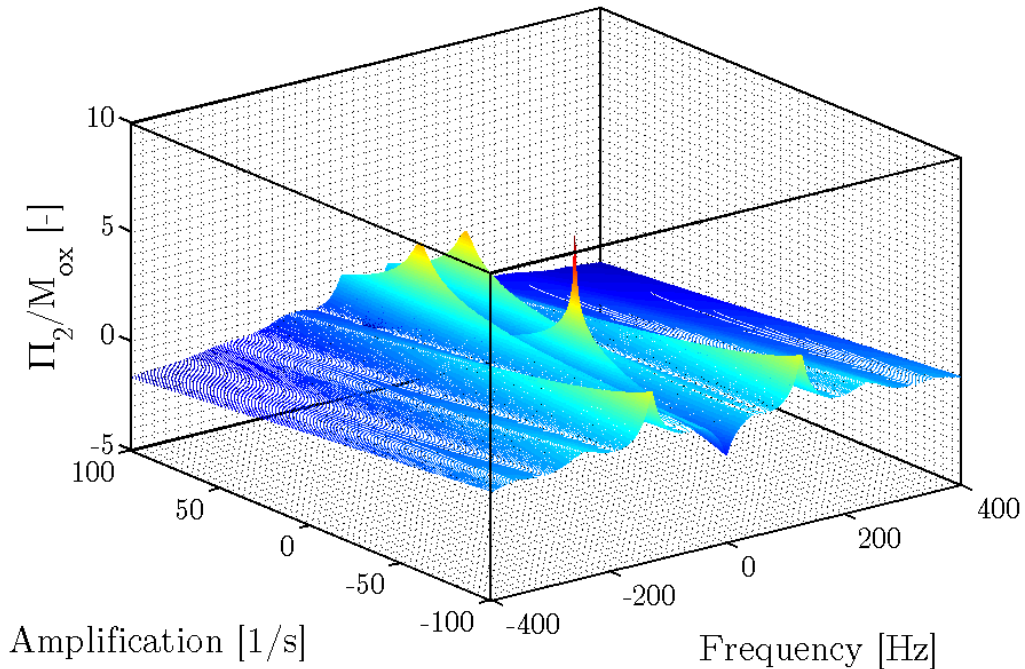


Figure 5.10: Surface plot of the transfer function for the nitrous oxide/paraffin example case with an isolating element installed.

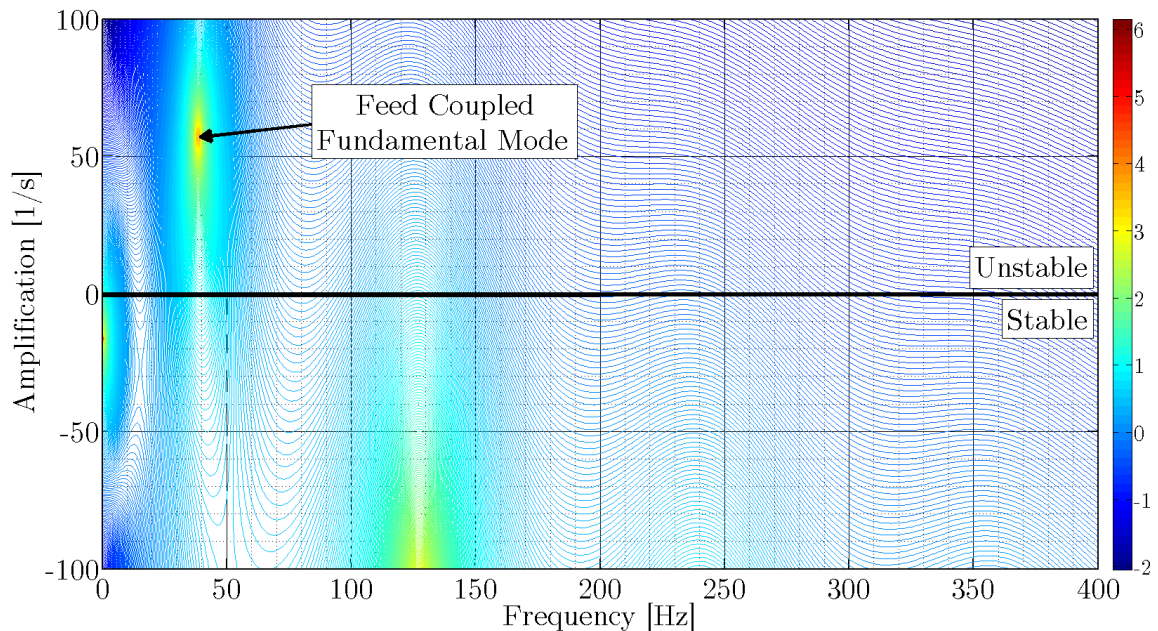


Figure 5.11: Contour plot of the transfer function for the nitrous oxide/paraffin example case with an isolating element installed.

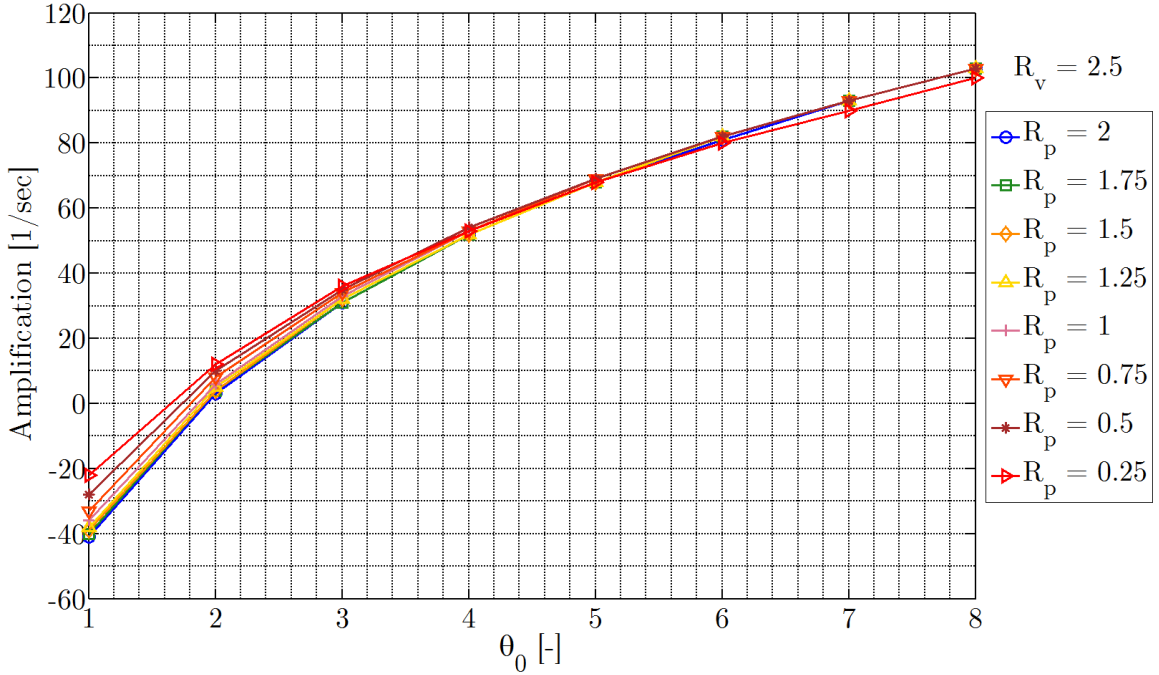


Figure 5.12: Feed coupled response amplification vs.  $\theta_o$  over a range of  $R_p$  values for the example case with feed system isolating element installed.

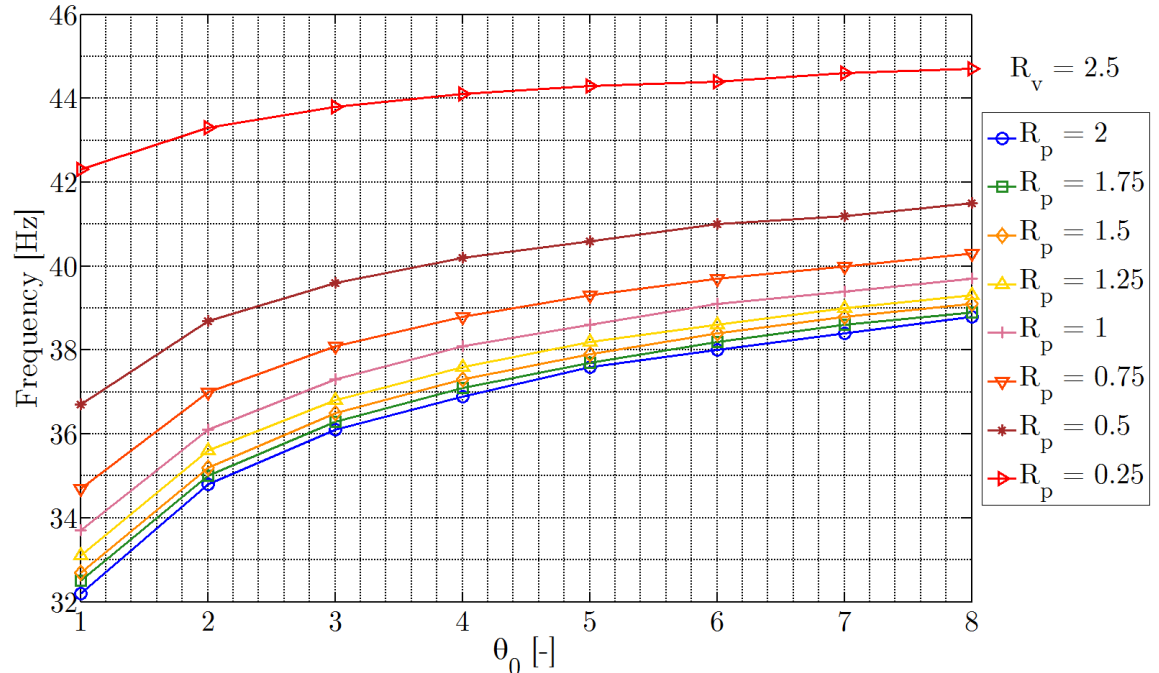


Figure 5.13: Feed coupled response frequency vs.  $\theta_o$  over a range of  $R_p$  values for the example case with feed system isolating element installed.

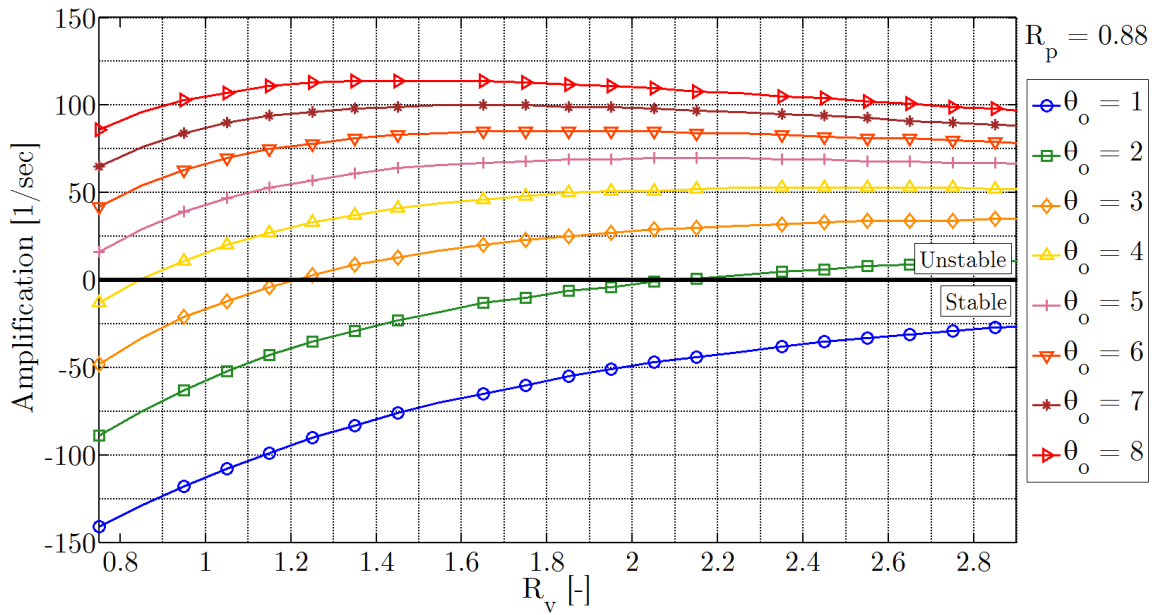


Figure 5.14: Feed coupled response amplification vs.  $R_v$  over a range of  $\theta_o$  values for the example case with feed system isolation element installed.

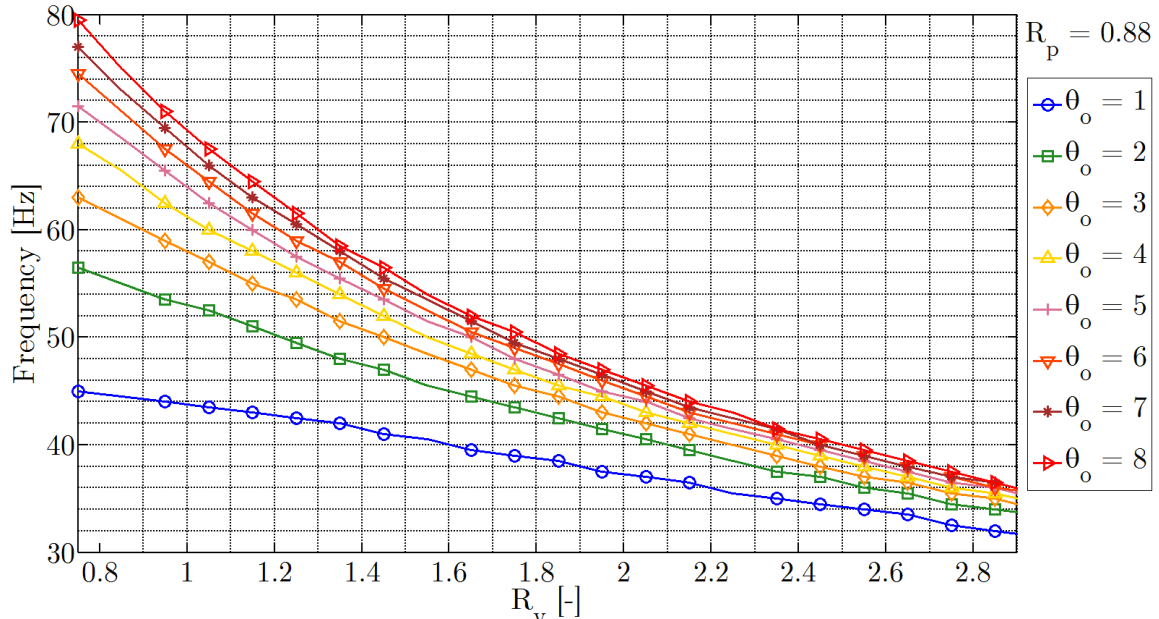


Figure 5.15: Feed coupled response frequency vs.  $R_v$  over a range of  $\theta_o$  values for the example case with feed system isolation element installed.

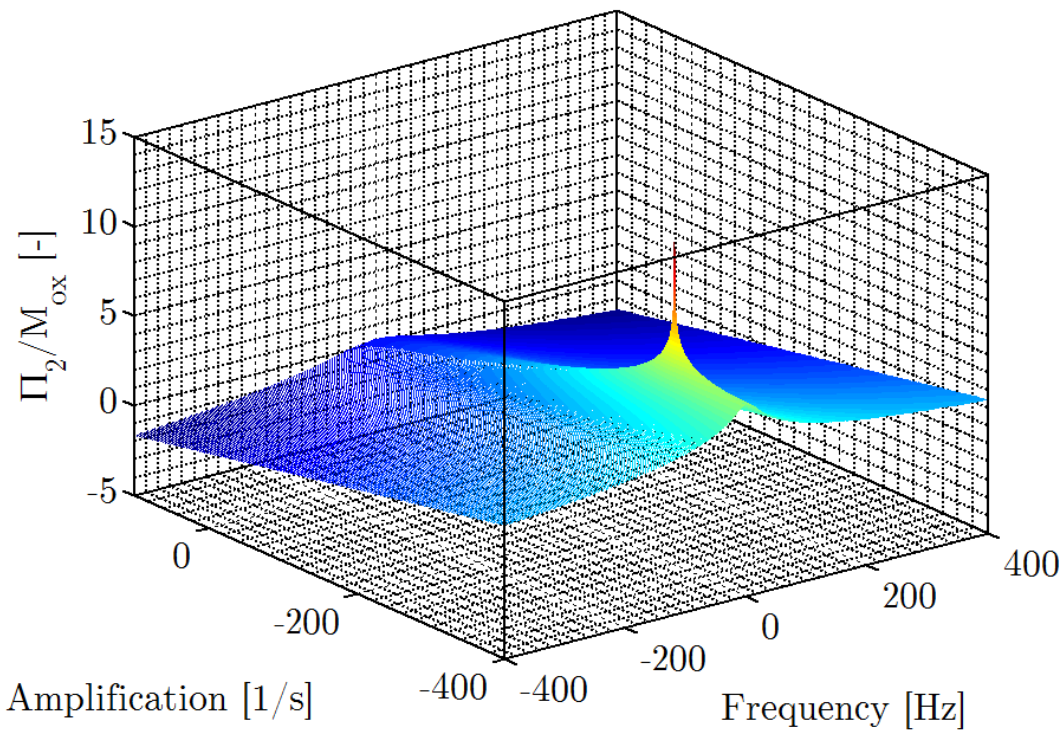


Figure 5.16: Surface plot of the transfer function for the nitrous oxide/paraffin example case with an isolating element installed and the pipe dynamics delay time parameter  $R_p$  set equal to 0 (infinitely fast responding pipe).

The results from this short treatment of the feed system coupled instability model presented by Karabeyoglu et al. result in four main suggestions for the design hybrid rockets when trying to avoid the possibility of feed system coupled instability [61]:

1. Minimize characteristic oxidizer vaporization delay time (promote rapid vaporization)
2. Minimize characteristic feed system pipe response delay time (decrease compressibility within and/or shorten feed system upstream of the injector)
3. Design for high injector pressure drop  $\Delta P$  under nominal motor operation
4. Use an isolation element if possible

The results from the modeling presented above were validated to a certain degree by Karabeyoglu et al. in Ref [61]. Based on the above recommendations, Karabeyoglu et al. were able to completely eliminate the feed coupled instability in an actual nitrous oxide based hybrid rocket by improving the injector design (minimize vaporization delay) and increase the injector pressure drop.

### **5.3 Suppression of Feed System Coupled Instabilities**

As described above, there are a variety of methods that can be employed in an attempt to eliminate feed couple instabilities in hybrid rocket motors. However, the implementation of these techniques are not always practical, and do not guarantee stable operation. For example, due to design constraints, it may not always be possible to shorten the feed system, especially for ground testing setups. Additionally, system constraints can limit the amount of injector pressure drop  $\Delta P$  that can be achieved, such as maximum allowable working pressures in the feed system, or minimum required combustion chamber pressures. For this reason, this section will focus on the use of isolation elements in the feed system.

### 5.3.1 Feed System Isolation

As described in Section 2.1.1.1, the mass flow rate of traditional liquid oxidizers through the injector is usually dependent on both  $P_1$  and  $P_2$ , the pressure upstream and downstream of the injector respectively. In order to achieve a mass flow rate that is independent of chamber pressure, an isolating element, such as a cavitating venturi is often placed in the feed system upstream of the injector. This has been shown to successfully minimize or completely eliminate feed system coupled instabilities in hybrid rockets [62, 63].

#### 5.3.1.1 Cavitating Venturis

The function of a cavitating venturi is to fix, or limit the mass flow rate of a liquid. A standard venturi tube as described in most elementary fluid mechanics courses generally consists of a converging section, a throat section which exhibits the minimum cross-sectional area, and a diverging section. Based upon the Bernoulli equation as shown in Eq. (2.9), as a liquid passes through the converging section, the flow velocity increases and the static pressure decreases. At the throat of the venturi, the flow velocity will be at a maximum, and the static pressure at a minimum. As the flow leaves the throat and passes through the diverging section, the flow velocity decreases and the static pressure increases. When the minimum throat pressure in a venturi is above the vapor pressure of the liquid, only liquid flow exists throughout the flow path. A schematic describing this mode of operation is shown in Fig. 5.17a. However, cavitating venturis are designed such that at a certain mass flow rate, the minimum pressure at the throat of the venturi is at or below the vapor pressure of the liquid, at which point the liquid starts to vaporize or cavitate near the throat wall. This introduction of vapor bubbles acts to partially block the passageway, and prevents an additional increase in mass flow rate due to any reduction of the downstream pressure (this vapor bubble formation may also occur at different minimum throat pressures due to the desorption of dissolved gases within the liquid). A schematic describing the cavitating mode of operation is shown in Fig. 5.17b. Changes in upstream pressure can still affect the mass flow rate through the cavitating venturi,

and the point at which the venturi begins to cavitate.

Cavitating venturis are often used in liquid rockets to fix the mass flow rate through a liquid propellant feed system. They are generally located upstream of the propellant injector in the main propellant transfer piping. Cavitating venturis are often implemented to simply establish propellant mass flow rates that are insensitive to changes in the downstream pressure. This type of application of the cavitating venturi is described in detail in Ref. [64]. In some cases, this effect is utilized in an effort to eliminate or reduce certain types of combustion instabilities linked to the feed system characteristics. When used in this fashion, the cavitating venturi is often described as an isolating element as in the previous sections, with the intent of isolating the parts of the feed system and tank upstream of the cavitating venturi from changes in pressure downstream of the cavitating venturi.

### 5.3.1.2 Injector as an Isolating Element

For many traditional rocket propellants such as liquid oxygen (LOX, O<sub>2</sub>), isolation is successfully achieved through the use of a standard propellant injector and a cavitating venturi operating in concert. The cavitating venturi is located in the main feed system pipe, upstream of the injector. This results in the formation and collapse of vapor bubbles in the main feed line. For systems using nitrous oxide, it can be hazardous to operate with nitrous oxide vapor in the feed system upstream of the injector due to the increased likelihood for an explosive decomposition reaction as outlined in Section 3.1.3.1. Further, due to local high temperatures associated with bubble collapse, a possible ignition source exists within the feed system that could lead to this type of decomposition explosion. Therefore, the use of a cavitating venturi in the feed system is potentially problematic for nitrous oxide based hybrid rockets, and will not be considered here. Fortunately, some of the mass flow rate studies presented earlier in this work identify a potential alternative to the cavitating venturi as a feed system isolating element. Recalling from both Chapter 2 and Chapter 3, when the pressure downstream of the injector falls sufficiently below the oxidizer vapor pressure, the mass flow rate not only reaches a maximum but

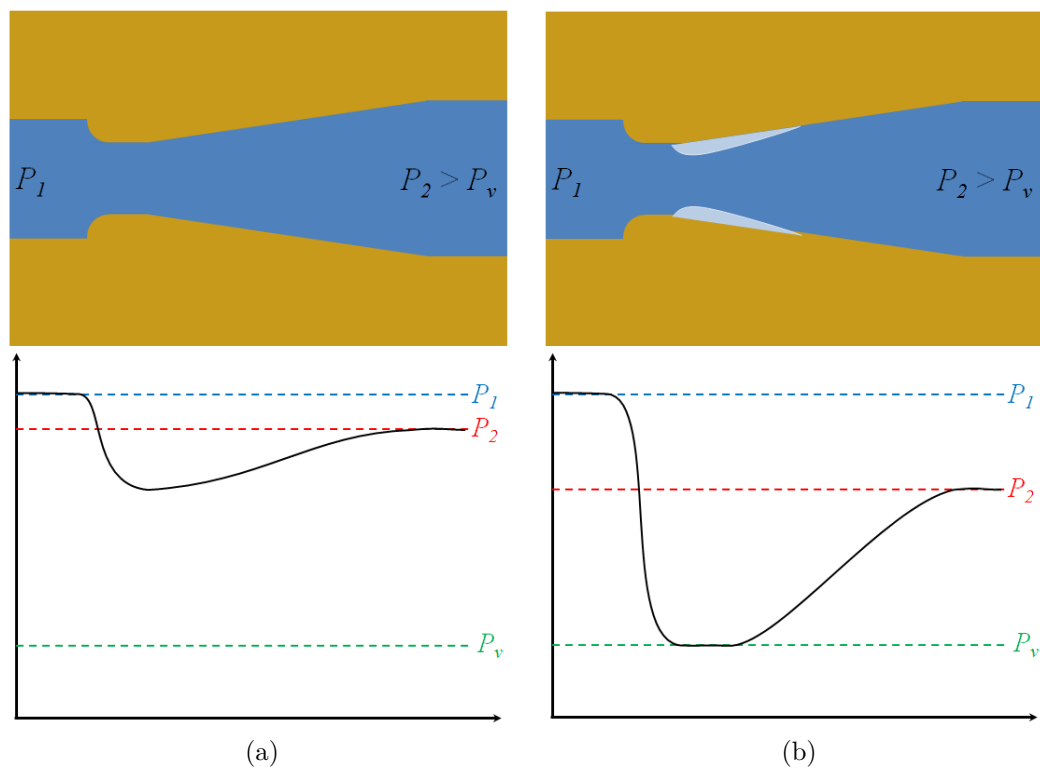


Figure 5.17: Schematic of the cavitating venturi in (a) non-cavitating operation and (b) cavitating operation.

becomes independent of the downstream pressure. It should be noted that this has been demonstrated for both large and small values of orifice  $L/D$ , however for smaller  $L/D$  injectors, critical flow within the injector element does not occur until downstream pressures much lower than  $P_v$  are achieved. Just as with the cavitating venturi, if the mass flow rate is “choked” by the injector element there is no longer a mechanism for hydrodynamic coupling between the combustion chamber and the feed system.

To assist in predicting the conditions necessary for this type of mass flow rate insensitivity, the data from Fig. 3.13 in Chapter 3 is reexamined. This time, mass flow rate is plotted against the ratio of downstream chamber pressure to the oxidizer saturation pressure ( $P_2/P_v$ ) in Fig. 5.18. It is observed that chamber pressure disturbances occurring well below the vapor pressure of the oxidizer ( $P_2/P_v$  less than approximately 0.8) should not be accompanied by any deviation in mass flow rate. As the chamber pressure disturbances approach but remain below the vapor pressure, the injector mass flow rate should start to become sensitive to changes in the chamber pressure, even though two-phase flow likely exists to some extent within the injector element. For chamber pressures above the saturation pressure of the oxidizer, single-phase flow is expected and pressure disturbances in the chamber should be reflected in the injector mass flow rate as predicted by the single-phase incompressible equation.

It is proposed that a hybrid rocket injection scheme can be set up in such a way to leverage the fact that a nitrous oxide injector operating in the critical flow regime can act as an isolating element itself. In this way the injector would serve as an alternative to the cavitating venturi, providing sufficient isolation functionality while avoiding some of the potential hazards associated with the use of a cavitating venturi with nitrous oxide. The following section includes a series of cold flow tests that serve as a proof of concept for this type of injector isolation. This will be followed by the full scale application of the proposed solution in an attempt to eliminate the feed coupled instability in the Peregrine Sounding Rocket heavyweight combustion facility.

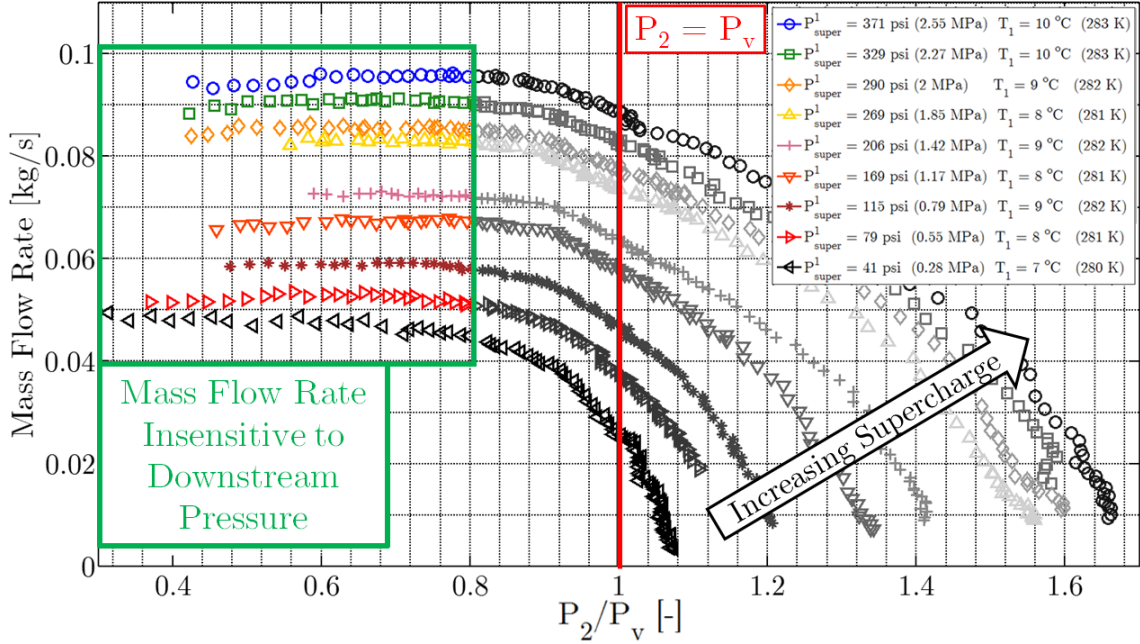


Figure 5.18: Mass flow rate vs. the ratio of chamber pressure to oxidizer saturation pressure ( $P_2/P_v$ ).

### 5.3.2 Cold Flow Testing: Simulated Chamber Pressure Oscillations

#### 5.3.2.1 Mass Flow Rate Insensitivity to Chamber Pressure

In order to verify the behavior outlined above and test the ability of a critical flow injector orifice to provide mass flow insensitivity during more realistic dynamic operation, the experimental test apparatus described in Chapter 3 was adapted to allow for rapid pressurization and depressurization of the downstream section in an oscillatory fashion. Pressurization was achieved by introducing a source of high pressure nitrogen, up to 2600 psig (18.03 MPa), that could be supplied to the downstream test section through a variable speed rapidly actuated motor driven ball valve. In order to allow for rapid depressurization, the downstream chamber was also connected to a large backpressure regulator ( $C_v = 3.0$ ) which vents to the atmosphere. With high pressure nitrogen supplied periodically to the test section, and the backpressure regulator relieving the corresponding pulses, simulated chamber

pressure oscillations were achieved with peak-to-peak amplitudes up to 200 psi (1.38 MPa) and at frequencies of up to 50 Hz. By varying the regulator pressure of the nitrogen supply and the set pressure of the backpressure regulator, the peak-to-peak amplitude and the mean pressure of the oscillations could be adjusted to the desired settings for a test.

A series of tests were performed with carbon dioxide in order examine the injector mass flow rate response to downstream oscillations at three different chamber pressure levels, with the results shown in Fig. 5.19 and Fig. 5.20. Injector number 2 was used for all of these tests, which flow carbon dioxide at room temperature of approximately  $T_1 = 20^\circ\text{C}$  (293 K). In order to most clearly present the results, data from all three tests are presented side by side using the same scales. Fig. 5.19 shows the pressure time histories for each of the three tests, and the corresponding mass flow rate responses are shown directly below for each test in Fig. 5.20. Moving left to right from Test 1 to Test 3, it can be observed that the upstream pressure  $P_1$  and the vapor pressure  $P_v$  are held relatively constant among the tests, while the mean value of the downstream pressure oscillations is increased. Fig. 5.19a shows the pressure time histories for Test 1, during which the chamber pressure is well below the saturation pressure ( $P_{2\text{avg}}/P_v = 0.78$ ). Fig. 5.20a below it shows the mass flow rate data for the same test, and it is clear that the response is insensitive to the downstream pressure oscillations. Moving to the right, Fig. 5.19b shows Test 2, where the chamber pressure is still below, but very close to the vapor pressure ( $P_{2\text{avg}}/P_v = 0.93$ ). As described earlier in this section, even though it is likely that there is vapor formation within the injector, the mass flow rate is still sensitive to the downstream pressure, and this is reflected in the mass flow rate response plotted in Fig. 5.20b. Finally, moving to Fig. 5.19c and Fig. 5.20c, the mass flow rate is highly sensitive to the downstream pressure as it rises above the saturation pressure ( $P_{2\text{avg}}/P_v = 1.03$ ), as is to be expected. A summary of some of the important test data can be found in Table 5.1.

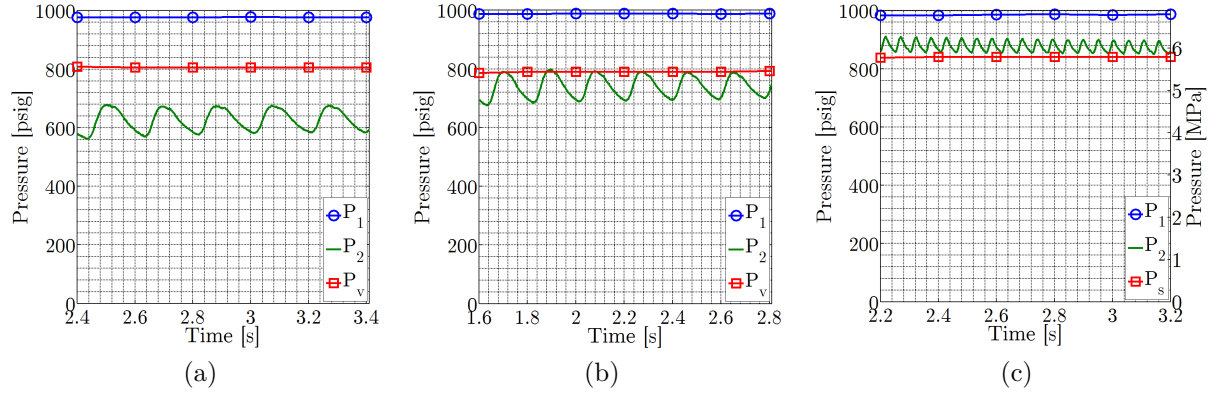


Figure 5.19: Pressure time histories for oscillatory tests: (a) Test 1:  $P_{2\text{avg}}/P_v = 0.78$ , (b) Test 2:  $P_{2\text{avg}}/P_v = 0.93$  and (c) Test 3:  $P_{2\text{avg}}/P_v = 1.03$ . All tests used injector number 2 with carbon dioxide at a temperature of approximately  $T_1 = 20^\circ\text{C}$  (293 K).

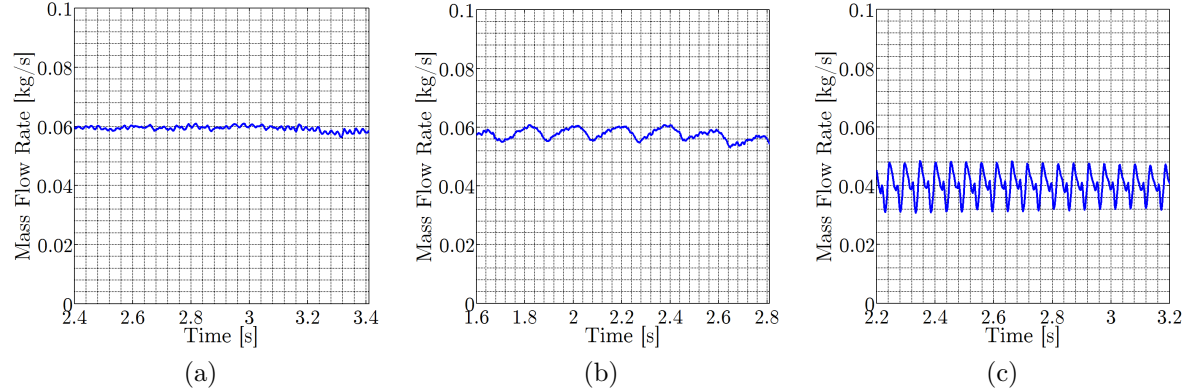


Figure 5.20: Mass flow rate data for oscillatory tests: (a) Test 1:  $P_{2\text{avg}}/P_v = 0.78$ , (b) Test 2:  $P_{2\text{avg}}/P_v = 0.93$  and (c) Test 3:  $P_{2\text{avg}}/P_v = 1.03$ . All tests used injector number 2 with carbon dioxide at a temperature of approximately  $T_1 = 20^\circ\text{C}$  (293K).

While the plots shown in Fig. 5.19 and Fig. 5.20 do suggest that the transition to “choked” injector response occurs as the chamber pressure drops below the oxidizer vapor pressure, it is important to prove that the transition is not merely dependent on the injector pressure drop. In order to perform this evaluation, two tests were performed at nearly identical pressure drops and oscillation characteristics, as shown in Fig. 5.21 with the resulting mass flow response shown in Fig. 5.22. These tests were also performed with carbon dioxide using injector number 2. The only difference between these two tests was the temperature of the oxidizer. The oxidizer temperature was varied in order to shift the saturation pressure from test to test. Fig. 5.23 shows the saturation pressure of carbon dioxide over a range of temperatures. The carbon dioxide temperature of the first test was approximately  $T_1 = 20^\circ C$  (293 K), and the temperature of the second test was approximately  $T_1 = -13^\circ C$  (260 K) corresponding to Tests 4 and 5 respectively. These temperatures correspond to saturation pressures of 830 psia (5.72 MPa) in Test 4 and 355 psia (2.45 MPa) in Test 5. More details of the test data can be found in Table 5.1. We are now able to compare the mass flow rate performance between the two tests without the effect of changing the pressure drop  $\Delta P$ . Fig. 5.21a and Fig. 5.22a from Test 4 show the insensitivity of mass flow rate to downstream pressure compared to that of Test 5 shown in Fig. 5.21b and Fig. 5.22b. In fact, the peak-to-peak amplitude of the mass flow rate response is increased by approximately 700 percent just by cooling the carbon dioxide and shifting the vapor pressure below the downstream oscillation pressure. These results confirm our earlier description of the mechanism resulting in mass flow rate insensitivity. Also of note, the mass flow rate in Test 5 is approximately 50 percent higher than in Test 4. This can be explained by two effects. First, the density of carbon dioxide decreases with increasing temperature, and the carbon dioxide used in Test 5 was significantly colder than in Test 4. More importantly, the mass flow rate in Test 4 is limited by the onset of vapor formation and critical flow, while in Test 5 the carbon dioxide is still all liquid and the mass flow can continue to increase. It should be noted that the mass flow rate profiles do not share the exact same character as the pressure oscillations for these tests. This is due to some electromagnetic interference caused by the “noisy” electrical motor driving the ball valve during the experiments. This

Table 5.1: Oscillatory Test Data Summary

Test	$P_{1\ avg}$ psia (MPa)	$P_{2\ avg}$ psia (MPa)	$P_{2pk-pk}$ psi (MPa)	$P_v$ psia (MPa)	$P_{2\ avg}/P_v$	Frequency Hz	$\dot{m}_{avg}$ kg/s	$\dot{m}_{pk-pk}$ kg/s
1	984 (6.78)	641 (4.42)	125 (0.86)	827 (5.70)	0.78	5	0.059	0.001
2	988 (6.81)	756 (5.21)	100 (0.69)	816 (5.63)	0.93	5	0.057	0.005
3	994 (6.85)	892 (6.15)	70 (0.48)	863 (5.95)	1.03	19	0.040	0.020
4	999 (6.89)	590 (4.07)	90 (0.62)	830 (5.72)	0.71	18	0.060	0.002
5	940 (6.48)	555 (3.83)	85 (0.59)	355 (2.45)	1.56	18	0.089	0.014

effect has been verified over a range of operating conditions and future testing should attempt to provide shielding of the mass flow rate instrumentation and wiring in order to produce higher quality measurements.

### 5.3.2.2 Pressure Disturbance Isolation

Section 5.3.2.1 has shown that critical flow injectors can potentially be used as a means of improving combustion stability by eliminating the dependence of mass flow rate on the downstream chamber pressure. However, in order to achieve stable, controlled combustion, it may also be important to isolate the feed system from acoustic propagation of pressure disturbances from the combustion chamber back through the injector. Pressure oscillations associated with combustion instabilities have been observed to transmit from the combustion chamber back upstream to the feed system in the development of hybrid rockets, particularly when purely liquid oxidizer is expected to be flowing through the injector [17]. However, it has been shown throughout the literature that the introduction of two-phase flow often results in the attenuation of acoustic pressure waves and shock waves due to increased

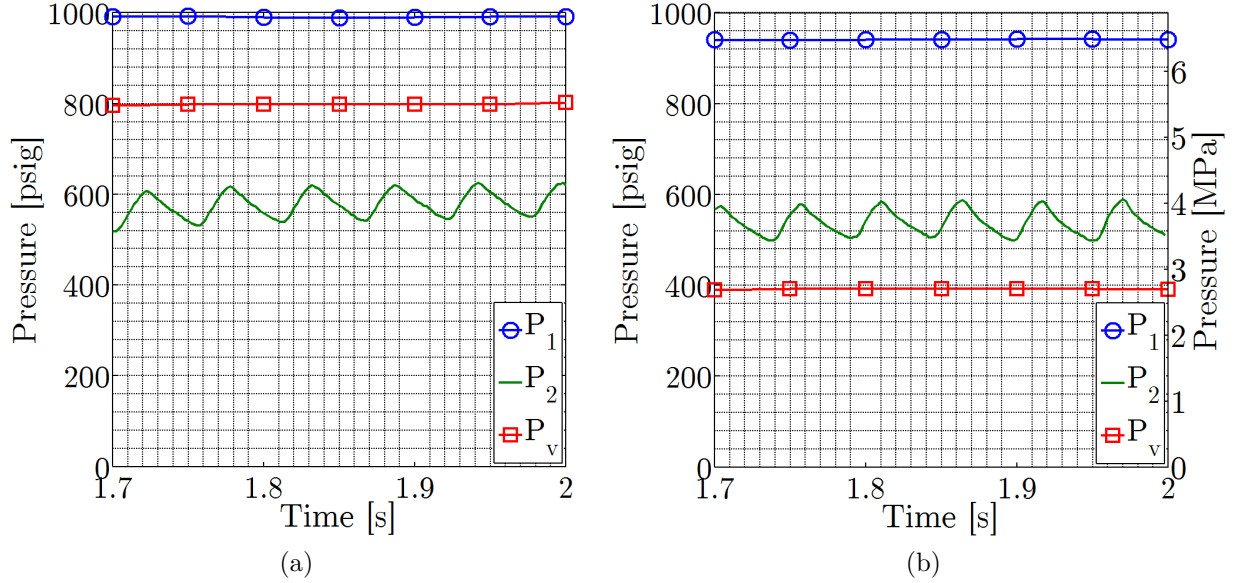


Figure 5.21: Pressure time histories for oscillatory tests: (a) Test 4:  $P_{2\text{avg}}/P_v = 0.71$  and (b) Test 5:  $P_{2\text{avg}}/P_v = 1.56$ . Both tests used injector number 2 with carbon dioxide at temperatures of approximately (a)  $T_1 = 20^\circ\text{C}$  (293 K) and (b)  $T_1 = -13^\circ\text{C}$  (260 K).

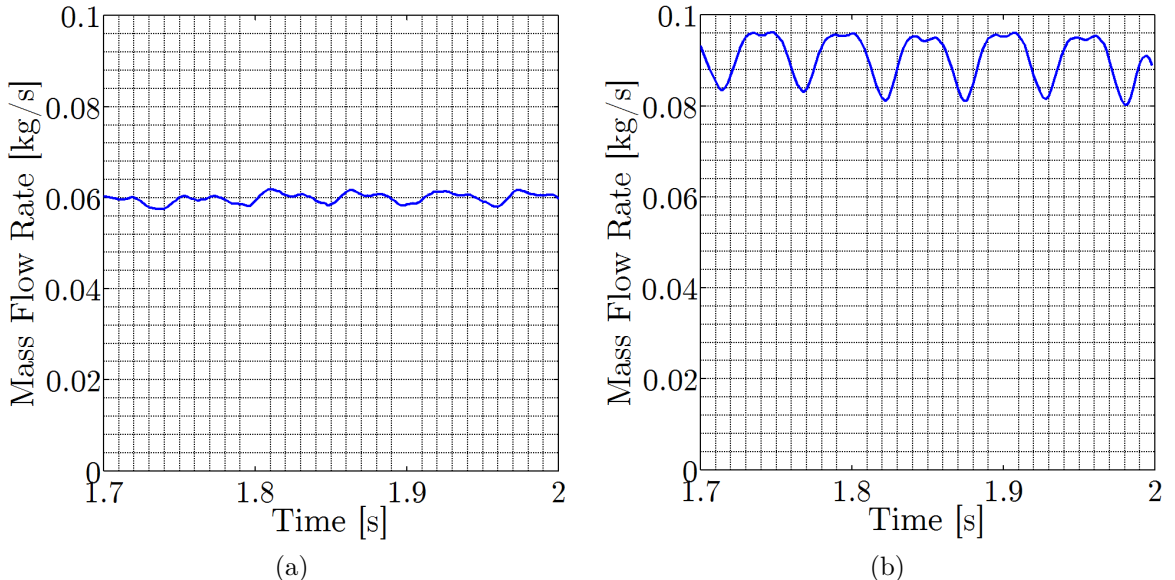


Figure 5.22: Mass flow rate data for oscillatory tests: (a) Test 4:  $P_{2\text{avg}}/P_v = 0.71$  and (b) Test 5:  $P_{2\text{avg}}/P_v = 1.56$ . Both tests used injector number 2 with carbon dioxide at temperatures of approximately (a)  $T_1 = 20^\circ\text{C}$  (293 K) and (b)  $T_1 = -13^\circ\text{C}$  (260 K).

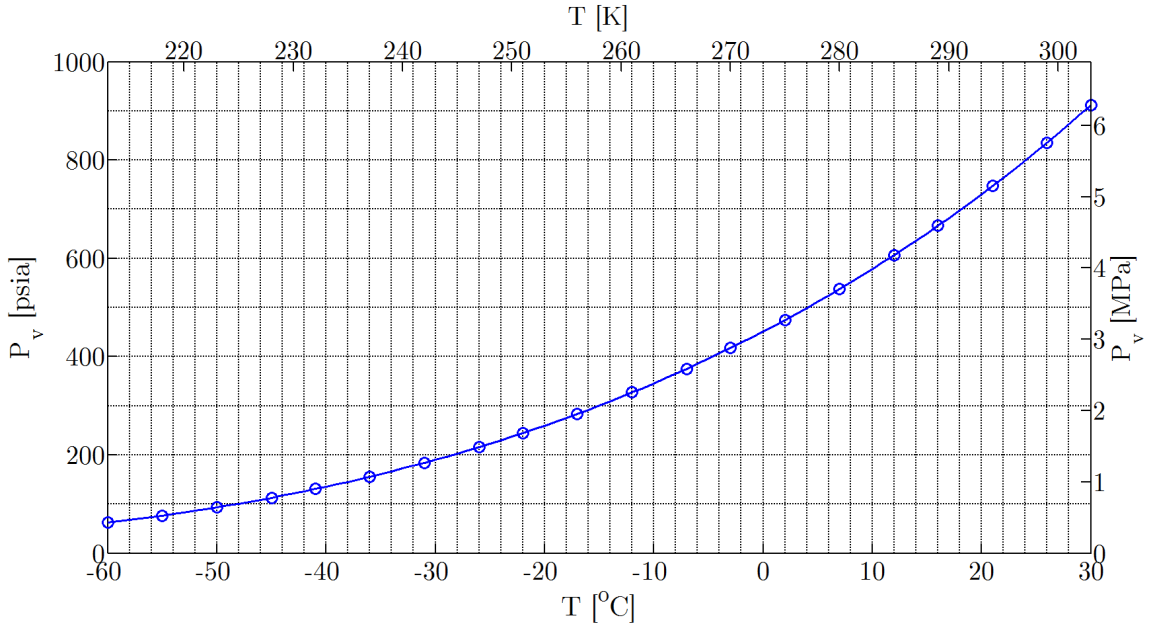


Figure 5.23: Saturation pressure  $P_v$  vs. temperature for carbon dioxide.

compressibility as well as interfacial phase boundary interactions [65]. Therefore, the presence of two-phase flow in a hybrid rocket injector element provides the potential for isolation of pressure oscillations being transmitted back to the feed system.

In order to evaluate the effectiveness of pressure wave attenuation in two-phase flow injectors, we will again examine some of the oscillatory test data presented in Section 5.3.2.1. Fig. 5.24 shows the same pressure time histories as seen in Fig. 5.19, however the range of pressures on each of the plots was narrowed to allow for better visibility of small fluctuations in the  $P_1$  signal. It is immediately clear that of the three tests presented, only Test 3 shown in Fig. 5.24c exhibits any noticeable pressure oscillations upstream of the injector (signaling a lack of isolation). This result does not necessarily mean that two-phase flow is necessary for isolation, or that no attenuation occurs with single-phase flow. However, it does confirm that two-phase flow is more effective at providing attenuation than single-phase liquid flow. Neither Test 1 nor Test 2 (Fig. 5.24a and Fig. 5.24b respectively) show any visible oscillations in the  $P_1$  pressure signal. It is important to note that even though Test 2 does not operate

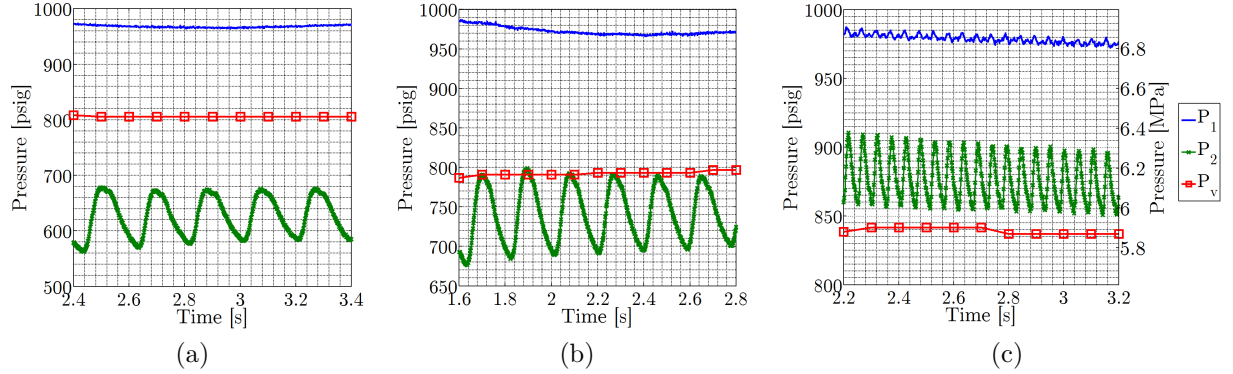


Figure 5.24: Pressure time histories for oscillatory tests: (a) Test 1:  $P_{2\text{avg}}/P_v = 0.78$ , (b) Test 2:  $P_{2\text{avg}}/P_v = 0.93$  and (c) Test 3:  $P_{2\text{avg}}/P_v = 1.03$ . All tests used injector number 2 with carbon dioxide at a temperature of approximately  $T_1 = 20^\circ\text{C}$  (293 K). Zoomed in for examination of oscillations in  $P_1$  signal.

in the critical flow regime, some vapor formation is expected, and these results show that some level of isolation is likely achieved.

The results presented in this section are encouraging in that a properly designed injection scheme could provide the necessary pressure disturbance attenuation to allow for well controlled, stable combustion. However, a complete study of the attenuation dependence on operating conditions and injector geometry has not been completed. Additionally, it has been shown in the literature that the attenuation level of acoustic waves can be dependent on the frequency of the oscillations [65]. Both of these topics provide the potential for exciting future research.

## 5.4 Application to Peregrine Combustion Stabilization

From the results shown in Section 4.4, it became clear that the Peregrine heavyweight combustion facility could serve as an ideal test bed for the validation of the proposed solution to the feed coupled instability presented above in Section 5.3. In short, the

solution requires setting up the heavyweight combustion facility in such a way that during operation, the chamber pressure will always stay at or below approximately 80% of the oxidizer vapor pressure value (for the high  $L/D$  injectors tested in this work). This can be accomplished in one of two ways:

- Decrease the chamber pressure
- Increase the vapor pressure of the oxidizer

For a variety of reasons, decreasing the chamber pressure is not an option. The main reason for this is that for any rocket system there are usually strict minimum thrust requirements, which depend highly on the chamber pressure that can be obtained. This is certainly the case for the Peregrine Sounding Rocket. For this reason, the attempt to suppress the feed coupled instability in the Peregrine heavyweight combustion facility was constrained to increasing the vapor pressure of the oxidizer. In order to achieve this, it was necessary to increase the temperature of the oxidizer. The relationship between nitrous oxide temperature and vapor pressure is included in Fig. 1.5. The operating parameters from Tests E2 and E3-2 are shown in Table 5.2 in order to give a starting point for the determination of the required oxidizer temperature for further testing. It can be seen that for both of these initial tests, the chamber pressure was well above 80% of the vapor pressure, thus the existence of the feed coupled stability is not surprising. In order to assess the effectiveness of an isolating injector with regards to suppressing the feed coupled instability, a proposed set of Peregrine heavyweight operating conditions were determined, and are shown in Table 5.2 as well, notably with an oxidizer temperature of 21.0 °C (294.2 K). Note that the sole difference between test E3-2 and the proposed tests is an increase in the oxidizer temperature of 6.5 °C (6.5 K).

Before presenting the resulting Peregrine test data, the expected test results using the proposed operating parameters should be discussed. It was expected that the feed system coupled instability should be of smaller amplitude, or be eliminated completely. However, with the reduction of the feed coupled instability, and thus a more steady oxidizer mass flow rate into the combustion chamber, it was predicted

Table 5.2: Operating parameters for Tests E2 and E3-2 with proposed parameters for suppression of the feed system coupled instability.

Parameter	Test E2	Test E3-2	Proposed
$T_{ox}$ , $^{\circ}C$ (K)	13.5 (286.7)	14.5 (287.7)	21.0 (294.2)
$P_v$ , psia (MPa)	629 (4.34)	644 (4.44)	747 (5.15)
$P_{2\ initial\ avg}$ , psia (MPa)	~575 (3.96)	~550 (3.79)	~550 (3.79)
$P_{2\ initial\ avg}/P_v$	~0.91	~0.85	~0.74

that the conditions would be more favorable for the establishment of the acoustic instability observed in Test E3-2. Therefore, it was expected that with the successful elimination of the feed coupled instability, a stronger and more coherent acoustic mode would be observed. This was the goal of Test E3-4 which will be described below. The resulting plan for the ensuing Peregrine Sounding Rocket heavyweight combustion facility test program was to first attempt to eliminate the feed coupled instability, and then shift efforts to eliminating the acoustic instability only after the feed coupled instability was solved.

#### 5.4.1 Test E3-4 Results

The operating conditions for Test E3-4 were set to the proposed parameter values listed in Table 5.2, specifically  $T_{ox}= 21.0$   $^{\circ}C$  (294 K) and an expected initial peak chamber pressure of  $P_{2\ initial\ avg}$  of 550 psi (3.79 MPa). This test was a 5 second developmental burn. The chamber pressure time-history for test E3-4 is shown in Fig. 5.25 and Fig. 5.26, and the results are quite noteworthy. As expected, over the majority of the burn, the amplitude of the low frequency feed system coupled instability was reduced to approximately 10-20 psi (0.07- 0.14 MPa) peak-to-peak amplitude. As predicted earlier, with the reduction of the feed system coupled mode, the acoustic instability was stronger and more coherent, as is clearly visible in Fig. 5.26. The amplitude of the acoustic instability during this tests starts off at approximately 150 psi (1.03 MPa) peak-to-peak, and is approximately 90 psi (0.62 MPa) peak-to-peak at the end of the test. These exciting results signaled a highly successful demonstration of the use of a critical flow injector as an effective flow isolating element. Since the

adoption of this new critical flow injector operating criteria, no tests have resulted in the observation of the feed system coupled combustion instability mode.

It should be noted that during the first 0.3 second of the burn, feed system coupled instability is observed, as is clearly visible in both Fig. 5.25 and in the spectrogram frequency content of Fig. 5.27. A long feed system pipe exists between the oxidizer tank and the injector face. The pipe material and the nitrous oxide contained within it are pre-chilled as part of the operating procedure for the heavyweight combustion facility. It is thought that initially cold (lower vapor pressure) nitrous oxide flows through the injector during this initial phase, resulting in the injector not operating under critical flow conditions. Further testing in this facility provided less cooling to the feed line to address this issue.

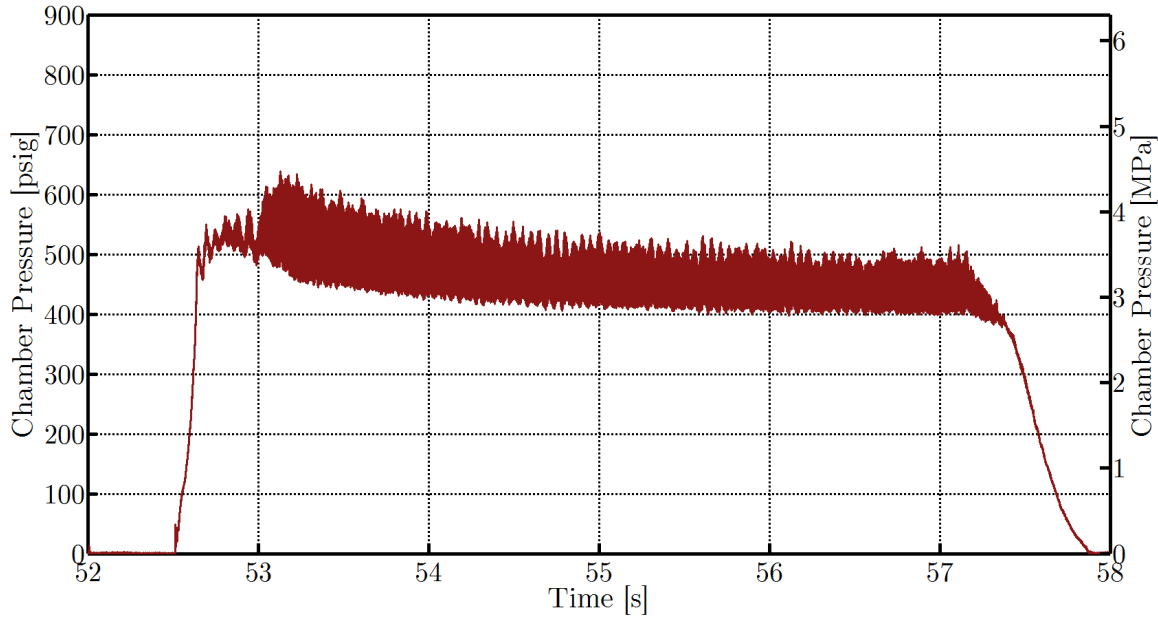


Figure 5.25: Chamber pressure time-history for Test E3-4 in the Peregrine heavyweight combustion tests facility with  $T_{ox} \approx 21.0^{\circ}C$  (294.2 K).

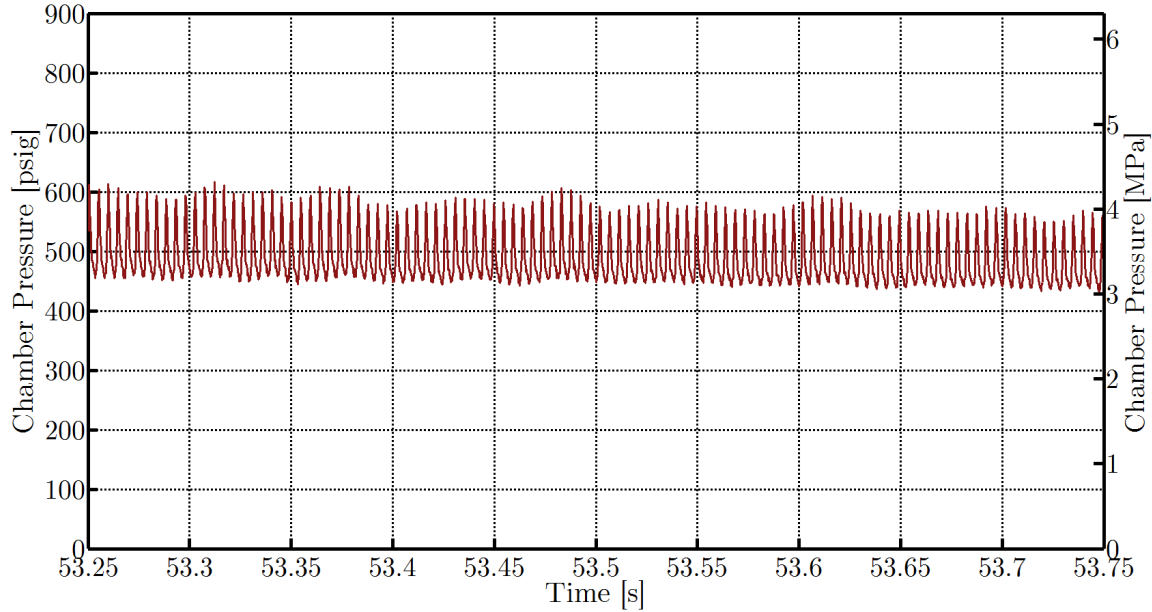


Figure 5.26: Zoomed in chamber pressure time-history for Test E3-4 in the Peregrine heavyweight combustion tests facility with  $T_{ox} \approx 21.0^{\circ}C$  (294.2 K).

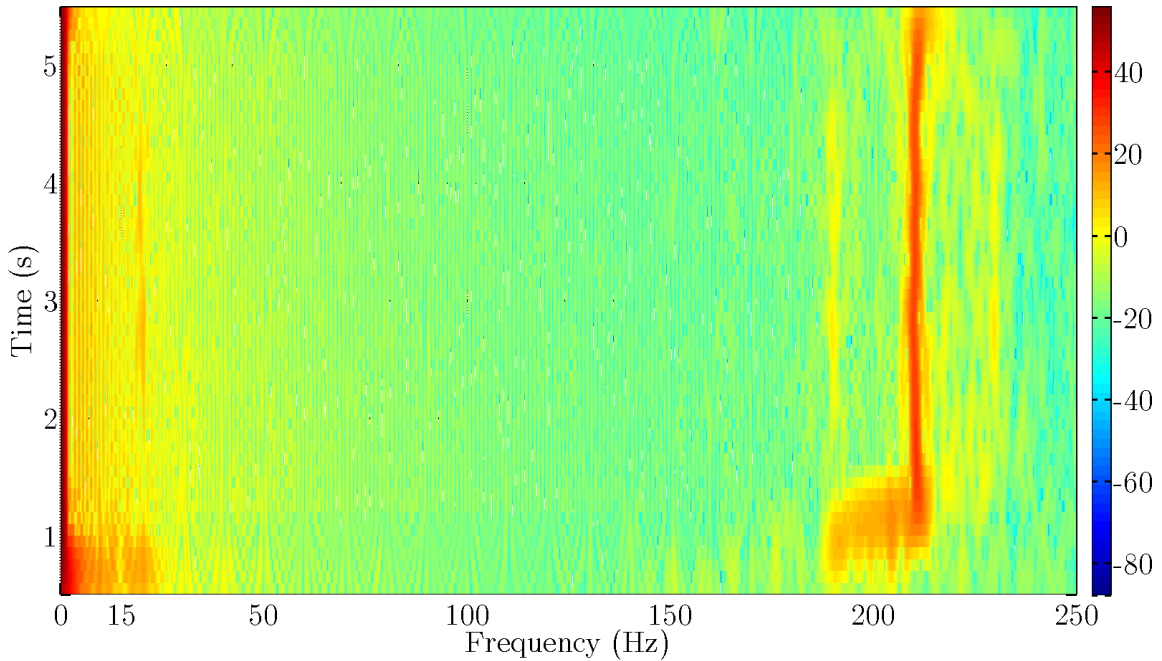


Figure 5.27: Chamber pressure signal frequency content (FFT) for Test E3-4 plotted over the duration of the burn with  $T_{ox} \approx 21.0^{\circ}\text{C}$  (294.2 K). Color is proportional to the power spectral density of the chamber pressure signal.

### 5.4.2 Test E4-1 Results

Once the elimination of the feed system coupled instability was achieved, the Peregrine program was able to focus on suppressing the acoustic instability. Over the course of 2 hot fire tests, some relatively simple changes to the internal geometry of the Peregrine heavyweight combustion facility were made in hopes of damping the acoustic instability observed in Test E3-4. The details of the geometry modification will not be presented here, but the results from the corresponding test (Test E4-1) will be included in order to provide the reader with the current state of the performance achieved in the Peregrine heavyweight combustion facility. Test E4-1 was a longer 8 second burn, using oxidizer at a temperature of  $22.5^{\circ}\text{C}$  (295.7 K). As can be seen from Fig. 5.28 and Fig. 5.29, the chamber pressure time-history from this test shows that the acoustic instability was damped to such a degree that motor exhibited extremely stable combustion. Again, as shown in Fig. 5.30, there is a small amount of low

frequency activity at the start of the burn around the feed coupled instability mode frequency, which still may be attributed to the feed line chilling procedure (which was in fact scaled back, but not removed completely). Looking closely at Fig. 5.28 this early low frequency activity can just barely be distinguished. It should be noted that while it may have been possible to remove the acoustic instability first, the success of the Peregrine heavyweight combustion facility test campaign was dependent on the elimination of the feed system coupled instability.

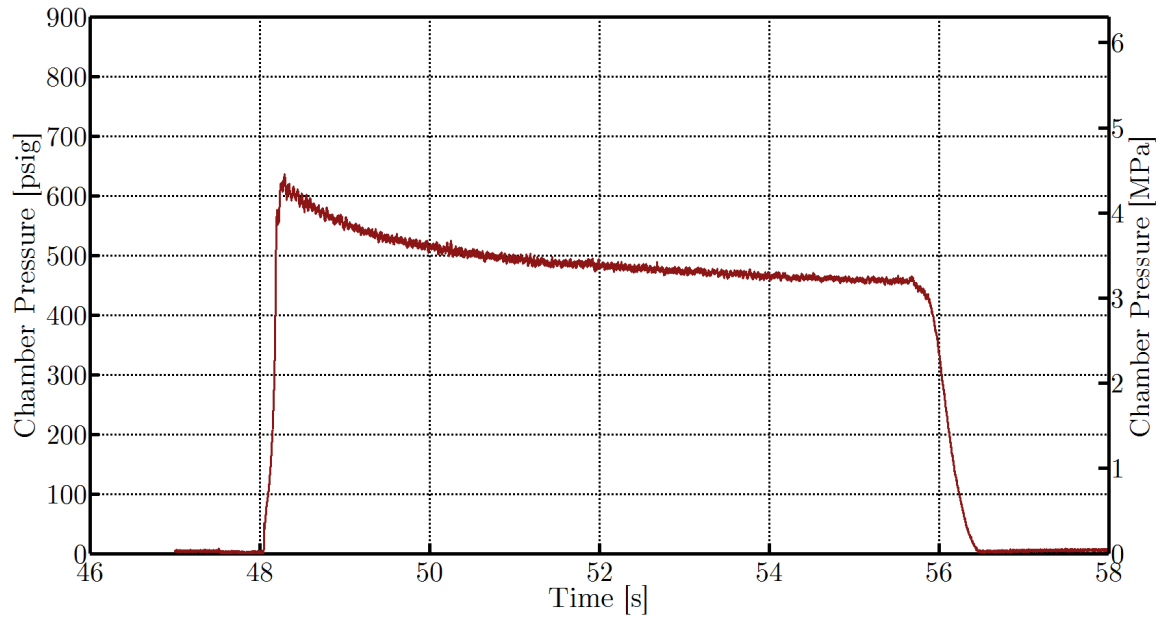


Figure 5.28: Chamber pressure time-history for Test E4-1 in the Peregrine heavyweight combustion tests facility with  $T_{ox} \approx 22.5^\circ C$  (295.7 K).

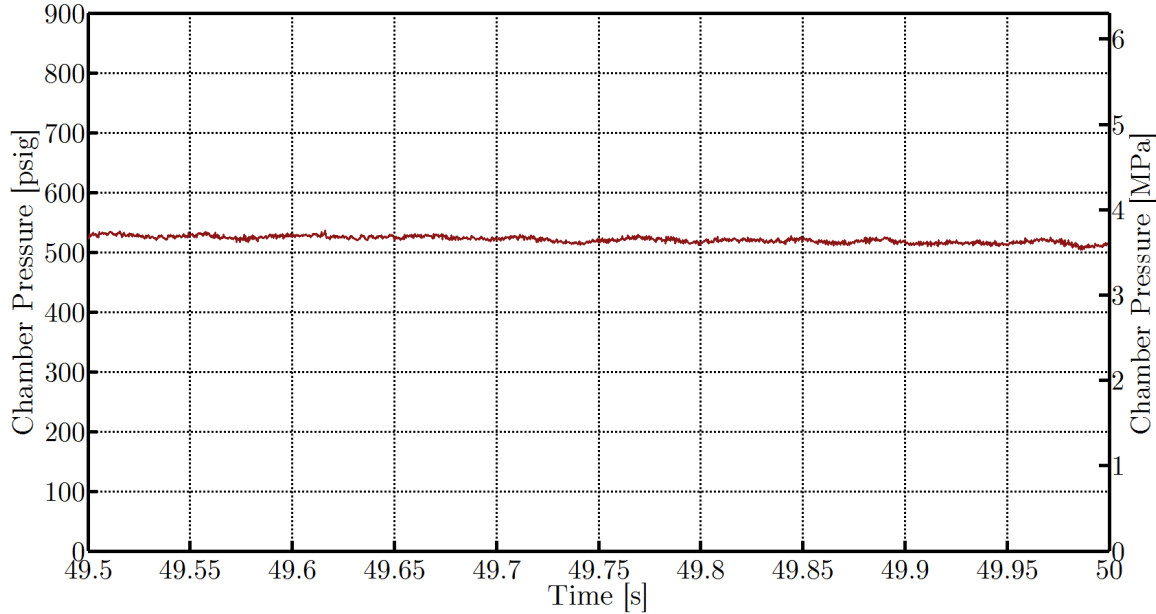


Figure 5.29: Zoomed in chamber pressure time-history for Test E4-1 in the Peregrine heavyweight combustion tests facility with  $T_{ox} \approx 22.5^\circ C$  (295.7 K).

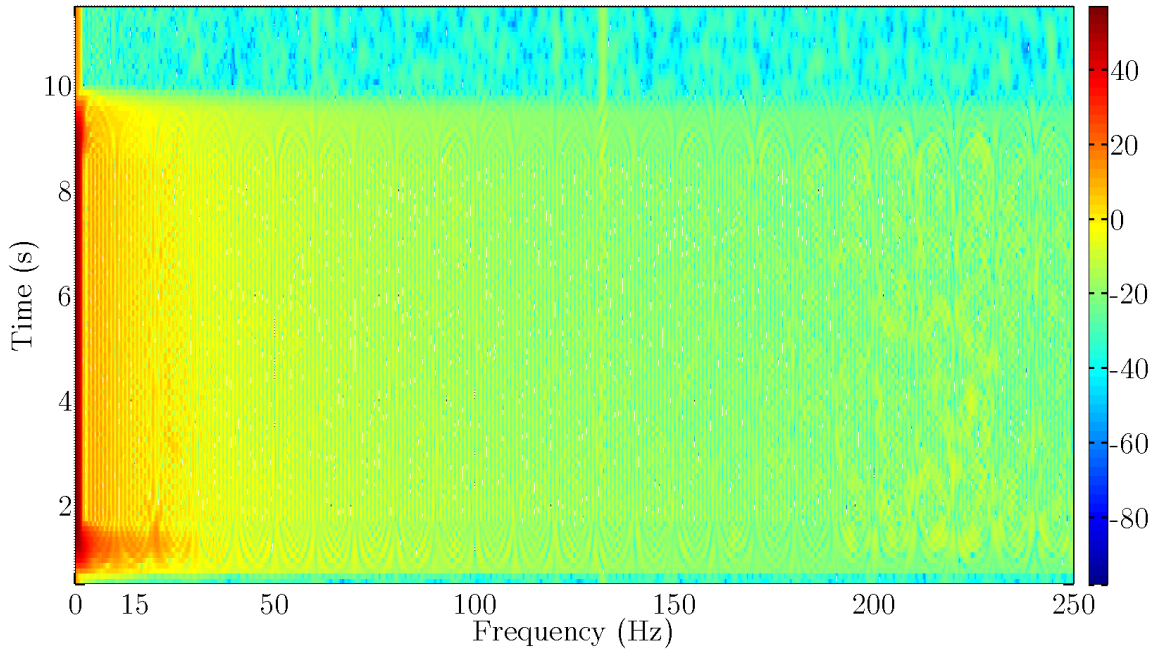


Figure 5.30: Chamber pressure signal frequency content (FFT) for Test E4-1 plotted over the duration of the burn with  $T_{ox} \approx 22.5^{\circ}\text{C}$  (295.7 K). Color is proportional to the power spectral density of the chamber pressure signal.

## 5.5 Combustion Instability Conclusions

Low frequency combustion instabilities have proven to be a major obstacle for hybrid rocket development programs over the past few decades. The feed system coupled combustion instability has been particularly problematic for hybrid rocket development programs utilizing nitrous oxide as the oxidizer. While cavitating venturis can be used as isolation elements in order to eliminate the feed system coupled instability from hybrid rockets which use LOX, the risk of a decomposition reaction explosion prohibits this solution for nitrous oxide systems. However, based upon the small scale injector cold flow results from Chapter 3, it was determined that a critical flow injector could provide the necessary isolation to suppress the feed system coupled instability. This theory was tested in the full scale Peregrine Sounding Rocket heavyweight combustion facility with tremendous success, leading to highly stable combustion. The results from Tests E3-4 and E4-1 signal a major step forward in the understanding

and suppression of combustion instabilities in hybrid rocket motors, not only for the Peregrine Sounding Rocket program, but for the industry as a whole. There are however some drawbacks to this solution of the feed system coupled instability which will be addressed in Chapter 6.

# **Chapter 6**

## **A Novel Hybrid Rocket Injection Scheme**

It was shown definitively in Chapter 5 that a properly designed injection scheme can result in the avoidance of feed system coupled combustion instabilities in hybrid rocket motors. Specifically, operating a hybrid rocket motor with an injector exhibiting critical flow has been shown to successfully eliminate feed coupled instabilities in full scale hybrid rocket tests. However, the aforementioned criteria used for suppressing feed coupled instabilities does result in certain restrictions on operating conditions and has a negative impact on the performance of the overall rocket system. These drawbacks will be outlined in this section. Fortunately, a novel hybrid rocket injection scheme has been developed which essentially removes the constraints imposed by the criteria presented in Chapter 5, while maintaining the critical flow injector isolation performance. This improvement will be outlined, and the results from a series of cold flow experiments will be presented to serve as a proof of concept.

## 6.1 Undesired Consequences of Stabilization Criteria

As described in Section 5.4, it is possible to provide resistance to the development of the feed system coupled instability by ensuring that the injector mass flow rate is independent of the chamber pressure. This is achieved for standard oxidizer injectors by setting the chamber pressure sufficiently below the vapor pressure to promote critical two-phase flow through the injector. The exact percentage to which the chamber pressure must be set below the vapor pressure depends upon the design of the given injector and the thermodynamic conditions of the oxidizer supplied to the injector. However, for the high  $L/D$  injectors using supercharged nitrous oxide studied by the author, a useful criteria for critical flow is shown in Eq. (6.1).

$$P_2 < 0.8P_v \quad (6.1)$$

While the benefits from the use of this criteria can be substantial, there are two main negative consequences of its use:

- Limitations on operating conditions
- Reduction in overall rocket performance (due to mass penalty)

In one form another, the rocket designer is constrained if this criteria is used. If there are operational upper limits on the temperature of the oxidizer being used, there will likely be little flexibility on the choice of chamber pressure. Further, for traditional low vapor pressure oxidizers, this criteria is essentially useless. Additionally, if a minimum chamber pressure is required, oxidizer below a certain temperature cannot be used. Depending on the oxidizer of choice, even with nitrous oxide, this could result in the inability to achieve performance goals. Overall, this criteria can severely restrict the design space for hybrid rockets.

In terms of performance, it is useful to examine the effects of this criteria on the overall mass of the rocket system. As an example, a hypothetical nitrous oxide based

hybrid rocket can be considered. Assuming a minimum chamber pressure is required in order to achieve some minimum thrust level, the nitrous oxide temperature will likely need to be set relatively high (as was done for Test E3-4 in Section 5.4.) This results in an increased oxidizer vapor pressure  $P_v$ , which is necessary to ensure critical flow through the injector. However, this also results in the storage of the oxidizer at a higher pressure, resulting in a thicker walled, thus heavier oxidizer tank. On top of that, it can be seen from Fig. 1.5 that as the temperature of nitrous oxide is increased, the liquid density can decrease significantly, especially nearing the thermodynamic critical point. This results in an increased volume of oxidizer to store, and a larger tank. With the requirement of a larger, thicker walled oxidizer tank, the impacts on overall  $\Delta V$  performance can be substantial. This may be fine for some development programs, but unacceptable for others.

For the reasons outlined above, an effort was made to develop a method of oxidizer injection which can operate in the critical flow regime for more arbitrary operating conditions, with regard to both chamber pressure and oxidizer temperature/vapor pressure. The following sections will describe one such method which has been proposed by the author.

## 6.2 Improved Isolating Injection Scheme

A new class of rocket propellant injectors has been proposed which allows for operation in the critical flow regime over essentially arbitrary conditions. While this improved injection scheme was conceived of with the use of nitrous oxide in mind, it applies equally as well to the use of traditional, low vapor pressure propellants. This section describes the injection scheme in detail and some important design considerations.

### 6.2.1 Goal

As mentioned previously, the goal in developing this injection scheme was to provide an isolating injector that could perform in the critical flow regime over a broader,

essentially arbitrary set of operating conditions. Specifically, these conditions can be outlined as:

- Arbitrary chamber pressure
- Broad range of oxidizer temperatures (vapor pressure)
- All propellants

For example, when using standard injector orifices with nitrous oxide, in order to achieve high chamber pressures, high temperature nitrous oxide must be used. It would be preferred if cold nitrous could be used in order to be stored at lower pressures and with higher density. Additionally, while the bulk of this work has focused on high vapor propellants such as nitrous oxide, an improved injection scheme should provide for isolation using traditional, low vapor propellents as well (such as LOX, kerosene, etc.)

### 6.2.2 Approach

Recalling the description of cavitating venturis in Section 5.3.1.1, it is well known that these can be designed to provide fixed mass flow rates for low vapor pressure propellants over a broad range of operating conditions. Again, these devices are generally located upstream of the injector in the main feed line. This approach is still not considered because it is not suitable for nitrous oxide systems, and additionally there are benefits to collocating the isolating element with the injector. First, avoiding the use of a dedicated cavitating venturi in the feed line results in weight savings, thus improved performance. Second, by collocating the isolating element with the injector, the entire feed system upstream of the injector will be isolated from the combustion chamber. With a dedicated cavitating venturi, a small portion of the feed system downstream of the cavitating venturi but still upstream of the injector will likely be in hydrodynamic communication with the combustion chamber.

In order to achieve the goals stated in Section 6.2.1, a novel, yet relatively simple approach is proposed. This injection scheme involves designing each individual

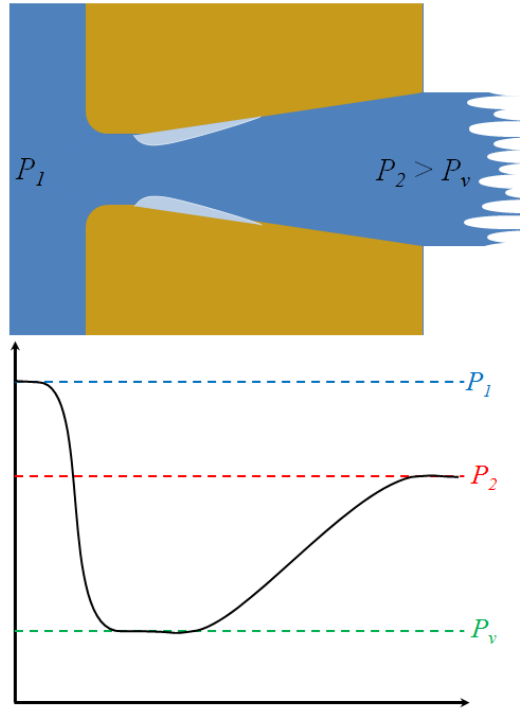


Figure 6.1: Schematic of the cavitating venturi style injector operating in the critical flow regime.

injector orifice in a similar fashion as that of a cavitating venturi. Specifically, the contour of each injector orifice must have a defined throat and a diverging section, termed the diffuser. A smooth converging section (rounded inlet) is preferable, but not necessary. The proposed injector orifice design provides the functionality of both the standard injector and the cavitating venturi in a single component. It is designed such that under the desired conditions for critical flow, the throat pressure is at or below the vapor pressure of the liquid. A schematic of the cavitating venturi style injector is shown in Fig. 6.1.

While the description of the standard cavitating venturi and the cavitating venturi style injector are quite similar, the functionality is actually quite different. Standard cavitating venturis are generally flow limiting devices, in that beyond a certain mass flow rate, cavitation begins, and the mass flow rate can be increased no more. The

pressure drop  $\Delta P$  across a typical cavitating venturi in both the cavitating and non-cavitating regimes is generally not large, and is not the driving force for the mass flow. The driving force for the mass flow rate is the pressure drop across the standard injector that is located downstream of the cavitating venturi in the feed system. On the other hand, the cavitating venturi style injector does exhibit a large  $\Delta P$ , providing the driving force for the mass flow rate, as well as mass flow rate limiting. Therefore these two factors of the component are linked, thus the design, analysis, and operation of a cavitating venturi style injector is quite different in practice than that of the standard cavitating venturi. For this reason, the next section will provide a sample analysis specific to this new class of rocket propellant injectors.

### 6.2.3 Sample Analysis

In order to demonstrate some design considerations which are unique to this new injection scheme, and example analysis will be provided in this section. The analysis will be carried out in a similar fashion to that of the Single Phase Incompressible flow model described in Section 2.1.1.1. This simplified style of analysis is chosen because it will aid in the understanding of this new class of injectors and their functionality. The assumptions made in this section do not constitute conditions under which the device must operate. On the contrary, this same analysis can be completed without the included assumptions to predict the behavior of this device under arbitrary conditions. This analysis also serves as a guide for the method of selecting the specific geometry of the device in order for it to perform as desired under known operating conditions.

A notional cross-section for one of these injectors is shown in Fig. 6.2. The actual shape of this cross-section is arbitrary and unimportant, but the cross-sectional areas of the indicated locations are the important information. The features of this injection scheme included for this analysis are the area upstream of the injector, the inlet, the converging section, the throat, and the diffuser section, ending at the injector exit. The analysis starts with conservation of mass throughout the device, under the

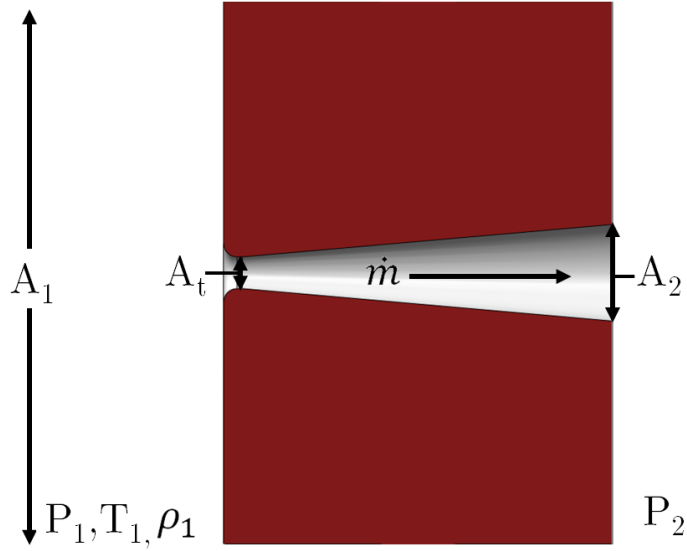


Figure 6.2: Notional cross-section of the proposed novel injection scheme, with important parameters labeled.

assumption of steady state operation, resulting in the continuity equation as shown in Eq. (6.2).

$$\rho_1 u_1 A_1 = \rho_t u_t A_t = \rho_2 u_2 A_2 \quad (6.2)$$

For this example calculation, it is assumed that the flow is incompressible liquid, thus the density is constant:

$$\rho_1 = \rho_t = \rho_2 = \rho \quad (6.3)$$

$$\rho u_1 A_1 = \rho u_t A_t = \rho u_2 A_2 \quad (6.4)$$

$$u_1 A_1 = u_t A_t = u_2 A_2 \quad (6.5)$$

This results in a list of useful relations which will be called upon later, as shown in Eqns. (6.6) - (6.11):

$$u_1 = \frac{A_t}{A_1} u_t \quad (6.6)$$

$$u_t = \frac{A_1}{A_t} u_1 \quad (6.7)$$

$$u_1 = \frac{A_2}{A_1} u_2 \quad (6.8)$$

$$u_2 = \frac{A_1}{A_2} u_1 \quad (6.9)$$

$$u_t = \frac{A_2}{A_t} u_2 \quad (6.10)$$

$$u_2 = \frac{A_t}{A_2} u_t \quad (6.11)$$

Next the Bernoulli equation is employed, again assuming incompressible liquid flow, to calculate the mass flow rate through the injector based on the conditions upstream (location 1) and at the exit of the injector (location 2) as shown in Eq. (6.12):

$$P_1 + \frac{1}{2}\rho u_1^2 + \rho g_o h_1 = P_2 + \frac{1}{2}\rho u_2^2 + \rho g_o h_2 \quad (6.12)$$

Assuming that the difference in gravitational potential energy between locations 1 and 2 is negligible, the resulting form can be simplified as in Eq. (6.13):

$$P_1 + \frac{1}{2}\rho u_1^2 = P_2 + \frac{1}{2}\rho u_2^2 \quad (6.13)$$

A useful expression for velocity at the exit,  $u_2$ , can be found by manipulating this form of the Bernoulli equation and by employing some of the useful relations presented above in Eqns. (6.6) through (6.11). This form is shown in Eq. (6.14):

$$u_2 = \sqrt{\frac{2(P_1 - P_2)}{\rho \left[ 1 - (\frac{A_2}{A_1})^2 \right]}} \quad (6.14)$$

Using the above relations, the mass flow rate through the injector can be calculated as shown in Eq. (6.16):

$$\dot{m}_{inj} = \rho u_2 A_2 \quad (6.15)$$

$$\dot{m}_{inj} = A_2 \sqrt{\frac{2\rho(P_1 - P_2)}{\left[1 - \left(\frac{A_2}{A_1}\right)^2\right]}} \quad (6.16)$$

The same as in Section 2.1.1.1, due to the possible presence of a vena contracta as well as definite frictional losses, the mass flow rate achieved is usually lower than the ideal value as predicted by the equation above. For this reason, an empirically determined discharge coefficient for the injector orifice is included as shown in Eq. (6.17):

$$\dot{m}_{inj} = C_{d,inj} A_2 \sqrt{\frac{2\rho(P_1 - P_2)}{\left[1 - \left(\frac{A_2}{A_1}\right)^2\right]}} \quad (6.17)$$

Now the same process can be repeated as above for the segment of the injector from the throat (location t) to the exit of the injector (location 2). This segment of the injector will be called the diffuser. The expression for the mass flow rate based on the diffuser calculation is shown in Eq. (6.18). It should be noted that a different discharge coefficient for only the diffuser section is included in this equation.

$$\dot{m}_{diff} = C_{d,diff} A_t \sqrt{\frac{2\rho(P_2 - P_t)}{\left[1 - \left(\frac{A_t}{A_2}\right)^2\right]}} \quad (6.18)$$

During steady operation, the mass flow rate through the injector and the diffuser section must be equal to one another, resulting in the equality shown in Eq. (6.20):

$$\dot{m}_{inj} = \dot{m}_{diff} \quad (6.19)$$

$$C_{d,inj} A_2 \sqrt{\frac{(P_1 - P_2)}{\left[1 - \left(\frac{A_2}{A_1}\right)^2\right]}} = C_{d,diff} A_t \sqrt{\frac{(P_2 - P_t)}{\left[1 - \left(\frac{A_t}{A_2}\right)^2\right]}} \quad (6.20)$$

The above equation can be solved for the throat pressure  $P_t$ , as a function of a given injector geometry ( $A_1, A_2, A_t$ ), the upstream and downstream operating pressures ( $P_1, P_2$ ), and the discharge coefficients for the injector and diffuser section ( $C_{d,inj}, C_{d,diff}$ ), as shown in Eq. (6.21):

$$P_t = P_2 - \left( \frac{C_{d,inj}}{C_{d,diff}} \right)^2 \left( \frac{A_2}{A_t} \right)^2 \frac{\left[ 1 - \left( \frac{A_t}{A_2} \right)^2 \right]}{\left[ 1 - \left( \frac{A_2}{A_1} \right)^2 \right]} (P_1 - P_2) \quad (6.21)$$

For a specific combination of injector geometry and operating pressures, if the throat pressure  $P_t$  is below the vapor pressure of the propellant  $P_v$ , it is expected that cavitation/vaporization will be present at the throat. This is the desired operation of the device, and the criterion for operation is simply stated in Eq. (6.22) and Eq. (6.23):

$$P_t < P_v \quad (\text{for critical flow}) \quad (6.22)$$

$$P_2 - \left( \frac{C_{d,inj}}{C_{d,diff}} \right)^2 \left( \frac{A_2}{A_t} \right)^2 \frac{\left[ 1 - \left( \frac{A_t}{A_2} \right)^2 \right]}{\left[ 1 - \left( \frac{A_2}{A_1} \right)^2 \right]} (P_1 - P_2) < P_v \quad (\text{for critical flow}) \quad (6.23)$$

Eq. (6.22) and Eq. (6.23) constitute the basis of operation for this new class of injector. Under these conditions, the injector will operate in the critical flow regime, providing isolation. However, the injector can be operated outside of the above criteria under conditions where the flow would not cavitate, and no choking or isolation should be expected. It should also be noted that the vapor pressure of the propellant may not remain constant as it passes through the injector. In some cases, the propellant temperature will be dropping as the liquid moves toward the throat of the injector (as described in Chapter 2). In this case, the local vapor pressure at the throat may be lower than the vapor pressure of the upstream propellant. Thus, the value of the throat pressure  $P_t$  resulting in mass flow rate choking can be significantly lower than those presented above, depending on the properties of the propellant. Other factors can also significantly affect the onset of mass flow rate

choking, such as the fluid existing in a metastable state, especially for propellants existing close to their vapor pressure upstream of the injector. This treatment could be supplemented using one of the two-phase flow models described in Chapter 2, but this presentation is not included here, as this analysis is just given as an example to show the necessary considerations for designing an isolating injector of this type. Instead, in order to ensure choking and isolation, a reasonable margin can be chosen between the throat pressure and the known upstream vapor pressure (e.g.  $P_t < 0.8P_v$  as described similarly in Chapter 5 for standard injectors) as shown in Eq. (6.24) and Eq. (6.25):

$$P_t < 0.8P_v \quad (\text{for critical flow with 20\% margin on } P_v) \quad (6.24)$$

$$P_2 - \left( \frac{C_{d,inj}}{C_{d,diff}} \right)^2 \left( \frac{A_2}{A_t} \right)^2 \frac{\left[ 1 - \left( \frac{A_t}{A_2} \right)^2 \right]}{\left[ 1 - \left( \frac{A_2}{A_1} \right)^2 \right]} (P_1 - P_2) < 0.8P_v$$

(for critical flow with 20\% margin on  $P_v$ ) (6.25)

If control of the propellant's vapor pressure is possible, this equation can be used to choose the vapor pressure  $P_v$  that will choke an injector of a given geometry and for the desired operating pressures. Additionally, for a given geometry, upstream pressure  $P_1$ , and vapor pressure  $P_v$ , the downstream pressure  $P_2$  corresponding to choking can be calculated directly. With the definition of a geometry based coefficient  $\omega$  as detailed below, the equations above can be manipulated into a simple and useful form for determining the downstream pressure  $P_2$  corresponding to choking shown in Eq. (6.29) and Eq. (6.30):

$$\omega = \left( \frac{C_{d,inj}}{C_{d,diff}} \right)^2 \left( \frac{A_2}{A_t} \right)^2 \frac{\left[ 1 - \left( \frac{A_t}{A_2} \right)^2 \right]}{\left[ 1 - \left( \frac{A_2}{A_1} \right)^2 \right]} \quad (6.26)$$

$$P_t = P_2 - \omega(P_1 - P_2) \quad (6.27)$$

$$P_2 = \frac{P_t + \omega P_1}{1 + \omega} \quad (6.28)$$

$$P_2 = \frac{P_v + \omega P_1}{1 + \omega} \quad (\text{for critical flow with no margin}) \quad (6.29)$$

$$P_2 = \frac{0.8P_v + \omega P_1}{1 + \omega} \quad (\text{for critical flow with 20\% margin on } P_v) \quad (6.30)$$

If instead, the operating pressures upstream and downstream of the injector are known, as well as the vapor pressure  $P_v$ , an expression for the corresponding geometry required for choking can be obtained in a similar fashion, and is shown below in Eq. (6.32) and Eq. (6.33):

$$\frac{A_2}{A_t} = \sqrt{1 + \left(\frac{C_{d,diff}}{C_{d,inj}}\right) \left(\frac{P_2 - P_t}{P_1 - P_2}\right) \left[1 - \left(\frac{A_2}{A_1}\right)^2\right]} \quad (6.31)$$

$$\frac{A_2}{A_t} > \sqrt{1 + \left(\frac{C_{d,diff}}{C_{d,inj}}\right) \left(\frac{P_2 - P_v}{P_1 - P_2}\right) \left[1 - \left(\frac{A_2}{A_1}\right)^2\right]} \quad (\text{for critical flow with no margin}) \quad (6.32)$$

$$\frac{A_2}{A_t} > \sqrt{1 + \left(\frac{C_{d,diff}}{C_{d,inj}}\right) \left(\frac{P_2 - 0.8P_v}{P_1 - P_2}\right) \left[1 - \left(\frac{A_2}{A_1}\right)^2\right]} \quad (\text{for critical flow with 20\% margin on } P_v) \quad (6.33)$$

From examination of the equation above, it is clear that the important geometric parameter highlighted is the ratio of the injector exit area  $A_2$  to the injector throat area  $A_t$ . It should be noted that the ratio of exit area  $A_2$  to upstream area  $A_1$  shows up on the right hand side of the equation. In a vast majority of injector

designs, the value of  $(A_2/A_1)$  is close to zero, and due to the fact that it is squared in the equation, the term  $[1 - (A_2/A_1)^2]$  is almost always negligible. This extends to all of the equations in this analysis, however, the term is kept in the analysis for completeness.

The discharge coefficients  $C_{d,inj}$  and  $C_{d,diff}$  do not depend strongly on the geometry of the diffuser and, again, are empirically determined as mentioned earlier. The injector discharge coefficient  $C_{d,inj}$  usually ranges from values of approximately 0.61 to 0.9 and is highly dependent on the geometry of the injector inlet (rounded, chamfered, square edged, etc.), with a slight dependence on Reynolds number. The value of  $C_{d,diff}$  is usually close to 1.0 and can be effected by the surface roughness of the diffuser surface. In cases where the flow separates within the diffuser,  $C_{d,diff}$  can drop significantly away from unity, and the effectiveness of the device can be adversely affected. It is required that the diffuser section for these injectors is designed to avoid separation (i.e. minimize diffuser half angle).

### 6.3 Sample Design/Performance Cases

Based on the above analysis, a few sample calculations have been performed for the design and performance of an isolating injector under varied hypothetical operating conditions. For all of the cases below, the values of  $C_{d,inj}$ ,  $C_{d,diff}$  and  $A_2/A_1$  are assumed to be 0.65, 0.99, and 0.1 respectively. Additionally, the following cases will include a 20% margin on choking with respect to  $P_v$  ( $P_t = 0.8P_v$ ) for the onset of choking. For each of the cases below, two samples of design charts will be included, with at least one for a high vapor pressure propellant (nitrous oxide) and some for a low vapor pressure propellant of interest.

### 6.3.1 Case #1

What is desired in this case is to calculate the minimum required diffuser area ratio  $A_2/A_t$  to provide choking for a propellant injector with a given propellant and temperature for a variety of different combinations of upstream and downstream pressure. The plots included in this section show the minimum required area ratio  $A_2/A_t$  versus the upstream pressure  $P_1$  for a variety of values for the exit pressure  $P_2$ . This type of plot is useful if there is a target downstream pressure, and it is necessary to determine the area ratio necessary for varying upstream pressure. Fig. 6.3 shows this type of analysis for liquid  $N_2O$  at -20 °C (253 K) and Fig. 6.4 is for LOX at -200 °C (73 K). It should be noted that even though the vapor pressures of the 2 fluids are quite different, 260 psia versus 2 psia (1.79 MPa versus 0.01 MPa), the resulting curves are not very different, and it takes careful examination to notice the differences in required area ratio. This is a positive outcome, because this shows that the novel injection scheme presented here is as applicable to low vapor pressure propellants as it is to high vapor pressure propellants.

### 6.3.2 Case #2

In this case, the goal is to calculate the required diffuser area ratio  $A_2/A_t$  to provide choking for a propellant injector with a given propellant and upstream pressure, depending on the combination of downstream pressure at choking and the temperature of the propellant (the vapor pressure of the propellant is a function of the temperature of the propellant). Fig. 6.5 shows results from this type of analysis for liquid  $N_2O$  at 1000 psia (6.89 MPa), and Fig. 6.6 is for liquid methane ( $CH_4$ ) at 1000 psia (6.89 MPa). These results are shown over the entire range of temperatures that each propellant exists as a liquid. Again, while the area ratios  $A_2/A_t$  that are necessary for the two propellants differ, even the liquid methane results show reasonable required area ratios.

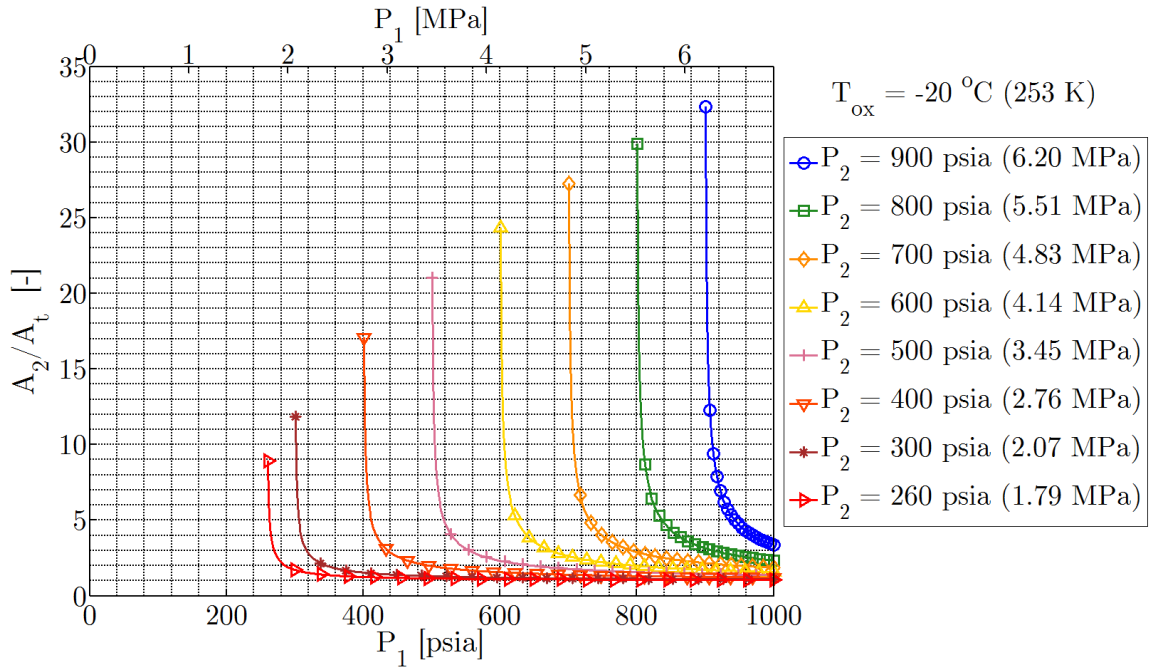


Figure 6.3: Novel injection scheme design plots for sample case #1 for liquid  $N_2O$  at  $-20^{\circ}\text{C}$  (253 K) and  $P_v = 260 \text{ psia}$  (1.79 MPa).

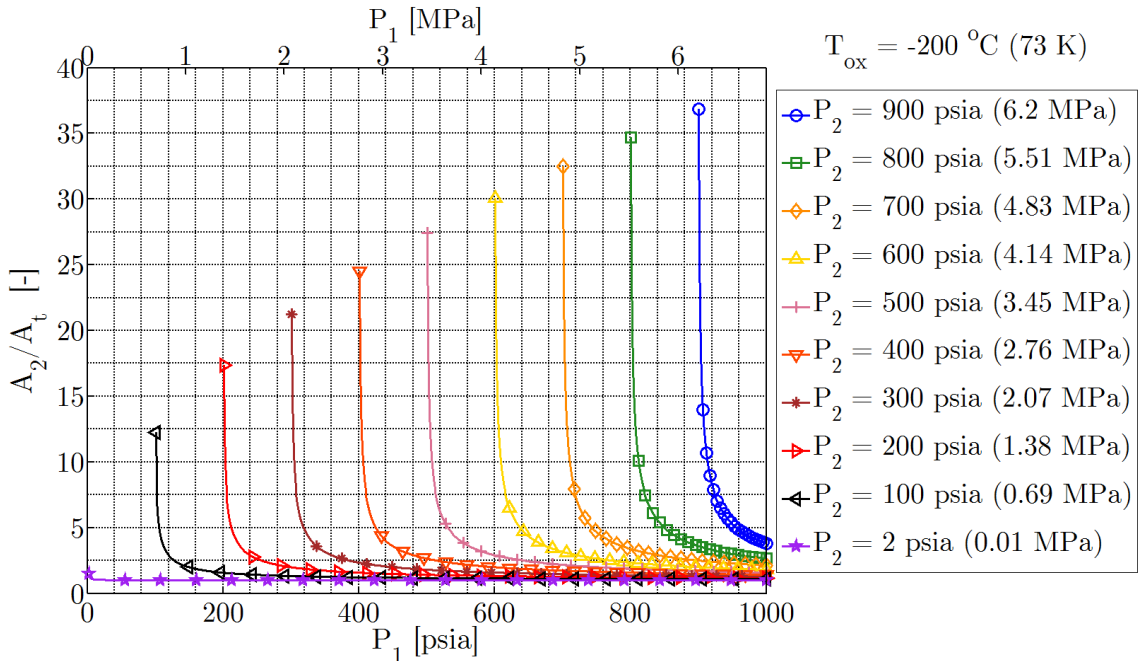


Figure 6.4: Novel injection scheme design plots for sample case #1 for LOX at  $-200^{\circ}\text{C}$  (73 K) and  $P_v = 2 \text{ psia}$  (0.01 MPa).

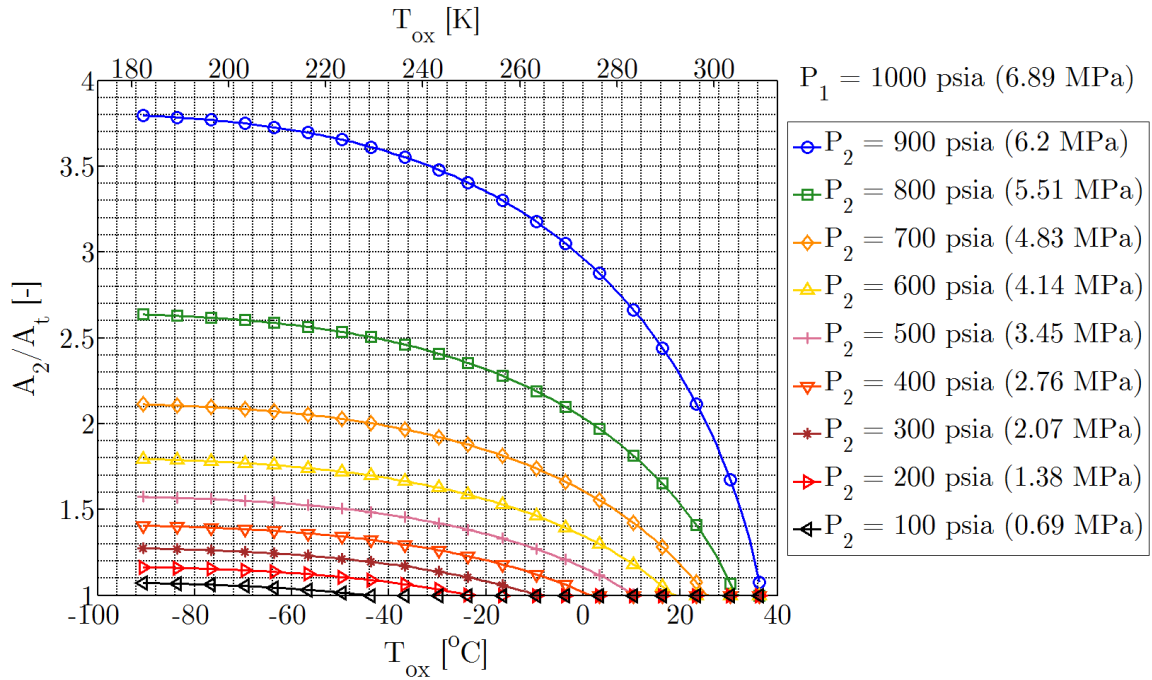


Figure 6.5: Novel injection scheme design plots for sample case #2 for liquid  $N_2O$  at 1000 psia (6.89 MPa).

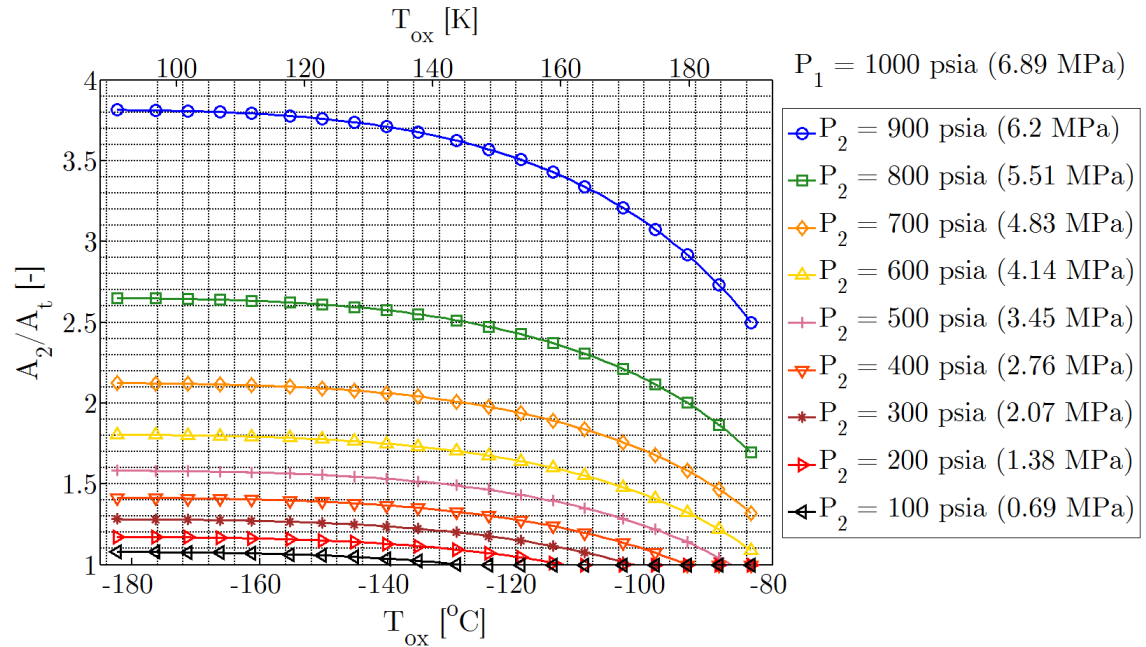


Figure 6.6: Novel injection scheme design plots for sample case #2 for liquid methane ( $CH_4$ ) at 1000 psia (6.89 MPa).

### 6.3.3 Case #3

This case is essentially the opposite as Case #2. This time it is desired calculate the minimum required propellant temperature to provide choking for a propellant injector with a given propellant and fixed geometry (diffuser area ratio  $A_2/A_t$ ) for a variety of different combinations of upstream and downstream pressure. This time we will plot the required propellant temperature versus the exit pressure  $P_2$  for a variety of values for the upstream pressure  $P_1$ . This type of plot is useful if you have an as built injector geometry, a target given upstream pressure, and want to determine the minimum propellant temperature. Fig. 6.7 shows some results for this type of analysis for liquid  $N_2O$  using an injector with an area ration  $A_2/A_t = 2$ , and Fig. 6.8 for  $N_2O$  with an area ration  $A_2/A_t = 5$ . It can be seen that with the larger area ratio injector the minimum temperature for critical flow is generally extremely low, which is expected. However, if an injector is designed with an oversized area ratio on the diffuser, critical flow will happen at a smaller  $\Delta P$  than desired, and insufficient mass flow rates may be achieved.

### 6.3.4 Case #4

In this final case, the goal is to calculate the maximum downstream pressure  $P_2$  where choking is still ensured for an injector with a given propellant and temperature over a range of values of upstream pressure  $P_1$ , with varied injector geometry  $A_2/A_t$ . Results for this type of analysis are included for -60 °C (213 K) liquid  $N_2O$  in Fig. 6.9 and for 20 °C (293 K) ethanol in Fig. 6.10.

## 6.4 Prototype Development and Cold Flow Testing

In order to provide a proof of concept of the novel injection scheme presented in this chapter, a demonstration of the critical flow behavior of a sample injector was performed in the cold flow test rig described in Chapter 3. For this proof of concept,

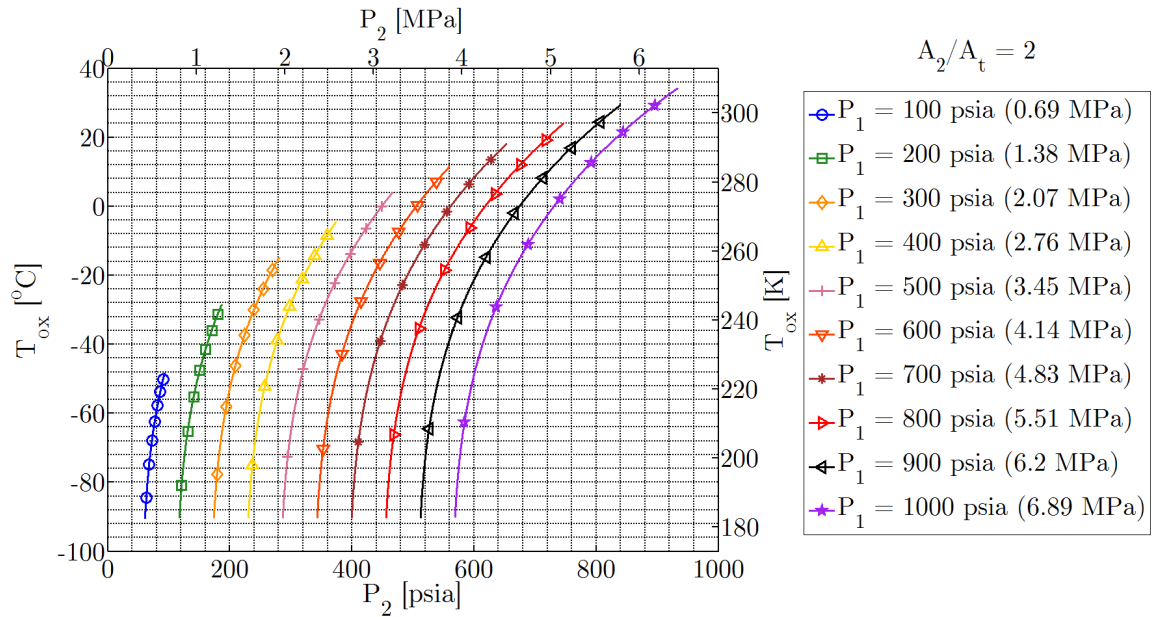


Figure 6.7: Novel injection scheme design plots for sample case #3 for liquid  $N_2O$  with  $A_2/A_t = 2$ .

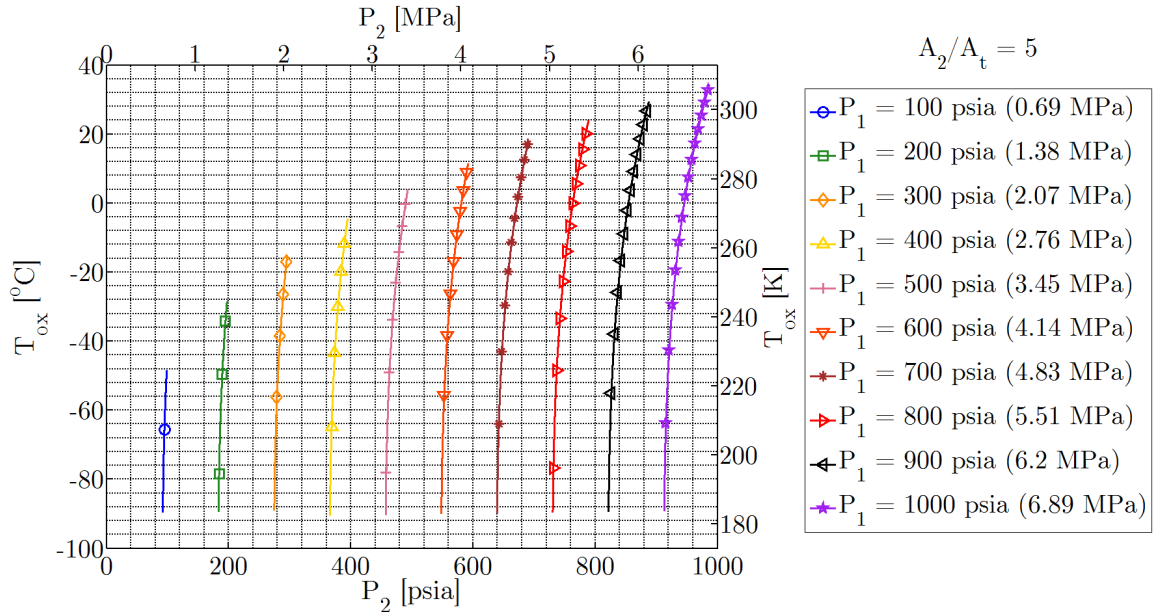


Figure 6.8: Novel injection scheme design plots for sample case #3 for liquid  $N_2O$  with  $A_2/A_t = 5$ .

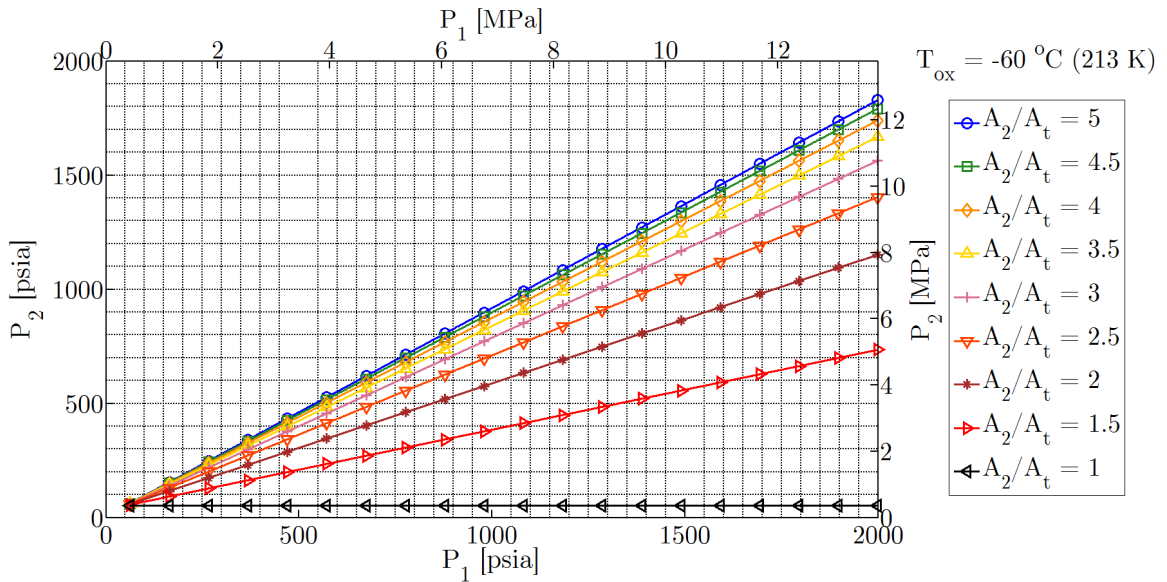


Figure 6.9: Novel injection scheme design plots for sample case #4 for liquid  $N_2O$  at  $-60^{\circ}C$  (213 K) and  $P_v = 61$  psia (0.42 MPa).

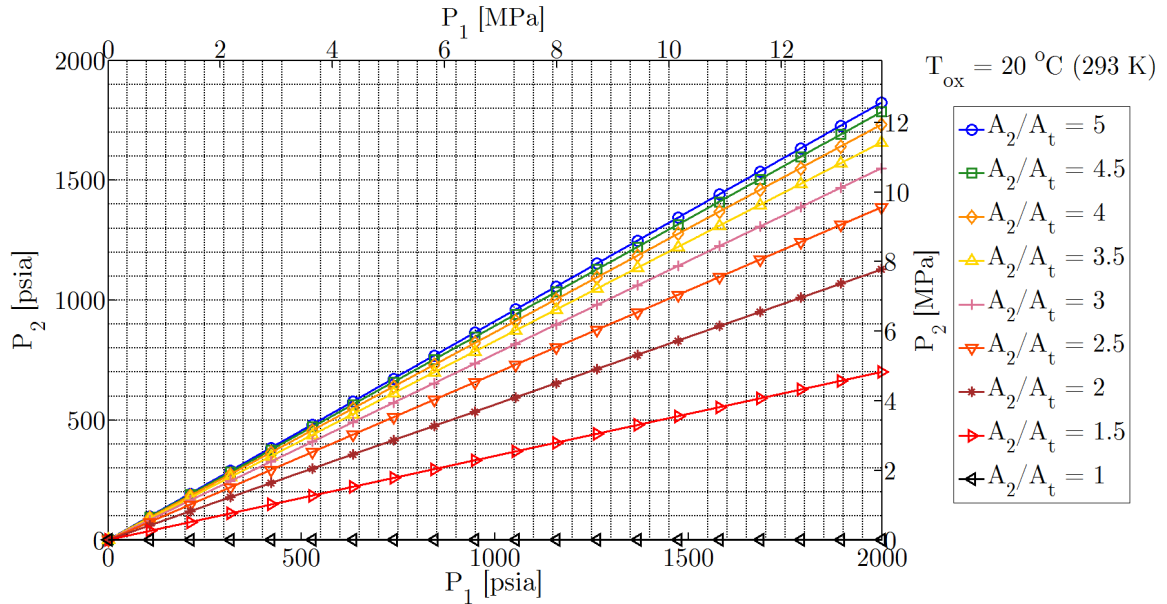


Figure 6.10: Novel injection scheme design plots for sample case #4 for liquid ethanol ( $C_2H_5OH$ ) at  $20^{\circ}C$  (293 K) and  $P_v = 61$  psia (0.42 MPa).

the goal was to design an injector for use with cold nitrous oxide near -20 °C (253 K) at an upstream pressure of approximately 1000 psia (6.89 MPa), that would transition to the critical flow regime at a  $\Delta P$  value in the range of 200-250 psi (1.38-1.72 MPa). Critical flow in this regime would occur with chamber pressures well above the vapor pressure of the nitrous oxide, and would sufficiently validate this technique.

#### 6.4.1 Prototype Design

In order to achieve mass flow rate insensitivity at the operating conditions described above, a sample injector element was designed with a 1.5 mm throat diameter. An area ratio  $A_2/A_t = 2$  was chosen in an attempt to achieve critical flow at the appropriate pressure drop, resulting in a required exit diameter of approximately 2.15 mm. The inlet was slightly rounded, though unfortunately in the as built condition somewhat sharp edges did still exist (this will be evident from the measured discharge coefficient in the single phase region). The overall length of the injector element was kept the same as most of the designs described in Chapter 3, and therefore, the rate of expansion of the diffuser section was only required to be at a half-angle of 1°. Due to this very narrow angle diffuser, there were no concerns about diffuser flow separation. A cross section of the prototype design is shown in Fig. 6.11. This is clearly a moderate design for this new class of injector, so successful results in this series of tests would be highly encouraging in terms of the application of this concept to more aggressive operating constraints.

#### 6.4.2 Cold Flow Testing

A series of cold flow tests were performed using the prototype injector with nitrous oxide at approximately -17 °C (256 K). The corresponding  $N_2O$  vapor pressure is approximately 286 psia (1.97 MPa). These tests were performed for range of supercharge values in order to sweep through many of the possible operating conditions that this sample injector could be practically applied. Fig. 6.12 shows the mass flow rate vs. chamber pressure  $P_2$  for a variety of tests at varying levels of supercharge. The vertical red line on the plot indicates the value of the vapor pressure  $P_v$  for

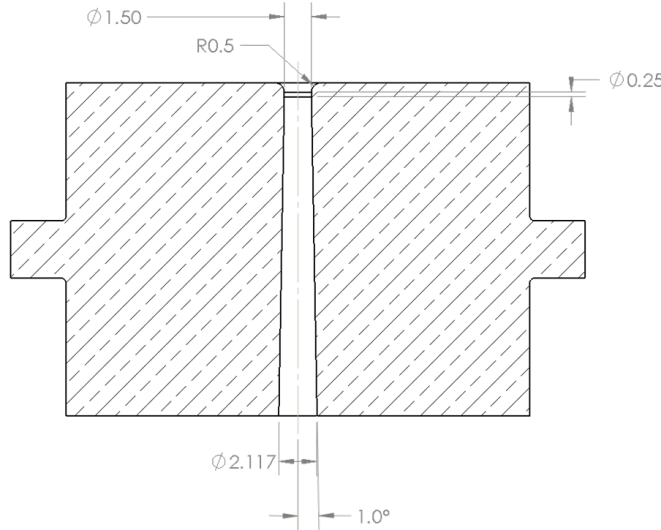


Figure 6.11: Cross-section of the novel injector prototype design (dimensions in mm).

this set of tests. For the same set of tests Fig. 6.13 reports the effective discharge coefficient values vs.  $P_2$ . These tests clearly show that this prototype novel injector design was successful in achieving critical flow at chamber pressures well above vapor pressure. Examining the design point which determined the chosen geometry of the prototype, it can be seen that for the test at 972 psia (6.70 MPa) upstream pressure, the critical flow regime began when the chamber pressure reached approximately 720 psia (4.96 MPa), which corresponds to a pressure drop of approximately 238 psi (1.64 MPa). This is squarely in the range that was targeted by the design. It is also interesting to note the performance at low values of supercharge. Comparing these tests to those performed in Chapter 3 using standard straight hole injectors, it appears that the behavior enters the critical flow regime at higher values of  $P_2/P_v$  using the new injection scheme (see Fig. 5.18). This earlier transition is indeed expected based on the analysis presented above, but these results highlight that the use of this novel injection scheme is likely beneficial in efforts to suppress the feed system coupled instability even at off nominal operating conditions. It is safe to say that these cold flow tests were successful in achieving the proof of concept for the critical flow operation of the new injection scheme proposed in this chapter.

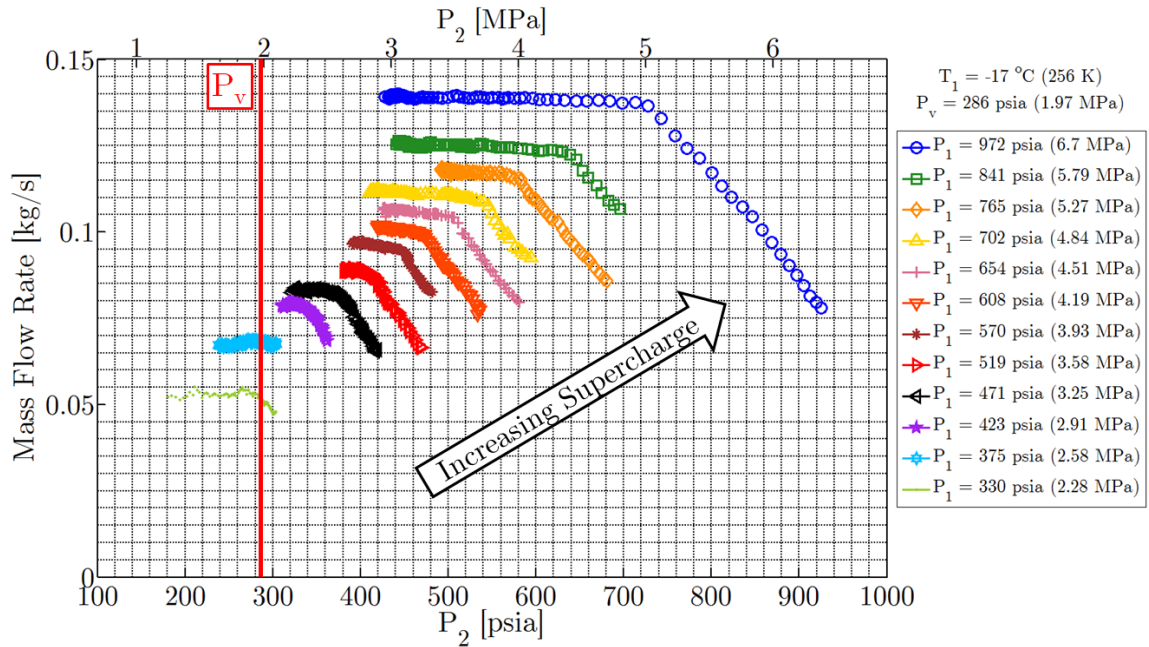


Figure 6.12: Measured  $\dot{m}$  vs.  $P_2$  during cold flow tests of the novel injector prototype using liquid  $N_2O$  at  $-17^\circ\text{C}$  (256 K) at various supercharge levels.

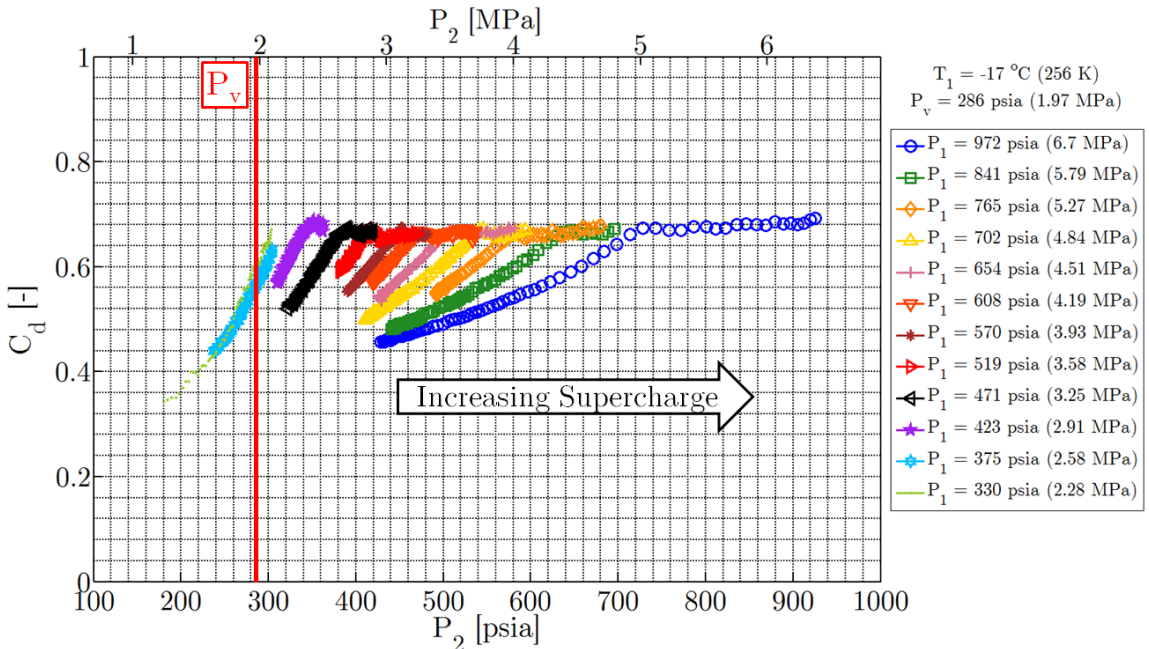


Figure 6.13: Measured  $C_d$  vs.  $P_2$  during cold flow tests of the novel injector prototype using liquid  $N_2O$  at  $-17^\circ\text{C}$  (256 K) at various supercharge levels.

## 6.5 Novel Injection Scheme Conclusions

The critical injector flow criteria for suppressing the feed system coupled instability developed in Chapter 5 can be extremely useful, but typically comes at the cost of overall rocket system performance and requires restrictions on the possible operating conditions of the motor. However, the novel injection scheme presented in this chapter addresses both of these shortcomings, and the author is highly encouraged that this style of injector could be used in an actual hybrid rocket motor resulting in significant improvements to both stability and performance. No hybrid rocket hot fire tests using this style of injector have been performed in the Peregrine heavyweight combustion facility to date, but there are plans to do so in the near future. It is expected that this technology will be adopted in the design of many current and future nitrous oxide based hybrid rockets in order to promote stable combustion. Additionally, while this new class of injector was certainly conceived of with nitrous oxide hybrid rockets in mind, it can be applied to any liquid rocket feed system, even those using traditional low vapor pressure propellants.

# Chapter 7

## Summary and Conclusions

This dissertation was essentially split up into three main parts. Chapter 2 can be described as a basic primer providing a background into the commonly used methods of predicting propellant injector mass flow rates in both the single and two-phase flow regimes. Chapter 3 describes a small scale experimental test apparatus that was used to perform a wide range of injector mass flow rate characterization studies, with some of the representative results highlighted. Chapters 4 through 6 describe the practical application of some of these small scale injector test results to the full scale Peregrine Sounding Rocket hybrid rocket development program, with an emphasis on the suppression of combustion instabilities. The summaries and conclusions from each section of this work are compiled below for convenience, with some important outcomes highlighted. Additionally some recommendations for possible follow-on research associated with injectors for use with high vapor pressure propellants are presented.

### 7.1 Mass Flow Rate Modeling

The simple “ $C_dA$ ” equation as shown in Eq. (2.17) is often the first method used to predict the mass flow rate of liquid propellants in rocket systems (followed by CFD). However, even for purely liquid injector operation, there are a variety of important factors which the engineer must consider in order to achieve accurate mass flow rate

predictions. While the simple “ $C_dA$ ” equation is a useful starting point, the following factors should be considered in order to achieve greater accuracy:

- Compressibility: Determination of compressible liquid correction factor based on isentropic power law formulation of Cornelius and Srinivas.
- Vena contracta: Estimation of the contraction coefficient  $C_{vc}$  using Nurick’s empirical correlation, especially for low L/D injectors.
- Frictional losses: Account for frictional losses at the inlet and along the length of the orifice using classical viscous flow theory of Darcy-Weisbach and Blasius in order to estimate the discharge coefficient  $C_d$ . Computational fluid dynamics (CFD) is also useful here.

This work has shown that with the introduction of two-phase flow, the simple “ $C_dA$ ” equation is not applicable with regard to mass flow rate predictions. A variety of models attempt to account for the effects of two-phase flow, and do seem to capture the general mass flow rate behavior that should be expected. Some highlights of these two-phase flow models are included below:

- Homogeneous equilibrium models are simple and can be easy to implement, but tend to underpredict flow rates. Improved homogeneous equilibrium methods can be computationally expensive.
- Non-homogeneous equilibrium models provide improved predictions compared to equilibrium models and are generally simple to implement. However they are not always generally applicable (e.g. Fauske).
- Frozen non-equilibrium models are straightforward to implement, but are almost exclusively empirically based.
- Generalized non-equilibrium models can be relatively complicated but can account for potential metastable liquid conditions through physical models

However, none of these models agree in the prediction of actual critical mass flow rate values over a wide range of operating conditions, and it is not obvious which models

are the most accurate for application to rocket propellant injectors. In fact, it was shown that none of these models predict the critical mass flow rate to much better than  $\pm 15\%$  over a wide range of operating conditions. Therefore, cold flow testing of nitrous oxide injectors is still necessary for the reliable prediction of injector mass flow rates during hot fire testing, and can be useful for assessing the accuracy of the different two-phase flow models.

## 7.2 Experimental Cold Flow Testing

The small scale cold flow test rig developed for this work has proven to be extremely useful in the characterization of nitrous oxide injector mass flow rate performance. Not only was this test apparatus useful for learning more about the behavior of nitrous oxide injectors operating in the two-phase flow regime, but it also allowed for the favorable assessment of carbon dioxide as an analog for nitrous oxide in these types of injector experiments. Results from testing in this rig constitute the beginnings of a new database for the recording of nitrous oxide injector mass flow rate performance data. Some of the important outcomes based on this experimental work are outlined below, and these experimental results verified the general trends predicted by the two-phase flow models described above:

- $C_d$  in the single-phase region is inversely proportional to the injector hole diameter and independent of supercharge level.
- Critical mass flow rate is proportional to supercharge level for a given injector.
- Small L/D injectors can exhibit higher critical mass flow rates than high L/D injectors of the same diameter. This is due to the fact that critical flow does not occur until lower values of  $P_2/P_v$  for low L/D injectors.
- Mass flow rate is enhanced by rounding or chamfering the inlet for both the single-phase and critical flow regimes. However, little improvement is seen by switching from chamfered to rounded

Using this data, the accuracy of a few of the two-phase flow models described in Chapter 2 has been evaluated, however more experimental cold flow data would be required to make a definitive ranking of model performance. However, at this point it is still useful to increase confidence in the mass flow rate performance predictions of a given injector geometry and operating conditions using a cold flow test setup like the one presented in this work. None of the two-phase flow models can provide the confidence that comes with experimental cold flow measurements.

## 7.3 Applications to Hybrid Rocket Combustion Instability

Low frequency combustion instabilities have proven to be a major obstacle for hybrid rocket development programs over the past few decades. The feed system coupled combustion instability has been particularly problematic for hybrid rocket development programs utilizing nitrous oxide as the oxidizer. While cavitating venturis can be used as isolation elements in order to eliminate the feed system coupled instability from hybrid rockets which use LOX, the risk of a decomposition reaction explosion prohibits this solution for nitrous oxide systems. However, based upon the small scale injector cold flow results from Chapter 3, it was determined that a critical flow injector could provide the necessary isolation to suppress the feed system coupled instability. This theory was tested in the full scale Peregrine Sounding Rocket heavyweight combustion facility with tremendous success, leading to highly stable combustion. The results from Tests E3-4 and E4-1 signal a major step forward in the understanding and suppression of combustion instabilities in hybrid rocket motors, not only for the Peregrine Sounding Rocket program, but for the industry as a whole.

The critical injector flow criteria for suppressing the feed system coupled instability developed in Chapter 5 can be extremely useful, but typically comes at the cost of overall rocket system performance and requires restrictions on the possible operating conditions of the motor. However, the novel injection scheme presented

in this dissertation addresses both of these shortcomings, and the author is highly encouraged that this style of injector could be used in an actual hybrid rocket motor resulting in significant improvements to both stability and performance. No hybrid rocket hot fire tests using this style of injector have been performed in the Peregrine heavyweight combustion facility to date, but there are plans to do so in the near future. It is expected that this technology will be adopted in the design of many current and future nitrous oxide based hybrid rockets in order to promote stable combustion. Additionally, while this new class of injector was certainly conceived of with nitrous oxide hybrid rockets in mind, it can be applied to any liquid rocket feed system, even those using traditional low vapor pressure propellants.

## 7.4 Future Work

As mentioned above, none of the two-phase flow models presented in this work have proven robust enough to completely replace cold flow testing when it comes to the determination of hybrid rocket injector mass flow rates for hot fire testing *a priori*. Therefore, continued model development is required, especially in a fashion integrated with modern CFD tools. This type of analysis is necessary in order to provide accurate predictions of both the single phase discharge coefficient of a particular injector design, as well as its critical flow rate characteristics over arbitrary operating conditions.

In order to facilitate the development and validation of improved models, more cold flow testing should be performed to continually expand on the existing injector performance characterization databases. Additionally, further cold flow testing should be used to study the effects of dissolved gas and its desorption on the inception of cavitation and critical flow within the injector. Not only should these types of studies be performed for the typically inert pressurant gases that are dissolved in nitrous oxide such as helium, but also reactive pressurants such as oxygen. This is of interest based on the possible use of a new and exciting class of oxidizer called Nytrrox [66], as well as for the design of hybrid rockets that use the pressurant as a

propellant, the advantages of which are described by Chandler et al. [67].

Another area of interest for cold flow testing of nitrous oxide injectors is related to the isolation performance as described in Section 5.3.1.2. Specifically, studies that allow for visualization of the cavitation environment within the actual injector element would provide useful information to improve the understanding of pressure disturbance isolation. A better knowledge of the actual location of bubbles within the injector could aid in the design of better isolating injectors.

With regard to the novel cavitating venturi style injectors described in Chapter 6, continued cold flow testing should be aimed at characterizing the design limitations with relation to critical flow. It would be useful to develop a set of guidelines pertaining to the allowable diffuser divergence angles and design criteria to ensure the flow remains attached within the diffuser section. Also, cold flow tests with some traditional low vapor pressure oxidizers such as LOX (or liquid nitrogen as an analog) should be performed to demonstrate the usefulness of this technology for a broad range of rocket applications.

Finally, next steps in the full scale Peregrine Sounding Rocket development program should include hot fire testing using the cavitating venturi style injector. While cold flow studies have proven that an appropriately designed cavitating venturi injector should provide critical flow under conditions which would improve the overall performance of the Peregrine hybrid rocket, the ability to suppress the feed system coupled instability under these conditions has not been demonstrated as of yet.

## Appendix A

### Cold Flow Reference Test Data

Table A.1: Description of injector design geometry.

Number	Style	D [mm]	L [mm]	L/D	Entrance Geometry
(1)	Straight	0.79	18.4	23.4	Square Edge
(2)	Straight	1.50	18.4	12.3	Square Edge
(3)	Straight	1.50	18.4	12.3	Rounded
(4)	Straight	1.50	18.4	12.3	Chamfered
(5)	Straight	1.93	18.4	9.5	Square Edge
(6)	Straight	1.50	3.2	2.1	Square Edge
(7)	Cavitating Venturi	1.50 (throat)	18.4	12.3	Rounded

Table A.2: Outline of Figures Included as Reference Data

Fig.	Data	Fluid	Injector	$\Delta P$	$P_{super}^1$	$T_1$	$P_1$
				psi (MPa)	psi (MPa)	°C (K)	psia (MPa)
A.1	$\dot{m}$	$N_2O$	1	25 - 425 (0.17-2.93)	129 - 382 (0.89-2.63)	4 - 8 (277-281)	631 - 929 (4.35-6.40)
A.2	$C_d$	$CO_2$	1	20 - 510 (0.14-3.52)	124 - 332 (0.85-2.29)	10 - 12 (283-285)	773 - 1025 (5.33-7.07)
A.5	$\dot{m}$	$N_2O$	2	10 - 690 (0.07-4.76)	90 - 422 (0.62-2.91)	7 - 10 (280-283)	632 - 1006 (4.36-6.93)
A.7	$\dot{m}$	$CO_2$	2	0 - 605 (0-4.17)	104 - 301 (0.72-2.07)	5 - 13 (278-286)	700 - 969 (4.83-6.68)
A.9	$\dot{m}$	$N_2O$	3	0 - 675 (0-4.65)	41 - 371 (0.28-2.56)	7 - 10 (280-283)	583 - 952 (4.02-6.56)
A.10	$C_d$	$CO_2$	3	0 - 700 (0-4.83)	59 - 317 (0.41-2.19)	8 - 10 (281-283)	686 - 970 (4.73-6.69)
A.13	$\dot{m}$	$CO_2$	4	0 - 705 (0-4.86)	85 - 372 (0.59-2.56)	8 - 10 (281-283)	702 - 1023 (4.84-7.05)
A.15	$\dot{m}$	$N_2O$	5	0 - 560 (0-3.86)	78 - 420 (0.54-2.9)	8 - 11 (281-284)	638 - 1002 (4.4-6.91)
A.17	$\dot{m}$	$CO_2$	6	0 - 840 (0-5.79)	59 - 395 (0.41-2.72)	6 - 10 (279-283)	706 - 1003 (4.87-6.91)
A.19	$\dot{m}$	$N_2O$	7	30 - 541 (0.21-3.73)	28 - 705 (0.19-4.86)	-19 - -15 (254-258)	330 - 972 (2.27-6.93)
A.20	$C_d$						

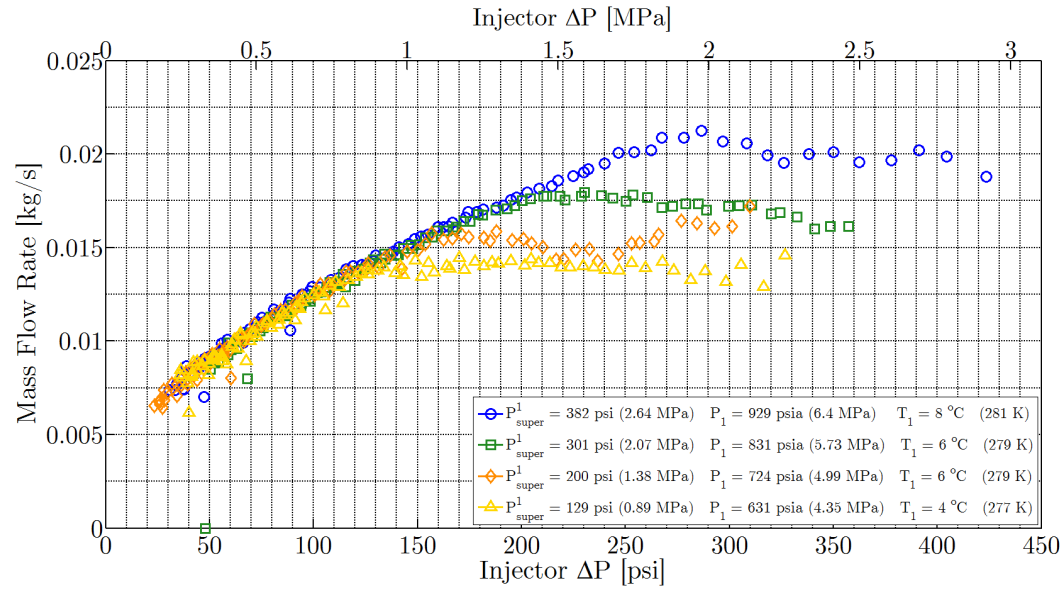


Figure A.1:  $\dot{m}$  vs.  $\Delta P$  and supercharge for injector number 1 with nitrous oxide.

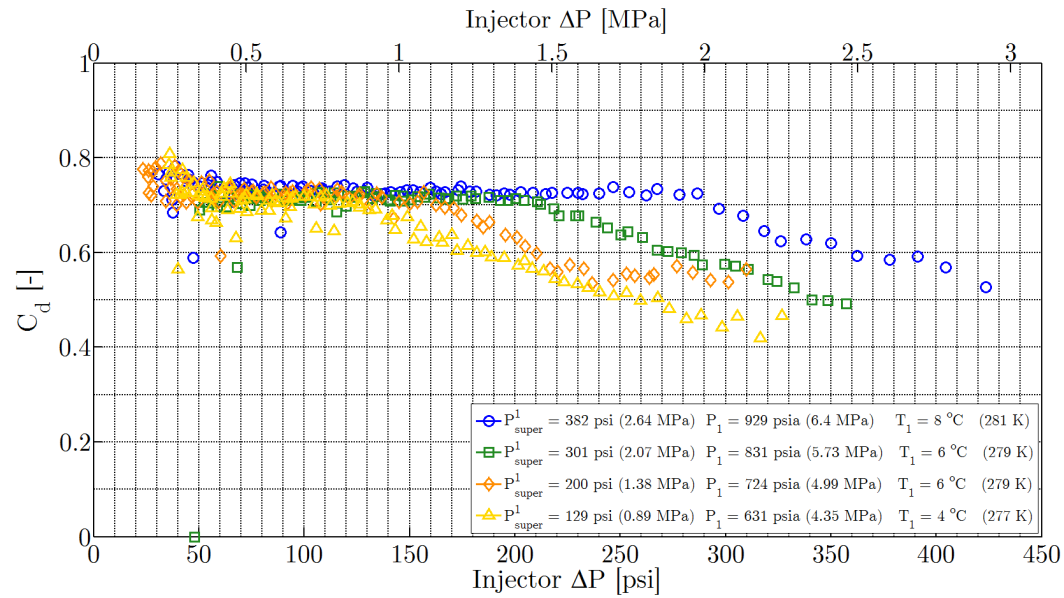


Figure A.2:  $C_d$  vs.  $\Delta P$  and supercharge for injector number 1 with nitrous oxide.

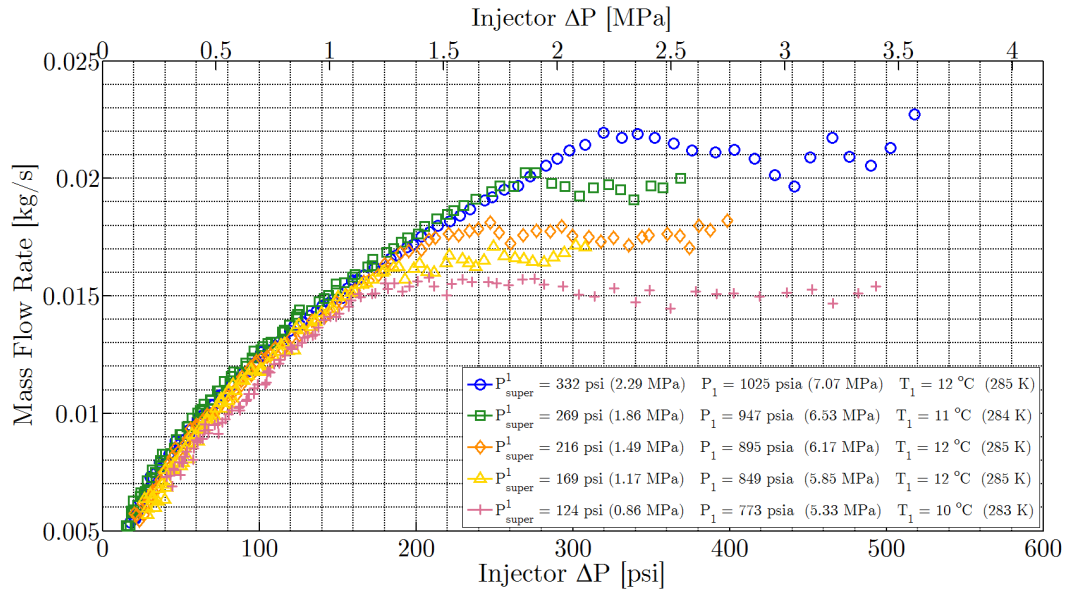


Figure A.3:  $\dot{m}$  vs.  $\Delta P$  and supercharge for injector number 1 with carbon dioxide.

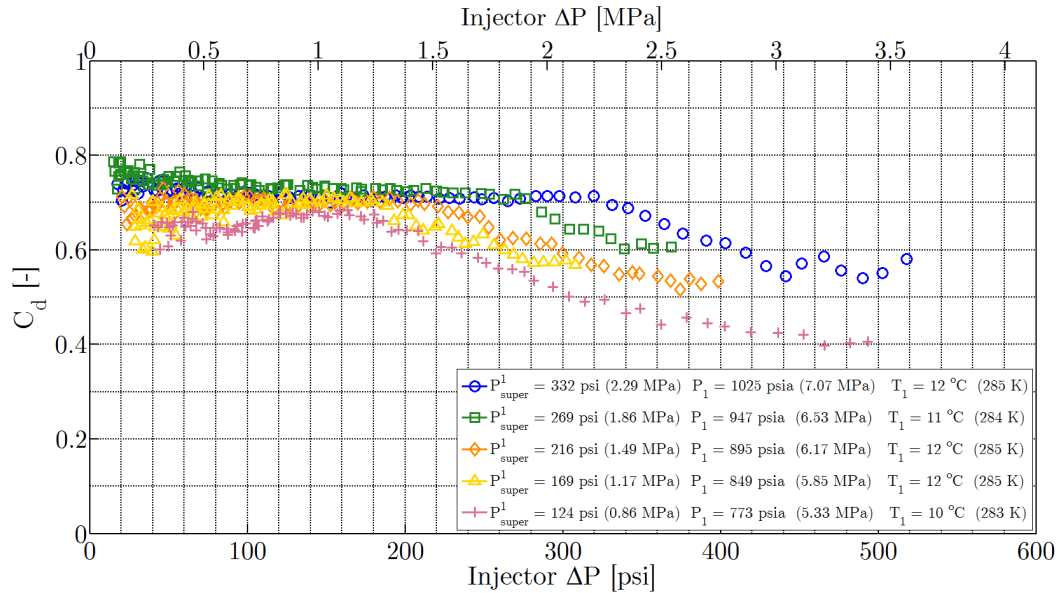


Figure A.4:  $C_d$  vs.  $\Delta P$  and supercharge for injector number 1 with carbon dioxide.

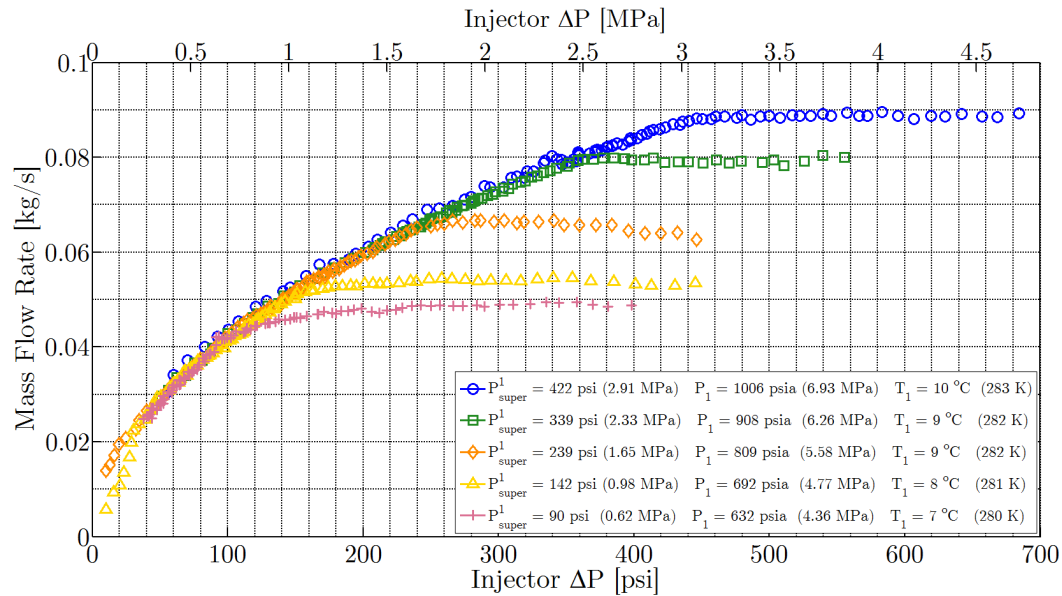


Figure A.5:  $\dot{m}$  vs.  $\Delta P$  and supercharge for injector number 2 with nitrous oxide.

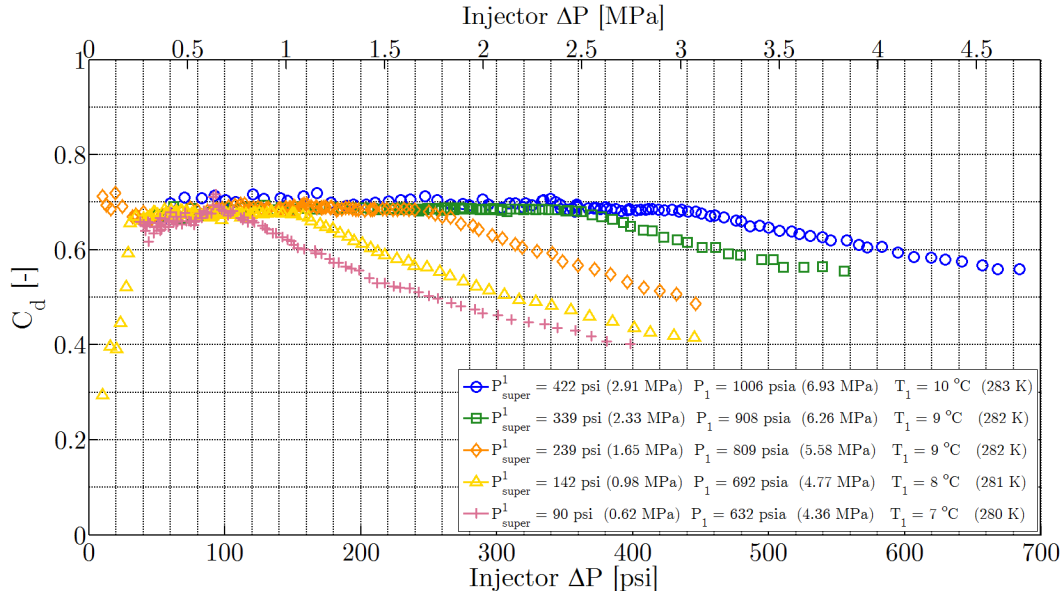


Figure A.6:  $C_d$  vs.  $\Delta P$  and supercharge for injector number 2 with nitrous oxide.

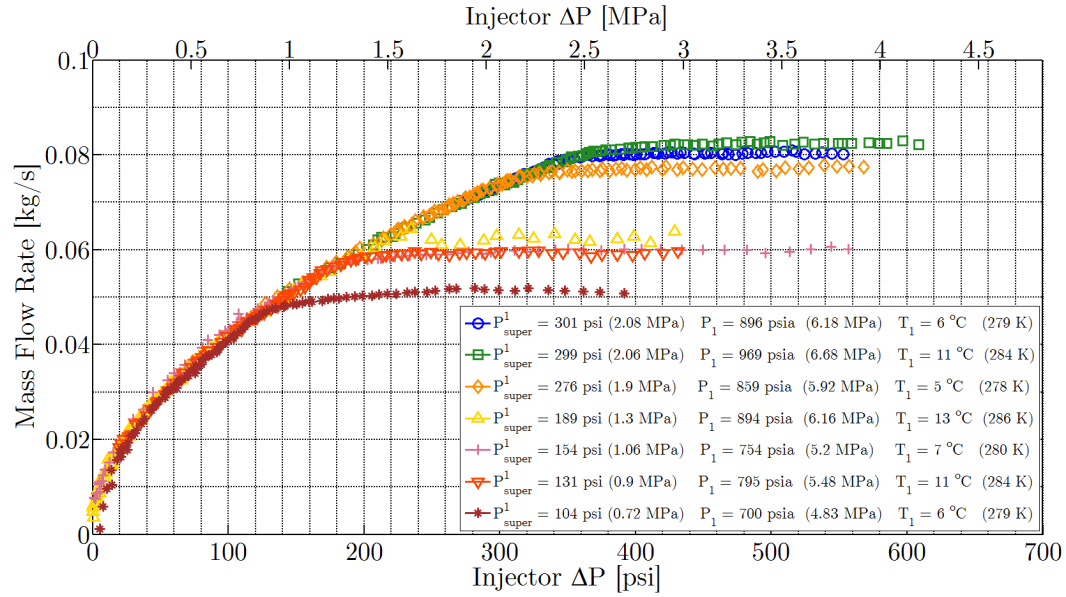


Figure A.7:  $\dot{m}$  vs.  $\Delta P$  and supercharge for injector number 2 with carbon dioxide.

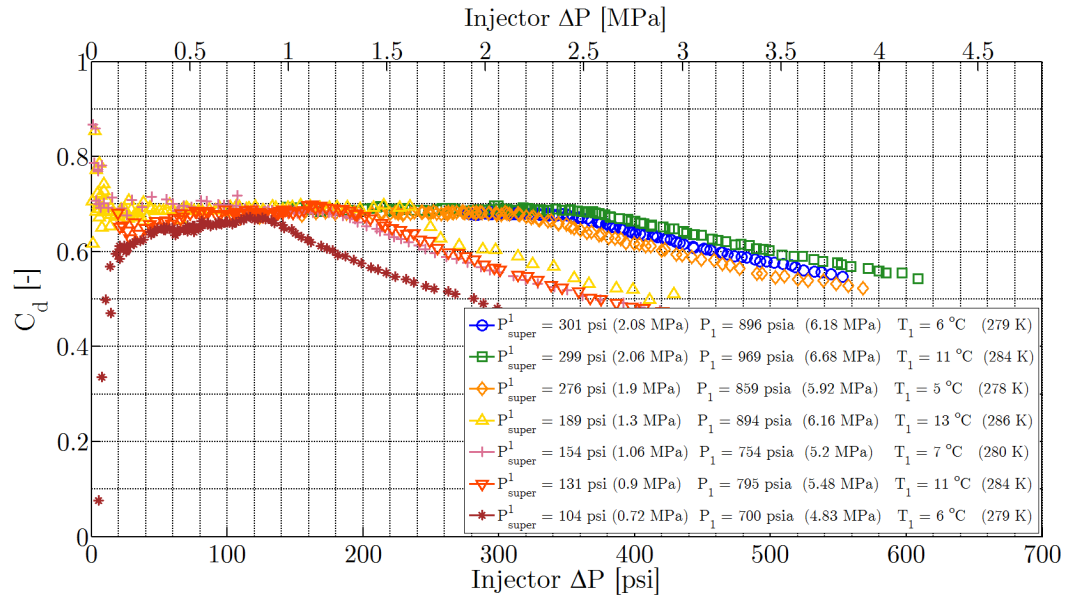


Figure A.8:  $C_d$  vs.  $\Delta P$  and supercharge for injector number 2 with carbon dioxide.

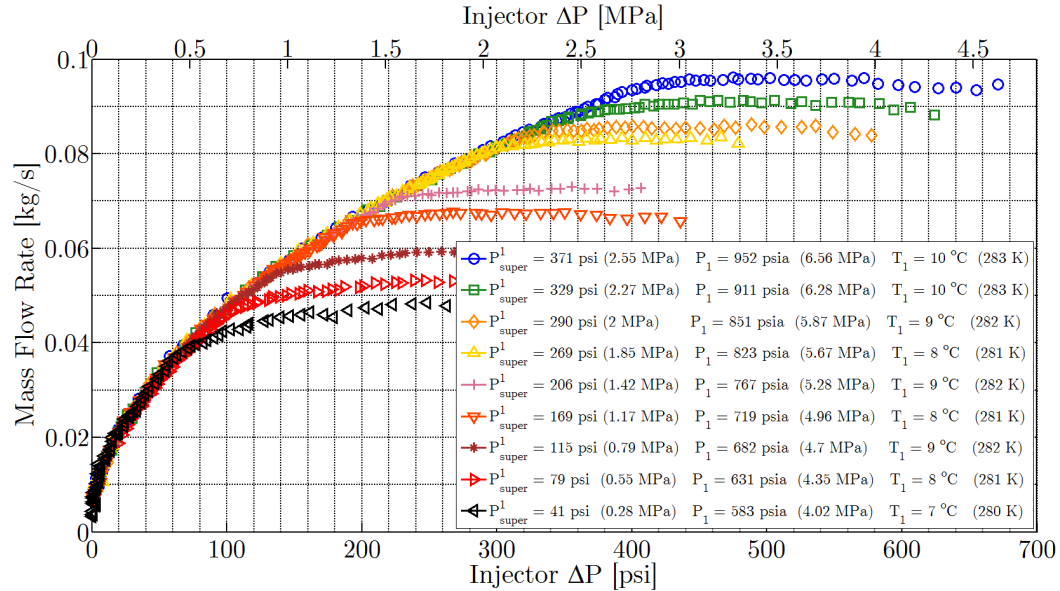


Figure A.9:  $\dot{m}$  vs.  $\Delta P$  and supercharge for injector number 3 with nitrous oxide.

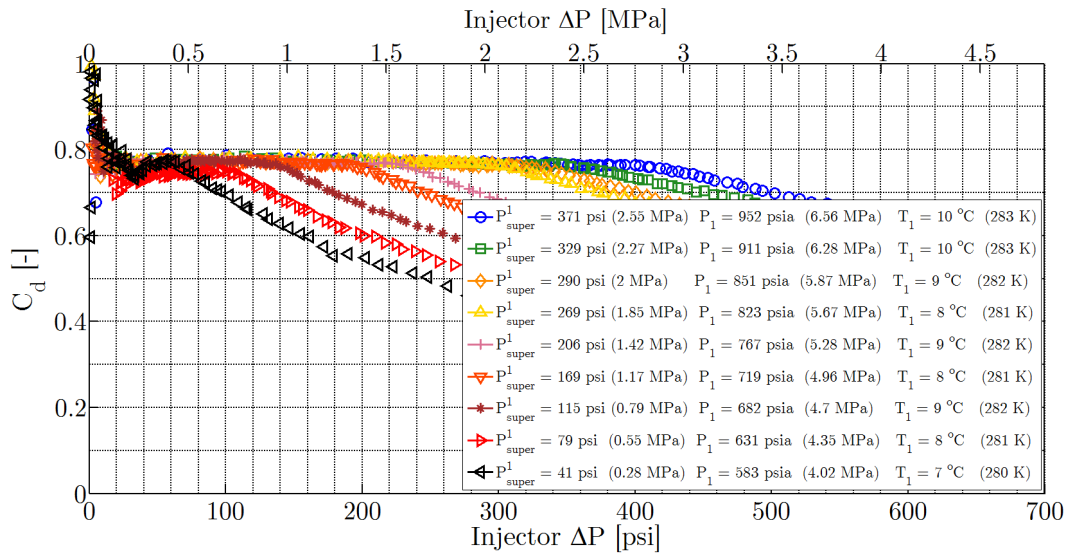
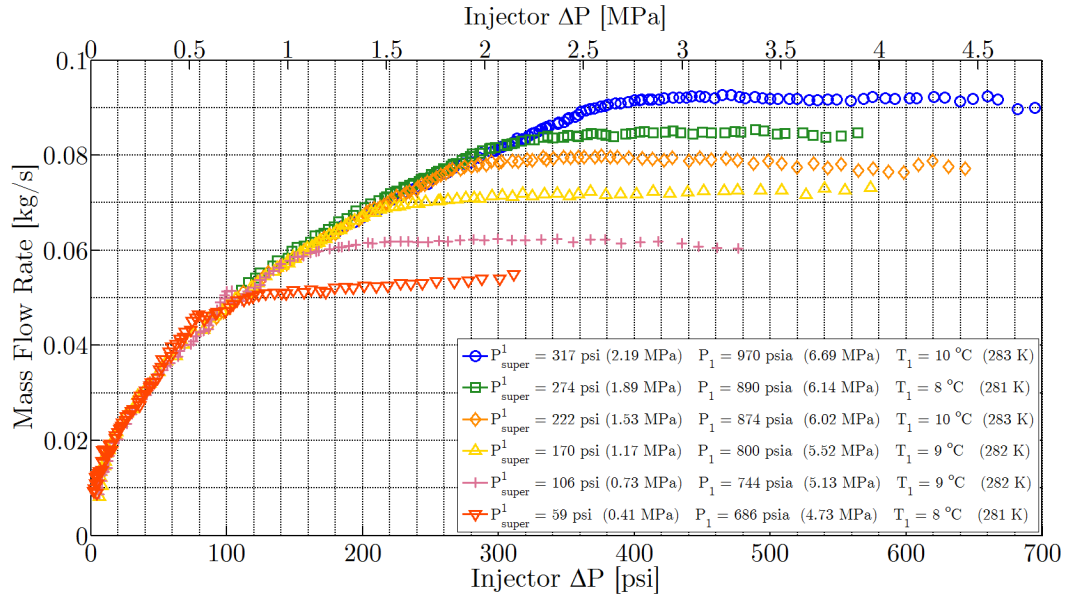
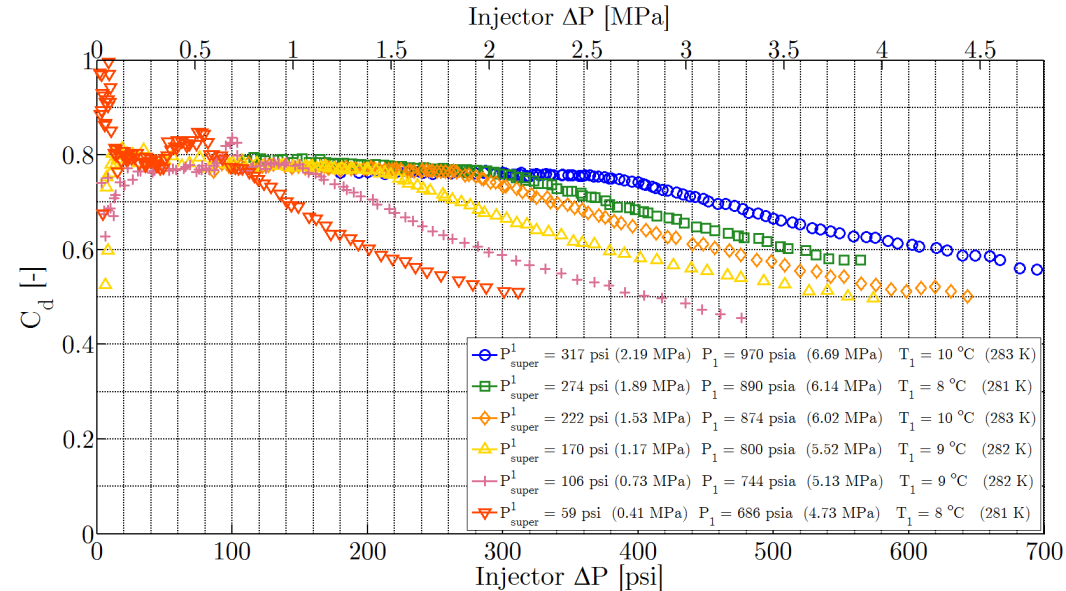


Figure A.10:  $C_d$  vs.  $\Delta P$  and supercharge for injector number 3 with nitrous oxide.

Figure A.11:  $\dot{m}$  vs.  $\Delta P$  and supercharge for injector number 3 with carbon dioxide.Figure A.12:  $C_d$  vs.  $\Delta P$  and supercharge for injector number 3 with carbon dioxide.

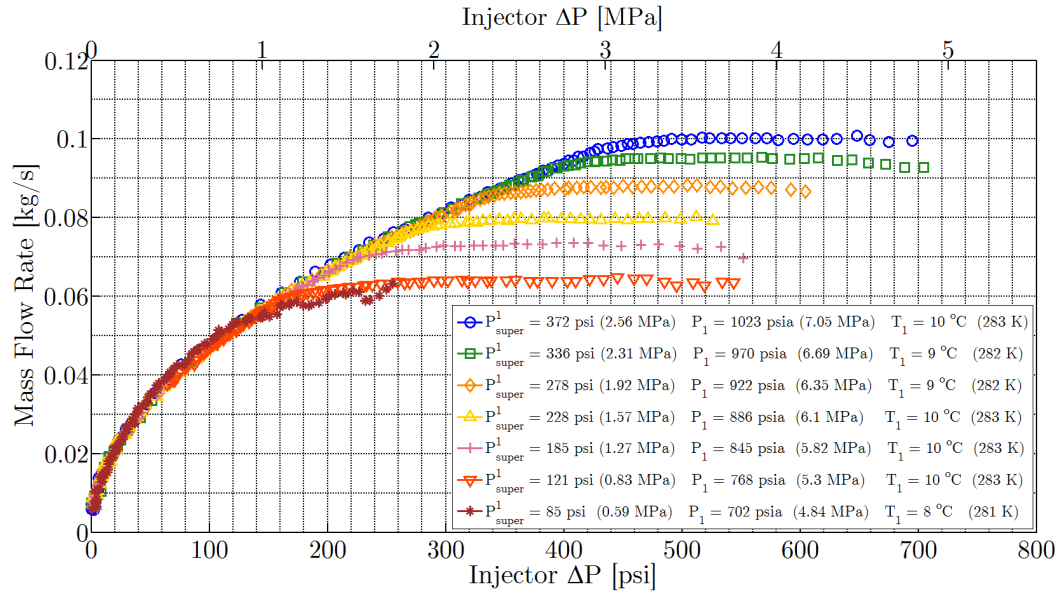


Figure A.13:  $\dot{m}$  vs.  $\Delta P$  and supercharge for injector number 4 with carbon dioxide.

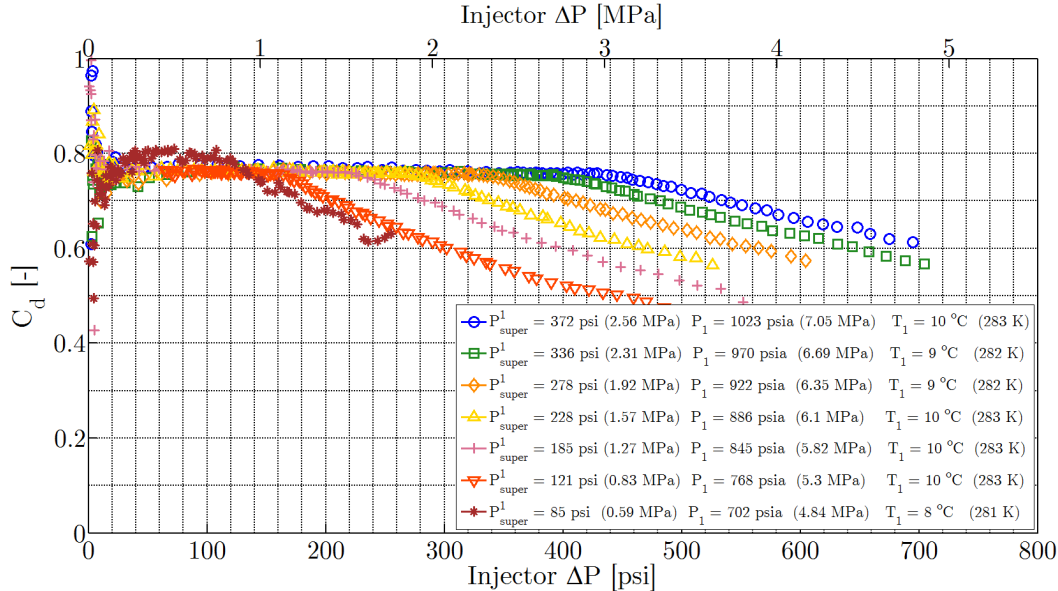
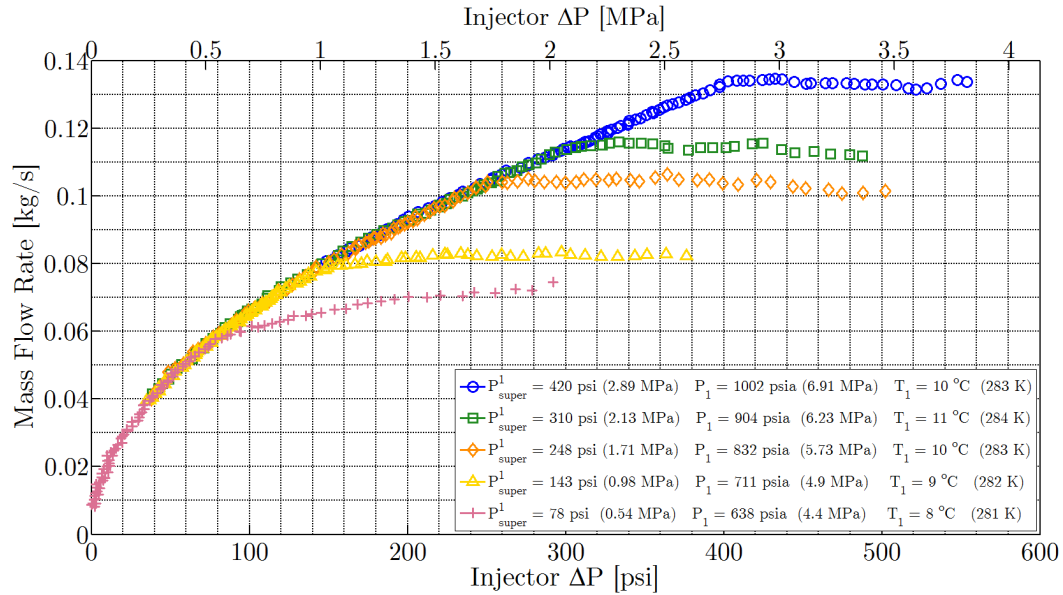
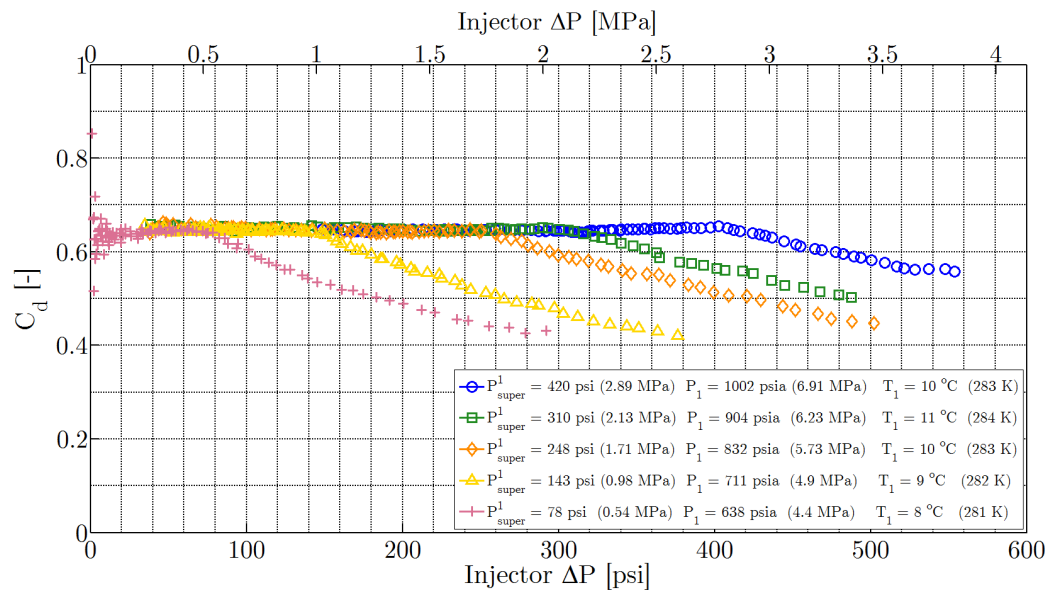


Figure A.14:  $C_d$  vs.  $\Delta P$  and supercharge for injector number 4 with carbon dioxide.

Figure A.15:  $\dot{m}$  vs.  $\Delta P$  and supercharge for injector number 5 with nitrous oxide.Figure A.16:  $C_d$  vs.  $\Delta P$  and supercharge for injector number 5 with nitrous oxide.

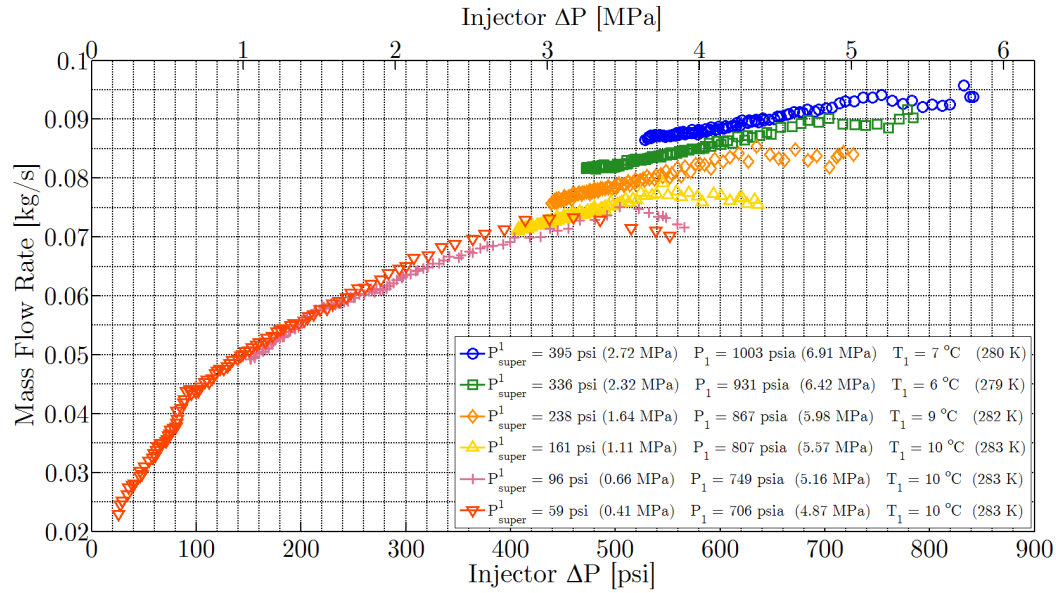


Figure A.17:  $\dot{m}$  vs.  $\Delta P$  and supercharge for injector number 6 with carbon dioxide.

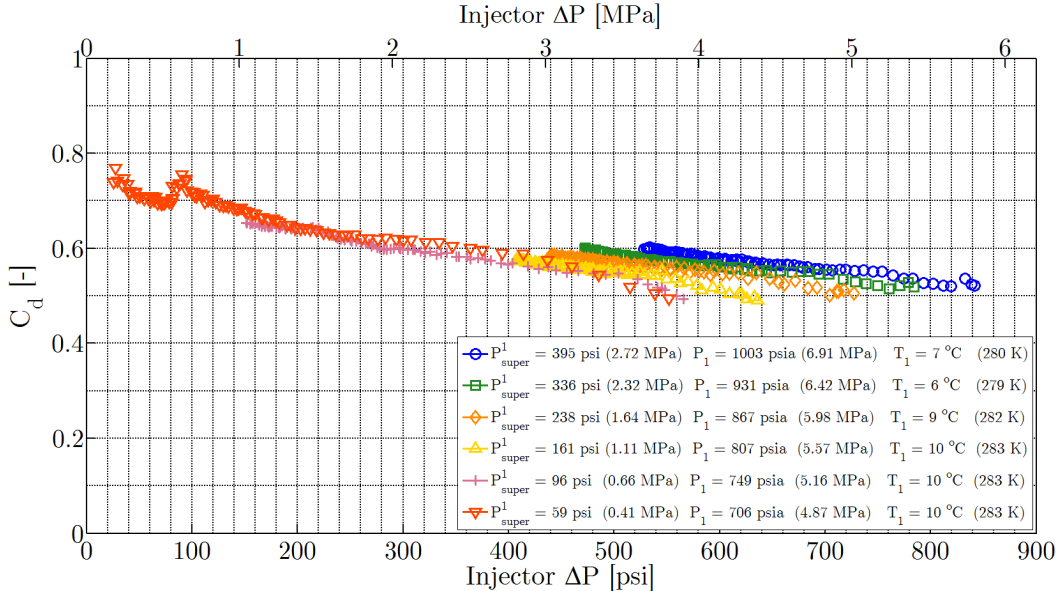


Figure A.18:  $C_d$  vs.  $\Delta P$  and supercharge for injector number 6 with carbon dioxide.

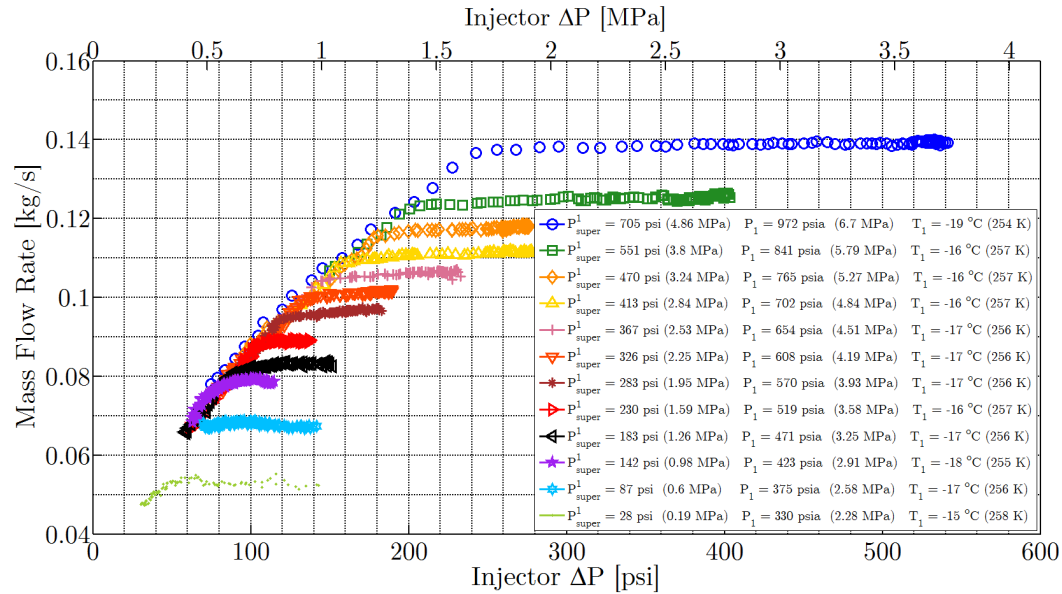


Figure A.19:  $\dot{m}$  vs.  $\Delta P$  and supercharge for injector number 7 with nitrous oxide.

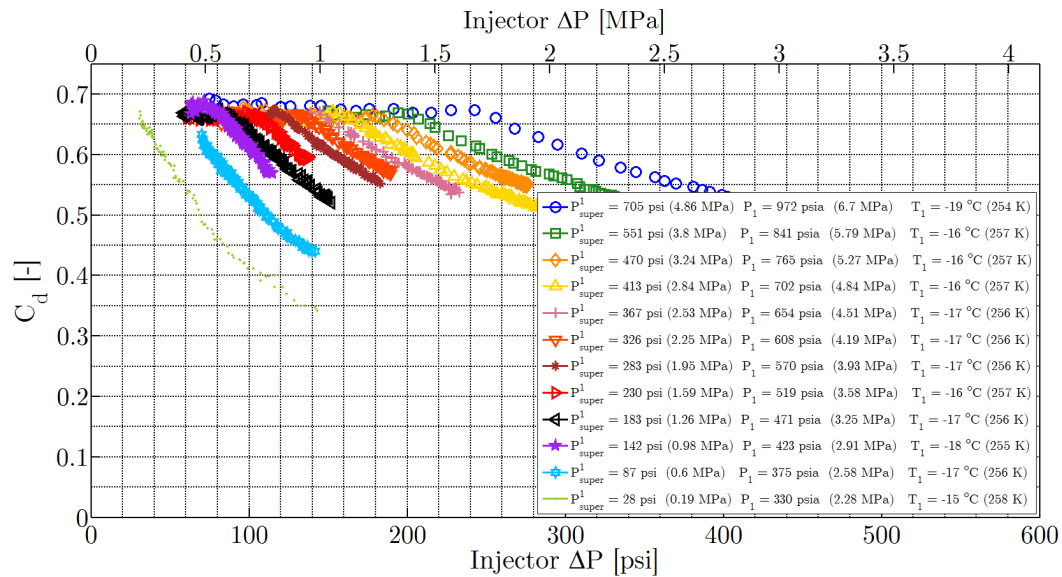


Figure A.20:  $C_d$  vs.  $\Delta P$  and supercharge for injector number 7 with nitrous oxide.

# **Appendix B**

## **Cold Flow Visualization Experiments**

### **B.1 Background**

Single element (i.e. non impinging) liquid propellant injectors usually operate by either the mechanical breakup or flash atomization of a liquid jet. The mechanical breakup mode is dominated by aerodynamic and viscous effects, wherein an unstable jet forms a droplet spray. Flash atomization can occur when a liquid jet becomes metastable in a superheated state due to the sudden pressure drop across the injector. With sufficient superheat and the presence of bubbles or nucleation sites, the jet can break up in a more violent manner due to rapid bubble growth, often resulting in sprays of much finer droplets than observed in the mechanical breakup mode (allowing for rapid evaporation and mixing). For traditional liquid propellants (e.g. LOX, hydrogen peroxide, kerosene, etc.), these different atomization regimes have been relatively well studied, due to their extensive use in the liquid rocket industry, in addition to the fact that they can often be treated as incompressible in the liquid phase, and as ideal gases in the vapor phase. This is not the case for the high vapor pressure propellant nitrous oxide, which is typically used as a compressible liquid.

In 1986, Kitamura et al. studied the transition between the mechanical breakup mode and flash atomization for superheated water and ethanol [68], and more recently Cleary et al. extended this analysis to describe a flashing transition region[69]. Correlations for critical superheating was presented based upon two dimensionless thermodynamic parameters, the vapor Weber number,  $We_V$ , and the Jakob number,  $Ja$ , as well as a density correction factor,  $\Phi$ , each defined in Eqns. (B.1-B.3) below.

$$We_V = \frac{\rho_V u^2 D}{\sigma} \quad (B.1)$$

$$Ja = \frac{\rho_L c_{p,L} (T - T_s)}{\rho_V h_{fg}} \quad (B.2)$$

$$\Phi = 1 - \exp \left( -2300 \frac{\rho_V}{\rho_L} \right) \quad (B.3)$$

where  $u$  is the liquid jet velocity,  $D$  is the hole diameter,  $\sigma$  is the liquid surface tension,  $c_{p,L}$  is the specific heat of the liquid,  $T$  is the liquid temperature,  $T_s$  is the saturation temperature corresponding to the downstream pressure  $P_2$ , and  $h_{fg}$  is the latent heat of vaporization. The liquid density,  $\rho_L$ , is based on the liquid flowing into the injector, while the vapor density,  $\rho_V$ , is calculated for the conditions just downstream of the injector. The Weber number represents the ratio of the inertia of a fluid to its surface tension, and is often used in the characterization of liquid jet sprays. Hence, there does not seem to be a clear physical basis for using the vapor Weber number in these correlations versus the liquid Weber number. The Jakob number is the ratio of sensible to latent enthalpy released by a fluid during the phase change from liquid to vapor. The correlations presented Kitamura and Cleary are plotted in Fig. B.1 below. While quite useful for some applications, these correlations are limited to Weber numbers of approximately 25 or lower, meaning they are not applicable to most rocket systems using liquid nitrous oxide injectors (Weber numbers greater than  $10^4$  are common due to high flow velocities and low surface tension).

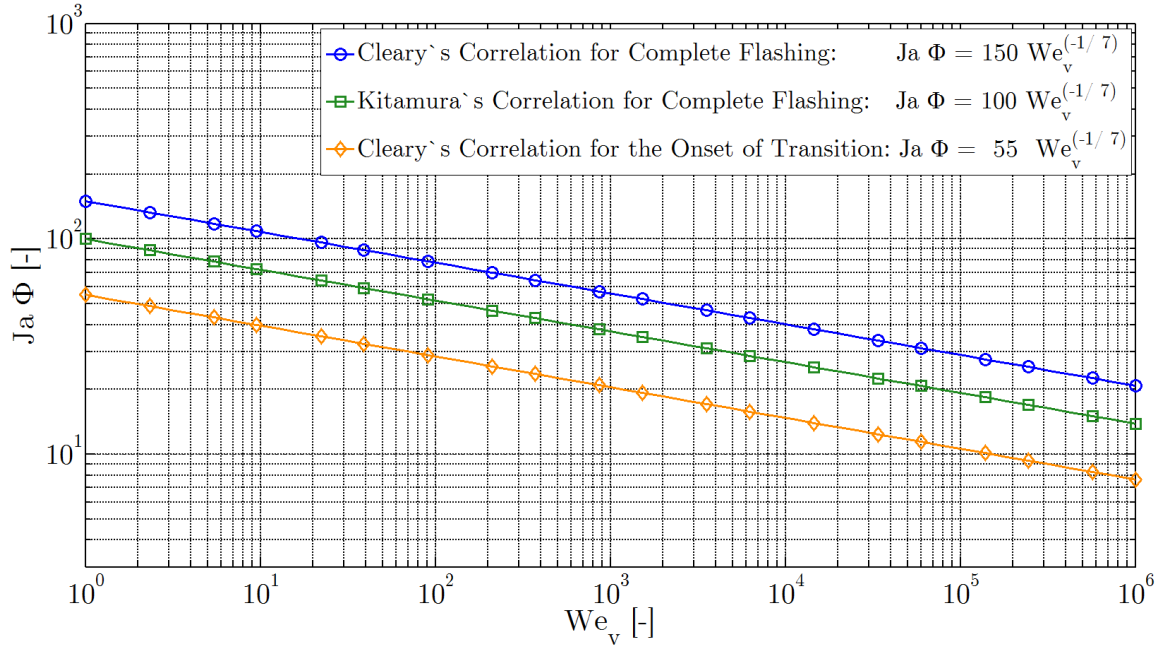


Figure B.1: Correlations of critical Jakob and Weber numbers as developed by Kitamura and Cleary et. al. [68, 69].

Unfortunately, nitrous oxide injector design is not well understood due to a lack of heritage, as well as the difficulties in modeling associated with non-ideal compressibility effects (compressibility factor  $Z \sim 0.13$  for saturated liquid,  $Z \sim 0.53$  saturated vapor). Work in 2007 by Dyer et al. addressed the compressible liquid and real gas effects in the modeling of two-phase injectors for self-pressuring oxidizers [30]. Their model demonstrates good agreement with regards to mass flow rate, specifically in comparison to measurements from sub-scale hybrid rocket tests for a variety of injector designs. However, as of yet, there have not been adequate studies into the modeling and experimental testing of nitrous oxide injector designs with regard to atomization characteristics. It is standard practice in the development of hybrid rockets to perform cold flow testing (oxidizer flow only, no ignition) in order to characterize a given injector design in terms of mass flow rate and atomization. However, most cold flow tests are not performed at the actual operating pressures observed during combustion testing. Of particular importance is the pressure drop  $\Delta P$  across the injector, which is the difference between  $P_1$  and  $P_2$ , the pressures immediately upstream

and downstream of the injector, respectively. Cold flow testing typically results in a much larger  $\Delta P$  than would be expected during tests involving combustion, which is a concern when it comes to understanding the mechanisms for atomization and vaporization of liquid jets. This appendix describes some initial visualization results achieved in the same facility used the cold flow testing of nitrous oxide injectors at realistic operating pressures.

## B.2 Experimental Setup

In order to characterize the breakup modes and atomization characteristics of different injector designs, the same cold flow testing apparatus described in Chapter 3 was used for the visualization of oxidizer flow fields just upstream and downstream of the interchangeable injector plate. Transparent polycarbonate tubes pressure vessels allow for optical access to the flow field created by the injector. The goal of this setup is to allow for the observation of the atomization process at realistic operating pressures downstream of the injector, while keeping track of the flow conditions upstream of it. A cut-away model of the optical test section along with a photo of the assembled hardware are shown in Fig. 3.1 in Section 3.1.1.1. A high-speed camera is used to record video of the flow field at frame rates ranging from 300 to 1200 frames per second. A laser sheet is employed to illuminate the center plane of the flow using standard 532 nm laser pointer and a borosilicate glass rod 3 mm in diameter. Additionally, pressure and temperature are measured in both the upstream and downstream polycarbonate chambers at sampling rates from 500 Hz up to 1,000 Hz. A process and instrumentation diagram (P&ID) with more details on the fluid handling and instrumentation of the system can be found in Fig. C.1. Pressure and temperature measurements are made in both the pre-injector volume and the downstream chamber, allowing for the instantaneous measurement of  $\Delta P$  and supercharge pressure, as well as a host of other fluid dynamic properties. An LED is precisely controlled and placed within the camera's field of view in order to facilitate the synchronization of high speed video with pressure and temperature data, and the creation of individual flow images overlayed with time-dependent flow

Table B.1: Description of injector designs included in initial experiments

Number	Style	$D$ (mm)	$\frac{L}{D}$	Entrance Geometry	Material
(1)	Single	1.50	12.3	Square Edge	Brass
(2)	Single	1.50	12.3	Rounded	Brass
(3)	Single	1.50	12.3	Chamfered	Brass
(4)	Single	0.79	23.3	Square Edge	Brass
(5)	Impinging	1.50	12.3	Rounded	Plastic

information.

An assortment of injector inserts have been manufactured for initial testing in the optical testing facility. This first set of injectors have been designed to investigate the atomization characteristics of injectors with varying hole diameter,  $D$ , and hole length to diameter ratio,  $L/D$ , as well as the effect of injector hole entrance geometry (square edge, rounded, chamfered etc). During initial testing, the length,  $L$ , of each injector hole is fixed at a typical injector plate thickness of approximately 18.4 mm. Future testing will allow for the variation of the injector insert thickness and hole length. The specific geometries of each injector insert are outlined in Table B.1, and cross-sections of each are shown in Fig. B.2. All of the single hole injector inserts are manufactured using brass, a metal commonly used in hybrid rocket injectors due to its heat transfer characteristics and machinability.

Interesting work performed in 1992 by Kuo et al. suggests that like-on-like impinging injector designs could improve flash atomization [70]. Specifically it was proposed that impinging flash atomizers could result in a wider, more thoroughly atomized spray fan, with finer, more evenly distributed droplets. Like-on-like impinging injectors have seen widespread use in the liquid rocket industry, and the associated atomization properties have been well studied. However, self-pressurized oxidizers such as nitrous oxide are virtually untested in like-on-like impinging injector designs. Therefore, the optical injector test setup will be used to characterize a range of different self impinging doublet designs, varying both the impingement included angle,

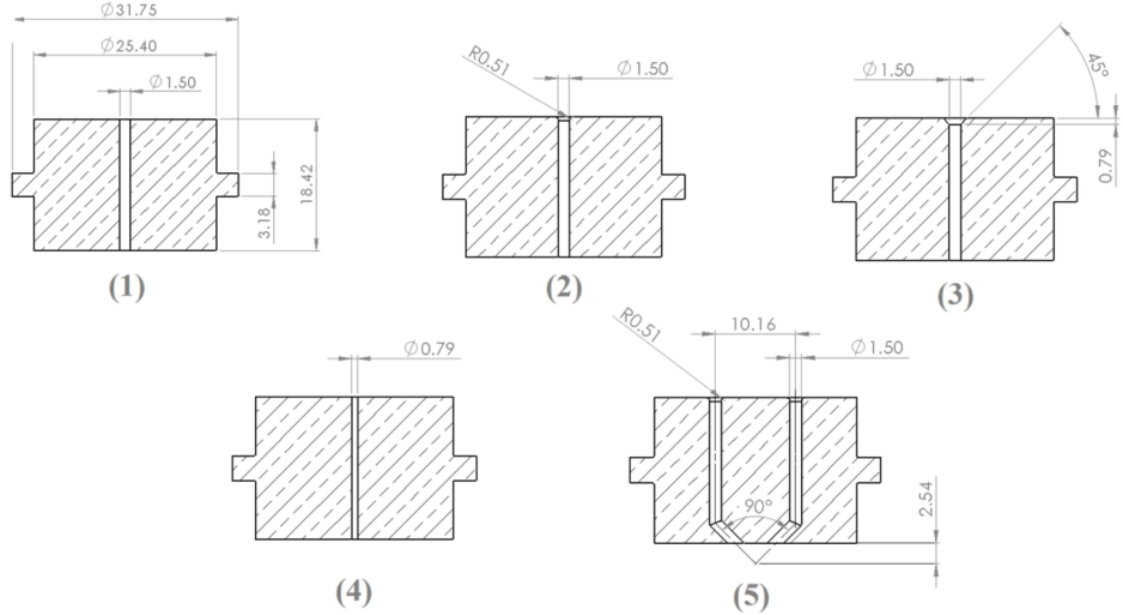


Figure B.2: Cross-sections of injector inserts tested during initial experiments (all dimensions in  $mm$ ) with numberings corresponding to descriptions in Table B.1.

$\theta$ , and impingement distance,  $x_i$ . One of these impinging injectors was tested during these initial experiments, with its geometry also detailed in Table B.1 and Fig. B.2. It should be noted that the impinging design tested in these experiments consists of a straight section followed by a bend to establish the impingement angle. This design requires minimal space laterally and allows for a large number of doublets to be placed in a full scale injector. The injector for these experiments has an included impingement angle of  $90^\circ$  and an impingement distance of  $2.54\text{ mm}$ . While machining the more complicated geometries from brass is possible, the impinging injector inserts are manufactured using rapid prototyping stereolithography for convenience. Plastic branded as Accura 60 (by 3DSystems) is used and has properties similar to polycarbonate, specifically with regard to strength and stiffness. Fig. B.3 shows a photo of one brass injector insert and one impinging plastic injector insert tested during the initial experiments. Future work will compare the results of identical hole designs using both brass and plastic to determine the effect of manufacturing methods and materials on atomization.

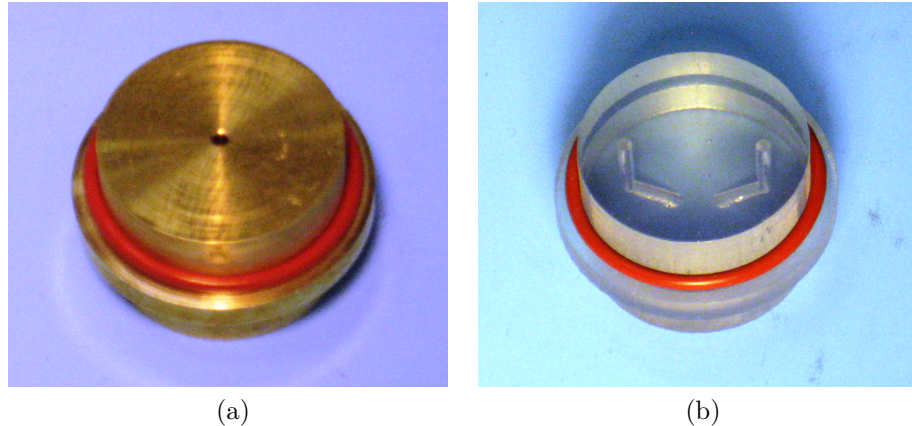


Figure B.3: Brass and plastic injector inserts for initial testing with corner O-rings installed.

### B.3 Visualization Results and Discussion

To date, over 200 tests have been performed in the new injector testing facility, investigating the jet characteristics of 5 different injectors using carbon dioxide. Experiments have been performed over a wide range of chamber pressures and  $\Delta P$  values, with chamber pressure ranging from atmospheric conditions up to approximately 1000 psia (6.89 MPa). In this section, some representative test results are presented, and images from the testing of each injector are compared to one another.

A typical test is prepared by filling the carbon dioxide run tank to a desired fill level. After letting the run tank contents settle to a stable temperature and pressure condition, the downstream chamber and pre-injector volume are pressurized to a predetermined level with compressed helium or nitrogen, and the run tank is supercharged using compressed helium to the desired initial run pressure. An exhaust valve is connected to the downstream section, as shown in Appendix C, but it remains closed until after the test is completed. Once the desired tank and chamber conditions are met, a pneumatically actuated ball valve located between the tank and the pre-injector volume is opened to initiate a test. During a test, both the pre-injector volume and the downstream chamber gradually increase in pressure.

The pressure drop,  $\Delta P$ , is established as the pressure in the pre-injector volume rises faster than in the chamber. Because the chamber exhaust valve remains closed, at a certain point the chamber pressure begins to catch up with the pre-injector volume until the pressure drop across the injector becomes zero, and the test is completed. This dynamic testing process allows for a sweep of operating pressures during a single test (future work will utilize a back pressure valve to perform tests with steady  $\Delta P$  conditions, which should allow for better visualization). Pressure time histories in the pre-injector volume and the chamber are shown for a typical test in Fig. 3.8, where the main ball valve is opened at time  $t = 0s$ .

During each test, high speed video at 300 frames per second or higher was recorded. After each test, every frame from the video was matched with the corresponding data points. In addition to measuring temperatures and pressures for each of the frames, a venturi flow meter and a Stellar Technologies, Inc. differential pressure transducer were used to calculate mass flow rate. However, a detailed analysis of the system mass flow rate and the characterization of injector discharge coefficients are currently ongoing, and will not be presented in this paper. In order to compare the atomization behavior for these initial experiments, images at various  $\Delta P$  values for each injector are shown in Figures B.4-B.8 below. All of these tests were performed at instantaneous chamber pressures ranging from 500 to 580 psia (3.45 to 4.00 MPa) and supercharge pressures of approximately 50 psi (0.35 MPa). Images from these tests demonstrate the flash atomization mode and are characterized by the creation of an aerosol “cloud” of small vaporizing droplets downstream of the injector.

From initial examination of the images in Figures B.4-B.8, it is observed that the jets developed by injectors (1) - (3) are relatively indistinguishable. Slight variations in the diameter and character of the initial jets can be seen as they leave the injectors, likely due to varying internal flow phenomena. Acquisition of higher resolution and more closely zoomed photos is ongoing and will be necessary to resolve these details. It is expected that these internal flow characteristics depend on both the level of supercharge and the value of  $\Delta P$ , and will significantly influence the mass flow rate characteristics of a particular injector, and thus the discharge coefficient. When

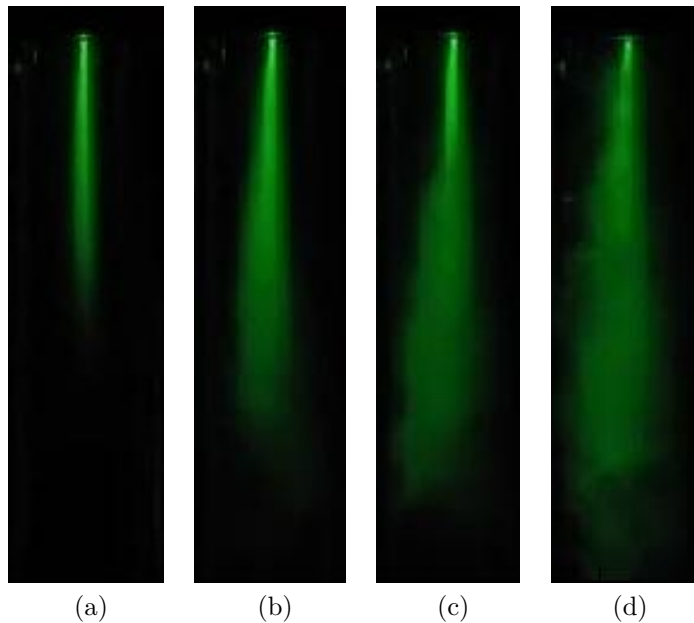


Figure B.4: Injector (1) images at (a)  $\Delta P = 5$  psi (0.03 MPa), (b)  $\Delta P = 50$  psi (0.34 MPa), (c)  $\Delta P = 100$  psi (0.69 MPa), and (d)  $\Delta P = 200$  psi (1.38 MPa).

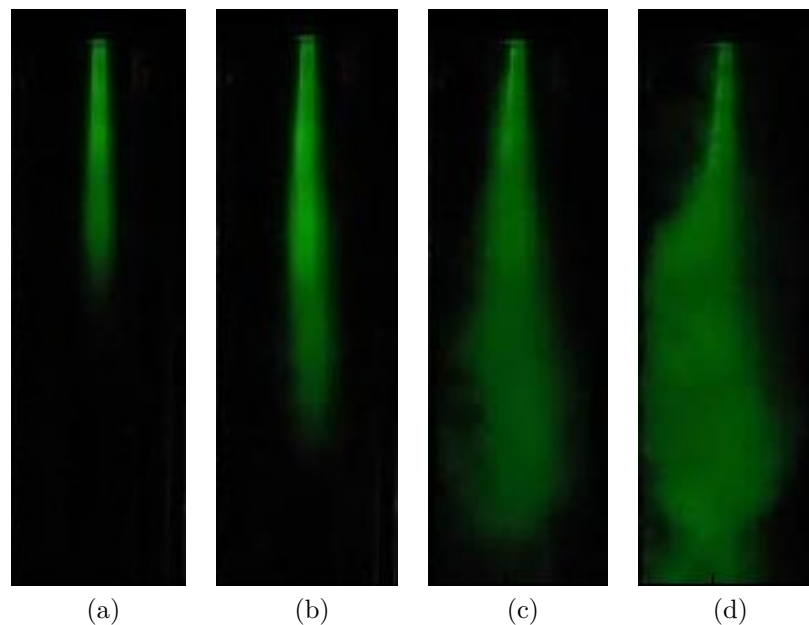


Figure B.5: Injector (2) images at (a)  $\Delta P = 5$  psi (0.03 MPa), (b)  $\Delta P = 50$  psi (0.34 MPa), (c)  $\Delta P = 100$  psi (0.69 MPa), and (d)  $\Delta P = 200$  psi (1.38 MPa).

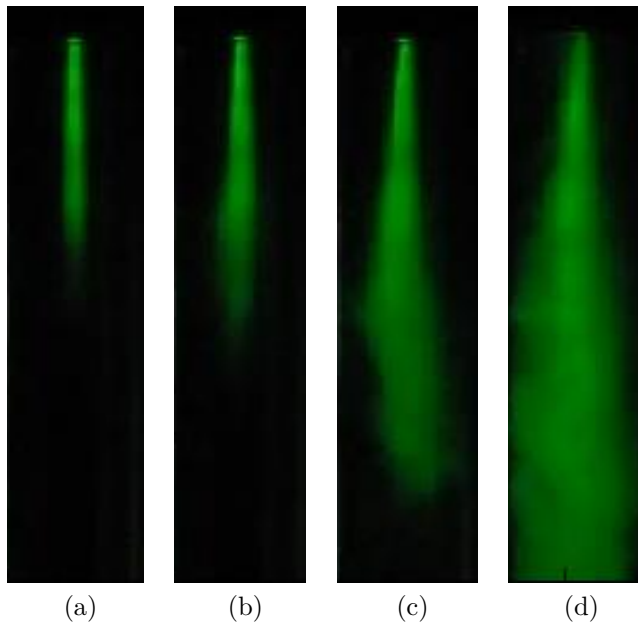


Figure B.6: Injector (3) images at (a)  $\Delta P = 5$  psi (0.03 MPa), (b)  $\Delta P = 50$  psi (0.34 MPa), (c)  $\Delta P = 100$  psi (0.69 MPa), and (d)  $\Delta P = 200$  psi (1.38 MPa).

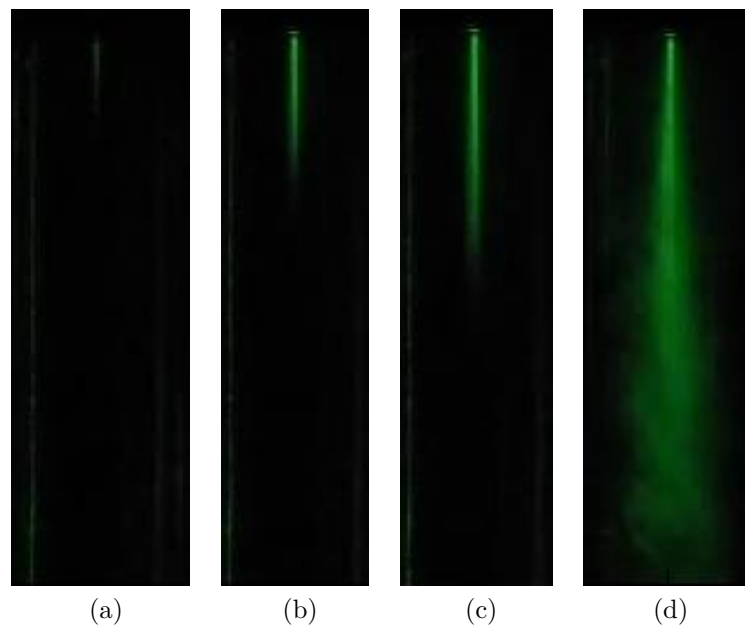


Figure B.7: Injector (4) images at (a)  $\Delta P = 5$  psi (0.03 MPa), (b)  $\Delta P = 50$  psi (0.34 MPa), (c)  $\Delta P = 100$  psi (0.69 MPa), and (d)  $\Delta P = 200$  psi (1.38 MPa).

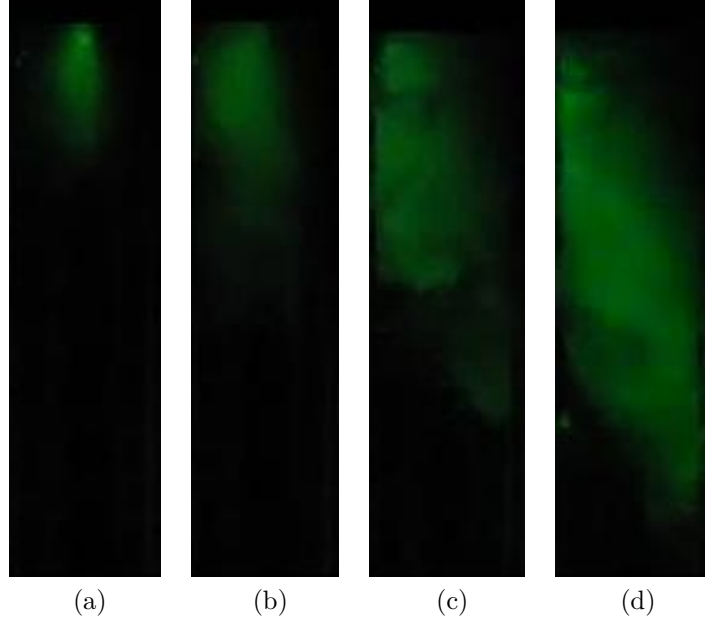


Figure B.8: Injector (5) images at (a)  $\Delta P = 5$  psi (0.03 MPa), (b)  $\Delta P = 50$  psi (0.34 MPa), (c)  $\Delta P = 100$  psi (0.69 MPa), and (d)  $\Delta P = 200$  psi (1.38 MPa).

comparing injectors (1) and (4), it is immediately obvious that the jet from injector (4) exhibits less widespread atomization of the jet for a given  $\Delta P$ , and generally seems to expand at a smaller angle compared to the similarly shaped, but larger orifice of injector (1).

The most interesting results from these initial tests come from those involving the self-impinging doublets used in injector (5). The impinging jets are oriented to lie in a vertical plane that passes through both the camera lens and the polycarbonate tube. It is obvious from examination of Fig. B.8 that for a wide range of  $\Delta P$  levels, this particular impinging design does a significantly better job atomizing and dispersing the carbon dioxide downstream of the injector. From the above results, the use of like-on-like self impinging injectors is recommended when achieving sufficient atomization is critical or problematic.

Throughout initial testing, the mechanical breakup mode was only observed during tests with both small values of  $\Delta P$  and large supercharge pressures simultaneously. These tests indicate that the mechanical breakup mode can dominate for carbon dioxide atomization over a limited range of operating conditions. However, more testing is necessary to develop correlations for the transition from the mechanical breakup mode to flash atomization. Two images of non-flashing injector operation for injectors (2) and (5) are shown in Fig. B.9 below, corresponding to a  $\Delta P$  of 5 psi (0.03 MPa) and supercharge pressures of approximately 300 psi (2.07 MPa). The non-flashing jets from these images are characterized by some breakup into larger visible droplets, and no apparent aerosol “cloud” as seen in the flashing operation of Figures B.4-B.8. The first image in Fig. B.9 corresponds to flow from an injector with a single hole, while the second image is from testing of the impinging doublet injector. As expected, these results suggest that impinging injectors provide improved atomization for non-flashing injector operations, in addition to the flashing jets described previously.

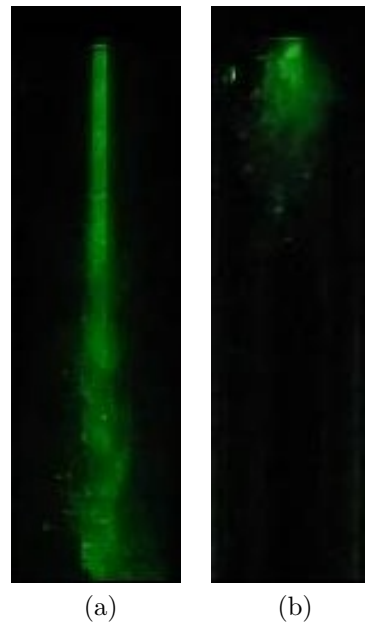


Figure B.9: Images of highly supercharged non-flashing jets using (a) single hole injector (2) and (b) impinging doublet injector (5), both at  $\Delta P = 5$  psi (0.03 MPa) and supercharge pressures of approximately 300 psi (2.07 MPa)

# Appendix C

## Instrumentation Specifications

Table C.1: Instrumentation Specifications

Name	Manufacturer (Model)	Specifications
Helium Pressure Transducer	Senstronics (OL01084-002)	0-2000 psia (0-13.79 MPa) 0-5 V
Test Section Pressure Transducers	Measurement Specialties (MS156-000004-01KPG)	0-1000 psia (0-6.89 MPa) 4-20 mA
Differential Pressure Transducer	Stellar Technology Inc. (DT140-50UD-119)	0-50 psid (0-0.34 MPa) 3 mV/V
Test Section Thermocouples	Omega (KMQSS-062G-3)	-270 to +1372 °C K type
Data Acquisition Board	National Instruments (USB-6210)	16 bit, 250 kHz
Digital Camera	Casio (EX-F1)	Up to 1200 fps Up to 1080p
Thermocouple Amplifier	Analog Devices (AD595CQ)	~10 mV/°C
Differential Pressure Transducer Amplifier	Analog Devices (AD624ADZ)	Gain = 137

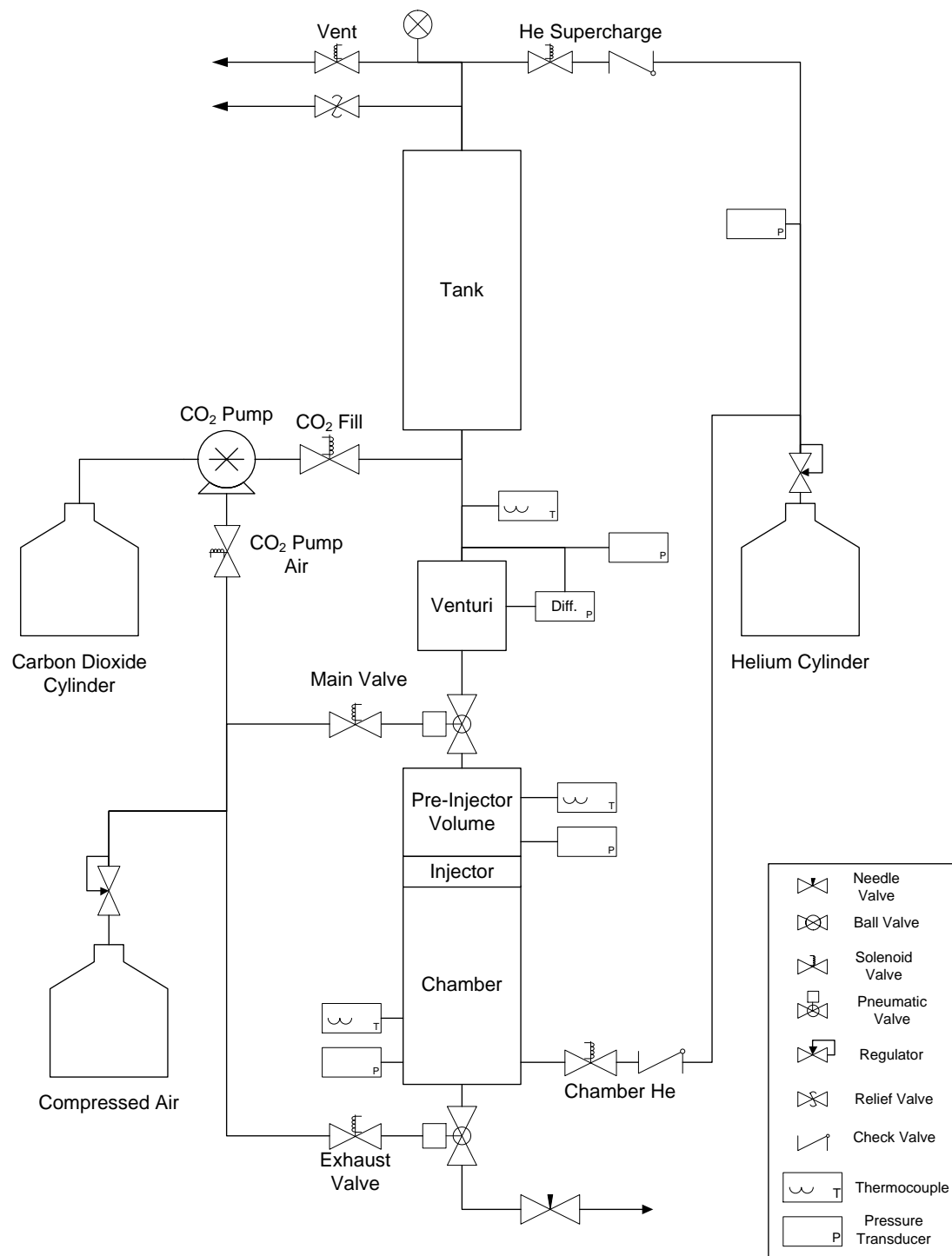


Figure C.1: Process and instrumentation diagram (P&ID) for injector and tank testing facilities

## Appendix D

# Uncertainty Analysis

Due to a careful calibration of the venturi mass flow meter used in testing with the small scale injector cold flow apparatus, the injector mass flow rate data presented in this work is expected to exhibit little experimental measurement uncertainty, especially at the mass flow rate values associated with the critical flow regime. However, due to a lack of the ability to make highly precise measurements of the injector geometries tested “as built,” the theoretical predicted values of mass flow rate which are calculated can potentially exhibit significant levels of uncertainty. While this uncertainty does not affect the readers ability to make assessments of the inception of critical flow and the absolute value of the mass flow rate measurements, it does result in uncertainties associated with the presentation of the experimentally determined injector discharge coefficients. For example, if the diameter of an injector orifice was measured slightly larger than the actual value, this would result in the overprediction of the Single Phase Incompressible mass flow rate for  $C_d = 1$  as calculated using Eq. (2.17), and thus an artificially low value of the measured discharge coefficient. In order to quantify this uncertainty in this predicted Single Phase Incompressible mass flow rate for  $C_d$  determination, a simple expression for the uncertainty propagation can be used as shown in Eq. (D.1) where  $U$  indicates the uncertainty.

$$U_{\dot{m}_{SPI}} = \sqrt{\left(\frac{\partial \dot{m}_{SPI}}{\partial A_2} U_{A_2}\right)^2 + \left(\frac{\partial \dot{m}_{SPI}}{\partial \Delta P} U_{\Delta P}\right)^2 + \left(\frac{\partial \dot{m}_{SPI}}{\partial \rho_1} U_{\rho_1}\right)^2} \quad (\text{D.1})$$

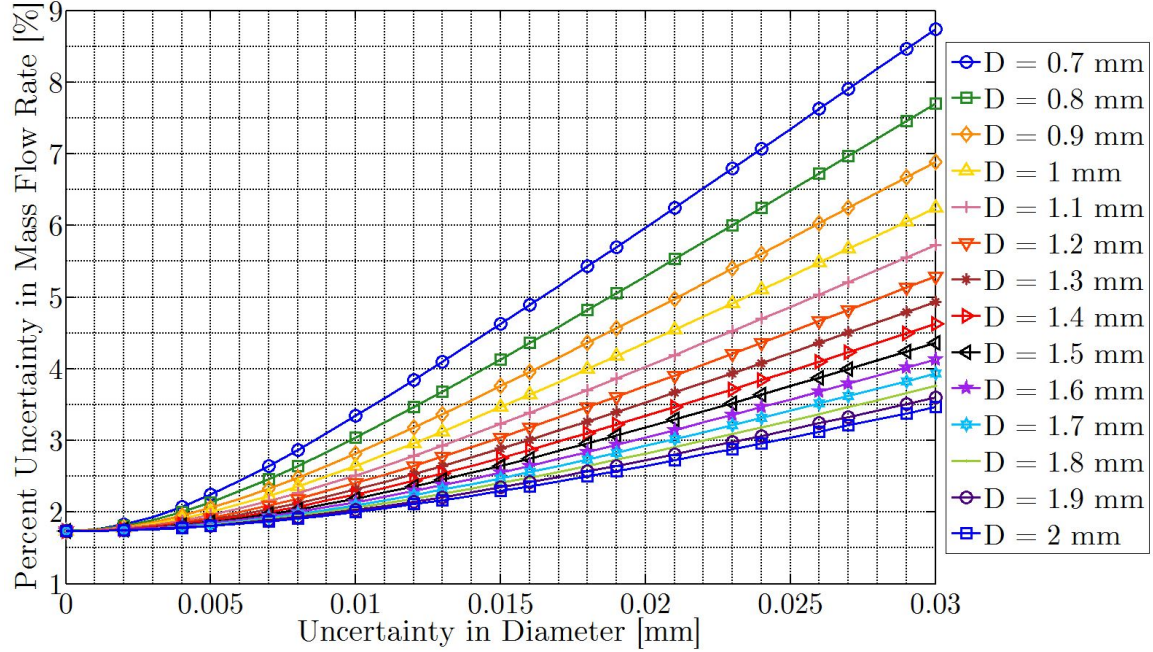


Figure D.1: Percent uncertainty in mass flow rate vs. uncertainty in measured injector hole diameter for sample uncertainty analysis.

In order to demonstrate the potential uncertainty in this type of calculation, Fig. D.1 shows the calculated uncertainty propagation for sample injectors operating under the conditions outlined below:

$$\Delta P = 200 \text{ psi} (1.38 \text{ MPa}) \quad \rho_1 = 830 \frac{\text{kg}}{\text{m}^3}$$

$$U_{\Delta P} = 5 \text{ psi} (0.03 \text{ MPa}) \quad U_{\rho_1} = 20 \frac{\text{kg}}{\text{m}^3}$$

As can be seen from Fig. D.1, it is quite beneficial to have highly accurate measurements of the injector geometry “as built” if it is desired to obtain reliable discharge coefficient data from experimental cold flow testing.

# Bibliography

- [1] Dyer, J., Doran, E., Dunn, Z., Lohner, K., Bayart, C., Sadhwani, A., Cantwell, B., and Karabeyoglu, A., “Design and Development of a 100 km Nitrous Oxide / Paraffin Hybrid Rocket Vehicle,” *43rd AIAA/ASME/SAE/ASEE Joint Propulsion Conference and Exhibit*, Cincinnati, OH, July 2007.
- [2] Thicksten, Z., Macklin, F., and Campbell, J., “Handling Considerations of Nitrous Oxide in Hybrid Rocket Motor Testing,” *44th AIAA/ASME/SAE/ASEE Joint Propulsion Conference and Exhibit*, Hartford, CT, July 2008.
- [3] Mungas, G., Vozoff, M., Rishikof, B., Strack, D., London, A., Fryer, J., and Buchanan, L., “NOFBX Monopropulsion Overview,” *14th Annual FAA Commercial Space Transportation Conference*, Washington, DC, Feb. 2011.
- [4] Sutton, G. and Biblarz, O., *Rocket Propulsion Elements*, Wiley and Sons, New York, 7th ed., 2001.
- [5] Karabeyoglu, A., Stevens, J., Geyzel, D., Cantwell, B., and Micheletti, D., “High Performance Hybrid Upper Stage Motor,” *47th AIAA/ASME/SAE/ASEE Joint Propulsion Conference and Exhibit*, No. August, San Diego, CA, Aug. 2011.
- [6] Karabeyoglu, M. A., *Transient combustion in hybrid rockets*, Ph.D. thesis, Stanford University, 1998.
- [7] Marxman, G. A. and Gilbert, M., “Turbulent Boundary Layer Combustion in the Hybrid Rocket,” *9th Symposium (International) on Combustion*, 1963, p. 371.

- [8] Marxman, G. A., Wooldridge, C. E., and Muzzy, R. J., "Fundamentals of Hybrid Boundary Layer Combustion," *Heterogeneous Combustion Conference*, No. 63, Palm Beach, FL, Dec. 1963.
- [9] Marxman, G. A., "Combustion in the Turbulent Boundary Layer on a Vaporizing Surface," *10th Symposium (International) on Combustion*, 1965, pp. 1337–1349.
- [10] Marxman, G. A., "Boundary-Layer Combustion in Propulsion," *11th Symposium (International) on Combustion*, Vol. 11, 1967, pp. 269–289.
- [11] Karabeyoglu, A., Zilliac, G., Cantwell, B. J., Dezilwa, S., and Castellucci, P., "Scale-Up Tests of High Regression Rate Paraffin-Based Hybrid Rocket Fuels," *Journal of Propulsion and Power*, Vol. 20, No. 6, 2004, pp. 1037–1045.
- [12] Karabeyoglu, A., "Stanford University AA 284a Advanced Rocket Propulsion Course Notes," 2013.
- [13] Karabeyoglu, A., Dyer, J., Stevens, J., and Cantwell, B., "Modeling of N<sub>2</sub>O Decomposition Events," *44th AIAA/ASME/SAE/ASEE Joint Propulsion Conference and Exhibit*, Hartford, CT, July 2008.
- [14] Lemmon, E. W., Huber, M., and McLindon, M., "NIST Standard Reference Database 23: Reference Fluid Thermodynamic and Transport Properties-REFPROP, Version 930," 2010.
- [15] Lemmon, E. W. and Span, R., "Short Fundamental Equations of State for 20 Industrial Fluids," *Journal of Chemical Engineering Data*, Vol. 51, 2006, pp. 785–850.
- [16] Waxman, B., Beckwith, R., Tybor, F., Zimmerman, J., and Stoll, A., "Paraffin and Nitrous Oxide Hybrid Rocket as a Mars Ascent Vehicle Demonstrator," *AIAA SPACE 2010 Conference and Exposition*, Anaheim, CA, Sept. 2010.
- [17] Zilliac, G., Waxman, B. S., Doran, E., Dyer, J., Karabeyoglu, M. A., and Cantwell, B., "Peregrine Hybrid Rocket Motor Ground Test Results," *48th*

- AIAA/ASME/SAE/ASEE Joint Propulsion Conference and Exhibit*, Atlanta, GA, Aug. 2012.
- [18] Anderson, J. D., *Fundamentals of Aerodynamics*, McGraw-Hill, New York, 4th ed., 2007.
  - [19] Perry, R. and Green, D., *Perry's Chemical Engineers' Handbook*, McGraw-Hill, 6th ed., 1984.
  - [20] Zimmerman, J. E., Cantwell, B., and Zilliac, G., "Initial Experimental Investigations of Self-Pressurizing Propellant Dynamics," *48th AIAA/ASME/SAE/ASEE Joint Propulsion Conference and Exhibit*, Atlanta, GA, Aug. 2012.
  - [21] Cornelius, K. C. and Srinivas, K., "Isentropic Compressible Flow for Non-Ideal Gas Models for a Venturi," *Journal of Fluids Engineering*, Vol. 126, No. 2, March 2004, pp. 238–244.
  - [22] Nurick, W. H., "Orifice Cavitation and Its Effects on Spray Mixing," *Journal of Fluids Engineering*, Dec. 1976, pp. 681–687.
  - [23] Vennard, J., *Elementary Fluid Mechanics*, Wiley, New York, 3rd ed.
  - [24] Moody, L. F., "Friction Factors for Pipe Flow," *Transactions of the A.S.M.E.*, Nov. 1944, pp. 672.
  - [25] White, F. M., *Viscous Fluid Flow*, McGraw-Hill, New York, 3rd ed., 2006.
  - [26] Lichtarowicz, A., Duggins, R. K., and Markland, E., "Discharge Coefficients for Incompressible Non-Cavitating Flow Through Long Orifices," *Journal of Mechanical Engineering Science*, Vol. 7, No. 2, 1965, pp. 210–219.
  - [27] Campbell, W. and Slattery, J., "Flow in the Entrance of a Tube," *Transactions of the A.S.M.E.*, Vol. 85, No. D, 1963, pp. 41.
  - [28] Langhaar, H., "Steady Flow in the Transition Length of a Straight Tube," *Journal of Applied Mechanics*, Vol. 64, 1942, pp. A55–A58.

- [29] Cantwell, B. J., *Fundamentals of Compressible Flow: A Course Reader*, 2006.
- [30] Dyer, J., Doran, E., Dunn, Z., Lohner, K., and Zilliac, G., "Modeling Feed System Flow Physics for Self-Pressurizing Propellants," *43rd AIAA/ASME/SAE/ASEE Joint Propulsion Conference and Exhibit*, Cincinnati, OH, July 2007.
- [31] Hesson, J. and Peck, R., "Flow of Two-phase Carbon Dioxide Through Orifices," *AIChE Journal*, Vol. 4, No. 2, 1958, pp. 207–210.
- [32] D'Auria, F. and Vigni, P., "Two Phase Critical Flow Models," Tech. rep., 1980.
- [33] Henry, R. E. and Fauske, H. K., "The Two-Phase Critical Flow of One-Component Mixtures in Nozzles , Orifices , and Short Tubes," *Journal of Heat Transfer*, May 1971, pp. 179–187.
- [34] Leung, J., "A Generalized Correlation for One-component Homogeneous Equilibrium Flashing Choked Flow," *AIChE Journal*, Vol. 32, No. 10, Oct. 1986, pp. 1743–1746.
- [35] Leung, J. C. and Grolmes, M. A., "A Generalized Correlation for Flashing Choked Flow of Initially Subcooled Liquid," *AIChE Journal*, Vol. 34, No. 4, April 1988, pp. 688–691.
- [36] Babitskiy, A., "Concerning the Discharge of Boiling Fluid," *Fluid Mechanic Soviet Research*, Vol. 4, 1975.
- [37] Moody, F. J., "Maximum Flow Rate of a Single Component , Two-Phase Mixture," *Transactions of the A.S.M.E*, Feb. 1965, pp. 134–141.
- [38] Fauske, H. K., "Contribution to the Theory of Two-Phase, One-Component Critical Flow," Tech. rep., 1962.
- [39] Lienhard, J. H. and Karimi, A., "Homogeneous Nucleation and the Spinodal Line," *Journal of Heat Transfer*, Vol. 103, No. 1, Feb. 1981, pp. 61–64.

- [40] Shamsundar, N. and Lienhard, J. H., "Equations of State and Spinodal Lines - A Review," *Nuclear Engineering and Design Journal*, Vol. 141, No. 1, 1993, pp. 269–287.
- [41] Burnell, J., "Flow of Boiling Water Through Nozzles, Orifices, and Pipes," *Engineering*, Vol. 164, 1947, pp. 572–576.
- [42] Zaloudek, F. R., "The critical flow of hot water through short tubes," Tech. rep., General Electric Co. Hanford Atomic Products Operation, Richland, Wash., 1963.
- [43] Solomon, B. J., *Engineering Model to Calculate Mass Flow Rate of a Two-Phase Saturated Fluid Through An Injector Orifice*, Masters thesis, Utah State University, 2011.
- [44] Zimmerman, J. E., Waxman, B. S., Cantwell, B. J., and Zilliac, G. G., "Comparison of Nitrous Oxide and Carbon Dioxide with Applications to Self-Pressurizing Propellant Tank Expulsion Dynamics," *60th Joint Army-Navy-NASA-Air Force (JANNAF) Propulsion Meeting (Available via email by contacting waxman@stanford.edu)*, Colorado Springs, CO, May 2013.
- [45] Cawthra, J. and Eisenstadt, M., "Summary of Nitrous Oxide Investigations," *TR-75-231*, July 1974, pp. 10–16.
- [46] "Solidworks Simulation Reference," 2014.
- [47] Reference, T., "Solidworks Flow Simulation Technical Reference," Tech. rep., 2012.
- [48] Wark, K. J., *Advanced Thermodynamics for Engineers*, McGraw-Hill, New York, 1995.
- [49] Span, R. and Wagner, W., "A New Equation of State for Carbon Dioxide Covering the Fluid Region from the Triple-Point Temperature to 1100 K at Pressures up to 800 MPa," *Journal of Physical and Chemical Reference Data*, Vol. 25, No. 6, 1996, pp. 1509–1596.

- [50] Shallcross, D., "Humidity Diagrams for Engineers," *Physical Property Data, Handbook of Psychrometric Charts*, p. 20.
- [51] Karabeyoglu, M. A., Altman, D., and Cantwell, B. J., "Combustion of Liquefying Hybrid Propellants : Part 1 , General Theory," *Journal of Propulsion and Power*, Vol. 18, No. 3, 2002, pp. 610–620.
- [52] Chadler, A. A., *An Investigation of Liquefying Hybrid Rocket Fuels with Applications to Solar System Exploration*, Ph.D. thesis, Stanford University, 2012.
- [53] Cantwell, B., Karabeyoglu, A., and Altman, D., "Recent Advances in Hybrid Propulsion," *International Journal of Energetic Materials and Chemical Propulsion*, Vol. 9, No. 4, 2010, pp. 305–326.
- [54] Doran, E., Dyer, J., Lohner, K., Dunn, Z., and Cantwell, B., "Nitrous Oxide Hybrid Rocket Motor Fuel Regression Rate Characterization," *43rd AIAA/ASME/SAE/ASEE Joint Propulsion Conference and Exhibit*, No. July, Cincinnati, OH, July 2007.
- [55] Doran, E., Dyer, J., Marzona, M. T., Karabeyoglu, M. A., Zilliac, G. G., Mosher, R., and Cantwell, B. J., "Status Update Report for the Peregrine Sounding Rocket Project : Part III," *45th AIAA/ASME/SAE/ASEE Joint Propulsion Conference and Exhibit*, Aug. 2009.
- [56] Walker, J. S., *Fast Fourier Transforms*, Vol. 24, CRC press, 1996.
- [57] Cohen, J. M., Proscia, W., and Delaat, J., "Longitudinal-Mode Combustion Instabilities: Modeling and Experiments," Tech. Rep. May, NASA, 2000.
- [58] Blomshield, F. S., "Lessons Learned in Solid Rocket Combustion Instability," *AIAA Missile Sciences Conference*, Monterey, CA, Nov. 2006.
- [59] Karabeyoglu, M. A., Zilwa, S. D., Cantwell, B., and Zilliac, G., "Transient Modeling of Hybrid Rocket Low Frequency Instabilities," *39th AIAA/ASME/SAE/ASEE Joint Propulsion Conference and Exhibit*, July 2003.

- [60] Yang, V. and Anderson, W., "Liquid Rocket Engine Combustion Instability," *Progress in Astronautics and Aeronautics*, Vol. 169, 1995.
- [61] Karabeyoglu, A., Stevens, J., and Cantwell, B., "Investigation of Feed System Coupled Low Frequency Combustion Instabilities in Hybrid Rockets," *43rd AIAA/ASME/SAE/ASEE Joint Propulsion Conference and Exhibit*, No. July, Cincinnati, OH, July 2007.
- [62] Carpenter, R. L., Boardman, T. A., and Claflin, S. E., "Hybrid Propulsion for Launch Vehicle Boosters : A Program Status Update," *31 st AIAA / ASME / SAE / ASEE Joint Propulsion Conference and Exhibit*, San Diego, CA, July 1995.
- [63] Rocker, M., "Modeling of Nonacoustic Combustion of Hybrid Instability in Simulations Motor Tests," Tech. rep., NASA, 2000.
- [64] Randall, L., "Rocket Applications of the Cavitating Venturi," *Journal of the American Rocket Society*, Vol. 22, No. 1, 1952, pp. 28–38.
- [65] Brennen, C., *Fundamentals of Multiphase Flows*, 2005.
- [66] Karabeyoglu, M. A., "Nitrous Oxide and Oxygen Mixtures (Nytrox) as Oxidizers for Rocket Propulsion Applications," *Journal of Propulsion and Power*, Vol. 30, No. 3, May 2014, pp. 696–706.
- [67] Chandler, A. A., Cantwell, B. J., Hubbard, G. S., and Karabeyoglu, A., "Feasibility of a single port Hybrid Propulsion system for a Mars Ascent Vehicle," *Acta Astronautica*, Vol. 69, Dec. 2011, pp. 1066–1072.
- [68] Kitamura, Y., Morimitsu, H., and Takahashi, T., "Critical Superheat for Flashing of Superheated Liquid Jets," *Industrial Engineering and Chemistry Fundamentals*, Vol. 25, No. 2, 1986, pp. 206–211.
- [69] Cleary, V., Bowen, P., and Witlox, H., "Flashing liquid jets and two-phase droplet dispersion I. Experiments for derivation of droplet atomisation correlations." *Journal of hazardous materials*, Vol. 142, No. 3, April 2007, pp. 786–96.

- [70] Kuo, K. K., Hsieh, W.H., Cheung, F.B., Yang, A.S., Kline, M.C., Woodward, R.D. and Brown, J., "Experimental Observation of Dense Spray and Mixing of Liquid Jets Emanating from Doublet Injectors," *NASA-CR-191222*, , No. Task 1, 1992.